Universities of Florence, Perugia and Minho

International Doctorate in Civil and Environmental Engineering - XXXII Cycle

Coordinator: Prof. Claudio Borri

An Innovative SHM Solution for Earthquake-Induced Damage Identification in Historic Masonry Structures

Ph.D. candidate: Alban Kita

Italian supervisors
Prof. Filippo Ubertini
Dr. Nicola Cavalagli

Department of Civil and
Environmental Engineering,
University of Perugia (Italy)

Portuguese supervisors
Prof. Paulo B. Lourenço
Dr. Maria Giovanna Masciotta

ISISE, Department of
of Civil Engineering,
University of Minho (Portugal)

2016 - 2019

Abstract

The present Ph.D. Thesis was developed within a collaboration between the Department of Civil and Environmental Engineering of the University of Perugia, Italy, and the Department of Civil Engineering of the University of Minho, Portugal.

The main objective of this research work concerned the development and validation of an innovative methodology aimed at the detection, localization and quantification of earthquake-induced damages in historic masonry structures. The high cultural, economic and political value set upon historic buildings spread out all over the world has made the earthquake-induced damage identification, as well as preservation and conservation of architectural heritage, a subject of outstanding importance. The proposed methodology, called DORI, is based on the combination of data-driven, as well as innovative model-based methods, addressing the Damage identification based on Operational modal analysis (OMA), Rapid surrogate modeling and Incremental dynamic analysis (IDA) for Cultural Heritage (CH) masonry buildings subjected to earthquakes. More in detail, the DORI methodology proposes the static-and-dynamic data fusion in the OMA-based damage detection method, and extends it through the introduction and implementation of two independent and complementary innovative model-based methods, for localization and quantification of earthquake-induced damage in permanently monitored historic masonry buildings: the former is a surrogate model-based method, a rapid tool which combines long-term vibration monitoring data (i.e. OMA) and numerical modeling, while the latter is based on non-linear seismic IDA.

The Thesis focuses on the validation of different aspects of the DORI methodology, through application to four case study structures: an internationally well-known laboratory masonry structure, called the *Brick House*, and three CH masonry buildings equipped with permanent Structural Health Monitoring systems, namely the *Consoli Palace*, the *Sciri Tower* and the *San Pietro Bell Tower*.

The adopted enhanced vibration-based SHM tool, by introducing crack amplitudes as predictors in the dynamic MLR model, was validated in the case of the Consoli Palace, enabling rapid and automated earthquake-induced damage detection, even for small struc-

tural damages at an early stage, conceivably caused by a moderate/light seismic event. Afterwards, the surrogate model-based procedure for earthquake-induced damage detection and localization was applied in the case of the Sciri Tower, using long-term vibration monitoring data and numerical modeling. In particular, a quadratic surrogate model is used, whose objective function considers not only experimentally identified and numerically predicted damage-induced decays in natural frequencies but also on changes in mode shapes. The procedure was validated by considering both simulated damage scenarios, as well as a slight change in structural behavior experimentally observed after a seismic event. Finally, the proposed seismic IDA-based method, introduced for the first time in this Thesis and aimed at localization and quantification of earthquake-induced damages in masonry structures, is applied to the Brick House and San Pietro Bell Tower. It relies on a priori IDA carried out from a numerical model and construction of multidimensional IDA curve sets relating meaningful local damage parameters to selected seismic intensity measures. The IDA-based procedure has demonstrated to correctly localize damage in specific parts of the structures and to quantify earthquake-induced damage with a good level of approximation. The results are particularly interesting in the case of the San Pietro Bell Tower due to the integration of the IDA-based damage identification with seismic SHM data recorded during the 2016 Central Italy seismic sequence, allowing the proposal and exploitation of some original response intensity measures.

In conclusion, the DORI methodology proposed in this Thesis for earthquake-induced damage detection, localization and quantification is a novel methodological approach, successfully applied and validated in historic masonry structures, constituting a promising tool for rapid post-earthquake damage assessment of CH structures under long-term SHM monitoring.

Keywords: *Earthquake-induced damage identification*; *Structural Health Monitoring*; *Historic masonry structures*; *Cultural Heritage*; *Preventive conservation*; *Finite Element modeling*; *Long-term monitoring*; *Temperature effects*; *Surrogate modeling*; *Incremental Dynamic Analysis*; *Earthquake*; *Intensity measure*; *Damage measure*; *Masonry tower*; *Masonry bell tower*; *Masonry palace*.

To Dori!

Thank you for being (in) my Life.

Acknowledgements

Contents

List of Figures

List of Tables

List of acronyms/abbreviations/symbols

$\alpha_{i,j}$ Weight coefficients

ϵ Flow potential eccentricity

γ Specific weight

μ Viscosity parameter

ν Poisson's ratio

ψ Dilation angle in the p–q plane

σ_c Compressive strength

σ_t Tensile strength

ASI_{NH} Nau and Hall P-Acceleration Spectrum Intensity

ASI_{VT} Von Thun Acceleration Spectrum Intensity

A_{95} Acceleration parameter

C_a Amplification of acceleration

C_d Amplification of displacement

C_v Amplification of velocity

DSI_{NH} Nau and Hall Displacement Spectrum Intensity

E_I Input Energy

I_A Arias Intensity

I_a Riddell and Garcia compound acceleration index

I_C Characteristic Intensity

I_D Cosenza and Manfredi Damage Factor

I_d Riddell and Garcia compound displacement index

I_F Fajfar index

I_H Housner P-Velocity Spectrum Intensity

I_S Sandi instrumental intensity

I_v Riddell and Garcia compound velocity index

M_w Moment magnitude

P_D Destructive Potential Factor

RI_A Response Arias Intensity

RI_C Response Characteristic Intensity

$S_{a,avg}$ The geometric mean of spectral acceleration

$S_a(T1)$ Spectral acceleration at T1

$S_d(T_1)$ Spectral displacement at T1

S_{paC} Inelastic spectral acceleration

$S_v(2T1)$ Spectral velocity at 2T1

$S_v(T1)$ Spectral velocity at T1

VSI_{HC} Hidalgo and Clough P-Velocity Spectrum Intensity

VSI_K Kappos P-Velocity Spectrum Intensity

VSI_{NH} Nau and Hall P-Velocity Spectrum Intensity

VSI_{VT} Von Thun Velocity Spectrum Intensity

$\bar{\varepsilon}_c^{\mathrm{pl}}$ Equivalent plastic strain

$\bar{\varepsilon}_t^{\mathrm{ck}}$ Cracking strain

$\varepsilon_1^{\mathrm{pl}}$ First principal plastic strain

ε_t Total strain

$\varepsilon_{0t}^{\mathrm{el}}$ Elastic strain of undamaged material

AVT Ambient Vibration Test

CAD Cumulative Absolute Displacement

CAV Cumulative Absolute Velocity

CBM Condition-Based Maintenance

CDP Concrete Damage Plasticity

CH Cultural Heritage

CSA Castelnuovo-Assisi seismic monitoring station

d_t Tensile damage variable

DM Damage Measure

DOF Degree of freedom

$DORI$ **D**amage identification based on **O**perational modal analysis & **R**apid surrogate modeling & **I**ncremental dynamic analysis for CH masonry buildings subjected to earthquakes

E Young's modulus

EDA Effective Design Acceleration

$EFDD$ Enhanced Frequency Domain Decomposition

EPA Effective Peak Acceleration

EPD Effective Peak Displacement

$EPRI$ Electrical Power Research Institute

EPV Effective Peak Velocity

ESD European Strong Motion

FDD Frequency Domain Decomposition

FE Finite Element

FEM Finite Element Method

FEMU FEM Updating

GMPE Ground Motion Prediction Equation

HERACLES HEritage Resilience Against CLimate Events on Site

IDA Incremental Dynamic Analysis

IM Intensity Measure

ITACA ITalian ACcelerometric Archive

LCL Lower Control Limit

LDA Linear dynamic analysis

LNEC Laboratorio Nacional de Engenharia Civil (in Portuguese)

LSA Linear static analysis

LVDT Linear Variable Displacement Transducer

MAC Modal Assurance Criterion

MID Maximum Incremental Displacement

MIV Maximum Incremental Velocity

MLR Multivariate Linear Regression

MSA Multiple Stripe Analysis

NLDA Non-linear dynamic analysis

NLSA Non-linear static analysis

NTC Norme tecniche per le costruzioni (in Italian)

NZS New Zealand Standards

OMA Operational Modal Analysis

OSS Osservatorio Sismico delle Strutture

PBEE Performance-Based Earthquake Engineering

PCA Principal Component Analysis

PEMAG Plastic strain magnitude

PGA Peak Ground Acceleration

PGD Peak Ground Displacement

PGV Peak Ground Velocity

PRA Peak Response Acceleration

PRD Peak Response Displacement

PRV Peak Response Velocity

RMS Root Mean Square

RMSA Root Mean Square Acceleration

RMSD Root Mean Square Displacement

RMSE Root Mean Square Error

RMSRA Root Mean Square Response Acceleration

RMSRV Root Mean Square Response Velocity

RMSV Root Mean Square Velocity

RSL Remaining Service Life

RSM Response Surface Method

SDOF Single-degree-of-freedom

SED Specific Energy Density

SF Scale Factor

SHM Structural Health Monitoring

$SIMBAD$ Selected Input Motions for Displacement-Based Assessment and Design

SM Surrogate model

SMA Sustained Maximum Acceleration

SMV Sustained Maximum Velocity

SPO Non-linear static pushover

SSI Stochastic System Identification

t_B Bracketed duration

t_D Significant duration

t_E Total duration

t_U Uniform duration

UCL Upper Control Limit

Chapter 1

Introduction and the new proposed DORI methodology

1.1 Motivation

Natural disasters are an effect of natural hazards (such as tornadoes, volcanic eruptions, landslides, tsunamis or earthquakes) that cause millions of deaths and severe socioeconomic impacts through the centuries, affecting the development of many countries. From this perspective, earthquakes rank among the most devastating natural hazards faced by mankind on Earth. According to (Hough and Bilham 2006), earthquakes caused six (6) million fatalities in 500 years (1500-2000). The costs associated with catastrophic collapses are often unsustainable. The cities are areas with a concentration of elements of risk (people, buildings, infrastructures, etc.) and the built environment is continuously exposed to the risk of structural damage due to aging effects, excessive loads, accidents, etc. Existing masonry buildings are one of the most vulnerable elements of risk. They were built for many centuries according to the experience of the builder, taking into account simple empirical rules of construction and without specific reference to any particular seismic code. Furthermore, in seismic areas, unreinforced masonry structures represent an important part

1

of the building stock. In recent decades, there is a great awareness and a strong increasing interest in the importance of conservation and safeguarding of heritage buildings as they make up vital assets with manifold positive socioeconomic effects. It is therefore reflected in the scientific literature. Based on a literature search on Scopus database concerning earthquake engineering, the top-5 (author) keywords are "masonry", "cultural heritage", "seismic vulnerability", "masonry structures" and "strengthening" (Plevris et al. 2019).

The vulnerability and structural assessment of Cultural Heritage (CH) structures, especially as it concerns the seismic hazard, is a compelling engineering challenge for the EU, in general, and for Italy, in particular. Italy has a considerable historical heritage, leading the 2019 UNESCO World Heritage List with 55 sites, and at the same time, it is characterized by a high seismic hazard, thus, the conservation of heritage buildings is of paramount importance. Maintenance and conservation of historic monumental buildings is a very onerous duty for public administrations, which typically have to preserve numerous CH constructions with a limited budget. Therefore, the development of tools capable of mitigating the effects of earthquakes on historic structures is of great interest. To track and keep under control the structural behavior, Structural Health Monitoring (SHM) systems are the best tools available up to date. They can provide valuable and nearly real-time information for assessing integrity, durability and reliability of structures, allowing quantifying changes in the structures' inherent characteristics and to early detect structural faults even if not visible to human eyes. Vibration-based SHM methods, based upon the monitoring of structural vibrations under operational conditions with no external excitation sources, can improve protection and conservation of CH buildings by providing real-time diagnostic and prognostic data, enabling Condition-Based Maintenance (CBM) instead of prevention-based or breakdown-based maintenance, with significant economic potential.

Advanced long-term vibration-based SHM tools allow to automatically detect earthquake-induced damages in historic masonry structures, relating the structural damage to permanent variations in the modal properties of the structure. The objectives of this Thesis focuses on the identification (detection, localization and quantification) of earthquake-induced structural pathologies through the continuous SHM of CH buildings and structural analysis on tuned numerical models. Preventive conservation and CBM constitute crucial aspects in post-earthquake decision-making, leading to optimal employment of the economic resources, prioritizing inspections and timely structural interventions.

1.2   Literature review

The SHM concept and definition date back to 1996. In general terms, SHM is defined as the process of implementing a damage detection strategy for aerospace, civil and mechanical engineering infrastructure, aimed at the automated assessment of structural performance and at tracking its evolution in time, using data acquired by sensing systems (Sohn et al. 2002a). In other words, SHM can be regarded as the systematic online process of observing, tracking and sampling data over a period of time, to assess the fitness for purpose of structural systems under inevitable aging and damage accumulation resulting from operational and environmental conditions (Masciotta et al. 2019). A first review of the technical literature concerning the detection, location, and characterization of structural damage via techniques that examine changes in measured structural vibration response can be found in (Doebling et al. 1996). The damage-identification methods according to required measured data and analysis technique are categorized, followed by applications that include changes in modal frequencies, changes in measured mode shapes, changes in measured flexibility coefficients and others. The main components of an SHM process are: (i) operational evaluation, (ii) data acquisition, fusion and cleansing, (iii) feature extraction and information condensation and (iv) statistical model development for feature discrimination.

Damage is defined as a change introduced into a system, in material and/or geometric properties, that adversely affects its current or future performance (Sohn et al. 2002a). It is not meaningful without a comparison between two system states, where one is often an initial or undamaged state. System changes include material and/or geometric property changes, changes in boundary conditions, and changes in system connectivity. The damage state of a system can be described along the lines of four (4) levels of damage identification, concerned as key stages in damage diagnosis. Based on the output features, a system of classification for damage identification methods, as presented by Rytter (Rytter 1993), defines four (4) levels:

- Level 1: Determination whether or not the damage is present in the structure - Detection.

- Level 2: Determination of the geometric location/position of the damage - Detection + Localization.

- Level 3: Extension and/or quantification of the severity of the damage - Detection + Localization + Quantification.

- Level 4: Prediction of the remaining service life RSL of the structure - Detection + Localization + Quantification + Prediction.

The quantification of damage and prediction of the remaining lifetime are the most difficult issues, particularly the latter. The Prediction level concerns the prognosis as the coupling of information from SHM, including monitoring of environmental and operational conditions, component and system-level testing, and modeling to estimate condition and useful life.

The field of SHM embraces different techniques which can be classified according to various criteria. In general, SHM techniques can be categorized in global and local. The former group concerns online vibration-based monitoring techniques suitable for investigations at the full-scale system-level, obtaining information about the overall response of the structure. The local group consists of offline inspection methods and investigations at the component-level, beneficial in particular when the target areas are known in advance (Masciotta et al. 2019). Depending on the type and configuration of sensing and data acquisition systems, SHM techniques can be also classified in traditional (or standard) and modern (or smart). Traditional approaches rely on tethered-based sensing systems that exploit coaxial cables to communicate the response measurements to a central data repository (low sensor densities). On the other hand, the modern SHM system includes wireless sensors, fiber optic sensors and more.

Among the different available approaches for SHM, such as data-driven methods, model-based methods and more, long-term vibration-based systems have received increasing attention, including applications for post-earthquake structural assessment. Such systems are typically based on the continuous acquisition of the dynamic response of a structure in operational conditions and in the application of suitable statistical tools aimed at continuous modal identification (Magalhães et al. 2009; Rainieri and Fabbrocino 2010; Reynders et al. 2012; Ubertini et al. 2013), removing the effects of changing environmental conditions and revealing the formation of small damage in the structure, the latter through automated inspection of anomalies in the time series of the natural frequencies of vibration by using unsupervised learning techniques (Fugate et al. 2001; Sohn et al. 2002b; Oh and Sohn 2009; Farrar and Worden 2012).

Dynamic signatures and, in particular, estimates of modal parameters are used in vibration-based SHM systems for automated structural performance assessment and early-stage damage detection (Deraemaeker et al. 2008), whereby structural damage can be in many cases detected as a modification in the global dynamic behavior of the structure (Alvandi and Cremona 2006; Materazzi and Ubertini 2011; Magalhães et al. 2012). In particular, natural frequencies of vibration have recently proved to be very effective and convenient damage sensitive features for vibration-based SHM. This automated detection of small changes in the structural performance (anomalies in the structural behavior associated with local changes in stiffness), typically produced by earthquakes or by other types of dynamic loadings, allows cost-effective management of maintenance and restoration (post-earthquake) interventions. In this context, SHM systems can improve protection and conservation of structures by providing real-time diagnostic and prognostic data, thus enabling condition-based maintenance instead of periodic or breakdown-based maintenance, with a significant optimization of economic expenses (Farrar and Worden 2007).

Vibration-based systems are very attractive in SHM due to the possibility of obtaining reliable modal parameter estimates from in-service response data through automated Operational Modal Analysis (OMA) techniques (Magalhães et al. 2009; Rainieri and Fabbrocino 2010; Reynders et al. 2012; Ubertini et al. 2013; Brincker and Ventura 2015), typically using a small number of sensors. Powerful tools allow tracking the evolution in time of the parameters associated with a specific structural mode (modal tracking). Furthermore, recent developments in the field have led to the definition of statistical tools that permit to remove the variance in the data associated with changing environmental conditions (typically temperature and humidity) and to detect anomalies in the structural behavior corresponding to very small variations in frequencies. These techniques are based on multivariate statistical analysis, such as Multivariate Linear Regression (MLR) (Worden et al. 2002), Principal Component Analysis (PCA) (Yan et al. 2005a; Yan et al. 2005b; Bellino et al. 2010) and novelty detection by means of statistical process control tools such as control charts (Worden et al. 2002; Farrar and Worden 2012; Magalhães et al. 2012; Mosavi et al. 2012; Dackermann et al. 2014; Dervilis et al. 2015). In this way, small changes in the structural behavior occurring after an earthquake can be automatically detected or, conversely, the same techniques assume the structure in the healthy state after the event if no significant deviations of the data from normal conditions are observed. If applied to a multitude of structures, it would be possible giving priority to those constructions that have exhibited the largest deviations from normal conditions after an earthquake.

While SHM systems can potentially offer the possibility to obtain accurate condition screenings of the structural health, problems, critical aspects and technical limitations for applications to CH structures still exist. The selection of the proper sensing hardware and signal processing tools, the minimum number of sensors, their appropriate configuration, just to mention a few, make the damage identification task very challenging. Damage, by its nature, is a highly localized phenomenon, thus the careful selection and deployment of sensors are critical for its spacial detection. To obtain reliable and high-quality structural information, it is important to monitor the structural behavior at the fine-grained level, ensuring a sufficiently large number of sensors (Masciotta et al. 2019). Recently, wireless technologies have emerged aiming at providing relatively inexpensive and densely distributed sensor platforms for autonomous SHM and damage detection. However, although these considerable advancements, wireless SHM systems still present several limitations which are preventing the full realization of their potential, such as inappropriate instrumentation and sensor overload, reliable network topology, data compression and transmission, data mining, energy consumption and storage cost, environmental and noise effects, and more (Brownjohn 2007). Nevertheless, they possess all the advantages of both Ambient Vibration Tests (AVT) and OMA that make them particularly attractive for applications, such as their fully non-destructive nature and the relatively inexpensive equipment that is necessary for testing, resulting in historical and architectural respect conforming to international criteria and protocols on cultural heritage preservation. Moreover, continuous tracking of the actual structural conditions, typically using a limited number of sensors, is enabled in a fully automated way (Overschee and Moor 1996; Reynders et al. 2012). Although vibration-based SHM and damage detection have unavoidable limitations in those cases where seismic damages affect only very limited portions of the structure scarcely influencing global vibration modes, they are useful for detecting different types of damages, including very small ones that do not affect the safety of the structure. In this context, considering the pros and cons, more widespread applications of continuous SHM for historic constructions are however having constantly growing interest.

The first significant developments in SHM originated from major construction projects in civil infrastructure, such as large dams (Comerford et al. 1992), large-scale bridges (Ko and Ni 2005), offshore platforms (Brederode et al. 1986), nuclear installations, tunnels and excavations, and more. The primary scope was to gain a better insight into the structural behaviour of such systems during construction activities, normal operation and extreme events (earthquakes, strong winds and floods), by tracking specific parameters suitable for

the extraction of information regarding the structural response and for the identification of possible anomalous changes (Masciotta et al. 2019). In the context of SHM for historic structures, several applications of AVT and OMA, aimed at vulnerability assessment through calibration of Finite Element (FE) models, can be found in the literature in the case of historic bridges (Calcada et al. 2002; Spyrakos et al. 2004; Brencich and Sabia 2008; Limongelli et al. 2018; Gkoktsi et al. 2019; An et al. 2019), monumental buildings (Bartoli et al. 1996; Jaishi et al. 2003; Casarin and Modena 2008; Pau and Vestroni 2008; Ramos et al. 2010; Ramos et al. 2011; Aras et al. 2011; Formisano et al. 2012; Ramos et al. 2013; Clementi et al. 2017; Formisano et al. 2018a; Lorenzo et al. 2019) and historic towers (Bennati et al. 2005; Ivorra and Pallares 2006; Gentile and Saisi 2007; Pena et al. 2010; Oliveira et al. 2012; Foti et al. 2012; Pieraccini et al. 2014; Gentile et al. 2015; Pellegrini et al. 2018; Bru et al. 2019; Ivorra et al. 2019), including applications as tools for non-destructive evaluation of the severity of damages caused by earthquakes (Tashkov et al. 2010; Krstevska et al. 2010).

While the applications of long-term permanent vibration-based SHM systems can be mentioned in the literature considering bridges, critical infrastructures (Materazzi and Ubertini 2011; Magalhães et al. 2012; Ubertini et al. 2013) and public buildings (Dolce et al. 2017), the implementation of multivariate statistical analysis techniques to historic and monumental constructions equipped with permanent vibration-based SHM systems is not yet widespread, with only a few examples (Bartoli et al. 1996; Ramos et al. 2010; Saisi et al. 2015; Ubertini et al. 2018; Kita et al. 2019b; Gentile et al. 2019). Most of the under monitoring structures have dealt with field data artificially modified for simulating damage effects (Ntotsios et al. 2008; Magalhães et al. 2012; Comanducci et al. 2015; Comanducci et al. 2016) and only few applications have experienced earthquake field data recorded on real structures undergoing actual damage (Saisi et al. 2015; Gentile et al. 2016; Ubertini et al. 2018; Gentile et al. 2019), also including the Osservatorio Sismico delle Strutture (OSS), an Italian network of permanent seismic monitoring systems installed in public buildings in Italy (Dolce et al. 2017; Cattari et al. 2019). A practical demonstration of the ability of a permanent vibration-based SHM system to efficiently detect an early stage earthquake-induced damage (not detected by a mere visual inspection), presenting to some extent, also damage quantification in the form of permanent variations in natural frequencies, can be found in (Ubertini et al. 2018).

1.3   The proposed DORI methodology

The DORI methodology proposed in this Thesis consists of an enhanced data-driven vibration-based method combined with two independent innovative model-based methods, aimed at the detection, localization and quantification of earthquake-induced damages in historic masonry structures. Specifically, **DORI** addresses the **D**amage identification based on **O**perational modal analysis & **R**apid surrogate modeling & **I**ncremental dynamic analysis for CH masonry buildings subjected to earthquakes. The general framework of the DORI methodology is summarized in the flow chart illustrated in Fig. 1.1, while the description is provided in the next paragraphs.

The very first activities to be carried out concern detailed preliminary investigations such as geometrical survey, on-site inspection and structural condition assessment (visual and instrumental/analytical), damage survey with the mapping of material degradation and structural crack pattern analysis, material characterization and so forth (Lourenço 2006; Ubertini et al. 2016). All these activities provide the necessary information for carrying out AVT, whose main objective is evaluating the baseline dynamic characteristics of the structure and, in particular, its natural frequencies, mode shapes and damping ratios. The overall results and information from these preliminary investigations and AVT serve as the basis for the development and installation of the permanent vibration-based SHM system, choosing, in particular, the best sensor's location for long-term SHM purposes, as well as for the construction and calibration of numerical models.

The development of long-term structural health monitoring systems for preventive conservation of historic masonry buildings has received increasing scientific interest. In this context, validated data-driven OMA-vibration-based SHM methods for damage detection combine automated mode tracking, multiple data regression and novelty detection. In light of these considerations, the first goal of this Thesis is to implement an enhanced OMA-vibration-based SHM tool for automated earthquake-induced damage detection. The DORI methodology proposes a data-driven damage detection method with a significant improvement in the removal of the effects of changes in environmental and operational conditions from identified natural frequencies, in other words, an enhanced data cleansing, which represents a key step for damage detection. The introduction of static measures (in addition to temperatures) as predictors to the statistical tools for the extraction of damage-sensitive features is proposed in this Thesis in the case of an historic stiff masonry

8
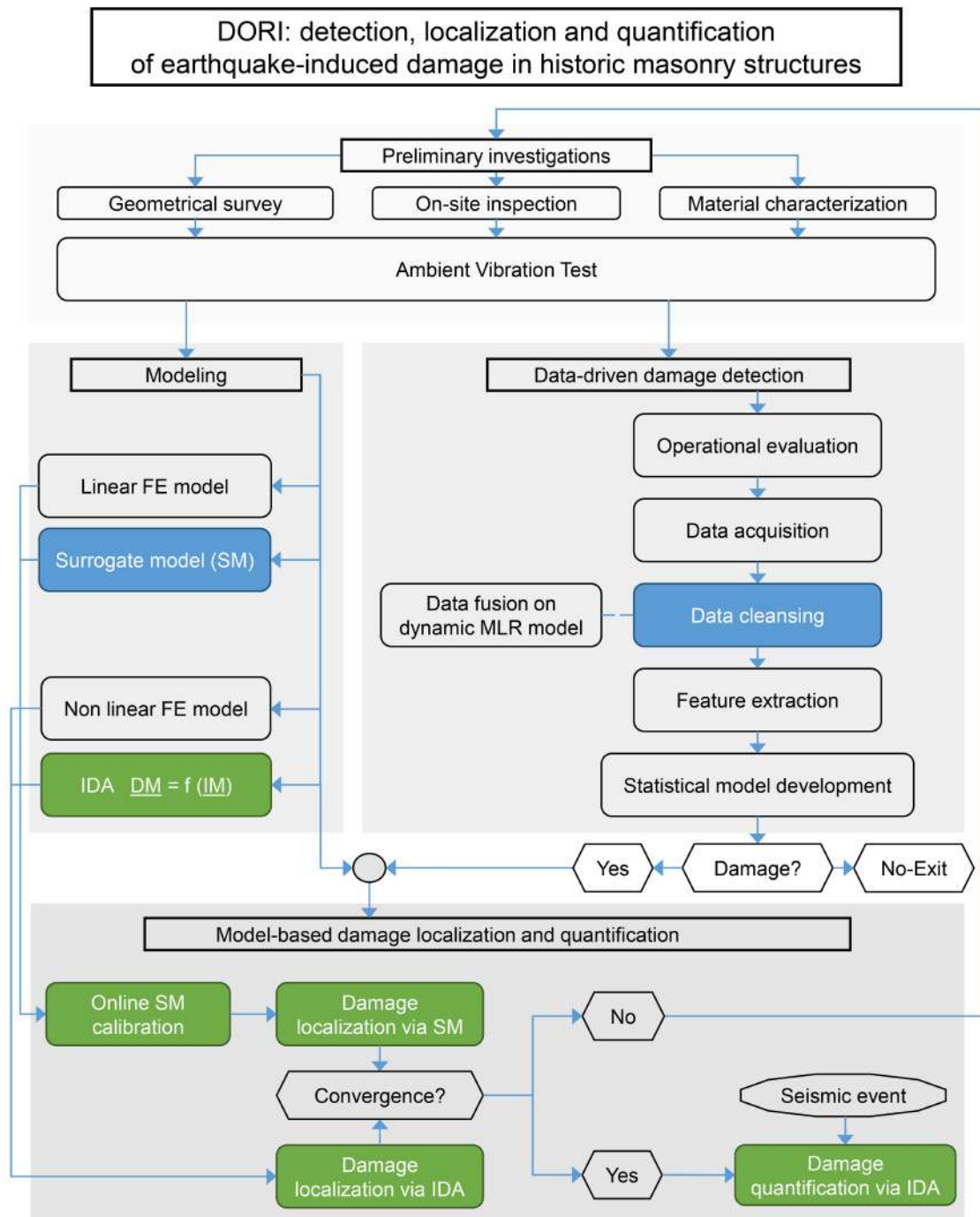
Figure 1.1: General framework of the DORI methodology: **D**amage identification based on **O**perational modal analysis & **R**apid surrogate modeling & **I**ncremental dynamic analysis.

building. The method is tested and validated on the Consoli Palace, an iconic monumental masonry building located in Gubbio, Italy, which is being continuously monitored by a permanent long-term static and dynamic SHM system since July 2017. First, the continuous modal identification is not common in the literature in the context of long-term monitoring of stiff masonry structures such as palaces, given the majority of validated modal tracking applications essentially concerning slender towers. In addition, the availability of continuous static features in the present case study, in particular, crack amplitude data, allows an enhancement of the dynamic MLR model, achieving a more accurate damage detection. The continuous monitoring data acquired over a sufficient time window, enable rapid and automated damage detection, even for small damages at an early stage (not yet detectable by visual inspections) caused by moderate earthquakes, thus constituting an effective low-cost tool for CBM and preventive conservation of historic masonry structures.

Subsequently to the OMA-based data-driven damage detection, methods addressing higher levels of damage identification with a certain accuracy represent a major challenge and are yet to be defined, especially when dealing with earthquake-induced damages. In this context, the second goal of this Thesis is to address the earthquake-induced damage localization and quantification task in historic masonry structures, by combining two innovative independent model-based methods, the former consisting in the use of a calibrated Surrogate Model (SM), while the latter based on Incremental Dynamic Analysis (IDA).

The SM-based method relies on the use of long-term OMA-vibration-based monitoring data, dynamic MLR models and numerical model updating. While damage detection can be essentially considered a data-driven process, damage localization typically requires the construction and the calibration of a FE model of the structure, in order to link identified modal parameters to variations of damage-related mechanical parameters. The tuned numerical FE model is ideally subdivided into distinctive macrostructural elements to discriminate such damage-dependent structural parameters belonging to different zones and bound the localization of damage. The real-time damage detection and localization are performed by using long-term monitoring data and by solving an inverse FE model calibration problem on a SM. To minimize the computational effort, a simple SM consisting of a quadratic expression relating natural frequencies and modal shape components to elastic parameters is considered. In this context, equivalent elastic properties of macrostructural elements are identified by minimizing an objective function considering experimentally identified and numerically predicted damage-induced decays in natural frequencies and

changes in eigenvector components. In particular, the continuous identification of these damage-dependent properties is carried out by the online minimization of the relative differences between experimental and numerical modal parameters. The innovative aspect of the proposed method of DORI is represented by defining the objective function that combines both natural frequencies and mode shapes, and not only natural frequencies. It allows increasing the number of degrees of freedom of the inverse problem, thus permitting to investigate the robustness of the obtained optimization solution and avoid false positive results. The SM-based method is applied and validated in the case of another medieval heritage masonry building, i.e. an historic civic tower in Perugia, Italy, called the Sciri Tower, which has been continuously monitored since December 2017. The validation is carried out by using simulated damage scenarios (artificially imposed damage-induced frequency decays) and a set of real far-field earthquake data, and considering the FE model of the tower including surrounding buildings, calibrated based on the obtained results from AVT. The proposed procedure is capable of correctly detecting and localizing earthquake-induced damages.

The IDA-based method completes the DORI methodology. It is based on multidimensional non-linear seismic IDA simulations carried out using a numerical FEM model together with seismic data recorded via long-term vibration-based SHM. IDA simulations are carried out at increasing levels of the earthquake input and relate a certain damage parameter to the intensity of the dynamic input. The construction and tuning of the numerical model representative of the structure under analysis are required, while the seismic/response intensity parameter is measured by the monitoring system and, through the IDA curves, is used to estimate the damage. The key aspect is the introduction of local multidimensional IDA curve sets, so as to allow a local estimation of damage with confidence intervals. In particular, IDA curves are built with reference to different specific portions of the structure, relating a set of meaningful local Damage Measures (DMs) against one or more selected earthquake ground motion Intensity Measures (IMs). A suitable damage parameter for masonry structures and a suitable seismic intensity measure should be defined on the basis of both theoretical considerations and numerical modeling in such a way to reduce as much as possible the variability of IDA curves so limiting the uncertainty in the estimated damage. In particular, a thorough overview of all IMs proposed in the literature is provided, since the use of the most efficient IMs represents an important aspect of IDA results and effectiveness. To this end, wide literature research, definition, classification and statistical correlation analysis considering one hundred (100) seismic records allow selecting the most

suitable, uncorrelated and efficient intensity measures for IDA purposes. Multidimensional local IDA curve sets are constructed and used in the way that, when an earthquake occurs, the seismic/response intensity parameter is measured by the monitoring system or directly computed from the measurements, and local damage conditions are immediately estimated using the prior multidimensional IDA analysis. The IDA-based method is validated through applications to the FE numerical model of a laboratory reduced-scale masonry structure, called the Brick House, and subsequently to the FE model of an iconic medieval masonry building located in Perugia, Italy, the San Pietro Bell Tower. Earthquake-induced damage localization and quantification are achieved with an acceptable level of approximation considering real earthquake acceleration records for both structures.

More in-depth descriptions of the innovative methods constituting the DORI methodology are presented in each Chapter, in particular, the enhanced data-driven method for damage detection in Chapter 2, the surrogate modeling in Chapter 3 and the IDA-based method in Chapter 4.

1.4   Novel aspects of the proposed DORI methodology

It should be emphasized that the proposed DORI methodology constitutes the original contribution of this Thesis. DORI incorporates several innovative aspects, aimed at earthquake-induced damage detection, localization and quantification in historic masonry buildings.

The first innovative aspect of the Thesis concerns the proposal of data fusion in data-driven damage detection method, in particular, the use of static measures as predictors in the dynamic MLR model for removing environmental effects from identified natural frequencies, in addition to temperature data.

The second and main innovative aspect proposed by the DORI methodology regards the introduction of two innovative independent model-based methods in the context of long-term OMA-based monitoring for localization and quantification of earthquake-induced damage. The surrogate model-based method is based on a linear finite element model and combines long-term vibration monitoring data (i.e. OMA) and numerical modeling. Given the simplicity and limited computational costs, it is a rapid tool for damage detection

and localization. In particular, the innovative quadratic SM exploits an objective function which is based also on variations in mode shapes, in addition to natural frequencies changes (damage-induced decays). On the other hand, the seismic IDA-based method is newly proposed for earthquake-induced damage localization and quantification, not observed so far in the literature. Unlike the SM, the IDA requires a non-linear model. Several benefits can be exploited by putting together OMA, SM and IDA-based methods. First of all, damage detection achieved by continuous OMA, e.g. in terms of frequency shifts and control chart (novelty detection), can be used for comparative purposes with damage identified with SM and IDA, allowing to avoid false positive results. Second, the combination of linear (SM), as well as non-linear (IDA) models can certainly enrich the accuracy of the DORI methodology. Afterwards, IDA uses the seismic response of an earthquake, whereas OMA and SM are based on long-term vibration monitoring data, thus, combining two independent approaches for damage identification purposes. Also, the combination of the SM with the IDA-based methods can be exploited for comparative and/or complementary scopes, in particular, it allows reducing the uncertainties related to IDA, together with the mitigation of the uncertainties in the localization task and the focus on the consistency between these two independent methods.

Overall, the proposed DORI methodology enables a rapid post-earthquake damage assessment of long-term monitored CH structures for condition-based maintenance and preventive conservation. After the occurrence of a seismic event, DORI allows to immediately reveal the presence of damage and to subsequently localize and quantify it with an acceptable level of confidence.

1.5   Outline and organization

This Thesis is organized in six (6) Chapters. The main contents of each Chapter are summarized as follows:

- **Chapter 1** provides an introduction to the work, with the motivation for innovative SHM solutions in CH masonry structures, the literature review on SHM basic concepts and a particular focus on vibration-based SHM damage detection. Afterwards, a general description of the proposed DORI methodology is provided, as well as, the outline of the Thesis.

- **Chapter 2** presents the basic theoretical background as well as the enhanced vibration-based SHM method for earthquake-induced damage detection, consisting in the novel use of static features as predictors in the data cleansing statistical tool (a dynamic MLR model), in particular, crack amplitude data, resulting into a clearly improved statistical reconstruction of natural frequencies aimed at damage-sensitive features extraction, a key aspect for novelty analysis by means of control chart. The proposed method is validated through the application to the Consoli Palace, an historic stiff masonry building, where a long-term permanent mixed static and dynamic SHM system is implemented since July 2017 and a vibration data automated modal analysis procedure has allowed to effectively track the evolution in time of the natural frequencies of six (6) identified modes, a novelty in the literature in the context of long-term monitoring of stiff masonry buildings such as palaces, whereas the majority of modal tracking applications to masonry structures are essentially concerned to slender towers. It is demonstrated that the adopted vibration-based SHM tool on the Consoli Palace enable rapid and automated earthquake-induced damage detection, even for small damages, simulated by artificial insertion of small frequency and crack amplitude shifts in the monitoring data, conceivably associated to a small structural damage at an early stage (caused by a moderate/light seismic event), thus constituting an effective low-cost tool for condition-based maintenance and preventive conservation of the stiff monumental palace.

- **Chapter 3** presents a detailed description of the surrogate model-based method aimed at real-time damage detection and localization using long-term vibration-based monitoring data and FE model updating. Damage localization is performed by solving an inverse model calibration problem on a surrogate model, based on variations of modal parameters observed through the processing of monitoring data. A simple surrogate model consisting of a quadratic expression relating natural frequencies and modal shape components to elastic parameters is considered, minimizing the computational effort. The surrogate model-based method is validated through application to the Sciri Tower, an historic civic masonry tower, where a simple permanent vibration-based SHM system is installed. A tuned numerical model of the structure is constructed and ideally subdivided into distinctive macrostructural elements to discriminate the damage-dependent structural parameters belonging to different zones. Simulated damage-induced natural frequency variations and frequency decays observed through the processing of monitoring data after a far-field earthquake have been used to detect and localize possible earthquake-induced damages. Using artifi-

cial damage scenarios have demonstrated that the proposed procedure is effective for both earthquake-induced damage detection and localization. Furthermore, the results obtained using field data and the real earthquake response have been validated through non-linear dynamic analysis and visual inspections.

- **Chapter 4** presents a detailed description of the innovative IDA-based method aimed at rapid localization and quantification of earthquake-induced damages in masonry structures. It is based on IDA carried out from a numerical model (non-linear finite element analysis) and using data recorded during seismic events, relying on the introduction of local multidimensional IDA curve sets relating meaningful local damage parameters to selected seismic intensity measures. An in-depth specific study consisting of wide literature research, definition, classification and statistical correlation analysis is carried out to investigate their interdependence and to subsequently select the most suitable, uncorrelated and meaningful intensity measures for IDA purposes. The proposed method is numerically validated through application to a reduced-scale masonry structure, namely the Brick House, a notable benchmark, object of previous studies by several authors. Ten (10) IDA curve sets, one for every part of the FE model, have been constructed considering tensile damage, plastic strain magnitude and first principal plastic strain as damage measures. Additionally, an in-depth investigation of dispersion, using root mean square errors of IDA curve sets, allowed identifying the most efficient intensity parameters in the case of tensile damage and first principal plastic strain. Finally, considering three acceleration records of the 2016 Central Italy seismic sequence, earthquake-induced damage localization and quantification (in terms of overall weighted average estimation of damage ranges and mean values) was achieved for the ten (10) parts of the structural model with an acceptable level of approximation. It is demonstrated that the proposed seismic IDA-based SHM procedure is capable of rapidly and correctly localizing and quantifying earthquake-induced damage, the latter in terms of overall weighted average estimation of damage ranges and mean values, thereby showing great potential for damage assessment of masonry structures in the context of monitoring for preventive conservation of architectural heritage.

- **Chapter 5** focuses on the application and numerically validation of the proposed IDA-based method through the case of the San Pietro Bell Tower, a monumental masonry building, which is under continuous monitoring for about five (5) years. The multidimensional IDA curve sets have been constructed relating meaningful local

damage parameters (associated with the shaft, belfry and cusp) to selected seismic intensity measures, as well as seismic response intensity measures. Seismic input and experimentally recorded seismic responses during important earthquakes of the 2016 Central Italy seismic sequence by the long-term vibration-based SHM system installed on the bell tower, have been used within the IDA curve sets for damage identification purposes. The benefits of using also response intensity measures have been investigated. Earthquake-induced damages have been localized and quantified in terms of overall weighted average estimation of damage ranges and mean values with an acceptable level of approximation.

- **Chapter 6** summarizes the main conclusions and the original contributions of the Thesis.

Two Appendixes with useful information about the work carried out during the study are reported at the end of this dissertation.

Chapter 2

Data-driven damage detection

Application and validation of an enhanced earthquake-induced damage detection method are presented in this Chapter. The main theoretical aspects are described first. The proposed vibration-based SHM method is implemented in the case of the Consoli Palace, an historic stiff masonry palace under permanent long-term static and dynamic monitoring since July 2017, newly in the literature because the majority of the documented successful applications are limited to masonry towers. The introduction of crack amplitudes as predictors, in addition to temperatures, for the statistical reconstruction of natural frequencies time histories, constitutes a novelty in the literature, not observed in SHM of historic masonry structures, and represents an effective approach to data fusion in the context of mixed static-dynamic monitoring. In this regard, it has proved quite effective in enhancing the MLR model. Subsequently, the presented results of novelty analysis provide a practical demonstration that the permanent long-term mixed static and vibration-based SHM system of the Consoli Palace enable rapid and automated earthquake-induced damage detection, even for small damages at an early stage caused by moderate earthquakes, thus constituting an effective low-cost tool for condition-based maintenance and preventive conservation of the stiff monumental palace.

2.1   Theory background

Data-driven methods for earthquake-induced damage detection have been developed in the literature within vibration-based long-term SHM, aimed at the preventive conservation of historic masonry buildings. Among them, those resorting to modal parameters as damage-sensitive features represent consolidated method for CH masonry structures, even at stages when damage is not yet detectable by visual inspections (Alvandi and Cremona 2006; Brencich and Sabia 2008; Ramos et al. 2010; Farrar and Worden 2012; Masciotta et al. 2017; Ubertini et al. 2018).

A permanent SHM system, constituted by a few sensors, allows providing, in nearly real-time, a diagnosis on the state of "health" of the structure and therefore an early warning on the occurrence of damage. The use of an advanced long-term vibration-based SHM tool enables to automatically detect earthquake-induced damages in heritage structures, relating the origin of structural damage to permanent variations in the modal properties (resonant frequencies, mode shapes and damping) of the structure. It can be regarded as a multi-stage process involving the following four (4) steps synthesized in Fig. 2.1: (i) the repeated or continuous measurement of the response of a structural system through a permanent monitoring system (permanent acquisition of the dynamic response of the structure in operational conditions), (ii) the estimation of the natural frequencies of vibration from acquired vibration signals and on tracking their evolution in time, (iii) removal of environmental and operational conditions from identified natural frequencies and for the extraction of damage-sensitive features (quantities that are insensitive to changes in
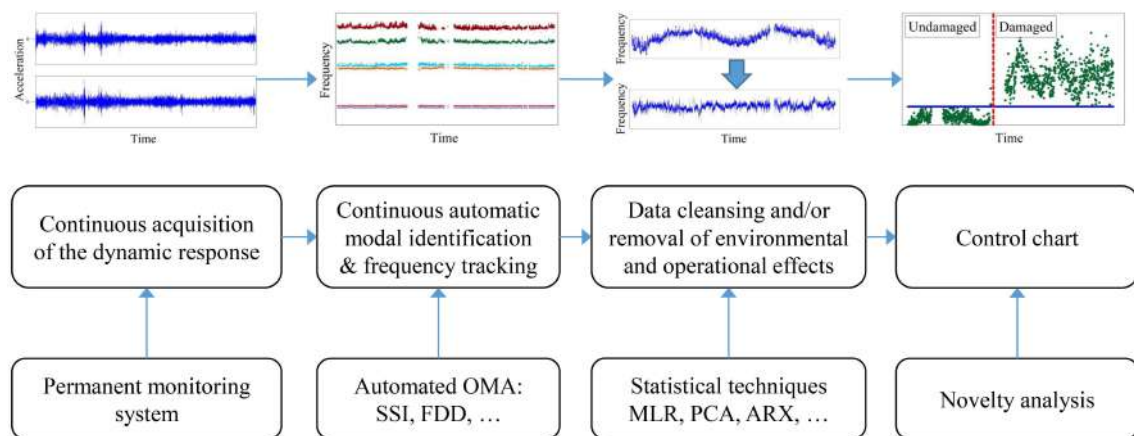
Figure 2.1: General framework of vibration-based earthquake-induced damage detection.

environmental and operational conditions) and (iv) novelty analysis for damage detection, consisting of a statistical analysis of damage-sensitive features to detect any novelty or anomaly/abnormal change in the investigated system (Farrar and Worden 2012).

The permanent dynamic monitoring allows highlighting any change in the dynamic behavior of a structure. The latter, conceivably associated with some developing damage patterns, is automatically detected by application of statistical process control tools to the time histories of continuously identified modal parameters (computed by automated modal identification from the data obtained from the permanent monitoring system, see Fig. 2.1). Prior to the detection, a particular aspect concerns the task of removing environmental and operational effects. It should be mentioned that environmental effects can mask changes in modal properties due to damage occurrence, thus it is extremely important to distinguish whether variations in the structural response are caused by exogenous factors, such as temperature, humidity, wind, etc., rather than endogenous factors linked to structural damage. In fact, modal properties of masonry structures are typically affected by changes in environmental effects (temperature and humidity) in a way that is likely more significant than variations induced by small damage. The effects of changes in environmental parameters need to be effectively investigated and accurately removed from identified frequency data for an effective performance assessment. Although sensitive to ambient fluctuations, natural frequencies have been proven to be effective features to detect small structural changes and damages (damage-sensitive features). Analysis of the influence of such environmental effects on the estimates of modal properties is needed. The statistical process control tools first remove the effects of changes in environmental and operational conditions from continuously identified natural frequencies and afterwards detect changes in them, in the form of statistical outliers, related to structural damage. The statistical techniques such as MLR (Dervilis et al. 2015), PCA (Yan et al. 2005a; Bellino et al. 2010), etc, are used for removing environmental and operational effects (data cleansing). Novelty Analysis addresses structural damage detection, the task of detecting deviations from normal conditions which is typically carried out by control charts based on proper statistical distances, such as Q^2 and T^2 statistics (Worden et al. 2000; Sohn et al. 2002b; Fuller 2009; Mujica et al. 2011; Farrar and Worden 2012; Mosavi et al. 2012).

Concerning the historic masonry structures studied in this Thesis, the main aspects and mathematical quantities needed for the Novelty Analysis are characterized in the following lines.

Tracked modal frequencies are collected in an observation matrix, $\mathbf{Y} \in \mathbb{R}^{n \times N}$, where n is the number of identified frequencies and N is the number of observations. The i-th column of matrix $\mathbf{Y}$ contains the values of the modal frequencies identified in the i-th data set. As already mentioned, changes in environmental and operational conditions affect modal frequencies. Due to this, quantities contained in matrix $\mathbf{Y}$ cannot be directly used as damage-sensitive features. Instead, quantities contained in a residual error matrix, $\mathbf{E} \in \mathbb{R}^{n \times N}$, are used for this purpose and computed as

$$\mathbf{E} = \mathbf{Y} - \hat{\mathbf{Y}} \tag{2.1}$$

where $\hat{\mathbf{Y}}$ are modal frequencies independently estimated through a proper statistical model. Under the assumption that such a model can reproduce the part of the variance in frequency estimates that is associated with changes in environmental and operational conditions, the error matrix only contains the residual variance in the data associated with errors in output-only modal identification and with un-modeled environmental and operational effects on modal frequencies. If a damage pattern develops, this affects data contained in $\mathbf{Y}$ but not those in $\hat{\mathbf{Y}}$. It follows that $\mathbf{E}$ contains quantities that are feasible for damage detection purposes. After computing matrix $\mathbf{E}$ in Eq. (2.1), a damage condition is identified as an anomaly in the residual errors, under the assumption that damage induces a change in the distribution of $\mathbf{E}$. To this aim, the classic statistical process control tool named *Novelty Analysis* is adopted. It consists of the use of control charts based on properly defined statistical distances in other words, on and index able to flag relevant natural frequency shifts. A well known and used in SHM is the Hotelling or Shewhart T^2-statistical distance (Farrar and Worden 2012), defined as

$$T^2 = r \cdot (\overline{\mathbf{E}} - \overline{\overline{\mathbf{E}}})^T \cdot \mathbf{\Sigma}^{-1} \cdot (\overline{\mathbf{E}} - \overline{\overline{\mathbf{E}}}) \tag{2.2}$$

where r is an integer parameter, referred to as *group averaging size*, $\overline{\mathbf{E}}$ is the mean of the residuals in the subgroup of the last r observations, while $\overline{\overline{\mathbf{E}}}$ and $\mathbf{\Sigma}$ are the mean values and the covariance matrix of the residuals, respectively. Both $\overline{\overline{\mathbf{E}}}$ and $\mathbf{\Sigma}$ are statistically estimated in a reference period, called the *training period* (denoted as t_t), during which the structure is in the healthy state, i.e. it can be considered undamaged and experiences the

normal environmental and operational conditions. Basically, it concerns an initial period necessary to build and train the statistical model for fully characterizing the normal conditions. Since temperature is the main environmental driver of changes in natural frequencies of structures, the full characterization of the normal conditions typically requires one year of training, which is necessary to observe long-term seasonal variations of environmental conditions. When sufficient training data have been collected, the SHM becomes effective.

An anomaly in the data is identified in the form of an outlier in the observed values of the residuals errors, which is a value of the statistical distance which lies outside fixed control limits. In the case of modal parameters continuous tracking, T^2 is positive by definition, and subsequently the Lower Control Limit (LCL) is 0, while the Upper Control Limit (UCL) is statistically computed as the value of T^2 corresponding to a cumulative frequency of 95% in the training period, t_t. In this way, if data collected in t_t are statistically meaningful (the training period is sufficiently long), there is approximately a 5% probability to observe an outlier when the structure is in the healthy state (false alarm). Conversely, if a relative frequency of outliers significantly greater than 5% is steadily observed over time, a change in the statistical distribution of the residuals is supposed to have occurred, denoting an anomalous structural condition not experienced during t_t. Changes in T^2 are therefore likely to occur after a seismic event, evidencing the development of a damage pattern in the structure.

The matrix $\hat{\mathbf{Y}}$ can be computed by statistical models such as MLR, PCA, and other approaches. When environmental conditions, such as temperature and humidity, are measured, statistical models can be built linking such quantities, treated as statistical predictors, to natural frequencies. This is, for instance, the case when using input–output models such as autoregressive models, multiple linear regressions (Dervilis et al. 2015), neural networks and so forth. MLR is a simple predictive statistical tool that exploits linear correlations between a set of n dependent variables and a set of p independent variables, called predictors. In the context of vibration-based SHM, dependent variables are represented by modal frequencies contained in matrix $\mathbf{Y}$, while independent variables can be environmental and operational factors, damping ratios, amplitudes of vibration and more.
Modal frequencies independetly estimated contained in the matrix $\hat{\mathbf{Y}}$, in the MLR approach are expressed as

$$\hat{\mathbf{Y}} = \boldsymbol{\beta}^T \mathbf{Z}^T \tag{2.3}$$

where $\mathbf{Z} \in \mathbb{R}^{N \times (p+1)}$ is a matrix that contains a first column of ones and N values of the p selected independent variables in the remaining p columns, while $\boldsymbol{\beta} \in \mathbb{R}^{(p+1) \times n}$ is a matrix containing constant terms, in the first row, and coefficients that weight the contribution of each independent variable in the remaining p rows.

Substituting Eq. (2.3) into Eq. (2.1), the residual error matrix, $\mathbf{E}$, between identified and predicted dependent variables is given by:

$$\mathbf{E} = \mathbf{Y} - \boldsymbol{\beta}^T \mathbf{Z}^T \tag{2.4}$$

which clarifies that $\mathbf{E}$ represents the prediction error of the statistical model, which is assumed to be random in nature, to have zero mean, constant variance and to be constituted by independent events. If the statistical model is successful in reproducing environmental effects on dependent variables, matrix $\mathbf{E}$ contains quantities that are only minimally affected (almost insensitive) by changes in environmental and operational conditions and therefore suitable to be used as damage sensitive features for detecting anomalies in the dynamic behavior of the structure. The coefficients of the statistical model contained in matrix $\boldsymbol{\beta}$ are estimated in a least-square sense by minimizing the norm of the prediction error, $\mathbf{E}$, in Eq. (2.4), in the reference t_t.

PCA is another well-known technique that can address the removal of environmental effects from identified natural frequencies when statistical correlations between natural frequencies and environmental parameters are linear (Yan et al. 2005a; Bellino et al. 2010). The main advantage of PCA is that it does not require to measure environmental conditions. PCA consists of remapping the original data into the more convenient vectorial space generated by the Principal Components (PCs) and only some of the PCs are retained to turn back to the original space. PCs are statistically independent variables that constitute an orthogonal basis and provide different contributions to the variance of the original data. The basic idea behind this operation is that the PCs that provide the largest contributions to the variance represent the independent environmental and operational factors that have to be retained for estimating $\hat{\mathbf{Y}}$ in Eq. (2.1). Remaining PCs are instead associated with residual errors and are neglected. Several improvements to classic PCA have been proposed in the literature to handle the more general case of non-linear correlations between damage-sensitive features, such as Kernel PCA and local PCA (Kambhatla and Leen 1997; Yan et al. 2005b). Nevertheless, the PCA technique is not the focus of this work, where, instead, the attention is devoted to the MLR technique.

2.2   The proposed method

The development of long-term SHM systems for preventive conservation of CH buildings is receiving a growing trend of scientific interest. Nevertheless, the damage detection effectiveness of these systems is still debated, especially for complex masonry buildings where both local and global failure mechanisms can be activated, whereby the majority of the documented successful applications are limited to masonry towers.

The methodology proposes an enhanced version of the data-driven earthquake-induced damage detection method presented in Section 2.1. With reference to the general framework illustrated in Fig. 2.1, particular focus is devoted to the 3rd step, i.e the removal of environmental and operational conditions from identified natural frequencies and the extraction of damage-sensitive features. An enhanced data cleansing is proposed by introducing static measures as predictors to the statistical tools for the extraction of damage-sensitive features (e.g. MLR). The availability of continuous static features in permanently monitored structures can lead to significant refinement of the dynamic regression model.

The proposed method is applied to the Consoli Palace, a masonry CH structure that has been under continuous static and dynamic monitoring for more than two years. The effectiveness of the adopted dynamic MLR tool, using past values of predictors, is investigated for removing temperature effects from identified natural frequencies and, in particular, catching delayed temperature-induced effects related to the thermal inertia. Also, the introduction of measured crack amplitude data is proposed to be used in addition to temperature data as predictors for the construction of dynamic MLR models, aiming at improving the statistical modeling of natural frequencies. Finally, the effectiveness of the adopted SHM tool with particular focus on the results of control charts is investigated by simulating earthquake damage effects in terms of frequency shifts artificially imposed to natural frequencies time histories.

2.3   Application example: the Consoli Palace

The implementation of a long-term static-dynamic SHM system in the Consoli Palace and the application of the proposed method are reported in this Section. The case study is briefly presented in Section 2.3.1 while results on data fusion are discussed in Section 2.3.2. Section 2.3.3 is devoted to the validation of the enhanced damage detection method. The main conclusions are summarized in Section 2.4.

2.3.1   Introduction to the case study

The Consoli Palace (in Italian *Palazzo dei Consoli*) is the most representative monument
of the medieval town of Gubbio, Italy, and is located in the heart of its historical center (see
Fig. 2.2). Several studies have been carried out on the Consoli Palace in the framework
of Horizon 2020 European HERACLES (HEritage Resilience Against CLimate Events on
Site) project, devoted to enhancing resilience of historic buildings against harmful events,
with reference to various types of hazards. It concerns a wide research programme planned
to develop effective SHM methodologies and protocols for application to historic masonry
palaces, a structural typology that has been rarely investigated in an SHM perspective
(Kita et al. 2018; Kita et al. 2019b; Cavalagli et al. 2019a; Cavalagli et al. 2019b; Garcia-
Macias et al. 2019). It constitutes the first example in the literature where continuous
modal identification and SHM based on frequency tracking has been applied to the case
of a stiff masonry palace, with the purpose of early detecting any damage or change in its
structural behavior following an earthquake.

Built in gothic style between 1332 and 1349, it presents an articulated internal distribution
of volumes and an elevation of more than 60 m (from the street level up to the top of the
small bell tower). The Palace is built in calcareous stone masonry and has a rectangular
plan of about 40x20 m, with foundations placed on two different levels. Geometrical and
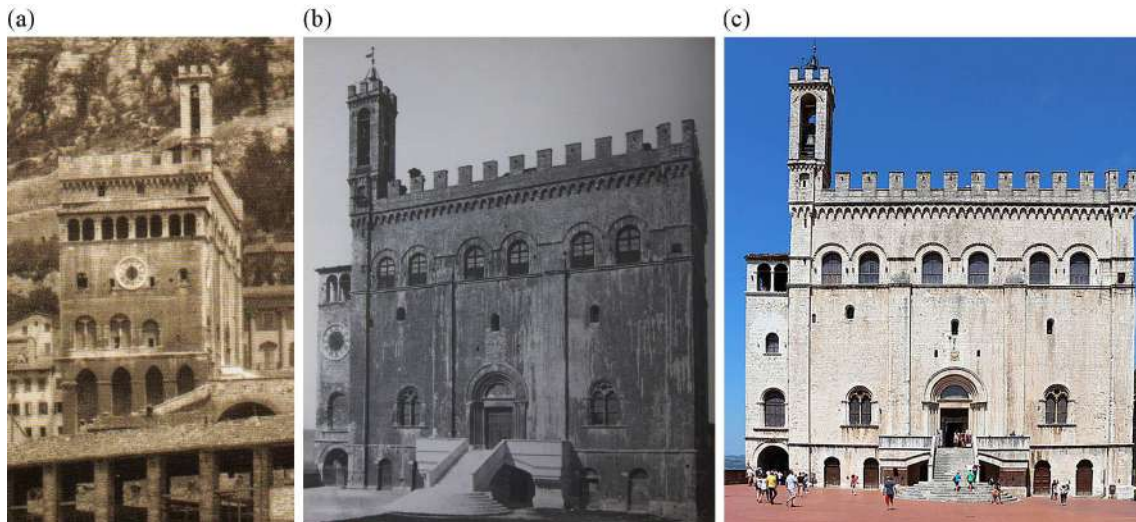
Figure 2.2: The Consoli Palace, historic pictures and today: unknown authors in 1907 (a)
and 1912 (b) and front view today (c).

structural damage surveys have highlighted existing cracks associated to a moderate state of structural damage. Revealed to be an effective diagnostic tool also in the case of the monumental stiff palace, AVT allowed the identification of six (6) modes of vibration within the range from 0 to 10 Hz: three global and three local (involving mostly the bell tower placed on the top) (Kita et al. 2019b). Overall, results on damage survey, AVT and numerical modeling have provided the necessary information for the conceptual development and installation of a simple low-cost mixed static and dynamic long-term SHM system in the Consoli Palace on July 5th 2017, which is currently active (see Fig. 2.3). It consists of two
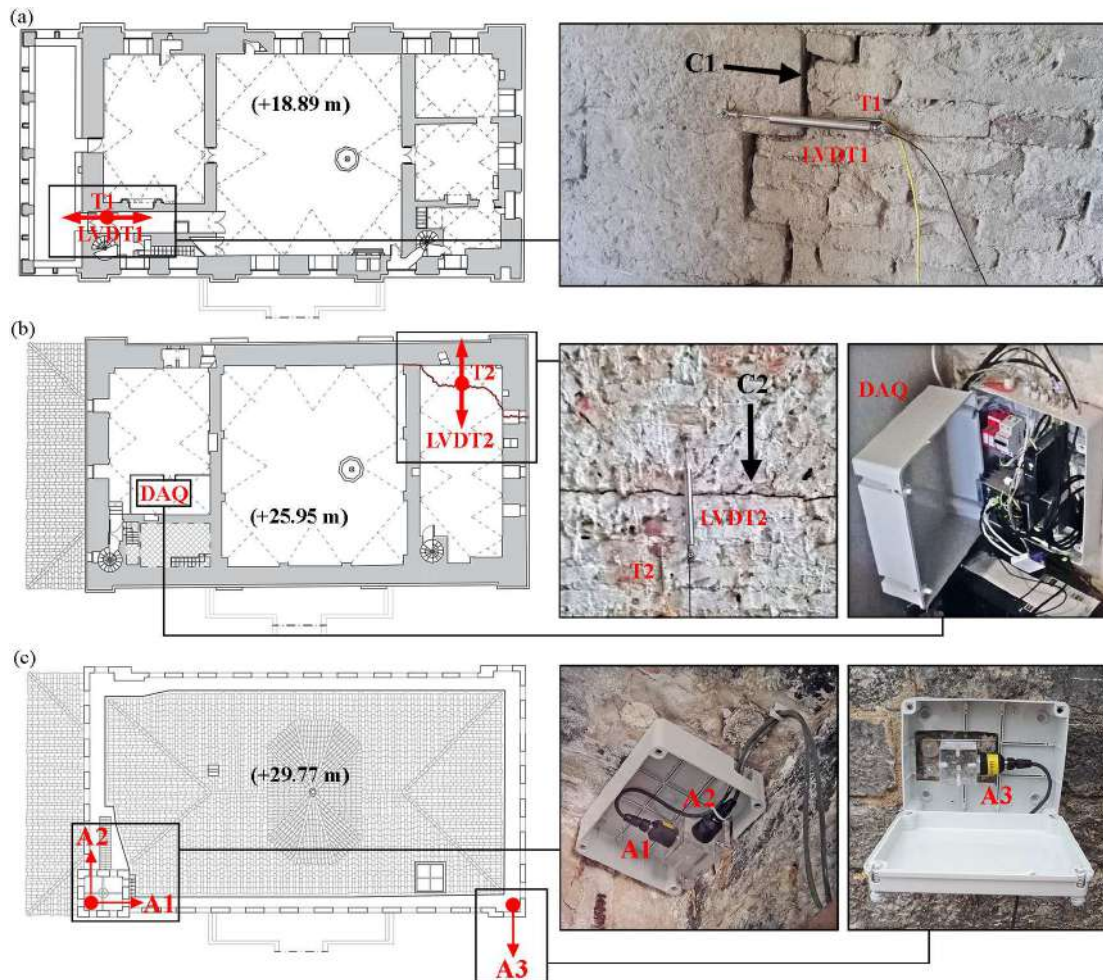
Figure 2.3: Long-term static-dynamic SHM system installed on the Consoli Palace: LVDTs and temperature sensors' layout with detailed view of positioning in correspondence of the 1st and 2nd main crack ((a) and (b), respectively, where the double arrows indicate the direction of opening of the monitored crack) and accelerometers locations (c).

crack meter sensors (LVDT1 and LVDT2), two surface temperature sensors (T1 and T2) and three high sensitivity accelerometers (A1, A2 and A3) to track the evolution of modal properties of the structure. The application of an automated Stochastic Subspace Identification (SSI) modal analysis procedure (Ubertini et al. 2013) has allowed to effectively track the evolution in time of the natural frequencies of the six (6) identified modes of the Palace, which represents a novelty in the literature in the context of long-term monitoring of stiff masonry buildings such as palaces, whereby previous applications of modal tracking to masonry structures were essentially limited to slender towers. Results of continuous modal identification and frequency tracking are presented in Fig. 2.4, while Fig. 2.5 shows the plot of the evolution in time of two monitored crack amplitudes and temperature data of the Consoli Palace.

The static and dynamic response of the Consoli Palace under ambient loading conditions have been continuously monitored for more than two years. Investigation of significant temperature effects for the first year of monitoring can be found in (Kita et al. 2019b). Differently from what observed in other literature works on vibration-based monitoring of
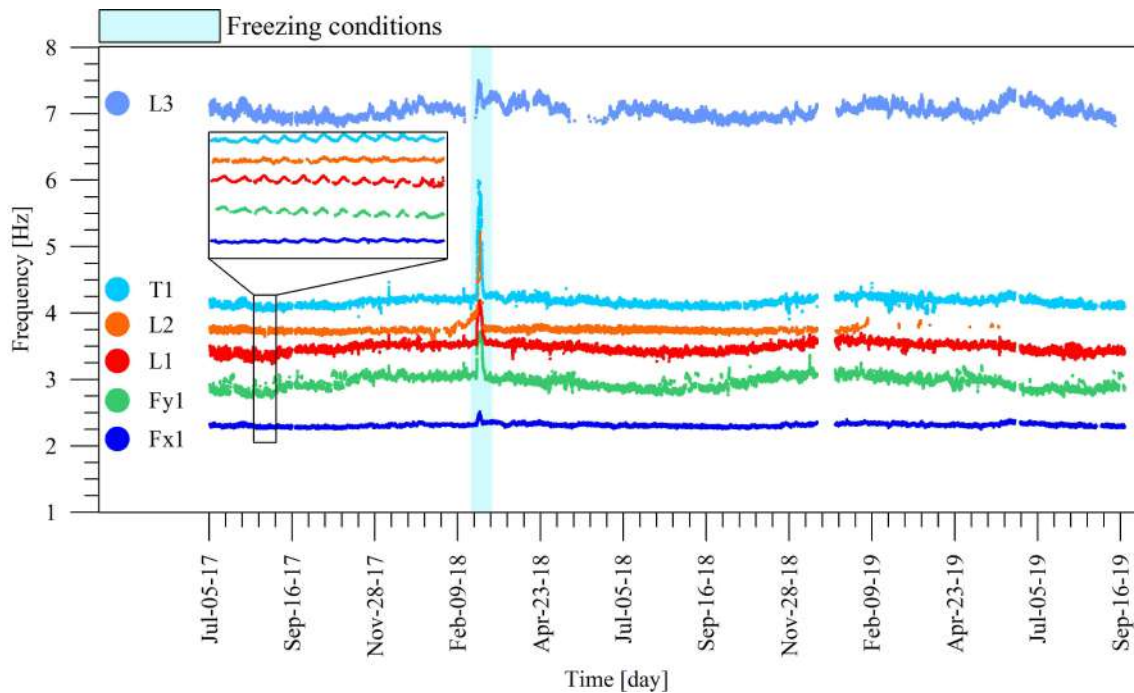
Figure 2.4: Time series of identified natural frequencies during the monitoring period (daily fluctuations are also evidenced with a detailed view).
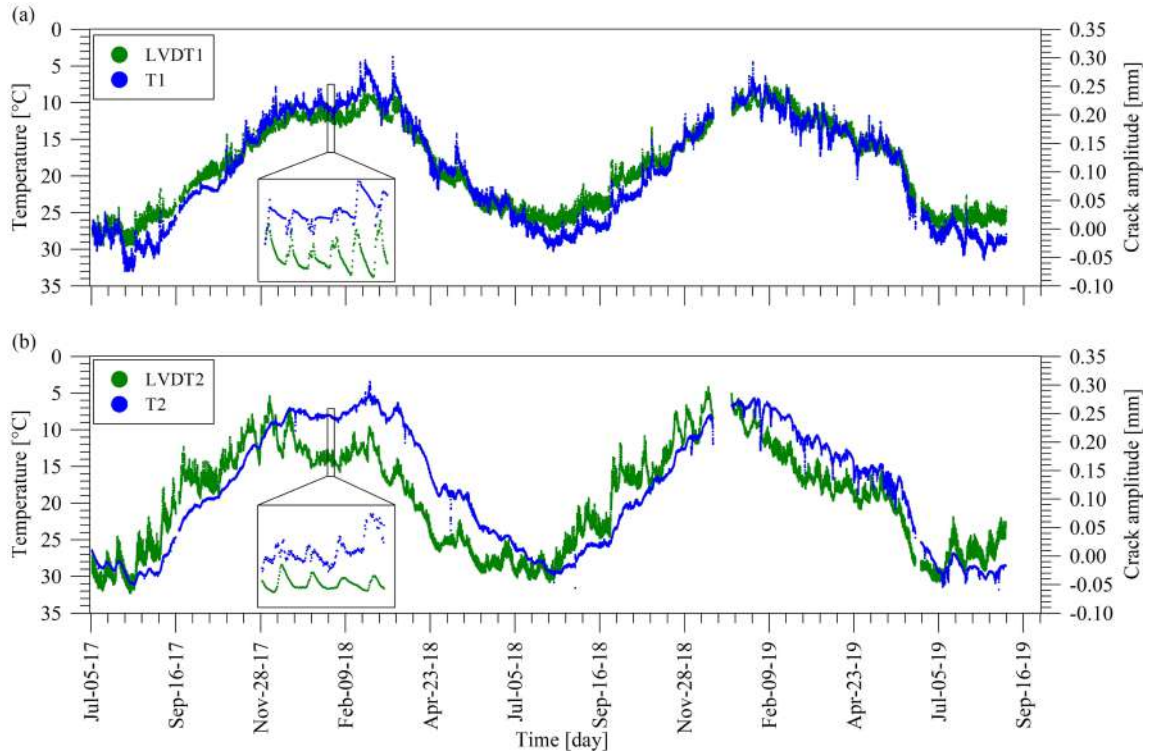
Figure 2.5: Evolution in time of two monitored crack amplitudes (LVDT1 and LVDT2) and temperature data (T1 and T2) of the Consoli Palace during the monitoring period (daily fluctuations are also evidenced with a detailed view).

masonry buildings, an unexpected negative correlation between natural frequencies and temperature has been found for the Consoli Palace. This negative correlation is indeed observed for the first time, compared to positive natural frequencies-temperature correlations of masonry structures such as slender towers and stiffer structures such as churches and/or cathedrals (Masciotta et al. 2016; Masciotta et al. 2017). Fig. 2.6 shows plots of 2nd and 5th natural frequencies versus temperature measured by sensor T1. The increase in natural frequencies of global vibration modes of the Palace with decreasing ambient temperature has been attributed to an increase in global structural stiffness due to strengthening effects of metallic reinforcements (tie rods shortening at lower temperatures) and the presence of a moderate structural damage state in the Palace. Also, remarkable freezing effects on natural frequencies have been observed during some exceptional cold days between February and March 2018 (see Fig. 2.4), resulting in sharp increases, conceivably caused by the stiffening effect produced by ice crystals forming within the masonry micro-pores.

27
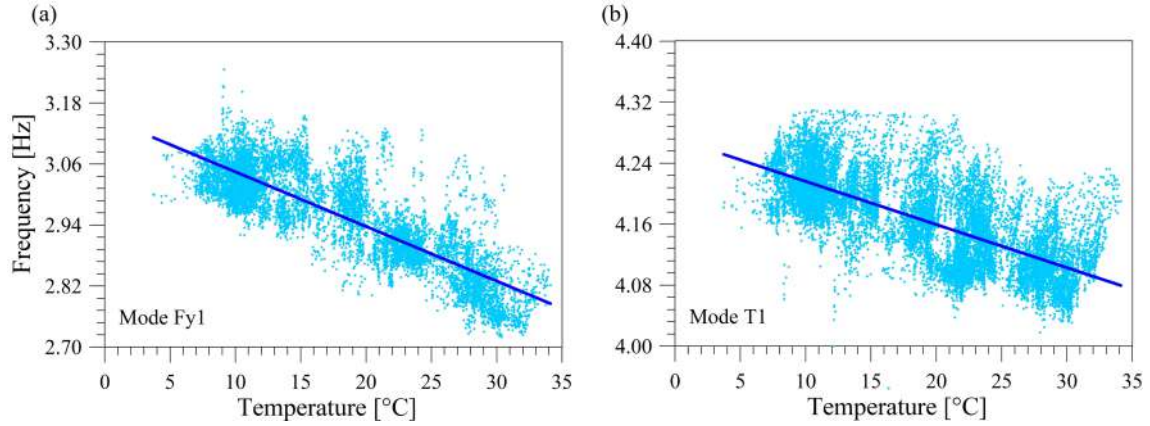
Figure 2.6: Correlation between natural frequencies and temperature: plots of frequencies of modes Fy1 (a) and T1 (b) versus temperature data T1.

2.3.2 Data fusion for enhancing statistical reconstruction of natural frequencies

As already introduced in the context of vibration-based SHM in Section 2.1, the effects of changes in environmental conditions can be removed from identified natural frequency data using statistical techniques (Yan et al. 2005a; Yan et al. 2005b; Bellino et al. 2010). In the case of the Consoli Palace, MLR filters have been adopted for the removal of temperature effects on identified natural frequencies, where linear correlations between a set of r dependent variables (natural frequencies) and a set of p independent variables (temperatures), called predictors, are exploited (see Eq. (2.4)). In particular, continuously tracked modal frequencies are the dependent variables, measured crack amplitudes can be regarded as either dependent or independent variables, while temperatures are independent variables. Due to some non-linear correlations observed between natural frequencies and temperature data (Kita et al. 2019b), whose effects are conceivably attributed to the thermal inertia of the masonry resulting in a time shift between changes in air temperature and changes in natural frequencies, a dynamic MLR model resulted very useful. In fact, the adopted dynamic MLR tool, using past values of predictors, has proved quite effective for removing temperature effects from identified natural frequencies and, in particular, catching delayed temperature-induced effects related to the thermal inertia. Moreover, the use of crack amplitudes as predictors have allowed to further improve the statistical modeling of natural frequencies, which is a key aspect and innovative in the SHM. The MLR model in Eqs. (2.3) and (2.4) is referred to as "static" when independent and dependent variables are sampled at the same time (contemporary), while it is referred to as "dynamic" when arrays

of past observations of temperatures and/or crack amplitudes are used to construct a set of independent variables.

In order to show the effectiveness of the adopted dynamic MLR model, Fig. 2.7 shows plots of the relative prediction errors of natural frequencies versus the length of the training period. In this way, the effect of a change in the length of the training period on the prediction error of the statistical model is investigated. Three types of model are presented, namely: (i) a static model considering temperatures T1 and T2 as predictors at time t (*model Static_ T*), (ii) a dynamic model considering temperatures T1 and T2 at time t, t-6h, t-12h, t-24h and t-48h (considering the past 48 h with steps of single hours) as predictors (*model Dynamic_ T*) and (iii) a dynamic model considering temperatures T1 and T2 and crack amplitudes C1 and C2 at time t, t-6h, t-12h, t-24h and t-48h as predictors (*model Dynamic_ T+C*). The results clearly highlight that the prediction errors of the MLR models are almost minimized after about $4 - 5$ months of training period length. In particular, the use of a dynamic model is seen to highly improve the quality of the prediction for the natural frequencies, getting more reliable damage-sensitive features. Furthermore, the advantage of including crack amplitudes as predictors is also quite evident in Fig. 2.7, which is conceivably attributed to the role of the existing moderate damage state of the Palace.
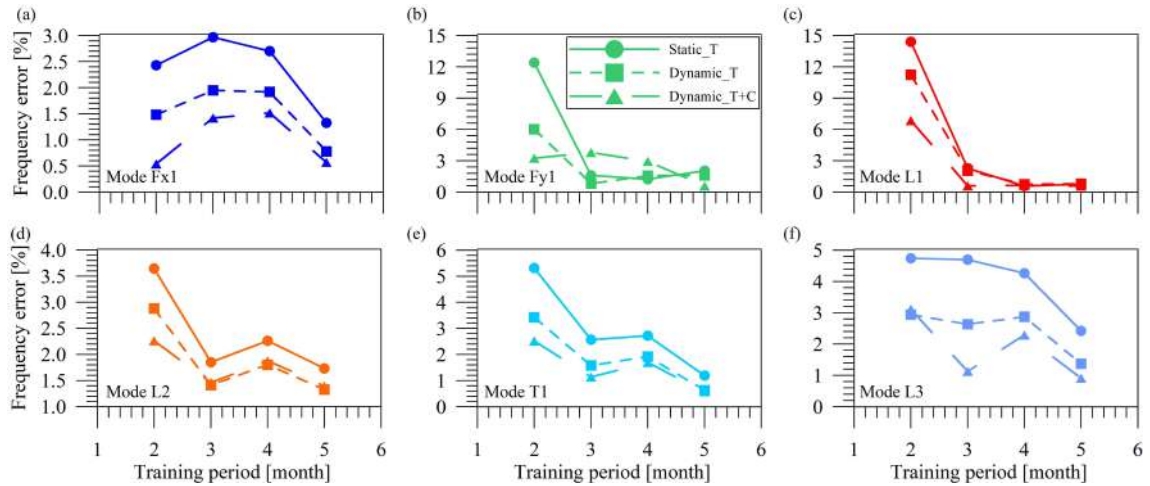
Figure 2.7: Relative error between identified and predicted natural frequencies for increasing training period length: Fx1 (a), Fy1 (b), L1 (c), L2 (d), T1 (e) and L3 (f).

In addition, Fig. 2.8 shows time series of identified as well as predicted (using the model Dynamic_T+C) natural frequencies, considering a training period of twelve months. It is shown that dynamic MLR models are able to catch daily and long-term fluctuations in dependent variables, therefore being well suited to be used to remove temperature effects from monitoring data and to derive damage sensitive features. Overall, it is noteworthy to mention that introducing crack amplitudes as predictors, in addition to temperatures, for the statistical reconstruction of natural frequencies time histories constitutes a novelty in the literature context, not observed in Structural Health Monitoring of historic masonry structures.

In order to further understand the advantage of using crack amplitudes as predictors, control charts with one year training period have been investigated, by applying Eq. (2.2). Fig. 2.9 shows control charts obtained with only temperatures as predictors (Figs. 2.9a-b)
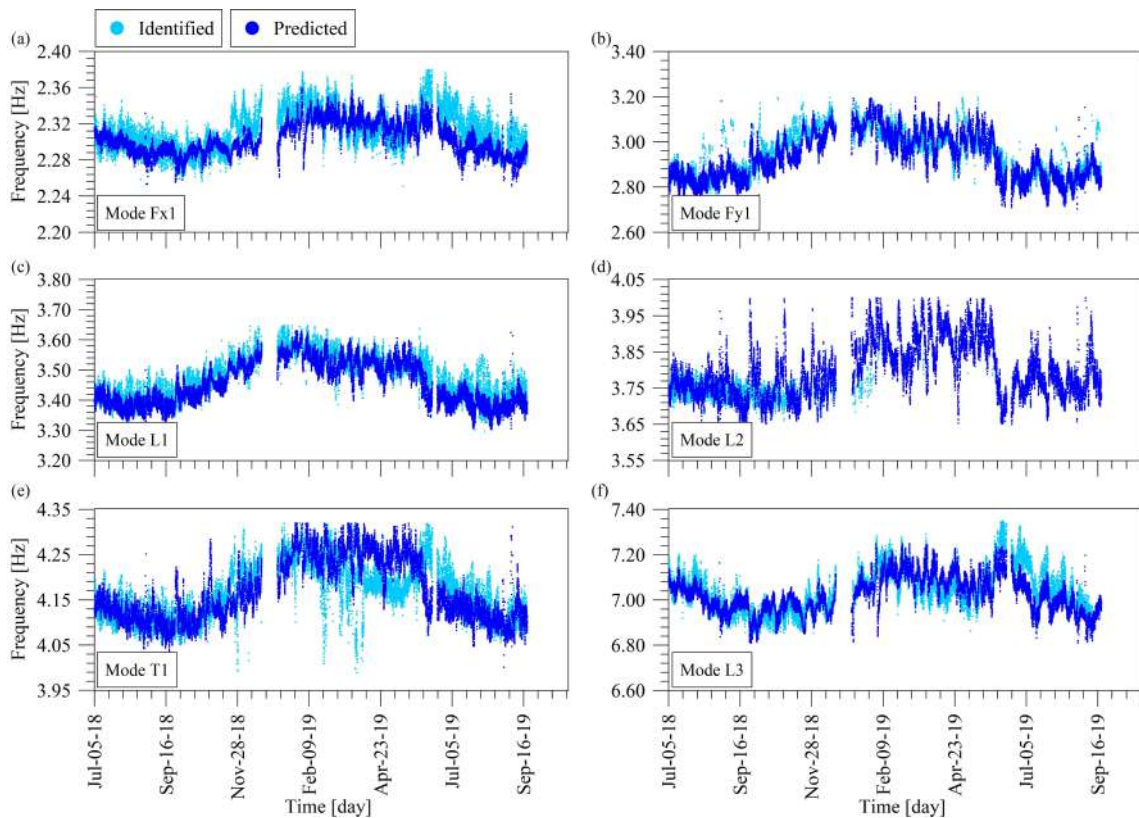
Figure 2.8: Statistical reconstruction of natural frequencies in the monitoring period after twelve months of training period: Fx1 (a), Fy1 (b), L1 (c), L2 (d), T1 (e) and L3 (f).
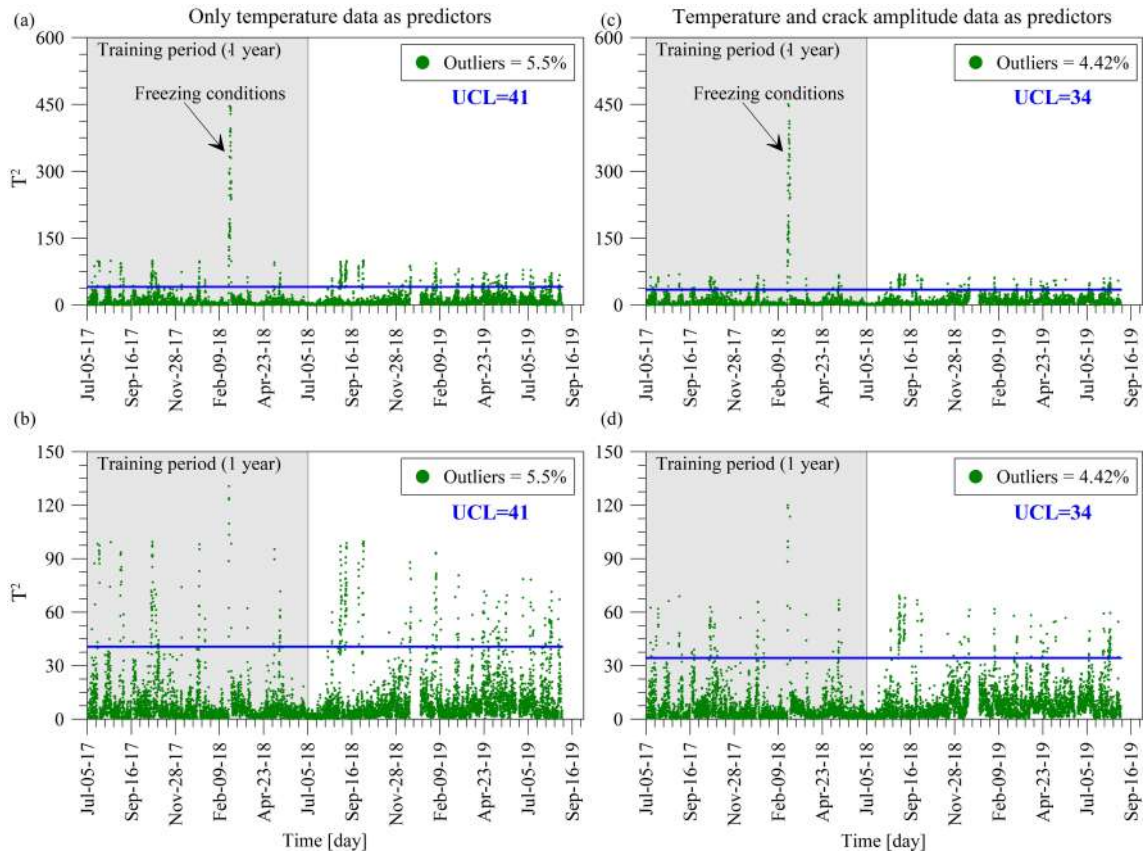
Figure 2.9: Control charts of the undamaged condition with only temperatures as predictors (a-b) and with temperatures and crack amplitude data as predictors (c-d).

and control charts when also crack amplitudes are considered (Figs. 2.9c-d). The number of outliers above the UCL line in the 2nd case is reduced with respect to the 1st one. Indeed, the percentage has decreased from 5.5% to 4.42%. Moreover, UCL has passed from 41 to 34. Overall, including crack amplitudes as predictors significantly improve the quality of the control chart. It reduces the probability to observe an outlier when the structure is in the healthy state (false alarm) and concentrates them at lower values of T^2. As a final remark in the presented results, it should be mentioned that the presence of ice on the structure results in outliers even in normal conditions without damage.

2.3.3   Application of enhanced vibration-based SHM damage detection

The acquired long-term monitoring data have been processed by means of the vibration-based SHM tool implemented for the Consoli Palace, based on the four (4) steps defined in Fig. 2.1, in order to detect deviations of the structural behaviour from normal conditions, as described in Section 2.1. In order to demonstrate the ability of the SHM system and the effectiveness of the adopted SHM tool to enable rapid and automated earthquake-induced damage detection, some frequency shifts have been imposed to natural frequencies time histories, thus, artificially inserting earthquake damage effects in the continuous monitoring data.

With reference to the SHM method sketched in Fig. 2.1, the crucial aspects in the third stage (removal of environmental and operational conditions from identified natural frequencies for the extraction of damage-sensitive features) are the choice of the length of the training period, t_t, needed for a proper estimation of matrix $\boldsymbol{\beta}$, and the proper choice of independent variables adopted for predicting natural frequencies. In the case of the Consoli Palace, t_t used is equal to one year, as suggested in the literature for significant environmental effects (Magalhães et al. 2012), and temperature data and measured crack amplitudes have been used as independent variables.

The Consoli Palace has not yet experienced any relevant seismic event while being permanently monitored. Aimed at earthquake-induced damage detection, the damage has been artificially inserted in the continuous monitoring data starting from January 2019, in terms of relative frequency changes Δf and relative shifts to crack amplitude time histories ΔC. Several damage scenarios summarized in Tab. 2.1 have been considered to be investigated. Relative shifts equal to -1.5% (and 3×(-1.5%)) have been applied to natural frequencies of global modes of vibration and -0.5% (and 3×(-0.5%)) to natural frequencies of local ones, either with (D1b and D2b) or without (D1a and D2a) crack amplitudes shifts equal to +1.0%. In addition, scenarios D3 and D4 have been considered in order to understand which frequencies influence the most control charts. Scenarios D3 and D4 are opposite to D1 and D2 in terms of frequency shifts because they are obtained by applying -0.5% (and 3×(-0.5%)) to global natural frequencies and -1.5% (and 3×(-1.5%)) to local ones. Damage scenarios Dia ($i = 1, .., 4$) consider only frequency shifts, while Dib ($i = 1, .., 4$) take into account also crack amplitudes shifts.

Table 2.1: Frequency and crack amplitude shifts according to eight (8) damage scenarios, obtained from different combinations of shifts A=-1.5%, B=-0.5% and C=+1.0%. Outliers percentages resulted from corresponding control charts are also reported.

Scenario	Frequency shifts						Crack shifts		Outliers
	Fx1	Fy1	L1	L2	T1	L3	C1	C2	(%)
Undamaged	-	-	-	-	-	-	-	-	4.42
Damage D1a	A	A	B	B	A	B	-	-	17.57
Damage D1b	A	A	B	B	A	B	C	C	57.57
Damage D2a	3A	3A	3B	3B	3A	3B	-	-	57.89
Damage D2b	3A	3A	3B	3B	3A	3B	C	C	57.91
Damage D3a	B	B	A	A	B	A	-	-	5.29
Damage D3b	B	B	A	A	B	A	C	C	49.22
Damage D4a	3B	3B	3A	3A	3B	3A	-	-	51.16
Damage D4b	3B	3B	3A	3A	3B	3A	C	C	51.89

In this context, control charts have been built with one year training period and using a dynamic MLR model with temperatures and crack amplitudes as predictors. The T^2 statistical distance has been calculated on the residuals of all natural frequencies (see Eqs. (2.2) and (2.4)), after artificially inserting the damage-induced effects by imposing small shifts to identified frequencies and crack amplitude data in January 2019, simulating an anomalous structural behavior. Fig. 2.10 and Fig. 2.11 show the control chart in the undamaged case ($\Delta f = 0.000$ and $\Delta C = 0.000$) and in damaged cases according to different shift scenarios reported in Tab. 2.1 and indicate the associated relative percentage of outliers observed in the damaged period.

By visually investigating all control charts and considering the obtained percentages of outliers, the following considerations can be written: (i) frequency shifts of the order of 1.5% (global modes) and 0.5% (local modes) clearly enable the detection of an early damage (see Figs. 2.10a-b), which could be associated with small structural damage, typically occurring after a moderate/light seismic event, (ii) by increasing frequency shifts three times, the number of outliers of the adopted statistical distance grows rapidly (there is a very clear jump of the outliers in all control charts), with a significant increment of the percentage (e.g. from D1a to D2a the percentage passes from 17.57% to 57.89%, see Figs. 2.10a-b), (iii) in the case where also crack amplitude shifts are considered, the number of outliers present a further increase with higher values of T^2 (e.g. from D1a to D1b the percentage passes from 17.57% to 57.57%, see Figs. 2.10b,d), (iv) when shifts equal to -1.5%
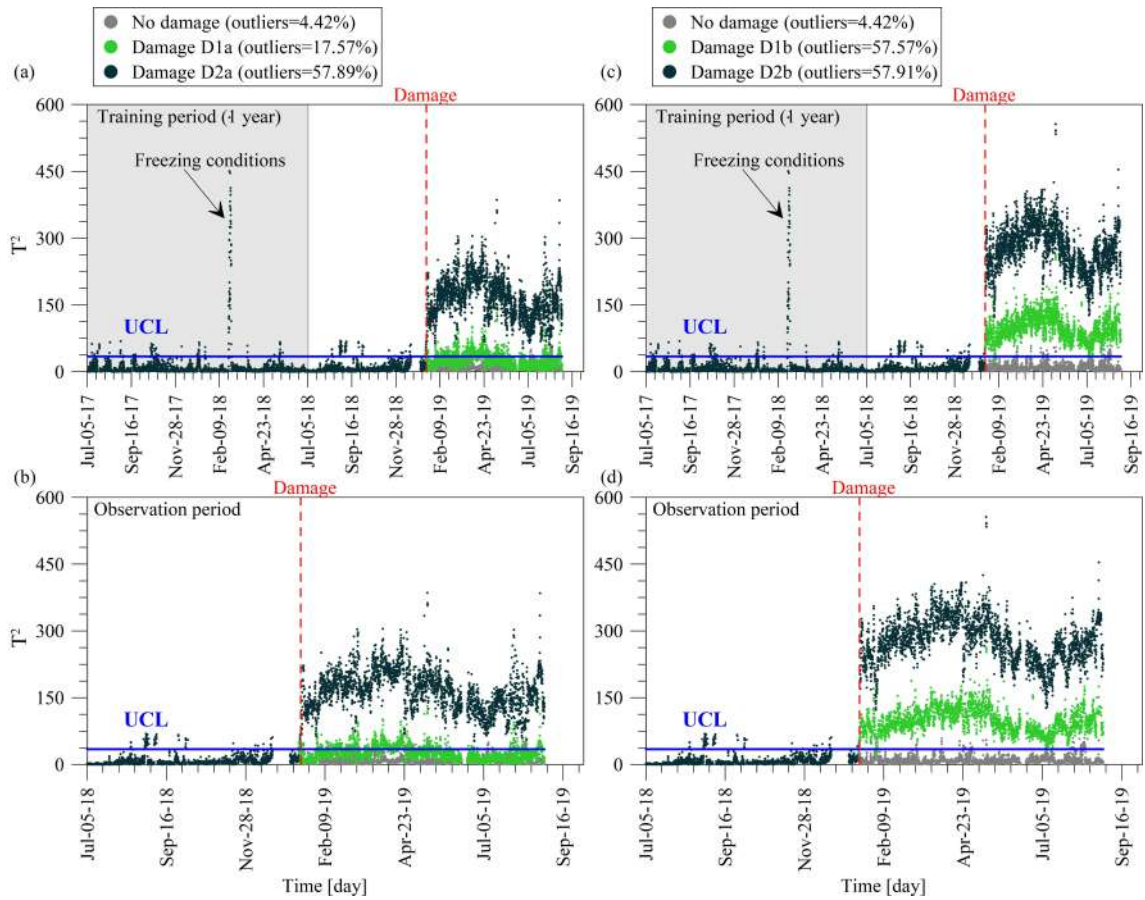
Figure 2.10: Control charts corresponding to the undamaged condition (outliers equal to 4.42%) and to simulated earthquake-induced damages associated to different shift scenarios applied to continuously identified natural frequencies time histories and crack amplitudes: damage scenarios D1a and D2a (a-b) and damage scenarios D1b and D2b (c-d), outliers percentages are written in brackets.

(and $3\times(-1.5\%)$) are applied to natural frequencies of global modes of vibration and -0.5% (and $3\times(-0.5\%)$) to natural frequencies of local ones, higher values of T^2 are obtained with respect to the viceversa shifts application (e.g. from D1a to D3a the percentage passes from 17.57% to 5.29%, see Fig. 2.10b and Fig. 2.11b), meaning that natural frequencies of global modes of vibration (Fx1, Fy1 and T1) make a larger contribution than local modes (L1, L2 and L3) to the structural behavior of the structure, (v) in the case of larger shifts for local modes of vibration (D3a,b and D4a,b), damage detection is achieved, meaning that local damages on the small bell tower of the palace are successfully detectable while the palace remains in a relatively good state of health. However, the need to increase the
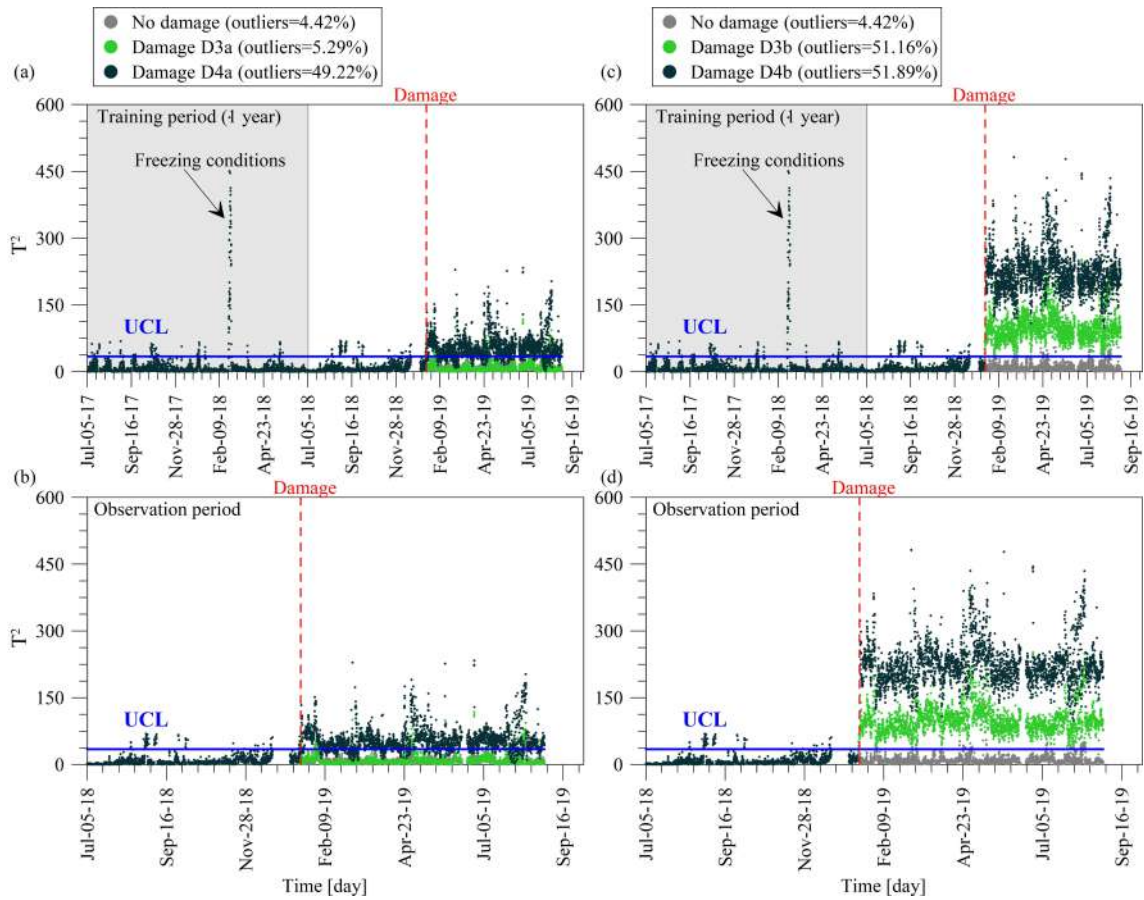
Figure 2.11: Control charts corresponding to the undamaged condition (outliers equal to 4.42%) and to simulated earthquake-induced damages associated to different shift scenarios applied to continuously identified natural frequencies time histories and crack amplitudes: damage scenarios D3a and D4a (a-b) and damage scenarios D3b and D4b (c-d), outliers percentages are written in brackets.

amount of information in order to better detect local changes in structural behavior (which affect higher and local modes), or local damage, points out. Although is clear that we can detect damages in the bell tower, still, we can conclude that it is necessary to increment the information to prove the detection of local damage.

Despite significant environmental effects on identified natural frequencies (Kita et al. 2019b), the proposed SHM method proved effective in detecting very small stationary variations in eigenfrequencies. The presented results show that all simulated earthquake-induced anomalies in the structural behavior have been clearly detected by means of the

adopted vibration-based SHM method combining automated mode tracking, multiple data regression and novelty detection (Fig. 2.1). The number of outliers of the adopted statistical distance grows rapidly with increasing damage severity (frequency change), such that a variation of the order of 0.5% and 1.5% has been clearly detected using the acceleration data and temperature. Similar frequency variations could be associated to small structural damage, typically occurring after a seismic event. Overall, the presented results provide a practical demonstration that the permanent vibration-based SHM system of the Consoli Palace enables automated earthquake-induced damage detection, even for small damages at an early stage caused by moderate earthquakes, thus constituting an effective low-cost tool for condition-based maintenance and preventive conservation of the monumental palace.

2.4   Conclusions

The main results of two years of continuous SHM of the Consoli Palace are presented in this Chapter. It is an historic stiff masonry palace, where a permanent long-term mixed static and dynamic SHM system has been in continuous operation since July 2017. Given the significant thermal effects on natural frequencies of the Consoli Palace, their removal represents a key step towards an effective use of this information for damage detection. The availability of static features, in particular, crack amplitude data, have allowed an enhancement of the vibration-based SHM method for earthquake-induced damage detection.

The main results are summarized below.

- An SSI-data fully automated modal identification procedure has allowed to effectively track the evolution in time of the natural frequencies of the six (6) identified modes of the Palace for two years. It represents a novelty in the literature in the context of long-term monitoring of stiff masonry buildings such as palaces because the majority of previous applications of modal tracking to masonry structures are essentially concerned to slender towers. It is interesting noting that, with a not very dense internal structure and its features more analogous to fortified masonry buildings, the Consoli Palace has peculiar characteristics compared to the more traditional masonry palaces, such that further applications to other stiff palaces may be necessary to consolidate the proposed method.

- A dynamic MLR model has successfully removed the temperature effects on identified natural frequencies after some non-linear correlations between natural frequencies and temperature data were observed, whose effects are conceivably attributed to the thermal inertia of the masonry. Using past values of temperature data as predictors, have proved quite effective for catching delayed temperature-induced effects.

- The use of crack amplitudes as predictors, in addition to temperatures, have allowed to further improve the quality of the natural frequencies prediction, as more reliable damage-sensitive features. In particular, their statistical reconstruction has been investigated through comparison of the relative prediction errors of natural frequencies obtained by three MLR models (static, dynamic and dynamic considering also crack amplitude data) with the increasing length of the training period.

- The advantage of using crack amplitude data as predictors has significantly improved the quality of the control chart in the case of undamaged structure. It has provided

a reduction of the percentage outliers and UCL, thus decreasing the probability to observe an outlier when the structure is in the healthy state (false alarm).

- Despite significant environmental effects on identified natural frequencies, the proposed SHM method has proved effective in detecting very small stationary variations in eigenfrequencies. Earthquake damage effects have been simulated by artificially imposing frequency shifts of the order of 1% to the time histories of monitoring data, which could be associated with small structural damage at an early stage, typically occurring after a moderate/light seismic event. Damages caused by earthquakes are more clearly revealed by the SHM system as the severity of the earthquake increases. The presented results of novelty analysis have demonstrated that all anomalies in the structural behavior have been clearly detected by means of the adopted vibration-based SHM method combining automated mode tracking, refined multiple data regression and novelty detection.

- When earthquake damage effects are simulated by inserting also crack amplitude shifts, in addition to frequency shifts, control charts have reported better results. Indeed, the number of outliers of the adopted statistical distance grows rapidly with increasing severity damage.

It is noteworthy to mention that introducing crack amplitudes as predictors, in addition to temperatures, for the statistical reconstruction of natural frequencies time histories constitutes a novelty in the literature context, not observed in Structural Health Monitoring of historic masonry structures. In this context, an enhanced version of the vibration-based SHM damage detection method is proposed and implemented in the case of the Consoli Palace, an historic stiff masonry palace under permanent long-term static and dynamic monitoring. The damage detection effectiveness of the adopted vibration-based SHM tool has been demonstrated, when frequency shifts, as well as crack amplitude shifts, have been imposed to natural frequencies time histories, thus, artificially inserting earthquake damage effects in the continuous monitoring data. Overall, the presented results provide a practical demonstration that the permanent long-term mixed static and vibration-based SHM system of the Consoli Palace enable rapid and automated earthquake-induced damage detection, even for small damages at an early stage caused by moderate earthquakes, thus constituting an effective low-cost tool for condition-based maintenance and preventive conservation of the stiff monumental palace.

Chapter 3

FEM-based damage localization using surrogate modeling

In this Chapter, the application and validation of the proposed surrogate model-based method are presented with reference to an historic civic masonry tower located in Perugia, Italy, called the *Sciri Tower*. The main theoretical aspects are first addressed, followed by a detailed description of the proposed method. After introducing the tower, together with AVT and long-term SHM data analysis, the calibration and the characteristics of the linear and non-linear FE models representative of the structure are presented. Finally, after the construction of a quadratic surrogate model, the remaining part of the Chapter is devoted to the detection and localization of simulated damage scenarios, as well as real earthquake-induced damage, the latter successfully validated also by non-linear FEM analysis.

3.1 Theory background

Vibration-based SHM methods are eminently efficient for damage detection and, to some extent, damage quantification in the form of permanent variations in natural frequencies (Ubertini et al. 2018; Gentile et al. 2019). While damage detection can be considered an essentially data-driven process, damage localization, on the contrary, can require the inverse calibration of a FE model of the structure, also called FEM Updating (FEMU). This procedure aims to minimize the mismatch between the numerical and experimental responses (typically natural frequencies and mode shapes) by the calibration of the model uncertain damage-related parameters (e.g. material properties, connectivity, or boundary conditions). Thus, changes on the modal features can be related to damage-induced variations in the mechanical parameters of the structure (Atamturktur and Laman 2012; Sehgal and Kumar 2016). However, given the complexity of the geometry of most historic buildings, along with the large number of simulations that are usually required in the minimization problem associated with the FEMU, the computational burden poses a major limitation in practice. On the other hand, the use of surrogate models offers great potential to bypass time demanding and costly numerical models when performing FEMU-based damage localization, thereby enabling continuous model updating to be performed in a computationally efficient way and compatible with continuous SHM systems (Cabboi et al. 2017; Torres et al. 2017; Venanzi et al. 2019). In this way, the model updating procedure for damage identification can be conducted in a computationally inexpensive way. Surrogate-assisted strategies suggest the use of efficient models, such as Response Surface Methods (RSMs), allowing an explicit relationship between FEM responses and structural parameters in a computationally efficient way.

There are only a few experiences in the literature on the application to model updating of historical structures (Cabboi et al. 2017; Torres et al. 2017; Venanzi et al. 2019). It is worth noting the work (Cabboi et al. 2017) who conducted an automated surrogate-based model updating of the San Vittore bell-tower in Milan (Italy), where the RSM for the real-time updating of a 3D FEM of the tower has been used. Also, (Torres et al. 2017) proposed an RSM-based FEM updating of the Metropolitan Cathedral of Santiago (Chile). The localization task can be performed by solving an inverse FEM calibration problem, where equivalent elastic properties of macrostructural elements are identified by minimizing an objective function considering experimentally identified and numerically predicted damage-induced decays in natural frequencies as well as changes in eigenvector compo-

nents. This can be performed by an efficient response surface meta-model, which allows minimizing the computational effort of the calibration procedure.

In general, the scope of a surrogate model is to bypass in a cost-effective way the input/output relationship of a computationally demanding model. Let us define m damage-sensitive parameters, $x_i \in \mathbb{R}$, $i = 1, .., m$, determining the response y of a FEM. A surrogate model serves as a black-box representation of the response of the FEM as $y(\mathbf{x})$, with $\mathbf{x}$ being the vector of design parameters $\mathbf{x} = [x_1, ..., x_m]^\mathrm{T}$. To construct the surrogate model, it is often necessary to obtain a training population by Monte Carlo simulations (MCS) using the FEM. A training population of N individuals is defined by a m x N matrix of design sites $\mathbf{X} = [\mathbf{x}^1, ..., \mathbf{x}^N]$, and an observation vector $\mathbf{Y} = [y_1, ..., y_N]^\mathrm{T}$, with $y_i \in \mathbb{R}$ being the system's response to the input x_i. Specifically, the modal properties obtained by linear modal analysis of the FEM can be assumed as outputs.

The Response Surface Method (RSM) constitute a collection of statistical tools for fitting empirical models and so alleviate the computational effort of iterative processes (Myers et al. 2016). The second-order quadratic RSM formulation can be written as follows:

$$y(x) = \alpha_0 + \sum_{j=1}^{m} \alpha_j x_j + \sum_{j=1}^{m} \alpha_{jj} x_j^2 + \sum_{j=1}^{m} \sum_{i \geq j}^{m} \alpha_{ji} x_j x_i + \epsilon \tag{3.1}$$

where coefficients α_0, α_j, α_{jj} and α_{ji} represent the intercept, linear, quadratic and interaction coefficients, respectively. The term ϵ is a normally distributed statistical error with zero mean, independent, and identically distributed at each observation.

3.2   The proposed method

The proposed method for earthquake-induced damage assessment is based on real-time damage detection and localization using long-term vibration monitoring data, which is performed by solving an inverse calibration problem on a quadratic surrogate model, to track variations of modal parameters observed through the processing of monitoring data. It concerns an enhanced version of the method proposed in (Cabboi et al. 2017), whereby the innovative aspects are presented next.
The outline of the procedure is summarized in the following steps:

- Step 1: Construction of a reliable numerical linear FE model, tuned based on AVT, and a surrogate model linking frequency shifts and eigenvector components to elastic parameters of macrostructural elements;

- Step 2: Perform OMA at time intervals δt_{id} by using monitoring data;

- Step 3: Removal of the fluctuations of natural frequencies caused by changing environmental and/or operational conditions through a dynamic MLR model;

- Step 4: Novelty analysis: construction of a control chart to detect the damage at time δt_{id};

- Step 5: If the damage is detected at step 4, localization of such damage at time δt_{id} by inspecting the time series of equivalent elastic parameters of macrostructural elements continuously obtained through the solution of an optimization problem using the surrogate model. The optimization problem may be solved by assigning different weights to natural frequencies and mode shape components to test the robustness of the solution and avoid false positives.

The procedure is detailed in the following lines.

Continuous modal identification is needed for the 2nd step of the procedure. Within the monitoring process, modal properties are continuously identified by means of an automated SSI technique (Ubertini et al. 2013). The monitored structure is modeled in by the following equations:

$$\mathbf{x}(k+1) = \mathbf{A}\mathbf{x}\,(k) + \mathbf{w}\,(k)$$
$$\mathbf{y}(k) = \mathbf{C}\mathbf{x}(k) + \mathbf{v}(k)$$
(3.2)

in which k is the time step, $\mathbf{x} \in \mathbb{R}^{q \times 1}$ is the state vector (with q order of the identified model), $\mathbf{y} \in \mathbb{R}^{L \times 1}$ is the vector collecting the L output measurements, $\mathbf{A} \in \mathbb{R}^{q \times q}$ is the system matrix from which modal information can be retrieved, $\mathbf{C} \in \mathbb{R}^{L \times q}$ is the corresponding output matrix, $\mathbf{w} \in \mathbb{R}^{q \times 1}$ and $\mathbf{v} \in \mathbb{R}^{L \times 1}$ are white noise vector processes representing the external input and the noise affecting the measurements, respectively.

In order to remove the effects of environmental conditions from identified natural frequencies (3rd step), a dynamic MLR model has been adopted, found to be crucial for catching delayed temperature-induced effects (see Section 2.1 and Section 2.3.2). With reference to Eqs. (2.3) and (2.4), dependent variables are stored in the observation matrix $\mathbf{Y}$ (the natural frequencies identified by eigenvalue analysis of matrix $\mathbf{A}$ in Eq. (3.2)), while their estimates in $\hat{\mathbf{Y}}$. Residuals in Eq. (2.4) can be used to obtain the time series of cleansed natural frequencies, contained in matrix $\mathbf{F}_{\mathrm{cleansed}}$ according to Eq. (3.3), by summing the vector containing average values of the natural frequencies observed in the training period, $\mathbf{F}_{\mathrm{t_t}}^{\mathrm{mean}}$, to the vector of statistical model residuals, $\mathbf{E}$.

$$\mathbf{F}_{\mathrm{cleansed}} = \mathbf{F}_{\mathrm{t_t}}^{\mathrm{mean}} + \mathbf{E} \tag{3.3}$$

The 4th step concerns the construction of a control chart for detecting the occurrence of damage at time δt_{id}, after removing the effects of environmental conditions. The control chart is the time history of the T^2 statistic computed on the basis of the residuals of the MLR model according to Eqs. (2.2) and (2.4).

A continuous model updating is carried out by optimizing a set of parameters of the FE model of the tower. Experimental natural frequencies and mode shapes, obtained from continuous monitoring as well as depurated/cleansed from thermal effects (only in the case of natural frequencies), are preliminarily evaluated at time intervals δt_{id}. Frequency changes, Δf^{exp}, with respect to reference values are also computed at the same time δt_{id}. The parameters to be updated, i.e. the design variables of the optimization problem, are collected into a vector $\mathbf{U} = (U_1, ..., U_n, U_{n+1}, ..., U_{2n}, U_{2n+1}, ..., U_{n \cdot m})$, where n is the number of uncertain parameters (e.g. the elastic modulus) and m is the number of different zones in which the tower can be ideally divided (macroelements). To assess the continuous variations of damage-related parameters, a functional J is defined as follows:

$$J(\mathbf{U}) = \sum_{i=1}^{l} (\alpha_i \epsilon_i(\mathbf{U}) + \beta_i \delta_i(\mathbf{U})) \tag{3.4}$$

where

$$\epsilon_i = \left| \frac{\Delta f_i^{\mathrm{exp}}}{f_i^{\mathrm{exp}}} - \frac{\Delta f_i^{\mathrm{FEM}}(\mathbf{U})}{f_i^{\mathrm{FEM}}(\mathbf{U})} \right|$$
$$\delta_i = 1 - MAC_{ii}(\mathbf{U})$$

(3.5)

The optimization problem is stated as follows:

$$\text{find } \mathbf{U}$$
$$\text{that minimizes } J(\mathbf{U})$$
$$\text{subjected to } \mathbf{U}_{lb} \leq \mathbf{U} \leq \mathbf{U}_{ub}$$

(3.6)

where $\mathbf{U}_{lb}$ and $\mathbf{U}_{ub}$ are the vectors storing the lower and upper bound values of the components of $\mathbf{U}$. In Eq. (3.4) and Eqs. (3.5), MAC represents the Modal Assurance Criterion between the identified mode shapes and those obtained by the model, $\Delta f_i^{\mathrm{FEM}}$ are the natural frequencies variations estimated with the FEM model with respect to the nominal values f_i^{FEM}, l is the number of identified modes and α_i and β_i are weighting coefficients that establish the relative importance of the two addends in Eq. (3.4). A gradient-based minimization technique can be used for convex objective space while a random optimization algorithm can be employed otherwise. The optimization problem is solved continuously for each set of identified modal data (natural frequencies and mode shapes) in order to track in time the damage-dependent parameters. As the choice of the weighting coefficients can significantly affect the localization results, a preliminary parametric analysis has to be carried out in order to determine the most appropriate sets of α_i and β_i.

In order to limit the computational time required by the optimization problem and allow an online estimation of equivalent parameters of macrostructural elements, a surrogate model is adopted to estimate f_i^{FEM} and their corresponding mode shapes. To this aim, a simple quadratic formulation is adopted (Douglas and Reid 1982):

$$f_i^{\mathrm{FEM}}(\mathbf{U}) = \sum_{j=1}^{n} A_{i,j} U_j^2 + \sum_{j=1}^{n} B_{i,j} U_j + C_i$$
$$\Phi_i^{\mathrm{FEM}}(\mathbf{U}) = \sum_{j=1}^{n} D_{i,j} U_j^2 + \sum_{j=1}^{n} E_{i,j} U_j + F_i$$

(3.7)

where $A_{i,j}$, $B_{i,j}$, C_i, $D_{i,j}$, $E_{i,j}$ and F_i, are coefficients relating the ith identified modal properties to the jth uncertain parameter ($j = 1, .., n$). With reference to Eq. (3.1), it can

be noted that the quadratic surrogate model used in the case of the Sciri Tower does not consider the mixed term. When the control chart highlights the presence of damage, this is expected to be localized in the macrostructural region experiencing decays in equivalent elastic constants obtained from the above presented continuous model tuning procedure.

As already stated at the beginning of this Section, the proposed method is an enhanced version of the method proposed in (Cabboi et al. 2017). Innovative aspects concern, in particular, the objective function in Eq. (3.4) which includes two terms: one related to resonant frequencies variations and the other one related to mode shapes variations. This leads to improve the accuracy of the results, as damage can influence not only the resonant frequencies but also the mode shapes. This can also improve the solution's robustness because a multi-objective optimization allows studying the stability of the solution with respect to changes in the weighting coefficients, distinguishing non-physical solutions from robust ones. Moreover, the term of the objective function related to natural frequencies (ϵ_i) is expressed in terms of relative changes, instead of using absolute changes. This makes relative changes ϵ_i assume similar values for every natural frequency and allows using a single weighting coefficient for all the resonant frequencies. Instead of a linear PCA approach adopted in (Cabboi et al. 2017), a dynamic MLR model is proposed. The latter uses present and past observations of measured temperature data, being effective in removing temperature effects also in the case of significant delays between changes in air temperature and changes in structural behavior due to the high thermal capacity of the structure.

The proposed method is applied to the Sciri Tower, an historic civic masonry tower located in Perugia, Italy, that has been continuously monitored for about two years. A complete FE model of the tower and the surrounding building aggregate is adopted to construct the surrogate model, instead of using a simplified model where the interaction between the tower and the surrounding building is modeled by local constraints.

3.3   Application example: the Sciri Tower

3.3.1   Introduction to the case study

The 2nd case study structure considered in this dissertation is the 41 m high civic tower located in *Via dei Priori* in the historical center of Perugia, Italy, named *Torre degli Sciri* (Garcia-Macias et al. 2019; Venanzi et al. 2020). Built in the 13th century for defensive purposes, the Sciri Tower represents today the only intact remaining tower of around 70 medieval towers of the city. Fig. 3.1 shows some historical medieval paintings and a current aerial view of the tower. Being incorporated into a building aggregate with approximate cross-section dimension of 20 x 25 m (plan view depicted in Fig. 3.2c), it is surrounded by neighboring masonry buildings up to the first 17 m on three sides, while the fourth side is free and facing *Via dei Priori* towards North (Figs. 3.1e and 3.2b). East and North fronts are shown in Figs. 3.2a-b, respectively. The masonry is homogeneous and regular and it is made of squared white limestone blocks. The tower has a quadrangular cross-section (7.15 x 7.35 m, as depicted in 3.2d) and it can be ideally divided into two structural portions, as depicted in Fig. 3.2: the lower and the upper parts. The lower part, up to a height of 8.4 m, is characterized by about 2.1 m thick walls with some small openings and a stone masonry vaulted slab which stands above the rooms of an old chapel. The upper part,
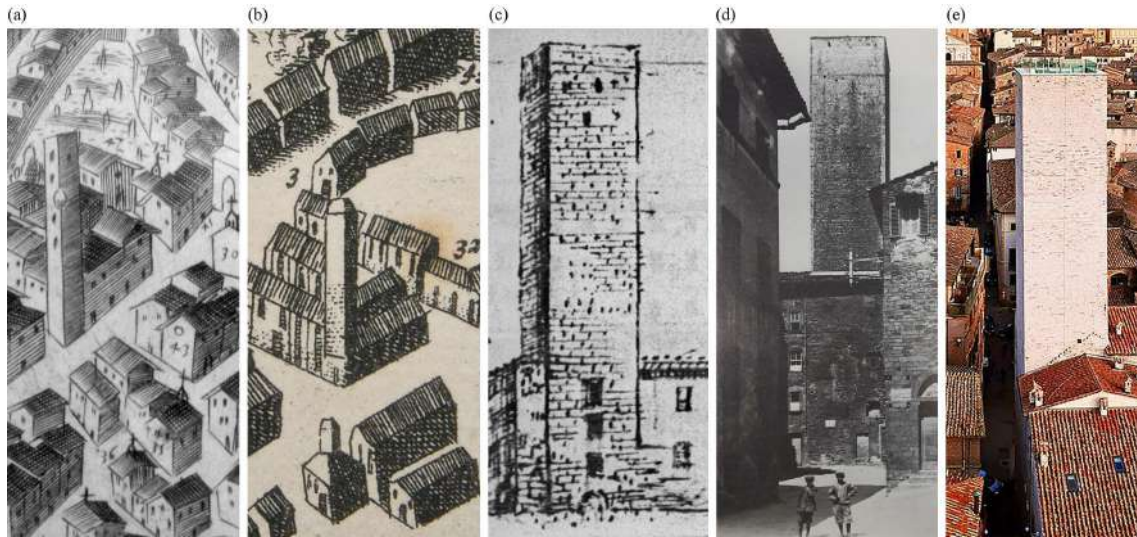
Figure 3.1: The Sciri Tower over the centuries, historic paintings and today: technical drawings of Augusta Perusia by Eusebio in 1602 (a) and Mortier in 1724 (b), unknown author in 1880 (c), photo by Raniero Gigliarelli in 1908 (d) and aerial view today (e).
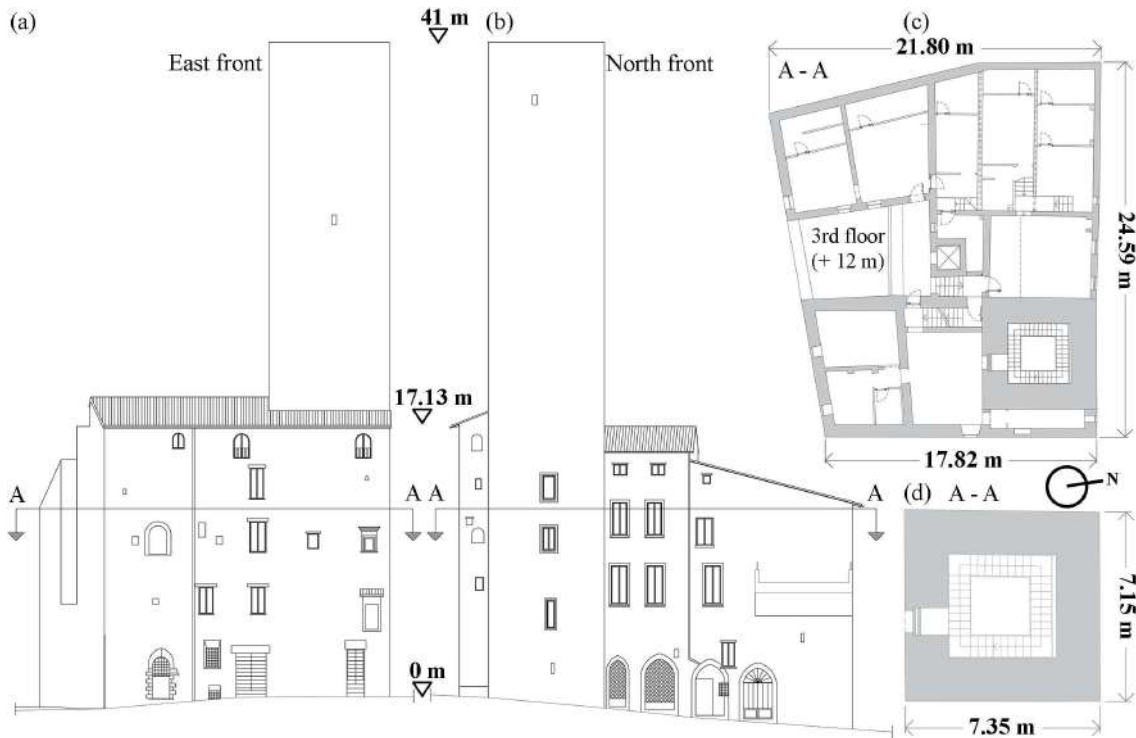
Figure 3.2: The Sciri Tower: East front (a), North front (b), plan view at 12 m height (c) and cross section of the tower (d).

rising up to 41 m, has slender continuous walls (thickness from 1.6 to 1.4 m) with four 1.5 m wide brick masonry vaulted slabs at different heights. Moreover, a brick masonry ceiling vault completes the tower on the top. Consolidated by the Municipality of Perugia in 2015, aiming at its seismic improvement and the conservative restoration of the entire complex, the Sciri Tower is in a very good state of preservation without any significant and visible damage pattern. Finally, no damages were observed after major earthquakes occurred in Italy in recent years: L'Aquila Earthquake, 2009, Emilia Earthquake, 2012, and Central Italy seismic sequence, 2016 (Cattari et al. 2019).

An AVT was carried out on the Sciri Tower on May 22nd 2017 with the main purpose of evaluating the baseline dynamic characteristics of the building and, in particular, its natural frequencies, mode shapes and damping ratios (Venanzi et al. 2020). It was conducted on the building using a total of 12 high sensitivity (10 V/g) uniaxial accelerometers, model PCB 393B12, installed on the structure to measure micro tremors induced by traffic and wind (operational conditions). The layout of the accelerometers (progressively denoted

as A1, A2,... A12) is depicted in Fig. 3.3b. Modal parameters from ambient vibration data have been estimated through two different tools: classical and enhanced version of Frequency Domain Decomposition (FDD and EFDD) and SSI. Seven (7) vibration modes have been identified within the range from 0 to 11 Hz: two flexural modes in NW direction (x direction as depicted in Fig. 3.3, denoted as Fx1 and Fx2, respectively), two flexural modes in SW direction (y direction, denoted as Fy1 and Fy2, respectively), one torsional mode, namely Tz1, and, finally, two higher-order flexural modes, Fx3 and Fy3. In particular, Figs. 3.3c-d show the first three singular values of the power spectral density matrix obtained from the AVT by means of the FDD technique, where seven (7) resonant peaks are clearly identified, and mode shapes obtained from the AVT data by means of the
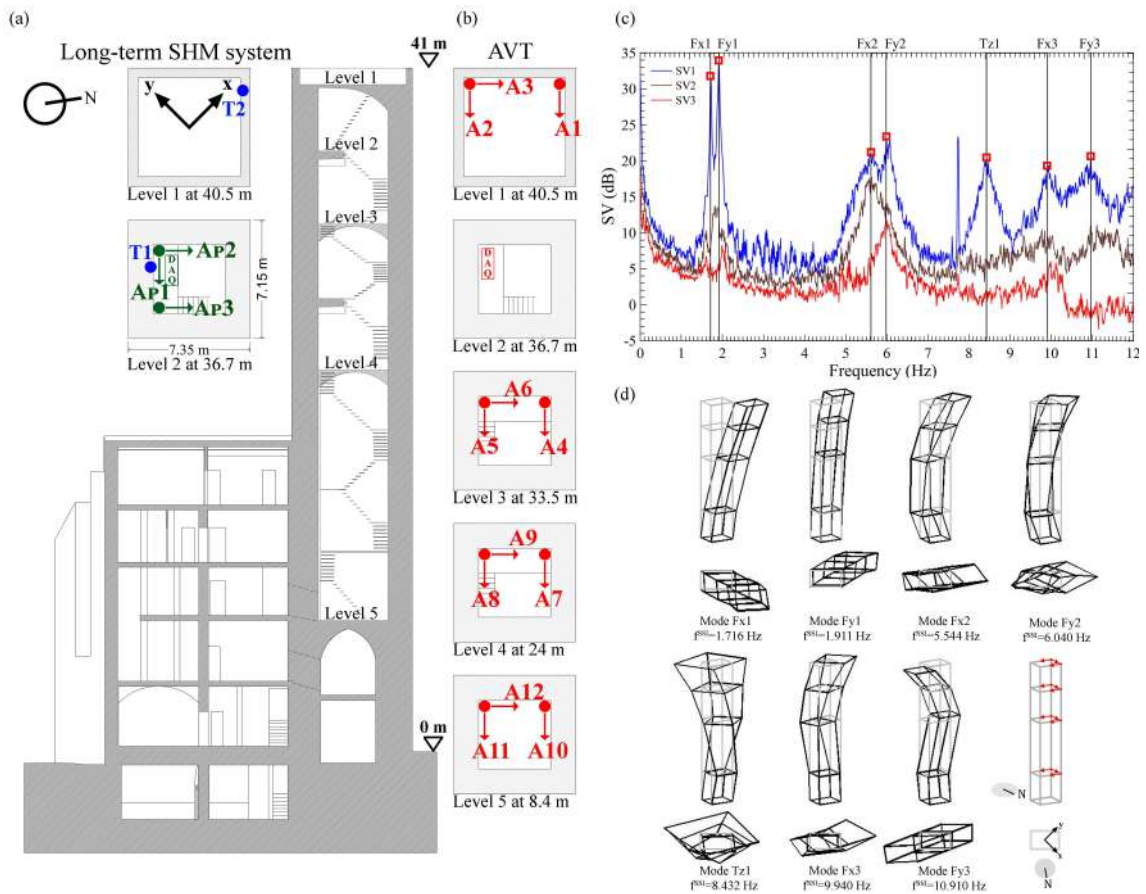
Figure 3.3: Accelerometers layout for continuous monitoring (a) and AVT (b). First three singular values (SV) of the power spectral density matrix (FDD) obtained from the AVT and identified resonant peaks with related modes of vibration (c) and mode shapes identified by automated SSI technique (d).

SSI technique, respectively. It can be noticed that the first two mode shapes are bending modes that are not classically oriented according to the main directions of the square cross-section. In fact, given the configuration within the building aggregate yielding restraints in two sides of the tower (see Fig. 3.2c), the direction of the first bending mode shapes is along the diagonal of the tower cross-section. The natural frequencies (f_i^{FDD}, f_i^{EFDD} and f_i^{SSI}) and damping ratios (ξ_i^{EFDD} and ξ_i^{SSI}) of the seven (7) identified modes from AVT are reported in Tab. 3.1. In addition, in order to take into account environmental effects, Tab. 3.1 summarizes natural frequencies obtained by means of MLR model at the reference temperature of 20°C (mean annual value for the city of Perugia), denoted as $f_{i,20°\mathrm{C}}^{\mathrm{MLR}}$. The latter have been used as target frequencies for the numerical model calibration, presented in the next Section.

Table 3.1: Experimental identified natural frequencies and damping ratios from AVT and frequencies estimated through MLR at 20° C.

Mode no.	Mode type	f_i^{FDD} [Hz]	f_i^{EFDD} [Hz]	f_i^{SSI} [Hz]	ξ_i^{EFDD} [%]	ξ_i^{SSI} [%]	$f_{i,20°\mathrm{C}}^{\mathrm{MLR}}$ [Hz]
1	Fx1	1.709	1.714	1.716	0.740	0.832	1.722
2	Fy1	1.914	1.913	1.911	0.932	0.792	1.925
3	Fx2	5.615	5.615	5.544	0.581	3.739	5.615
4	Fy2	5.986	6.013	6.040	1.054	1.429	6.006
5	Tz1	8.428	8.439	8.432	2.081	1.660	8.399
6	Fx3	9.902	9.944	9.940	1.638	1.063	9.896
7	Fy3	10.970	10.910	10.900	1.740	2.946	10.928

3.3.2   Continuous SHM and FE modeling

Subsequently to AVT, with the purpose of monitoring the structural integrity and of promptly detecting small damages caused by low-return period earthquakes, a simple low-cost vibration-based SHM system was installed on the tower and is active since December 13th 2017 (Venanzi et al. 2020). Fig. 3.3a shows the configuration of the continuous permanent vibration-based SHM system installed on top of the tower: three high-sensitivity uni-axial piezoelectric accelerometers (denoted as Ap1, Ap2 and Ap3) and two K-type temperature sensors (denoted as T1, indoor, and T2, outdoor) measuring the surface temperature of the wall. The data acquisition system (NI Compact DAQ-9185) is located inside the tower and connected via the INTERNET to a dedicated remote server in the

Laboratory of Structural Dynamics of the Department of Civil and Environmental Engineering of the University of Perugia, where continuous data are consecutively stored in separate files containing 30 minute acceleration time series with a sampling frequency of 100 Hz and processed through an ad-hoc developed MatLab code, for automated modal identification (Ubertini et al. 2013). Results of continuous modal identification and frequency tracking are presented in Fig. 3.4.

Considering the continuous monitoring period from December 13th 2017, Fig. 3.5 shows the identified natural frequencies versus temperature data measured by thermocouple T2. Frequency-temperature correlations are essentially bi-linear (including freezing conditions) and, in accordance with what observed in other literature works on vibration-based monitoring of masonry towers (Saisi et al. 2015; Gentile et al. 2016; Ubertini et al. 2017; Saisi et al. 2018), these correlations are positive above 0° C and negative below. Considering the dynamic MLR model adopted in the case of the Sciri Tower, Fig. 3.6 shows the time series of identified and predicted first and second natural frequencies, as well as the natural frequencies depurated/cleansed from thermal effects, obtained by applying Eq. (3.3).
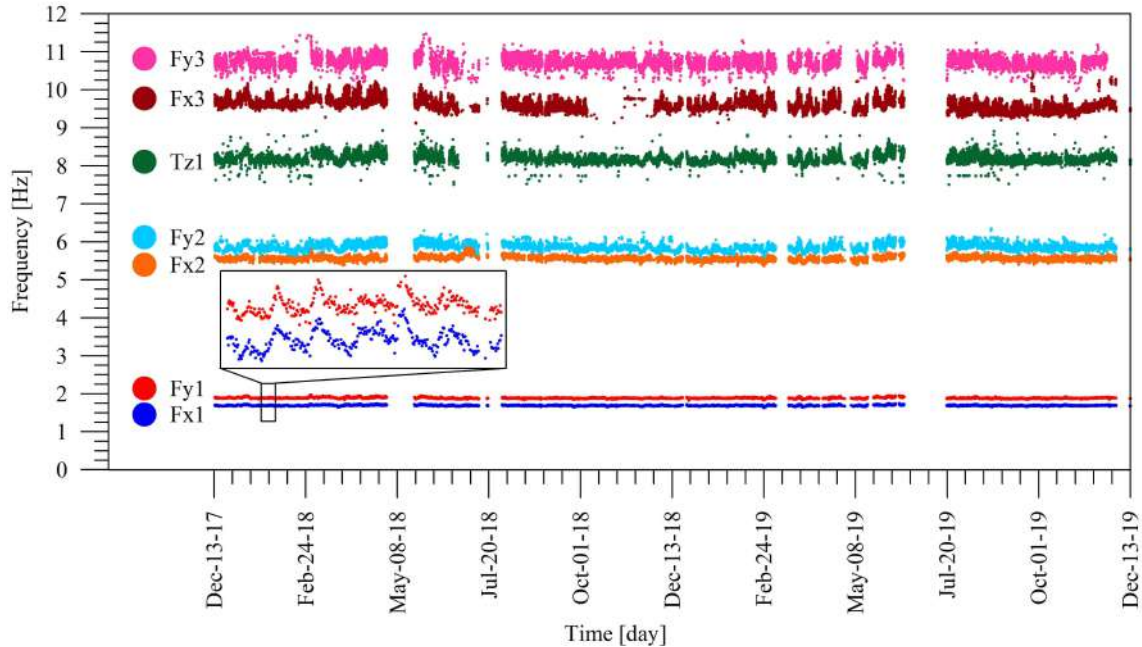
Figure 3.4: Time series of identified natural frequencies during the monitoring period (daily fluctuations are also evidenced with a detailed view).

50
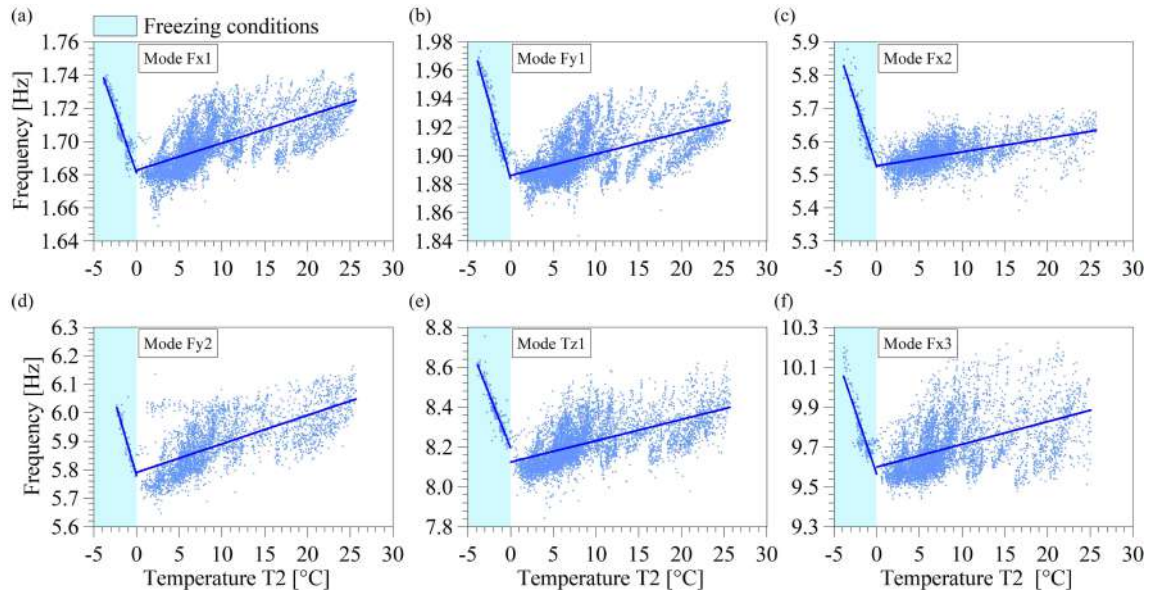
Figure 3.5: Identified natural frequencies versus temperature T2.
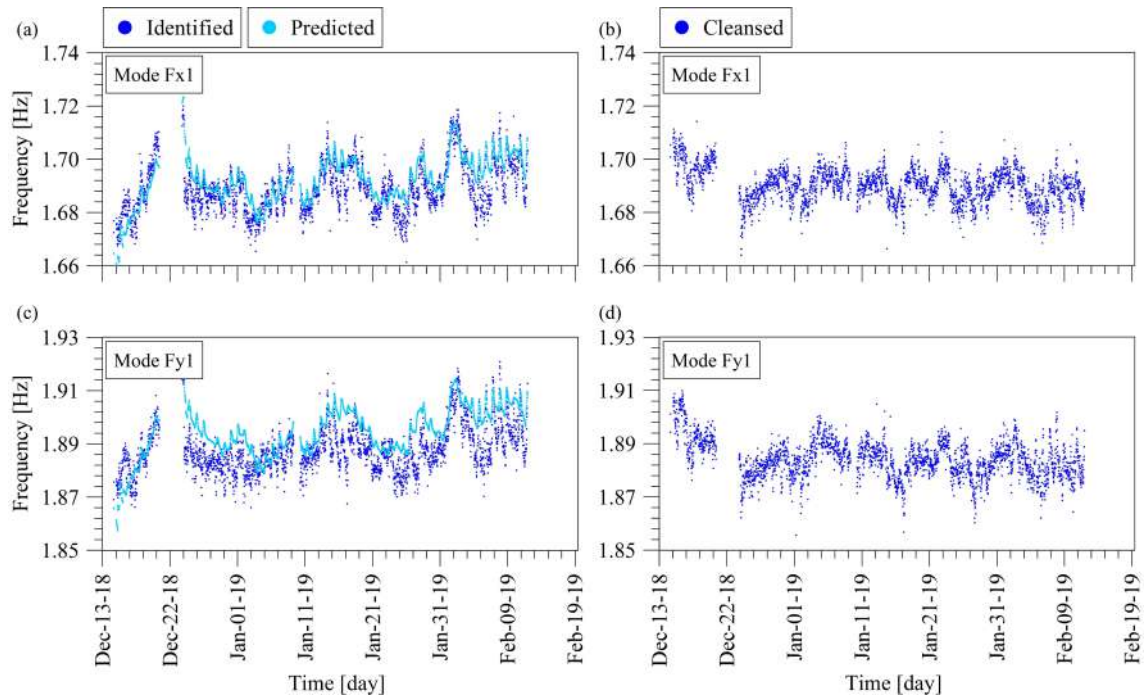
Figure 3.6: Identified and predicted natural frequencies compared to those cleansed from thermal effects after one year of training period.

In order to properly interpret the monitoring data and to assist the damage localization task, a 3D numerical model of the Sciri Tower and the surrounding aggregate has been built in the framework of the Finite Element Method (FEM) by using the ABAQUS 6.10 platform (Simulia 2010) (see Fig. 3.7). A free meshing of solid tetrahedral elements, with mean elements' dimension of about 50 cm, has been adopted (245149 and 411140 the total number of finite elements and nodes, respectively). It is noteworthy to stress that, for obtaining consistency between numerically and experimentally identified modes of vibration, a proper modeling of the constraints given by the neighboring buildings in the lower part, described by means of tie connection at the interfaces, resulted to be crucial. In fact, in application to towers, particular attention should be focused on the effects of surrounding aggregate buildings. In order to localize damage, a simplified modeling of the surrounding aggregate buildings in the FE model may not be sufficient to accurately simulate the building's behavior (Formisano 2017; Fagundes et al. 2017; Castellazzi et al. 2018; Bartoli et al. 2019; Torelli et al. 2019). FEM materials have been modeled with isotropic constitutive behavior. The initial mechanical parameters of the material (Young's modulus E, Poisson's ratio ν and specific weight γ) considered for square stone masonry according to the Italian technical standard code (NTC08 2008; NTC18 2018), as explained in (Cavalagli et al. 2018), are summarized in Tab. 3.2.
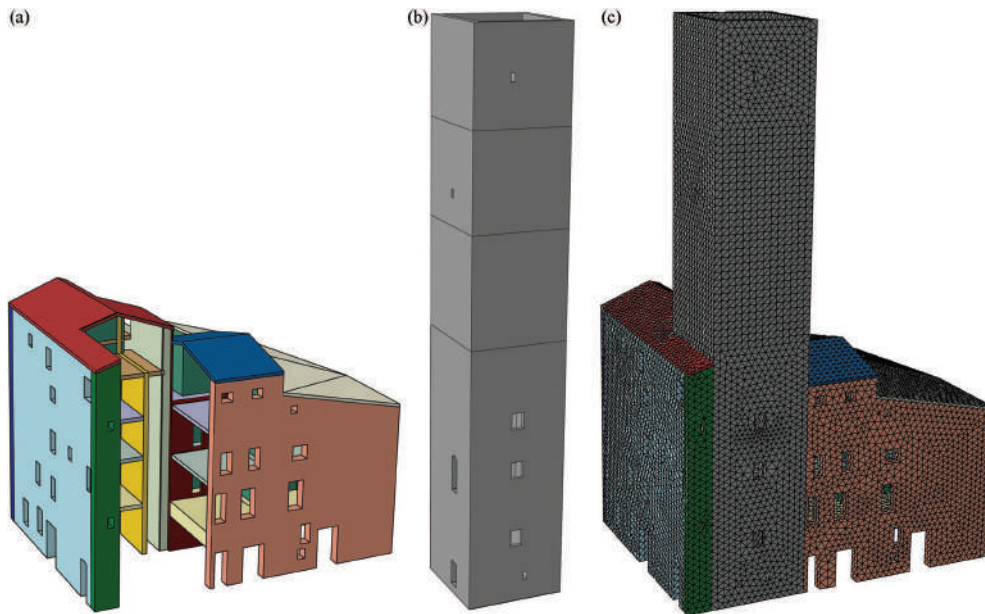
Figure 3.7: Finite element model of the building aggregate (a) and the Sciri Tower (b) and tetrahedral discretization view (c).

Table 3.2: Mechanical parameters of the FE model before tuning.

E [kN/m^2]	ν [-]	γ [kN/m^3]
4.032e+06	0.25	21.6

For FEM tuning, the model has been partitioned into several regions to allow discrimination of the materials of the walls and floors. A total of seventeen (17) different materials have been assigned to the model (highlighted with different colors in Fig. 3.7) relative to the tower, the nine (9) walls of the building aggregate, the four floors and the three parts of the roof of the building aggregate. For each material, both E and the γ have been considered as uncertain parameters, for a total of thirty-four (34) quantities to be calibrated. Then, model updating has been carried out through modal sensitivity analysis and a linear single-step procedure. The FEM model has been used to construct the following approximate linear relationship between the vector of estimated natural frequencies, $\mathbf{f}^{\text{FEM}}$, and the vector of uncertain parameters to be calibrated (E or γ of each wall to calibrate), $\mathbf{X}$:

$$\mathbf{f}^{\text{FEM}} = \mathbf{f}_0^{\text{FEM}} + \mathbf{S}(\mathbf{X} - \mathbf{X}_0) \tag{3.8}$$

where $\mathbf{X}_0$ stores the initial guess of the parameters, $\mathbf{f}_0^{\text{FEM}}$ collects the corresponding natural frequencies and $\mathbf{S}$ is a matrix containing sensitivity coefficients of natural frequencies with respect to changes in model parameters that have been estimated through a series of numerical modal analysis considering small variations of such parameters one at a time. The updated values of the uncertain parameters $\mathbf{X_1}$ can be computed as:

$$\mathbf{X_1} = \mathbf{X_0} + (\mathbf{S}^{\text{T}}\mathbf{S})^{-1}\mathbf{S}^{\text{T}}(\mathbf{f}^{\text{ID},20°\text{C}} - \mathbf{f}_0^{\text{FEM}}) \tag{3.9}$$

where $\mathbf{f}^{\text{ID},20°\text{C}}$ is the vector containing $f_{i,20°\text{C}}^{\text{MLR}}$. It should be noted that in order to have Eq. (3.9) well-posed, the non-singularity and invertibility of matrix $\mathbf{S}^{\text{T}}\mathbf{S}$ has been checked before application of such equation. The calibration of the thirty-four (34) parameters has led to accurate tuning of the modal characteristics. By applying Eqs. (3.8) and (3.9), the calibrated value of the Young's modulus of the material constituting the tower is $E = 5.77e+06$ kN/m^2 and its specific weight is $\gamma = 21.6$ kN/m^3. Tab. 3.3 summarizes the comparison between the target frequencies, $f_{i,20°\text{C}}^{\text{MLR}}$, and those numerically predicted from the tuned FE model, f_i^{FEM}. The comparison in terms of relative difference of frequencies ($\Delta f_i/f_i$) results in a mean error value equal to $(\Delta f/f)_{\text{mean}} = 2.181\%$. Tab. 3.3 also reports MAC

Table 3.3: Comparison between experimental and numerical modal parameters after tuning.

Mode	$f_{i,20°C}^{MLR}$ [Hz]	f_i^{FEM} [Hz]	$\Delta f_i/f_i$ [%]	MAC [-]
Fx1	1.722	1.754	1.870	0.970
Fy1	1.925	1.967	2.140	0.973
Fx2	5.615	5.770	2.757	0.972
Fy2	6.006	6.195	3.152	0.651
Tz1	8.399	8.005	-4.686	0.747
Fx3	9.896	9.894	-0.022	0.965
Fy3	10.928	10.858	-0.641	0.840
			$(\Delta f/f)_{mean} = 2.181\%$	$MAC_{mean} = 0.874$

coefficients between experimental (obtained during the AVT of May 22nd 2017) and numerical mode shapes, computed considering 12 modal displacement components. Overall, a good agreement is achieved between model and field data ($MAC_{mean} = 0.874$), whereby relatively larger differences in the modes Fy2 and Tz1 are probably due to a high degree of modal complexity for the identified mode shapes. The accuracy achieved in Tab. 3.3 is assumed as sufficiently good for the purposes of the present investigation.

In addition to the linear FE model, a non-linear model has also been constructed to simulate earthquake-induced damage scenarios and validating the proposed damage localization procedure. In this regard, the non-linear FE modeling and mechanical behavior of the masonry material have been here reproduced using the classical Concrete Damage Plasticity (CDP) constitutive model proposed by Lubliner (Lubliner et al. 1989) and subsequently modified by Lee and Fenves (Lee and Fenves 1989) for cyclic loading and damage implementation. Based on concepts of isotropic elasticity in combination with isotropic tensile and compressive plasticity (scalar isotropic damage with distinct damage parameters in tension and compression), the CDP model is widely used in the literature on seismic vulnerability and non-linear dynamic analysis (Valente and Milani 2016; Cavalagli et al. 2018; Ubertini et al. 2018; Formisano et al. 2018b; Valente et al. 2019; Abbati et al. 2019). The few lines that follow deserve a basic description of CDP, whereby the main scheme is illustrated in Fig. 3.8.

Originally developed to describe the non-linear behavior of concrete, the CDP model is a continuum plasticity-based damage model commonly accepted in the literature for quasi-brittle materials (concrete, rock and masonry) with non-linear behavior, both in tension (tensile cracking) and compression (crushing). It considers a modification of the yield surface shape of the Drucker-Prager criterion by means of specific parameters. In particular, the trace of the failure surface in the deviatoric plane is not circular anymore, but resembles more to the shape of Mohr-Coulomb's criterion, thereby resulting more consistent in describing the behavior of quasi-brittle materials. According to Eqs. (3.10), damage parameters are locally defined on the basis of the equivalent plastic strain $\tilde{\varepsilon}_c^{\mathrm{pl}}$ and of other field variables θ_i, differentiating tension from compression. They reduce the initial stiffness values, e.g. the Young's modulus E_0 (see Eq. (3.11)).
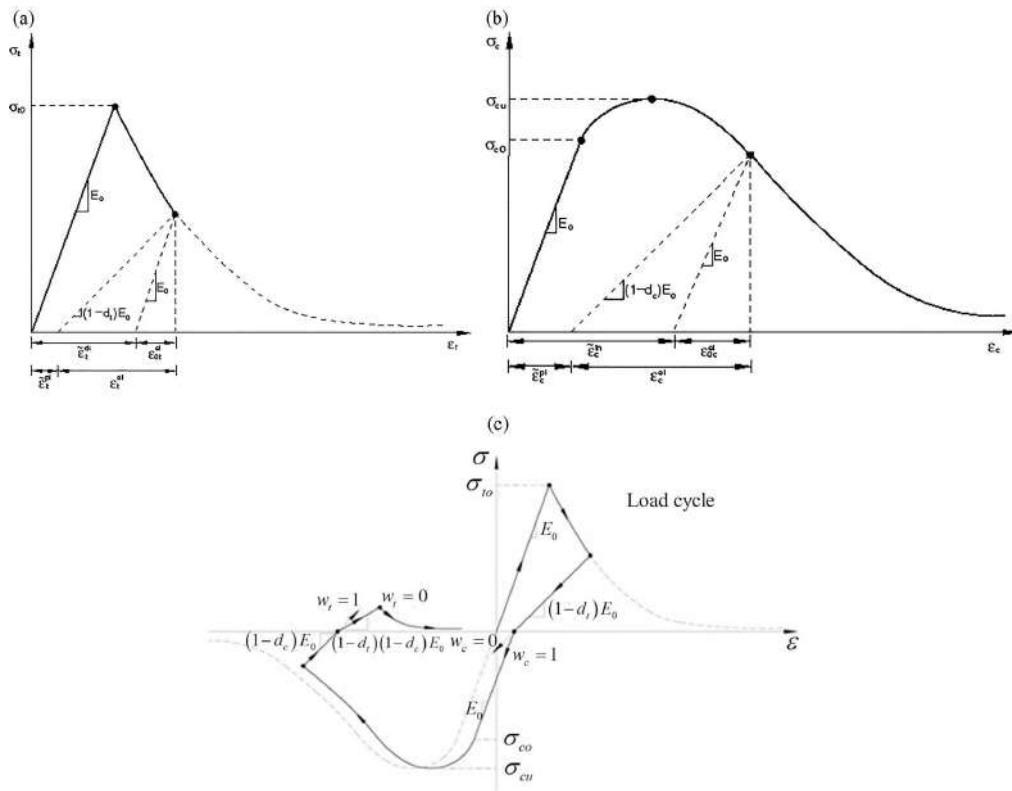
Figure 3.8: Stress-strain relationships of the Concrete Damage Plasticity (CDP) constitutive model: tension curve (a), compression curve (b) and uniaxial load cycle assuming default values for the stiffness recovery factors (w_t=0 and w_c=1) (c).

$$d_c = d_c(\tilde{\varepsilon}_c^{\mathrm{pl}}, \theta_i)$$
$$d_t = d_t(\tilde{\varepsilon}_t^{\mathrm{pl}}, \theta_i)$$

(3.10)

$$E_d = (1 - d)E_0$$

(3.11)

The solution algorithm for non-linear dynamic analysis has been based on the classical Newton-Raphson formulation. In particular, the cracking strain, $\tilde{\varepsilon}_t^{\mathrm{ck}}$, is defined as $\tilde{\varepsilon}_t^{\mathrm{ck}} = \varepsilon_t$ - $\varepsilon_{0t}^{\mathrm{el}}$, where ε_t is the total strain and $\varepsilon_{0t}^{\mathrm{el}}$ the elastic strain corresponding to the undamaged material, $\varepsilon_{0t}^{\mathrm{el}} = \sigma_t/E_0$ (see Fig. 3.8).

For tension stiffening, the description of the failure condition and of the post-peak behavior depends upon the tensile stresses, σ_t, the cracking strains, $\tilde{\varepsilon}_t^{\mathrm{ck}}$, and the tensile damage variable, d_t. The behavior of the masonry has been reproduced up to the ultimate limit state, considering damage in tension only. Given the lack of results of specific on-site tests, the mechanical properties assigned to the materials have been estimated based on the Italian technical standard code, NTC08 and NTC18 (NTC08 2008; NTC18 2018), and from the literature (Gams et al. 2017; Cavalagli et al. 2018). Tab. 3.4 summarizes the adopted damage parameters in tension for the Sciri Tower.

Table 3.4: Uniaxial stress-strain values and scalar tension damage values utilized in the CDP model for masonry.

σ_t [kN/m^2]	$\tilde{\varepsilon}_t^{ck}$ [$-$]	d_t [$-$]
160	0.00e-00	0.00
120	1.75e-04	0.55
84	3.77e-04	0.80
16	7.59e-04	0.90

3.3.3   Detection and localization of simulated damage

For the purpose of continuously assessing and localizing the damage, the FE model has been subdivided into four (4) macroelements, as illustrated in Fig. 3.9a:

- Macroelement 1 (M1): the building aggregate and a portion of the tower up to the top height of the roof of the same aggregate (0-18.9 m);
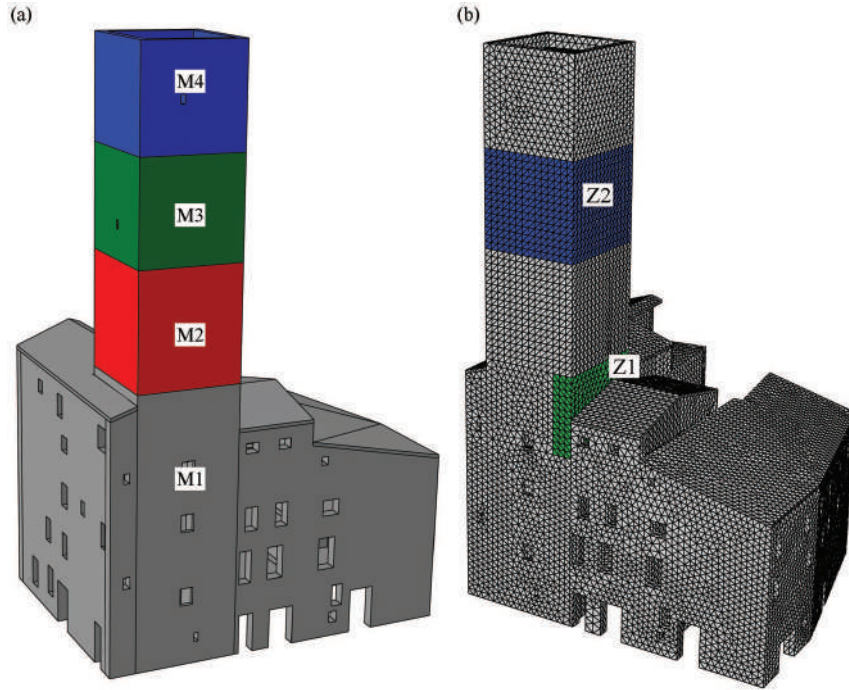
Figure 3.9: Macroelements M1, M2, M3 and M4 defined for damage localization (a) and zones Z1 and Z2 in which damage is simulated according to damage scenarios D1 and D2, respectively (b).

- Macroelement 2 (M2): the portion of the tower between the height of 18.9 and 26.8 m;

- Macroelement 3 (M3): the portion of the tower between the height of 26.8 and 33.8 m;

- Macroelement 4 (M4): the portion of the tower between the height of 33.8 and 41.0 m.

According to this partition of the structure, the parameters to be identified have been discriminated for each macroelement and collected in the vector of the design variables of the optimization problem **U**, as follows:

$$\mathbf{U} = (k_1, k_2, k_3, k_4) \tag{3.12}$$

where $k_i (i = 1, ..., 4)$, are coefficients that multiply the elastic moduli of materials belonging to M1, M2, M3 and M4, respectively. The variation of the components of vector **U**

with respect to initial values, identified by the damage localization procedure, is related to the occurrence of damage in the structure. A more significant decrease in one component of $\mathbf{U}$ with respect to the others indicates that the damage is concentrated in that specific portion of the structure.

A surrogate quadratic model has been adopted in the online optimization procedure, as introduced in Eqs. (3.7). To compute the coefficients of the quadratic model, $A_{i,j}$, $B_{i,j}$, C_i, $D_{i,j}$, $E_{i,j}$, F_i, with $i = 1, ..., l$, (l is the number of identified modes) and $j = 1, ..., n$, (n is the total number of uncertain parameters), each component of $\mathbf{U}$ has been varied by $\pm 5\%$ and the corresponding natural frequencies and mode shapes have been computed from the FE model. The coefficients of the quadratic models (see Eqs. (3.7)) have been calculated by imposing equivalence between the first and second derivative of $f_i^{\mathbf{FEM}}$ and $\Phi_i^{\mathbf{FEM}}$, expressed in terms of the unknown coefficients, with the first and second-order finite differences obtained from the analysis. The assumption of quadratic equations to describe the relationship between the design variables (U_i) and the modal parameters ($f_i^{\mathbf{FEM}}$ and $\Phi_i^{\mathbf{FEM}}$) is acceptable in a range around the initial values. To demonstrate the acceptability of the hypothesis, a parametric analysis has been carried out by varying individually each component of $\mathbf{U}$. The natural frequencies and modal displacements have been obtained for both the full 3D FE model and the surrogate model. The results of the parametric analysis in terms of natural frequencies and mode shapes demonstrate that the surrogate model is reasonably suitable to represent the variation of the modal parameters of the structure, in the neighborhood of the initial value of $\mathbf{U}$. In particular, Figs. 3.10a-c show the first and second natural frequencies obtained with the surrogate model (f_1^s and f_2^s) and the FE model (f_1^{FEM} and f_2^{FEM}), while Figs. 3.10b-d show the MAC of the first and second mode obtained with the surrogate model (MAC_1^s and MAC_2^s) and the FE model ($\mathrm{MAC}_1^{\mathrm{FEM}}$ and $\mathrm{MAC}_2^{\mathrm{FEM}}$). The maximum relative difference between the two models concerns f_1 and is equal to 0.54% in the range of $k = \pm 3\%$, that is considered acceptable for the purpose of early-stage damage localization.

Once the surrogate model is set, in order to demonstrate the effectiveness of the procedure, two damage scenarios have been simulated:

- Damage scenario 1 (D1): localized damage at Z1 - the contact between the tower and the aggregate/roof, possibly related to deformations between the tower and the surrounding building, obtained with a 20% reduction of the elastic modulus;
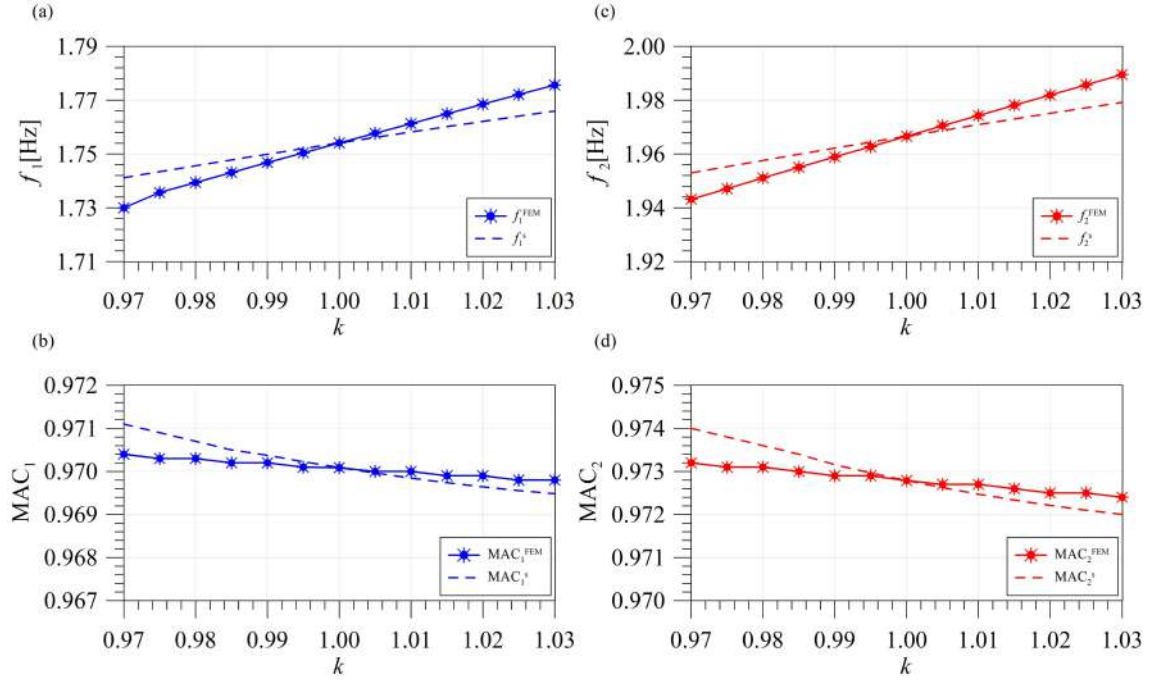
Figure 3.10: First two natural frequencies (a, c) and MAC (b, d) obtained with the FE model and the surrogate model.

- Damage scenario 2 (D2): damage in Z2/M3 (possible crack formation due to the presence of two openings) simulated with a 40% reduction of the elastic modulus.

The portions Z1 and Z2 in which damage occurs for the two damage scenarios are shown in Fig. 3.9b. Tab. 3.5 summarises the numerical relative frequency decays obtained for the two damage scenarios, while Fig. 3.11 shows the corresponding control charts obtained by calculating the T^2 statistical distance on the residuals of the first two natural frequencies (Eqs. (2.2) and (2.4)), after artificially applying such damage-induced frequency shifts corresponding to D1 and D2. The frequency shifts have been artificially inserted in the time series of the identified natural frequencies assuming that damage occurred in the middle of the observation period after one year of training period. These results show how D1 and D2 can be detected from the control charts and how the damage localization is triggered.

In order to localize damage, the optimization problem in Eqs. (3.4) and (3.5) has been solved, by exploiting the surrogate model in Eqs. (3.7). The lower and upper bounds vectors in Eq. (3.6) are $\mathbf{U}_{lb} = (0, 0, 0, 0)$ and $\mathbf{U}_{ub} = (1, 1, 1, 1)$, respectively, with 0

Table 3.5: Relative frequency decays obtained for the considered damage scenarios (in percentage).

	D1	D2
Δf_1	-0.99	-1.11
Δf_2	-0.88	-1.41
Δf_3	-0.25	-1.75
Δf_4	-0.54	-2.97
Δf_5	-0.96	-4.35
Δf_6	-0.46	-4.28
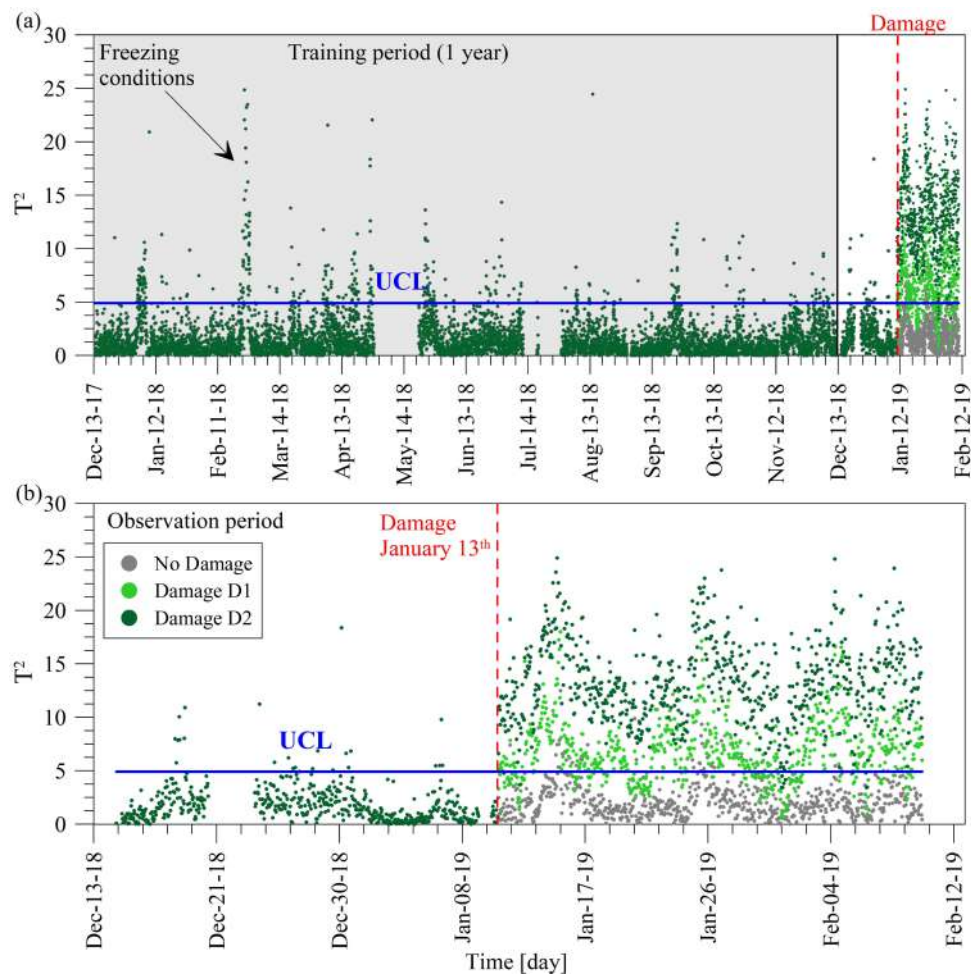
Figure 3.11: Control chart of the observation period with no damage and with damage scenarios D1 and D2 applied on January 13th 2019.

meaning complete damage and 1 meaning no damage occurred to the macroelement. The selected optimization algorithm is a classical genetic algorithm that has been chosen for its computational effectiveness. The parameters of the genetic algorithm have been established through a preliminary parametric analysis: the population size has been set to 1000 in order to achieve good repeatability of the results. The optimization has been repeated by adopting different values of the coefficients α and β, in order to weight differently the two terms of Eq. (3.4) and search for stable solutions in order to avoid unfeasible results. Tab. 3.6 shows the results of the localization for D1 and D2, considering one single data set. When $\alpha \geq \beta$, for damage type D1 the coefficient k_2 is smaller than one, indicating that damage has occurred on M2, at the contact between the tower and the surrounding buildings. The coefficient k_3 experiences the highest variation for D2, denoting that damage has occurred in M3. In the cases when $\alpha \leq \beta$ some solutions that significantly deviate from the others are observed. This highlights that considering the term related to MAC in addition to the term related to frequency in the objective function of the inverse identification problem, it allows investigating the robustness of the solution with respect to the weighting coefficients variation, distinguishing between the solutions that significantly differ from the expectations and the robust ones. It is also clear from the results in Tab. 3.6 that the contribution of the term related to MAC to the solution accuracy is limited due to only 3 mode shape components available (only 3 sensors are used for continuous monitoring). Nonetheless, the contribution can substantially increase with data from a larger number of sensors at different levels of the tower.

Table 3.6: Results of the localization obtained for the simulated damage scenarios D1 and D2. Note that if components $k_i(i = 1, ..., 4)$ of **U** are equal to 1, it means no damage occurred to the macroelement.

Damage scenario	α	β	k_1	k_2	k_3	k_4
D1	1	0	1.00	0.86	1.00	1.00
D1	10	1	1.00	0.86	1.00	1.00
D1	1	1	1.00	0.86	1.00	1.00
D1	1	10	0.99	0.97	1.00	0.39
D1	0	1	0.68	1.00	1.00	0.36
D2	1	0	1.00	0.93	0.05	0.89
D2	10	1	1.00	0.93	0.06	0.80
D2	1	1	1.00	0.92	0.09	0.55
D2	1	10	1.00	0.98	0.08	0.09
D2	0	1	1.00	1.00	0.02	0.06

The localization method has also been applied to track the variation in time of the damage-dependent parameters. To this aim, frequency decays obtained for damage scenario D1 and D2, reported in Tab. 3.5, have been applied to identified natural frequencies cleansed by thermal effects (Fig. 3.6) one month after the end of the training period of one year (December 2017-December 2018). Fig. 3.12 shows the tracking in time of the components of vector $\mathbf{U}$ (see Eq. (3.12)) for damage D1. It is possible to observe that the coefficient k_2 experiences the highest and clearest variation as a consequence of the simulated frequencies decays, confirming that damage is mainly localized in M2. After damage occurs, an increase in k_4 is also observed. Since a damage is never expected to increase stiffness, this change has to be attributed to numerical reasons related to the solution of the inverse problem and should not be considered as a damage indicator. In this regard, the use of a regularization term in the objective function may help in limiting possible numerical problems. A similar trend would, however, need some tuning and calibration to avoid masking damage effects.
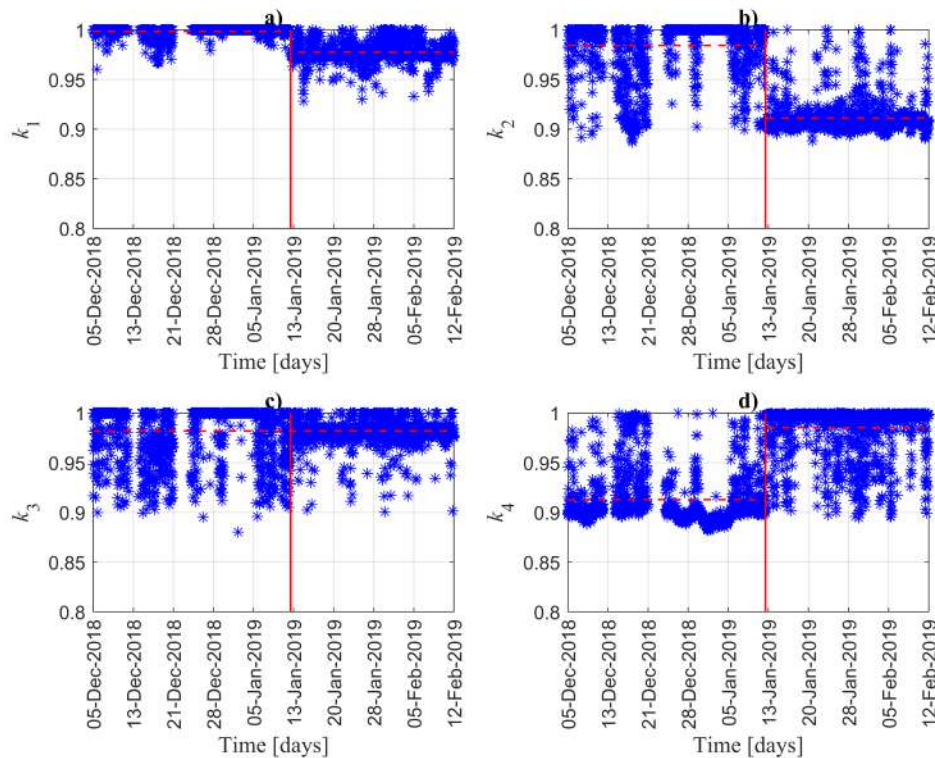
Figure 3.12: Tracking in time of the components of $\mathbf{U}$ after the end on the training period considering damage condition D1 simulated on January 13th 2019.

3.3.4   Localization of earthquake-induced damage

In the previous Section, the damage localization procedure has been validated with reference to simulated damage scenarios, D1 and D2, by numerically applying frequency shifts, corresponding to specific damage events. In the present Section, the procedure is further validated using real frequency shifts, measured after a seismic sequence occurred in January 2017, during a preliminary monitoring period of the structure.

In the context of an initial dynamic investigation, preliminary to the continuous monitoring, the tower has been monitored for one week, from January 16th to January 23rd 2017, through a simple vibration-based SHM system which comprised accelerometers A4, A5 and A6 (see Fig. 3.3b). In this period, an important seismic sequence occurred on January 18th 2017 with epicenters close to L'Aquila, in central Italy, at about 100 km distance from the Sciri Tower (Venanzi et al. 2020). Four (4) main shocks with moment magnitude higher than $M_w = 5$ were recorded from 09:25 to 13:33 UTC. Moreover, four (4) additional shocks with $4 \leq M_w \leq 5$ occurred in the same period of time. The acceleration time histories of these earthquakes have been taken from the strong motion network database provided by the Department of Civil Protection (DPC) and by the Italian seismic network of the National Institute of Geophysics and Vulcanology (INGV). Tab. 3.7 reports moment magnitude M_w, time and distance from epicenters of the four main shocks measured by the seismic stations closest to epicenters, together with E-W, N-S and vertical components denoted as PGA_{E-W}, PGA_{N-S} and PGA_Z, respectively. Fig. 3.13 shows the E-W and N-S components of the time histories of horizontal accelerations recorded by accelerometers A5 and A6, respectively, during the first two shocks, those that led to the higher seismic responses of the tower, together with the geographic location of the epicenters with respect to Perugia. It is noted that, due to the large distance (about 100 km) between Perugia

Table 3.7: Synthetic information regarding the four main shocks of January 18th 2017 seismic sequence as recorded by seismic stations placed nearby epicenters (PGA_{E-W}, PGA_{N-S}, PGA_Z denote PGA values in E-W, N-S and vertical directions, respectively).

Epicenter	Mw [-]	Time UTC [hour]	Distance [km]	PGA_{E-W} [cm/s^2]	PGA_{N-S} [cm/s^2]	PGA_Z [cm/s^2]
Montereale	5.3	09 : 25	95	195.39	361.17	124.24
Capitignano	5.4	10 : 14	98	442.64	566.15	188.35
Capitignano	5.3	10 : 25	102	407.89	591.07	161.58
Cagnano Amiterno	5.1	13 : 33	102	272.61	284.87	101.74
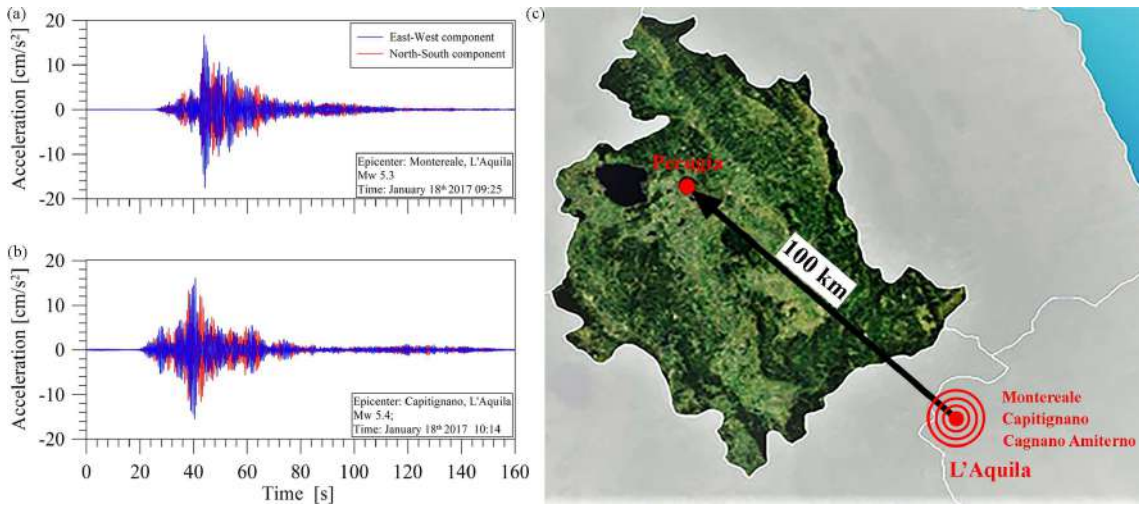
Figure 3.13: Seismic accelerations recorded during the main seismic events of January 18th 2017 (a-b) and geographic location of the epicenters with respect to Perugia (c).

and the epicenter of the earthquake sequence, the response acceleration levels of the tower were relatively low. Acceleration in the E-W direction was predominant in both shocks, with peak values equal to 18.86 cm/s^2 and 16.66 cm/s^2, respectively.

The seismic events did not produce any visible damage to the structure but led to non-negligible variations of its natural frequencies. Figs. 3.14a-b show the time histories of the natural frequencies of vibration of six (6) modes of the tower continuously identified and tracked during the preliminary monitoring period (modes Fx1, Fy1, Fx2, Fy2, Tz1 and Fy3) from January 16th to January 23rd 2017. As it is visible from the figures, the seismic events clearly led to small frequency decays. The vertical dashed lines in all plots represent the date and hour of the major earthquakes of the seismic sequence, highlighting the instantaneous decays in natural frequencies induced by the same events. In addition, Fig. 3.14c reports the relative frequency decays after the first two seismic events. Only the first six (6) frequency decays have been computed since the SSI continuous identification was able to detect the first six (6) natural frequencies during that week of monitoring, as a consequence of the adopted sensors configuration in the preliminary monitoring system. They have been computed considering the average of 5 frequency samples measured before the event occurred at 09:25 UTC and 5 frequency samples after the shock occurred at 10:14 UTC. It is noteworthy to stress that, during the day-night of the seismic sequence, positive temperature has been recorded, ranging from 1.7 to 3.7°C. In these conditions, with pos-
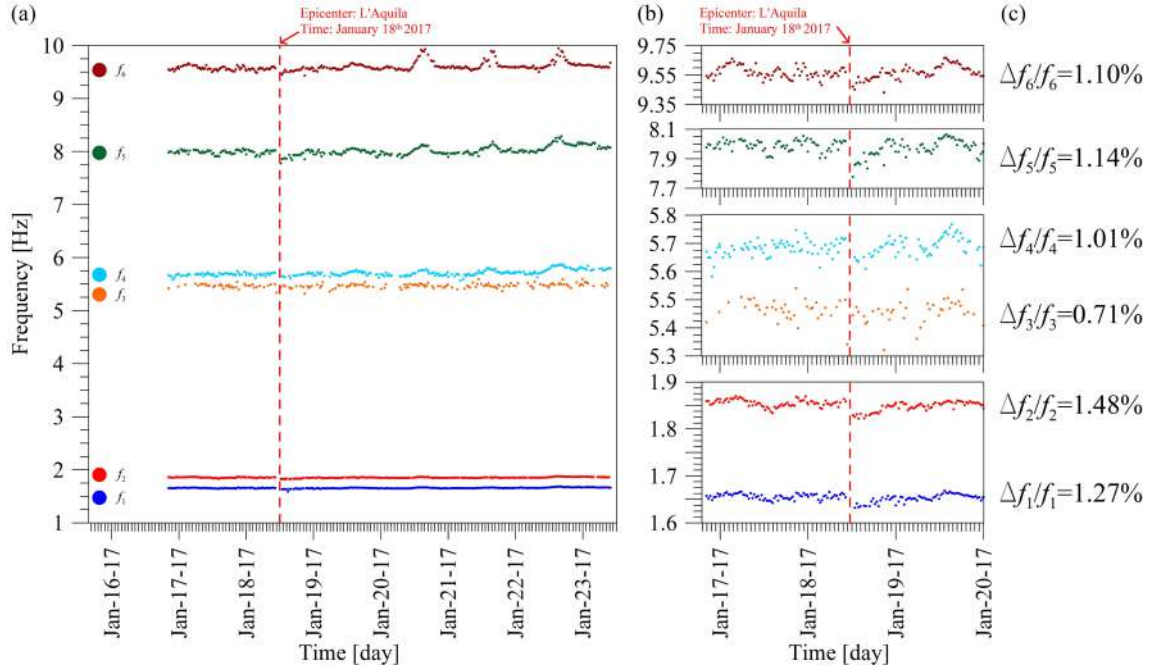
Figure 3.14: Frequency tracking around the seismic event of January 18th 2017 (a-b), with the indication of the percentage values of the relative frequency decays (c)

itive frequency-temperature correlations, a small thermal recovery of the frequency shifts has to be expected, leading to slightly lower decays. However, considering very limited temperature fluctuations, this effect is neglected. It is worth mentioning that earthquake-induced effects on the dynamic response of the tower could have been also highlighted by the control chart generated as the output of the vibration-based SHM system, but given the short preliminary monitoring period, there was not enough data for its construction.

The experimental frequency decays reported in Fig. 3.14 have been used to run the localization procedure. The analyses have been repeated for different weights α and β of the two terms in Eq. (3.4). Tab. 3.8 reports the results of the damage localization, highlighting that all the analyses, except the one with $\alpha = 1, \beta = 10$, provide consistent outputs and locate damage at macroelement M2. This is probably due to the fact that, during the seismic event, the different deformations of the tower and the surrounding building aggregate led to a slight deterioration of the connection between the two parts of the structure. In order to check that the earthquake-induced damage is concentrated at M2, as suggested by the results of the localization procedure, a non-linear dynamic FE analysis has been carried out using the model presented in Section 3.3.2 and considering the real recorded

Table 3.8: Results of localization of the earthquake-induced damage. Note that if components $k_i(i = 1, ..., 4)$ of $\mathbf{U}$ are equal to 1, it means no damage occurred to the macroelement.

α	β	k_1	k_2	k_3	k_4
1	0	1.00	0.71	1.00	1.00
10	1	1.00	0.71	1.00	1.00
1	1	1.00	0.71	1.00	1.00
1	10	0.91	0.10	1.00	0.43
0	1	1.00	0.27	1.00	1.00

earthquakes of January 18th 2017. To this aim, the accelerograms of the two main shocks recorded by the seismic station closest to the Sciri Tower, i.e. Castelnuovo-Assisi (less than 15 km distant), have been used as inputs for the analysis. With reference to the scaling factors adopted in (Ubertini et al. 2018), the ground motion waveforms have been scaled to reproduce the PGA expected values at the site of the tower and the experimental Peak Response Accelerations (PRAs) measured on top of it, that is, by matching measured and numerically estimated peak acceleration structural responses. However, the scaling procedure, which considers also applying the Ground Motion Prediction Equation (GMPE) attenuation law (Bindi et al. 2009) to characterize the medium crossed by the earthquake and the waveform propagation, goes beyond the purposes of the present investigation. The comparison between experimental and numerical responses is reported in Tab. 3.9.

Non-linear dynamic analyses have been carried out with the purpose of numerically localizing earthquake-induced structural damages in the tower by considering the two main scaled waveforms concatenated. Fig. 3.15 highlights the contour plot of the tensile damage

Table 3.9: Comparison between experimental (Exp) and dynamic non-linear FE model Peak Response Accelerations (PRAs) at level 3 of the Sciri Tower (see Fig. 3.3b).

Seismic event		PRA^{A4} $[\mathrm{cm/s^2}]$	PRA^{A5} $[\mathrm{cm/s^2}]$	PRA^{A6} $[\mathrm{cm/s^2}]$
Montereale (Mw=5.3)	Exp	18.86	17.52	10.45
	FEM	19.11	15.19	14.89
Capitignano (Mw=5.4)	Exp	16.66	16.16	13.25
	FEM	17.77	14.23	14.97

of the FE numerical model (only the tower), obtained by the numerical analysis. Some small damage is clearly localized at the contact between the tower and the building aggregate. In particular, it is triggered at the outer corners of the tower (internally to the aggregate), in correspondence to the horizontal elements and structural walls (see Figs. 3.15b-d). Furthermore, in the contact with the roof of the aggregate, the damage represents a continuous pattern in the West façade of the tower. Visual inspections revealed a very limited, yet clearly visible, damage state in the aforementioned contact points between the tower and the aggregate, that has been reported by building occupants as occurred after the 2016-2017 Central Italy seismic sequence. In-situ photo evidence of such damages are also reported in Fig. 3.15b. Overall, the results of the FE model non-linear dynamic analysis confirm those obtained from the localization procedure presented in Section 3.3.3, which are also validated, to some extent, by in-situ damage visual inspections.
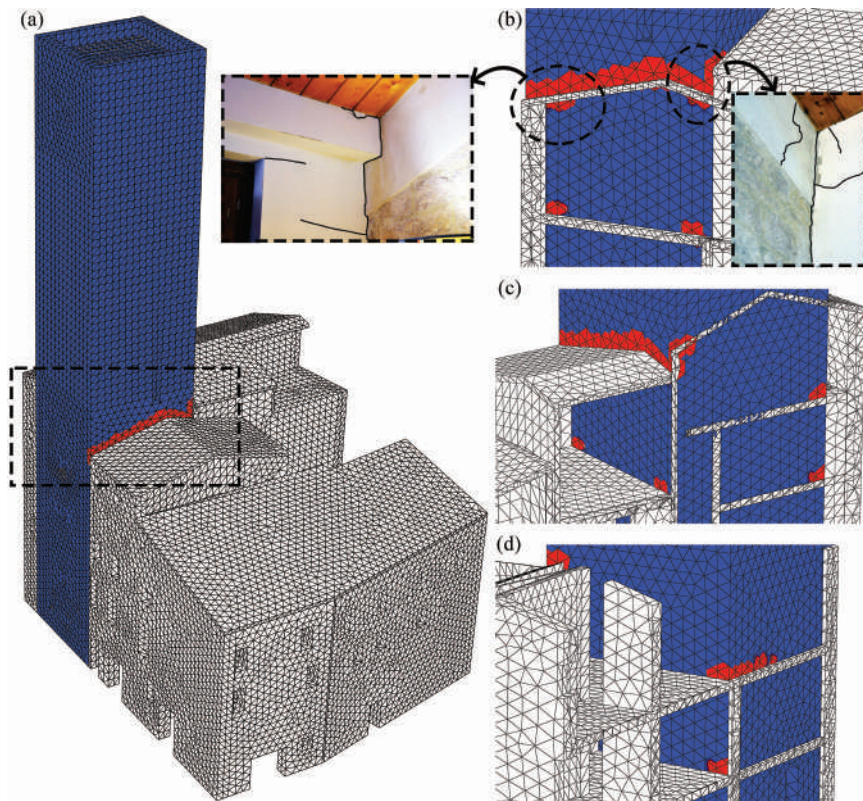
Figure 3.15: Small localized damage predicted by numerical simulation after the sequential application of the two main shocks of January 2017: general overview of the damaged FE model (a) and zoom of damage in the West, South and East façades, in correspondence to the roof and restraining horizontal elements and with some photo evidence (b-d).

3.4   Conclusions

An improved version of a surrogate model-based method for earthquake-induced damage detection and localization in masonry towers using long-term vibration monitoring data and numerical modeling, as well as its validation based on field data, has been presented. The method has been applied to the Sciri Tower, an historic civic masonry tower located in Perugia, Italy, equipped with a long-term dynamic monitoring system that has been in continuous operation for about two years.

The main results are summarized below.

- The proposed methodological improvement mainly consists of considering also mode shapes and not only natural frequencies for damage localization, which increases the number of degrees of freedom of the inverse problem, thus allowing to investigate the robustness of the solution and avoid unphysical results. Data of continuous monitoring recorded on the case study tower have been used to perform online OMA through SSI in order to obtain the evolution of structural modal parameters with time.

- The validation of the proposed procedure has been pursued by considering both simulated damage scenarios and an experimental slight change in structural behavior observed after a far-field earthquake. According to the proposed procedure, a control chart based on frequency tracking has been used to highlight any anomalous deviation from normal conditions and to trigger the damage localization task.

- Simulated damage-induced natural frequency variations and frequency decays observed through the processing of monitoring data after the above mentioned far-field earthquake have been used to detect and localize possible earthquake-induced damages. The results using artificial damage scenarios have demonstrated that the proposed procedure is effective for both damage detection and localization.

- Damage localization task is performed by solving an inverse FE model calibration problem, where equivalent elastic properties of macrostructural elements have been identified by continuous minimization of an objective function containing experimentally identified and numerically predicted damage-induced decays in natural frequencies and changes in mode shapes. To minimize the computational effort of this calibration procedure, a quadratic surrogate model has been constructed using a tuned numerical FE model of the structure.

- The results obtained using field data and the real earthquake response have been also validated by means of a non-linear dynamic analysis carried out using the FE model, demonstrating that the proposed procedure was capable of correctly localizing some slight earthquake-induced damage at the connection between the tower and the aggregate, which was also confirmed by visual inspections.

The proposed method can, therefore, be considered as an effective and quick tool for rapid post-earthquake damage identification in historic masonry towers based on long-term dynamic monitoring.

Chapter 4

Damage localization and quantification via IDA

In this Chapter, the application and validation of the proposed IDA-based method, aimed at rapid localization and quantification of earthquake-induced damages, are presented with reference to a laboratory shaking table application, named the *Brick House*. The main theoretical aspects of IDA are first presented. The proposed method, based on IDA carried out from a numerical model and using data recorded during seismic events, is subsequently described in detail. It concerns an a priori construction of local multidimensional IDA curve sets relating meaningful local damage parameters to selected seismic intensity measures. A specific study consisting of wide literature research, definition, classification and statistical correlation analysis is carried out in order to select the most suitable and meaningful measures for IDA purposes. Finally, the best non-linear seismic IDA curve sets relating several intensity measures versus damage measures are reported. Localization and quantification of earthquake-induced damage for the ten (10) parts of the structural model in case of three real seismic events are achieved, in terms of overall weighted average estimation of damage ranges and mean values.

4.1   Theory background

The development of computer processing power and structural analysis software has made possible a continuous drive towards increasingly accurate but at the same time more complex analysis methods. The state of the art holds the use of several analysis methods for the design and assessment of masonry buildings, from (elastic) linear static analysis (LSA) to linear dynamic analysis (LDA), and from non-linear static (NLSA) to non-linear dynamic analysis (NLDA). The NLSA (or pushover, SPO), with suitable scaling of the static force pattern, allows to obtain a "continuous" picture as the complete range of structural behavior is investigated, from elasticity to yielding and finally collapse (Cattari and Lagomarsino 2013; Cattari et al. 2015; Lagomarsino and Cattari 2015a; Lagomarsino and Cattari 2015b). The NLDA consists of running several different records, each producing several "single-point" analyses, and may be performed either by using a large number of records (Cloud Method and/or Multiple Stripe Analysis (MSA)) or considering a proper selection of time histories, scaled in order to perform IDA (Lagomarsino and Cattari 2015b). Passing from a single static analysis to the incremental SPO provides the basic conceptual development of the extension of a single time-history analysis into an incremental one, where the seismic loading is scaled. This concept has been first mentioned in 1977 (Bertero 1977), and subsequently considered in many researchers' works (Bazzurro and Cornell 1994a; Bazzurro and Cornell 1994b; Luco and Cornell 2000; Psycharis et al. 2000). Adopted by the U.S. Federal Emergency Management Agency guidelines (FEMA 2000a; FEMA 2000b) as the incremental dynamic analysis, it has been established as the state-of-the-art method to determine the global collapse capacity. Despite the potential information that can be derived by the IDA, the application to CH masonry structures is comparatively less common with respect to other types of structures, such as RC frames, due to the high computational costs (Basone et al. 2017; Masaeli et al. 2018).

(Vamvatsikos and Cornell 2002) proposed a computational-based methodology called Incremental Dynamic Analysis (IDA), which involves a series of non-linear dynamic time-history analyses, a powerful, multi-purpose and widely applicable parametric analysis method, capable of thoroughly estimating the structural performance under increasing seismic intensity. It considers the numerical model of a structure subjected to one (or more) ground motion record(s), the latter scaled to multiple levels of intensity, thus producing one (or more) curve(s) of response parameterized versus the intensity level itself. An IDA study allows a thorough understanding of the range of response or "demands" versus the range

of potential levels of a ground motion record, as well as a better comprehension of the structural response/implications as the ground motion intensity increases to more severe levels and its stability considering the record-to-record variability. However, recently, the procedure of scaling (up) accelerograms is sometimes seen as a critical aspect and/or drawback of the IDA approach. In this context, very high scaling factors are not encouraged. Finally, in the framework of Performance-Based Earthquake Engineering (PBEE), the assessment of demand and capacity is viewed through the lens of an IDA study. The IDA curve contains the necessary information to assess performance levels or limit states.

IDA's fundamental hierarchical concepts (Vamvatsikos and Cornell 2002) are defined below:

- *Unscaled ground motion record*: time history representing a seismic event (generally accelerogram), $\mathbf{a}_1$, defined as a vector $\mathbf{a}_1(t_i)$, t_i=0,t_1,...,t_{n-1}.

- *Scale Factor* (SF): the non-negative scalar $\lambda \in [0, +\infty)$ that produces a scaled accelerogram $\mathbf{a}_\lambda = \lambda \cdot \mathbf{a}_1$.

- *Intensiy Measure*: the non-negative scalar IM $\in [0, +\infty)$ of the scaled accelerogram, that constitutes a function IM=$f_{\mathbf{a}_1}(\lambda)$.

- *Damage Measure*: DM $\in [0, +\infty)$, non-negative scalar representing the output of IDA on the structural model.

- *Single-Record IDA Study*: a dynamic analysis study of a given structural model parameterized by the SF applied to $\mathbf{a}_1(t_i)$.

- *IDA Curve*: plot of a DM recorded in an IDA study versus one or more IMs that characterize $\mathbf{a}_\lambda$ (+2D plot).

- *Multi-Record IDA Study*: a collection of *Single-Record IDA Studies* of the same structural model, under different accelerograms.

- *IDA Curve Set*: a collection of *IDA Curves* of the same structural model under different accelerograms, all parameterized by the same IMs and DM.

The selection of appropriate ground motion records or seismic inputs is of significant importance since an IDA study is accelerogram- and structural model-specific. In fact, given the record-to-record variability of structural responses, the choice of suitable strong ground-motions represents a first key aspect for IDA. Several studies dealt with the selection of suites of real ground-motions (Bommer and Acevedo 2004; Iervolino and Cornell 2005).

Seismic action can be represented through different types of time histories: (i) natural accelerograms; (ii) artificial and (iii) simulated time histories. In recent years, the increasing availability of online databases of strong-motion records has shifted the focus towards the use of natural accelerograms, recorded during real earthquakes and considering information like seismic hazard, site conditions, target spectrum, etc. The input ground-motions to IDA can be either representative of earthquake scenarios that control the site hazard or compatible with a target elastic response spectrum. Technical standards suggest the use of a suite of ground motion records, aimed at covering a full range of responses and with different seismic characteristics in terms of amplitude, energy or frequency content. According to the Italian (NTC08 2008; NTC18 2018) and European (EN 1998-1 2005) codes, at least seven (7) time-history analyses need to be performed and mean output values are to be considered (Karanikoloudis and Lourenço 2018). Alternatively, if fewer analyses are conducted (e.g. with three groups of accelerograms), one can consider the maximum output values. Also, the combination of the used accelerograms should present an average response spectrum consistent with the prescribed elastic one. In general, the combination of at least seven (7) accelerograms is highly recommended for structural analysis, with effects on the structure represented by the averages of the maximum values obtained from the analyses. Usually, the seismic input for IDA is represented by spectrum-matched accelerograms, in other words, acceleration time series whose response spectra result compatible with a specific target response spectrum (Atik and Abrahamson 2010; Pena et al. 2010). Previous works gave a description of the rationale and advantages of using spectrum-matched accelerograms (Atik and Abrahamson 2010), demonstrating that spectrum matching does not lead to bias in structural analysis results (Grant and Diaferia 2012).

The next key aspect for IDA analysis concerns the choice and/or definition of representative and efficient intensity measures (IMs) and reasonable and meaningful damage measures (DMs) (Vamvatsikos and Cornell 2002; Riddell 2007). There is a relatively large number of parameters or IMs of a ground motion proposed over the years in the literature (Housner 1952; Arias 1970; Kramer 1996; Cosenza and Manfredi 2000; Riddell and Garcia 2001; Riddell 2007; Douglas et al. 2015). In general, a single parameter cannot successfully and fully characterize the strength and intensity of ground motions. In this context, a thorough overview of the IMs proposed in the literature followed by an in-depth analysis is needed. In order to thoroughly characterize an earthquake, an IM should be able to describe three main ground motion characteristics/features of earthquake engineering significance, such as amplitude, frequency content and duration. All of these characteristics can scientifically

influence the earthquake damage. The selection of IMs should consider their capability in providing information about one or more of these characteristics. Generally speaking, IMs can be classified as peak or integral parameters, and as seismic input measures or response measures. Peak parameters are based on the computation of one single value while integral measures take into account also the duration of an earthquake. Seismic input measures are considered as structure independent, because of their computation directly from the ground motion record, whereas response measures depend on the structure's characteristics. Moreover, taking into consideration specific period ranges, IMs can further be categorized into three subgroups: acceleration-related, velocity-related and displacement-related measures. A detailed analysis of IMs for IDA-based damage assessment is reported in Section 4.3.

A wise choice of IMs concerns investigating their main property: the efficiency for predicting DM and/or the structural response (Vamvatsikos 2002). An efficient IM is defined as one that yields relatively small variability of DMs for a given IM level, in other words, the one that provides a relatively low dispersion of values of DMs. In this context, the comparison among different IMs, in particular, the investigation of the dispersions of the DMs associated with various IMs, is needed. An efficient IM leads to less dispersion in an IDA curve set. Another advantage of using an efficient IM, i.e. having lower dispersion of DM given IM, is reflected in the smaller sample of records and fewer non-linear IDA runs necessary. Therefore, a desirable property of a candidate IM is to yield a small dispersion.

The Damage Measure (DM) represents an observable quantity that is part of the output (or can be deduced from) of the corresponding non-linear dynamic analysis (Vamvatsikos 2002). There are different possible choices such as maximum base shear, inter-story drift ratio, floor peak inter-story drift angles, Park & Ang index (Park and Ang 1985), and so forth. Other DMs can be quantities and/or numerical outputs of the non-linear constitutive model used in the specific application. A very interesting constitutive model is the well-known Concrete Damage Plasticity, previously described in Section 3.3.2. It is widely used in the literature in the case of non-linear dynamic analyses (Valente and Milani 2016; Valente and Milani 2018; Cavalagli et al. 2018; Ubertini et al. 2018; Formisano et al. 2018b; Sarhosis et al. 2018; Valente et al. 2019; Valente and Milani 2019a; Valente and Milani 2019b; Abbati et al. 2019). In particular, tensile damage, as a cumulative parameter, can certainly represent a reasonable DM. Moreover, selecting a suitable DM depends on the application and the structure itself. It may be useful to use two or more DMs (all resulting from the same analyses) to assess different response characteristics.

4.2   The proposed method

The proposed method is based on non-linear seismic Incremental Dynamic Analysis (IDA) (Vamvatsikos and Cornell 2002) combined with earthquake data, aimed at damage localization and quantification. It requires the construction and tuning of a numerical model of the structure under analysis. In this regard, IDA simulations are carried out from the calibrated numerical model at increasing levels of the earthquake input, considering a suitable non-linear constitutive model for the masonry material, and relate a set of reasonable local damage measures (DMs) against one or more selected earthquake ground motion intensity measures (IMs). Each IDA curve is referred to individual specific parts of the structure (numerical model). The introduction of local IDA curves (i.e. generated with reference to different portions of the structure) represents a key aspect, allowing a local estimation of damage with confidence intervals. To this end, an in-depth analysis of the IMs proposed in the literature is needed since the use of the most suitable IMs represents a pivotal aspect of IDA effectiveness. Suitable parameters for damage in masonry structures and for intensity measures should be considered on the basis of both theoretical considerations and numerical modeling in such a way that the variability of the IDA curves is reduced as much as possible, so limiting the uncertainty in the estimated damage. Finally, multidimensional IDA curve sets are constructed, where multidimensional indicates that during any IDA, each analysis point conceptually contains a vector of DMs that corresponds to a vector of IMs for that scaled incarnation of the single record. In practical terms, when an earthquake occurs, IMs computed from the seismic data (e.g. the base acceleration and/or seismic response measured by the monitoring system installed on the structure or measurements from a nearby seismic station) are used and local damage conditions are immediately estimated using the mathematical relation obtained through prior multidimensional IDA analyses.

The outline of the proposed seismic IDA-based SHM procedure, whose sketch is depicted in Fig. 4.1, is summarized in the next steps:

- Step 1: Construction and calibration of a detailed FE model;

- Step 2: Ideal subdivision of the model into n meaningful parts for damage localization purposes;

- Step 3: Selection of seismic input: given the record dependency of IDA and the record-to-record variability of structural responses, a suite of ground motion records is considered (l earthquakes for IDA);

- Step 4: Incremental Dynamic Analyses run;

- Step 5: Selection of the most relevant m IMs by means of an appropriate correlation study and decision on significant DMs;

- Step 6: Construction of multidimensional IDA curve sets:

$$\mathbf{DM} = f(\mathbf{IM}) \tag{4.1}$$

where $\mathbf{DM} = (DM_1, DM_2, ..., DM_n)$ and $\mathbf{IM} = (IM_1, IM_2, ..., IM_m)$, with n indicating the number of parts in which the structure is subdivided and m the total number of considered IMs. Assuming monotonic IMs, the IDA curves in Eq. (4.1) become multidimensional functions ($\mathbb{R}^{*m} \to \mathbb{R}^{*n}$), being $\mathbb{R}^*$ the set of non-negative real numbers;

- Step 7: Investigation of the dispersion of IDA curve sets and the most efficient m^* IMs through the mean values of the Root Mean Square Errors (RMSE) of single curves computed with respect to the mean curve:

$$RMSE_{i,j} = \frac{1}{l} \sum_{k=1}^{l} \sqrt{\frac{\sum_{p=1}^{q} \Delta DM_{i,j}^{k,p^{\,2}}}{q}} \tag{4.2}$$

where $\Delta DM_{i,j}^{k,p} = DM_{i,j}^{k,p} - DM_{i,j}^{\mathrm{mean},p}$ represents the difference between the kth and mean damage (obtained from the kth and mean curve, respectively), while $i = 1, .., n$ (n parts), $j = 1, .., m^*$ ($m^* \leq m$), $k = 1, .., l$ (l the number of earthquakes considered for IDA) and $p = 1, .., q$ (q is the number of samples of the mean curves).

- Step 8: Regression analysis of IDA curves:

$$DM_{i,j} = g_{i,j}(IM_j) + \varepsilon_{i,j} \tag{4.3}$$

where $g_{i,j}$ represents an appropriate analytical function (e.g. a polynomial function and/or a spline), $\varepsilon_{i,j}$ indicates the error terms, while $i = 1, .., n$ and $j = 1, .., m^*$;

- Step 9: Occurrence of a seismic event and computation of earthquake-specific $\mathbf{IM}^* = (IM_1^*, IM_2^*, ..., IM_{m^*}^*)$ using seismic records;

- Step 10: Damage identification: use of intensity measures contained in $\mathbf{IM}^*$ into Eq. (4.3) for IDA-based localization and quantification of earthquake-induced damage in each i-th part, denoted as $DM_{i,j}^*$. The latter is averaged in terms of weighted mean ranges (maximum and minimum value) and weighted mean values by the following equation:

$$DM_i^* = \frac{\sum_{j=1}^{m^*} \alpha_{i,j} DM_{i,j}^*}{\sum_{j=1}^{m^*} \alpha_{i,j}} \tag{4.4}$$

where the coefficients $\alpha_{i,j}$, representing the weights of the m^* most efficient IMs, depend on the IDA curve sets dispersion and are computed as the inverse of $RMSE_{i,j}$ defined in Eq. 4.2. The final equation for weighted average damage quantification becomes:

$$DM_i^* = \frac{\sum_{j=1}^{m^*} \frac{1}{RMSE_{i,j}} DM_{i,j}^*}{\sum_{j=1}^{m^*} \frac{1}{RMSE_{i,j}}} \tag{4.5}$$
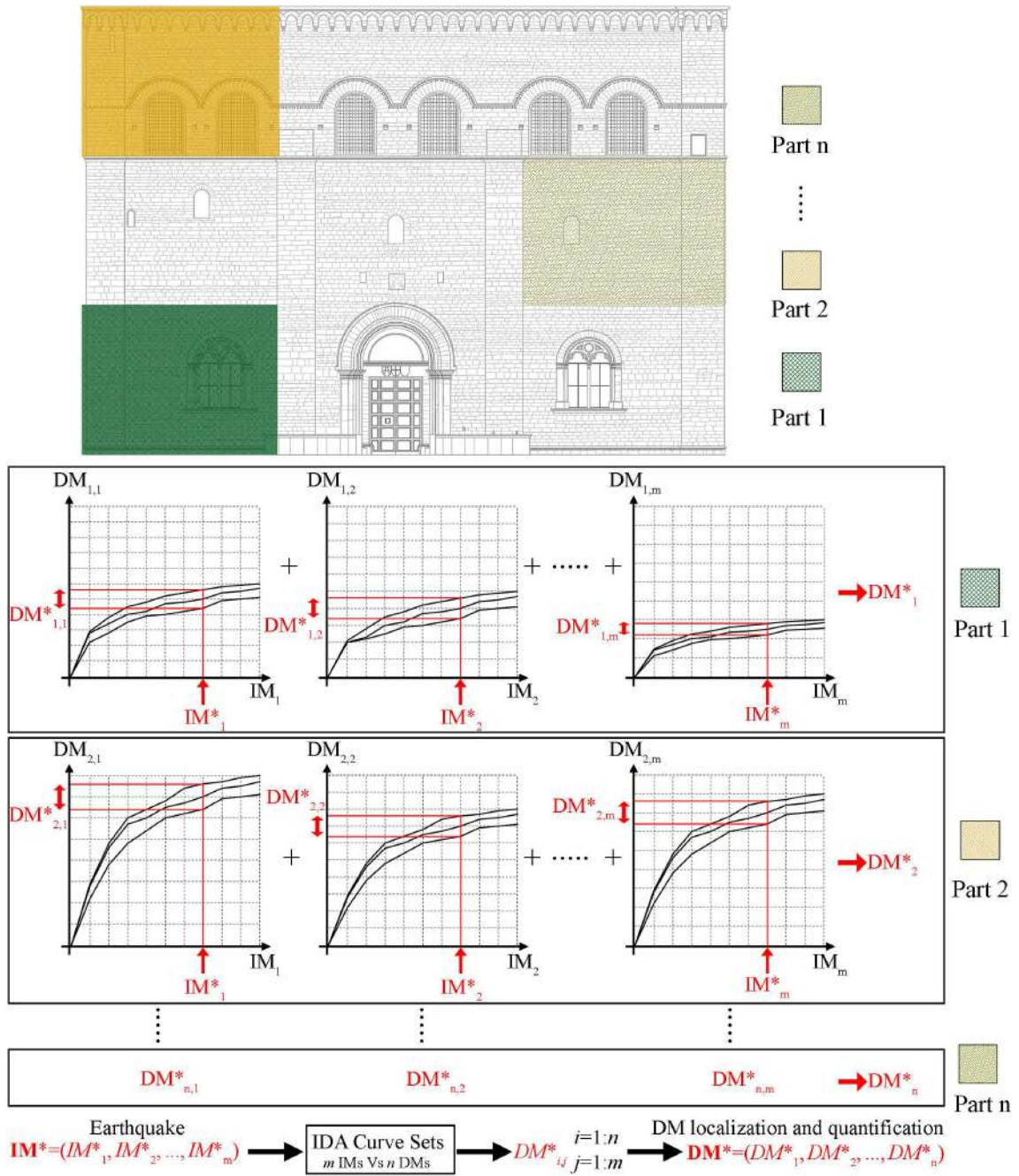
Figure 4.1: Scheme of the proposed method based on multidimensional non-linear seismic IDA: localization and quantification of earthquake-induced damage in n distinct parts of the structural model, $\mathbf{DM}^* = (DM_1^*, DM_2^*, ..., DM_n^*)$, by using the IMs of a seismic event, $\mathbf{IM}^* = (IM_1^*, IM_2^*, ..., IM_m^*)$, within a priori built IDA curve sets relating n local DMs to m IMs.

4.3   Analysis of intensity measures for IDA-based damage assessment

One of the most important aspects of a *multi-record IDA study* concerns the definition and choice of IMs (Vamvatsikos and Cornell 2002). The relationship between **DM** and **IM** is multidimensional, whereby the results of an IDA study expressed by Eqs. (4.1) and (4.3) can be presented in a multitude of different IDA curves, depending on the choices of IMs. A particular focus is here dedicated to the in-depth analysis of the IMs proposed in the literature since the use of the most suitable IMs represents an important aspect of the IDA results and effectiveness. To this end, a statistical correlation study between IMs has been carried out, considering one hundred (100) seismic records from the ITalian ACcelerometric Archive (ITACA) strong motion database (Pacor et al. 2011). The objective of this specific study is to avoid the use of highly correlated independent variables, providing a robust justification of the choices made in the selection of IMs used in the rest of the work.

In order to thoroughly characterize an earthquake, an IM should be able to describe three main ground motion characteristics/features of earthquake engineering significance: amplitude, frequency content and duration. A relatively large number of intensity parameters has been proposed in the literature, each of them providing information about one or more of these characteristics. In practice, it is usually necessary to resort to more than one IMs to adequately characterize a ground motion, an aspect of particular importance for IDA.

Ground motion amplitude is measured based on acceleration, velocity and displacement time series, as the size of the oscillations on an earthquake recording. In general, peak ground motion parameters result to be particularly poor for characterizing the overall nature of the motion because they only reflect the amplitude of a single isolated peak. The most common IMs used to describe ground motion amplitude include Peak Ground Acceleration (PGA), Peak Ground Velocity (PGV) and Peak Ground Displacement (PGD). The simplest and most worldwide used measure is PGA, which corresponds to the largest absolute value of acceleration in the time-series (the horizontal peak amplitude is considered separately from the peak vertical motion). It concerns a basic measure of earthquake potential but not totally reliable. Although the inertial force is directly related to the acceleration, from an engineering perspective PGA does not capture the frequency content, duration and energy of the acceleration time history, all features that can strongly influence the earthquake shaking damage. In fact, a large PGA recorded during a short duration im-

pulse can conceivably cause a smaller amount of structural damage with respect to a more moderate PGA associated with a long duration impulse. PGV is an additional general parameter for characterization of ground motion amplitude, with the additional advantage of being associated with a period range of more general importance to earthquake response. For buildings sensitive to loadings in this intermediate-frequency range (e.g., tall or flexible structures), the peak velocity may provide much more accurate evidence of the damage potential with respect to the peak acceleration. Finally, PGD is generally associated with ground motions of very long period, not a particularly helpful measure of the potential effects of strong shaking. Also, its reliability is questionable due to the double-integration from acceleration. As a result, peak displacement is less commonly used as a measure of ground motion in comparison to its acceleration or velocity counterparts.

The frequency content of an earthquake concerns identifying the amount of energy imparted at different frequencies. The dynamic response of structures is very sensitive to the frequency at which they are subjected to. The resonance effect, tend to amplify the response of the structure when the frequency contents of the ground motion are concentrated around its natural frequency (the ground motion and the building are in resonance with one another). In this context, buildings suffer the greatest damage from ground motion at a frequency close or equal to their own natural frequency. Generally, the frequency content is measured by the response spectrum and the Fourier spectrum. In the present study, the main frequency content measures selected are response spectra-based (spectral parameters). Another frequency content measure is the frequency ratio PGV/PGA, generally used to emphasize the effects of local site conditions. It provides information on the frequency content and the strong-motion duration of the ground motion (Zhu et al. 1988).

The strong motion duration of an earthquake is another obviously important property. It represents the time interval in which a strong ground motion occurs and can remarkably affect the amount of damage due to an earthquake or its potential. Many physical processes in certain types of structures, such as the degradation of stiffness and strength or the presence of minor cracks, can progress to major failures, being sensitive to the number of load or stress reversals that occur during an earthquake. Experience has confirmed that a motion of short duration may not produce enough load reversals to damage a structure, even with a high amplitude of the motion. On the other hand, a strong ground motion with moderate amplitude but long duration can result in more load reversals and cause substantial damage, aspect of utmost importance in terms of structural stiffness degra-

dation. The duration of a seismic event is related to the time required for the release of accumulated strain energy by the rupture along the fault. In general, an earthquake accelerogram contains all acceleration impulses from the time the earthquake begins until the time the motion has returned to the level of background noise. For earthquake engineering purposes, only the strong motion portion of the accelerogram is of interest. Different approaches have been considered in the literature for evaluating the duration of strong motions in accelerograms. The main definitions of earthquake duration are represented by the total, bracketed, uniform and significant duration, as defined below:

- Total duration, t_E.

- Bracketed duration (Kawashima and Aizawa 1989), t_B, defined as the total time elapsed between the first and the last exceedances of a fixed threshold acceleration (default is 5% of PGA). Considering only the first and last peaks of a threshold, it ignores what happens in the between (e.g. small events can occur after the main shock, with lower seismic contribution, but still the overall resulting in long duration).

- Uniform duration (Bommer and Martinez-Pereira 1999), t_U, defined as the sum of the time intervals during which the acceleration is larger than a fixed threshold (default is 5% of PGA). It is better than the bracketed duration, but it does not define a continuous time window during which the shaking can be considered strong.

- Significant duration (Husid 1969; Trifunac and Brady 1975), t_D, based on the Husid plot is usually defined as the time interval between the points at which 5% and 95% of the total energy has been recorded: $t_D=t_2\text{-}t_1$ with $I(t_1) = 0.05 \cdot I_A$ and $I(t_2) = 0.95 \cdot I_A$ (I_A is Arias Intensity, defined in the following). Its main advantage relies on considering the characteristics of the entire accelerogram, defining a continuous time window in which the motion may be considered as strong. Also it is based on the integral of acceleration, thus on the concept of cumulative energy.

Other definitions of duration have been proposed in the literature, like the corner period, i.e. the transition between the constant displacement and velocity segments of the spectrum (Boore 1983), or the rate of change of cumulative Root Mean Square (RMS) acceleration (McCann and Shah 1979), among others (Perez 1974; Vanmarcke and Lai 1977; Trifunac and Westermo 1977). In the present work, considering the pros and cons, the total and significant durations have been selected to describe the duration of a ground motion. Also, these are the most commonly used for earthquake engineering purposes.

Numerous ground motion intensity measures have been proposed over the years in the literature to capture the abovementioned different aspects of the earthquake shaking (Housner 1952; Arias 1970; Thun et al. 1988; Kramer 1996; Cosenza and Manfredi 1997; Riddell and Garcia 2001; Riddell 2007; Yakut and Yilmaz 2008; Ye et al. 2013; Douglas et al. 2015). Since earthquake is a complex non-stationary phenomenon, the satisfactory characterization of its strength and intensity by the use of one simple parameter has been discussed for a long time. Housner and Jennings clearly stated that the difficulties are fundamental (Housner and Jennings 1982): "It is inherently impossible to describe a complex phenomenon by a single number, it would be a great simplification and a great deal of information is inevitably lost when this is attempted". IMs are differently suitable in the three characteristic spectral regions: short-period range (acceleration-sensitive systems), intermediate-period (velocity controlled structures), and long-period range (displacement-sensitive systems). These regions were formalized by Newmark and Hall in a simple and comprehensive representation of elastic spectra (Newmark and Hall 1982). Moreover, (Riddell 2007) gives a great contribution to a better understanding of ground motion intensity indices used for specification of design ground motions, considering twenty-three (23) IMs into three groups (acceleration, velocity and displacement-related) and then investigating their correlation with four different structural response variables. The results indicated that no single IM has a satisfactory correlation with the structural response in all period ranges (over the entire frequency range) simultaneously: acceleration-related IMs are more efficient in the acceleration-sensitive region of the spectrum (rigid systems), velocity-related parameters are the best in the velocity-sensitive region (intermediate-frequency systems) and displacement-related ones for more flexible system (Riddell 2007). Moreover, acceleration-related indices, present high correlation within their subgroup, while their correlation with velocity-related indices is poor, and they do not correlate at all with displacement-related indices. The same also applies to velocity and displacement-related IMs.

Besides vector-valued IMs containing more than one parameter, the majority of indices typically used in the literature are scalar (i.e. single parameter), due to their simplicity and practical use. The present work relies mainly on the use of scalar measures. IMs can be subdivided into several categories. They can be computed as peak or integral parameters (a measure of the overall cumulative energy of the record). Also, they can be considered as seismic input measures (computed directly from the ground motion record, hence structure-independent or non-structure-specific) or response measures (structure-dependent or structure-specific). Structure-specific IMs can be calculated from response

spectra of ground motion time histories: response spectral ordinates at certain periods and from the integration of response spectra over a defined period range. With reference to specific period ranges and the modal properties of the structure in question, each group of IMs is further categorized in acceleration-related, velocity-related, displacement-related and mixed or hybrid (Cosenza and Manfredi 2000; Riddell 2007). A general classification of IMs investigated in this Thesis is reported in Tab. 4.1: (i) peak or integral, (ii) seismic input or response and (iii) acceleration, velocity and displacement-related. Considering their subgroups, the classification is reported in Tabs. 4.2, 4.3, 4.4 and 4.5, in which $\ddot{u}_g(t)$, $\dot{u}_g(t)$ and $u_g(t)$ represent the seismic input time histories of acceleration, velocity and displacement, respectively. T1 is the fundamental period of the structure. Notations, definitions, as well as amplitude (A), frequency content (F) and duration (D) characterizations are considered. Some of the intensity measures describe ground motion amplitude, some describe frequency content and others describe duration. Other parameters reflect two or more of these important characteristics. The presented ground motion intensity measures are consistently evaluated with respect to their ability in considering these ground motion characteristics.

Table 4.1: General classification of IMs.

IMs	Peak parameters			Integral parameters		
	Acceleration	Velocity	Displacement	Acceleration	Velocity	Displacement
Seismic input	PGA	PGV	PGD	RMSA	RMSV	RMSD
	SMA	SMV	-	I_C	-	-
	EDA	-	-	I_A	-	-
	I_a	I_v	I_d	A_{95}	-	-
	-	I_F	-	P_D	SED	-
	-	-	-	CAV	CAD	-
	-	-	-	MIV	MID	-
	-	-	-		E_I	
			I_D			
Seismic response	$S_a(T1)$	$S_v(T1)$	$S_d(T1)$	-	I_H	-
	-	$S_v(2T1)$	-	ASI_{VT}	VSI_{VT}	-
	EPA	EPV	EPD	-	VSI_K	-
	S_{paC}	-	-	-	VSI_{HC}	-
	$S_{a,avg}$	-	-	ASI_{NH}	VSI_{NH}	DSI_{NH}
	C_a	C_v	C_d	-	-	-
		I_S		-	-	-

Table 4.2: Acceleration-related IMs (A: amplitude, F: frequency content, D: duration).

Not.	Name	A	F	D	Definition	Ref.
PGA	Peak Ground Acceleration	x			$PGA=\max|\ddot{u}_g(t)|$	(Kramer 1996)
SMA	Sustained Maximum Acceleration	x			-	(Nuttli 1979)
EDA	Effective Design Acceleration	x			-	(Reed et al. 1988)
I_a	Riddell&Garcia compound index	x		x	$I_a=PGA \cdot t_D{}^{1/3}$	(Riddell and Garcia 2001)
RMSA	Root Mean Square Acceleration	x	x		$RMSA=\sqrt{\frac{1}{t_E}\int_0^{t_E}\ddot{u}_g(t)^2 dt}$	(Kramer 1996)
I_C	Characteristic Intensity	x	x	x	$I_C=RMSA^{1.5} \cdot t_E{}^{0.5}$	(Park et al. 1985)
I_A	Arias Intensity	x	x	x	$I_A=\frac{\pi}{2g}\int_0^{t_E}\ddot{u}_g(t)^2\, dt$	(Arias 1970)
A_{95}	Acceleration parameter	x	x	x	-	(Sarma and Yang 1987)
P_D	Destructive Potential Factor	x	x	x	$P_D=I_A/\nu^2$	(Araya and Saragoni 1980)
CAV	Cumulative Absolute Velocity	x	x	x	$CAV=\int_0^{t_E}|\ddot{u}_g(t)|\, dt$	(Cabanas et al. 1991)
MIV	Maximum Incremental Velocity	x	x		-	(Anderson and Bertero 1987)
$S_a(T1)$	Spectral acceleration	x	x		-	(Kramer 1996)
EPA	Effective Peak Acceleration	x	x		$EPA=avg(S_a)|_{0.1}^{0.5}/2.5$	(Kramer 1996)
S_{paC}	Inelastic behavior spectral acceleration	x	x		$S_{paC}=S_a(T1) \cdot \left(\frac{S_a(2T1)}{S_a(T1)}\right)^{0.5}$	(Mehanny and Cordova 2004)
$S_{a,avg}$	The geometric mean of spectral acceleration	x	x		-	(Bianchini et al. 2009)
ASI_{VT}	Von Thun Acceleration Spectrum Intensity	x	x		$ASI_{VT}=\int_{0.1}^{0.5}S_a dT$	(Thun et al. 1988)
ASI_{NH}	N&H P-Acceleration Spectrum Intensity	x	x		$ASI_{NH}=\frac{1}{0.157}\int_{0.028}^{0.185}S_{pv}dT$	(Nau and Hall 1984)
C_a	Amplification of acceleration	x	x		$C_a=S_a(T1)/PGA$	(-)

Table 4.3: Velocity-related IMs.

Not.	Name	A	F	D	Definition	Ref.
PGV	Peak Ground Velocity	x			$PGV=\max|\dot{u}_g(t)|$	(Kramer 1996)
SMV	Sustained Maximum Velocity	x			-	(Nuttli 1979)
I_v	Riddell&Garcia compound index	x		x	$I_v=PGV^{2/3} \cdot t_D^{1/3}$	(Riddell and Garcia 2001)
I_F	Fajfar index	x		x	$I_F=PGV \cdot t_D^{0.25}$	(Fajfar et al. 1990)
RMSV	Root Mean Square Velocity	x	x		$RMSV=\sqrt{\frac{1}{t_E}\int_0^{t_E}\dot{u}_g(t)^2 dt}$	(Kramer 1996)
SED	Specific Energy Density	x	x	x	$SED=\int_0^{t_E}|\dot{u}_g(t)|^2 dt$	(Kramer 1996)
CAD	Cumulative Absolute Displacement	x	x	x	$CAD=\int_0^{t_E}|\dot{u}_g(t)| dt$	(Mackie and Stojadinovic 2003)
MID	Maximum Incremental Displacement	x	x		-	(Anderson and Bertero 1987)
$S_v(T1)$	Spectral velocity	x	x		-	(Kramer 1996)
$S_v(2T1)$	Spectral velocity	x	x		-	(Kramer 1996)
EPV	Effective Peak Velocity	x	x		$EPV=avg(S_v)|_{0.7}^{2.0}/2.5$	(Kramer 1996)
I_H	Housner P-Velocity Spectrum Intensity	x	x		$I_H=\int_{0.1}^{2.5}S_{pv}dT$	(Housner 1952)
VSI_{VT}	Von Thun Velocity Spectrum Intensity	x	x		$VSI_{VT}=\int_{0.1}^{2.5}S_v dT$	(Thun et al. 1988)
VSI_K	Kappos P-Velocity Spectrum Intensity	x	x		$VSI_K=\int_{0.8T1}^{1.2T1}S_{pv}dT$	(Kappos 1991)
VSI_{HC}	H&C P-Velocity Spectrum Intensity	x	x		$VSI_{HC}=\int_{0.1}^{1.0}S_{pv}dT$	(Hidalgo and Clough 1974)
VSI_{NH}	N&H P-Velocity Spectrum Intensity	x	x		$VSI_{NH}=\frac{1}{1.715}\int_{0.285}^{2.0}S_{pv}dT$	(Nau and Hall 1984)
C_v	Amplification of velocity	x	x		$C_v=S_v(T1)/PGV$	(-)

Table 4.4: Displacement-related IMs.

Notation	Name	A	F	D	Definition	Ref.
PGD	Peak Ground Displacement	x			$PGD=\max|u_g(t)|$	(Kramer 1996)
I_d	Riddell&Garcia compound index	x		x	$I_d=PGD\cdot t_D^{1/3}$	(Riddell and Garcia 2001)
RMSD	Root Mean Square Displacement	x	x		$RMSD=\sqrt{\frac{1}{t_E}\int_0^{t_E}u_g(t)^2 dt}$	(Kramer 1996)
$S_d(T_1)$	Spectral displacement	x	x		-	(Kramer 1996)
EPD	Effective Peak Displacement	x	x		$EPD=avg(S_d)|_{2.5}^{4.0}/2.5$	(Kramer 1996)
DSI_{NH}	N&H Displacement Spectrum Intensity	x	x		$DSI_{NH}=\frac{1}{8.333}\int_{4.167}^{12.5}S_{pv}dT$	(Nau and Hall 1984)
C_d	Amplification of displacement	x	x		$C_d=S_d(T1)/PGD$	(-)

Table 4.5: Mixed/hybrid IMs.

Notation	Name	A	F	D	Definition	Ref.
PGV/PGA	Frequency content$_1$		x		PGV/PGA	(Kramer 1996)
PGD/PGV	Frequency content$_2$		x		PGD/PGV	(Kramer 1996)
I_D	C&M Damage factor	x	x	x	$I_D=\frac{2g}{\pi}\frac{I_A}{PGA\cdot PGV}$	(Cosenza and Manfredi 1997)
I_S	Sandi instrumental intensity	x	x		$I_S=\log_4(EPA\times EPV)+I_0$	(Sandi 1985)
E_I	Input Energy	x	x	x	$E_I=\int_0^{t_E}|\ddot{u}_g(t)\dot{u}_g(t)|\,dt$	(Cosenza and Manfredi 2000)

Peak seismic input parameters are PGA, PGV, PGD. Other measures can be Sustained Maximum Acceleration (SMA) and Sustained Maximum Velocity (SMV) defined as the third highest absolute peak value of acceleration and velocity time history, respectively, (Nuttli 1979), and Effective Design Acceleration (EDA) (Reed et al. 1988). While PGA is not totally reliable, the PGV seems to be a more representative measure of earthquake intensity as it is directly connected with the energy content (Housner and Jennings 1982). In addition, Riddell and Garcia found that compound parameters could minimize the dispersion of hysteretic energy-dissipation spectra of inelastic single-degree-of-freedom (SDOF) systems (Riddell and Garcia 2001): I_a, I_v and I_d are considered as ground motion measures with respect to fundamental periods in the lower, intermediate and higher period range, respectively. Also, Fajfar proposed a compound IM, I_F, for structures with fundamental periods in the intermediate-period range (Fajfar et al. 1990). Notations, definitions, as well as amplitude, frequency content and duration characterizations, are reported in Tabs. 4.2, 4.3, 4.4 and 4.5.

Integral seismic input parameters can be the Root Mean Square Acceleration (RMSA), Velocity (RMSV) and Displacement (RMSD). They are much more effective for engineering purposes for incorporating the effect of frequency content and duration and for measuring the energy content of a seismic event. Two measures of earthquake destructiveness based on the RMSA are the Arias intensity, I_A, and the Saragoni Factor, P_D. I_A, is defined as the time integral of the square of the seismic ground acceleration and can be related to the energy content of an earthquake given the proportionality to the square of acceleration (Arias 1970). A plot of the build-up of I_A with time is known as a Husid plot (Husid 1969). Arraya and Saragoni have shown that I_A predicts the destructiveness capacity in an appropriate mode only when the frequency content of different earthquakes is similar (Araya and Saragoni 1980; Araya and Saragoni 1984). They have introduced a sort of normalization of I_A, defined as Destructive Potential Factor, P_D, a more effective measure which can be expressed as a function of the duration, maximum ground acceleration and frequency content of the strong ground motion. P_D is computed as the ratio between I_A and the square of zero crossings of the record in the time unit (ν^2), the latter incorporating the frequency content. Acceleration parameter, A_{95}, represents the level of acceleration which contains up to 95% of I_A (Sarma and Yang 1987). Another integral parameter is the Characteristic Intensity, I_C, based on the total duration and the RMSA (Park et al. 1985). It has been shown to be linearly related with measures of observed damage for

both experimented and actual damaged buildings. Cosenza and Manfredi have proposed a damage factor, I_D, that is related to the energy content of the earthquake (Cosenza and Manfredi 1997). In addition, Maximum Incremental Velocity (MIV) and Displacement (MID) have been proposed for characterizing the damage potential of earthquake motions in the near-fault region (Anderson and Bertero 1987). MIV and MID are computed as the maximum area under an acceleration and velocity pulse (between two consecutive zero acceleration and velocity crossings), respectively. Moreover, the Cumulative Absolute Velocity (CAV), originally proposed by Kennedy and Reed (EPRI 1988) in a study sponsored by the Electrical Power Research Institute (EPRI), is defined as the area under the absolute ground acceleration during the total duration of the record, also interpreted as incremental velocities sum. RMSA, RMSV, RMSD, I_C, I_A, P_D, MIV, MID and CAV, besides integral parameters, are concerned also as seismic input IMs. Notations, definitions, as well as amplitude, frequency content and duration characterizations, are reported in Tabs. 4.2, 4.3, 4.4 and 4.5.

Intensity measures based on the response of a linear elastic SDOF system are identified as spectral parameters, considered as structure-specific IMs. Acceleration, velocity and displacement response spectra represent the response of SDOF systems. The response spectrum represents the most basic tool of earthquake engineering and most of the design standards define hazard intensity based on the spectral acceleration of the ground motion. The response spectrum describes the frequency content of ground motions in a manner that is more fundamental to earthquake response than the traditional Fourier spectrum, because of the inclusion of the damping effects. The fundamental period and the damping ratio (generally 5%) are the only parameters needed to characterize dynamically a SDOF system. The most widely used spectral IM is the acceleration response at the first mode period of vibration of the structure (5% damped), $S_a(T1)$. It represents a measure of the maximum strength demand of the earthquake, being proportional to the maximum seismic force acting on the structure. Other spectral IMs are the velocity and displacement response at the first mode period of vibration of the structure, $S_v(T1)$ and $S_d(T1)$, respectively. In addition, the Effective Peak Acceleration (EPA), Velocity (EPV) and Displacement (EPD) were firstly introduced in the code design previsions (ATC 1978, BSSC 1984) by Applied Technology Council (Kramer 1996) to characterize the intensity of design ground motions. They are defined as the average spectral acceleration, velocity and displacement over a certain period range divided by 2.5 (the standard response amplification

factor for a 5% damping spectrum). EPA considers a period range $0.1 \leq T \leq 0.5$ seconds, EPV the period range $0.7 \leq T \leq 2.0$ seconds while EPD is computed over the period range from 2.5 to 4.0 seconds. $S_a(T1)$, $S_v(T1)$, $S_d(T1)$, and EPA, EPV, EPD constitute peak seismic response IMs. Notations, definitions, as well as amplitude, frequency content and duration characterizations, are reported in Tabs. 4.2, 4.3, 4.4 and 4.5.

Spectrum intensity measures evaluated by the integration of the response spectrum in a given period range (spectrum intensity parameters) can explicitly account for higher modes effects as well as period lengthening due to structural softening. Although the elastic response spectrum cannot directly define damage on a structure (which is essentially inelastic deformation), it captures in one curve the amount of elastic deformation for a wide variety of structural periods and, therefore, may be a good overall measure of ground motion intensity. On this basis, Von Thun Acceleration Spectrum Intensity, ASI_{VT}, has been proposed by (Thun et al. 1988), whereas for velocity-spectrum-sensitive structures, Housner defined a measure for expressing the destructiveness severity of earthquakes computed as the area under (integral) the pseudo-velocity spectrum in the period range $0.1 \leq T \leq 2.5$ seconds (Housner 1952). Housner Intensity, I_H, has such integration limits in a way that a range of typical periods of vibration of urban buildings has been taken into account. Accordingly, I_H may be considered as an overall measure of the capability of an earthquake to excite a population of buildings with fundamental period between 0.1 and 2.5 seconds. There are other definitions of Velocity Spectrum Intensity (VSI) suggested by several Authors. Hidalgo and Clough considered I_H and a new definition of spectrum intensity, defined as VSI_{HC}, where the upper integration limit was reduced to 1.0 second (Hidalgo and Clough 1974). Kappos proposed another definition of spectrum intensity, VSI_K, where the integration limits are depended on the natural eigenperiod of the structure T1 (Kappos 1991): the suggested period-intervals are t1 = 0.8T1 and t2 =1.2T1. Other examples of VSI can found in the literature (Nau and Hall 1984; Thun et al. 1988). These spectrum intensity parameters, ASI_{VT}, ASI_{NH}, I_H, VSI_{VT}, VSI_K, VSI_{HC}, VSI_{NH}, can be classified as integral seismic response IMs. Notations, definitions, as well as amplitude, frequency content and duration characterizations, are reported in Tabs. 4.2, 4.3, 4.4 and 4.5.

With a complete overview on many IMs, a statistical correlation study has been carried out considering about fifty (50) intensity measures, aimed at investigating the interdependence among them and at understanding the most suitable and reasonable measures for IDA purposes. To this end, a total of one hundred (100) strong ground motions from earthquakes with moment magnitude $M_w \geq 5$ have been selected from the ITACA strong motion database (Pacor et al. 2011), taking into consideration: (i) normal, thrust and strike-slip faulting mechanisms, (ii) ordinary and pulse-like near-fault ground motions, (iii) epicentral distance range of 2-80 km and (iv) all subsoil categories (A, B, C, D, E). Detailed information about ground motions is reported in Appendix A. It is noteworthy to stress that, although input acceleration, velocity and displacement time histories are given in East and North directions, IMs have been computed using their mean direction. Considering the aforementioned ground motions, correlation coefficients R have been computed between acceleration-related (Fig. 4.2a), velocity-related (Fig. 4.2b), displacement-related (Fig. 4.2c) and mixed IMs (Fig. 4.2d), allowing to rate their degree of interdependence: high correlation ($1 > R > 0.9$), medium correlation ($0.9 \geq R > 0.6$) and low correlation ($0.6 \geq R$). In general, a high degree of correlation inside each subgroup can be observed. These results are in clear agreement with those presented by (Riddell 2007). IMs belonging to different subgroups are badly correlated between them, as shown in Fig. 4.2e. Besides the selection of the most uncorrelated measures, at least one seismic peak and one seismic integral IM, as well as one response peak and one response integral parameter, have been chosen as pivot parameters from each subgroup for IDA purposes. Considering (as an example) the case of response integral velocity-related parameters, the applied rule aimed at uncorrelated IMs selection would imply the following steps: first the pivot IM is chosen (I_H) and then the ones featuring $R \leq 0.9$ with respect to the pivot are taken into account, while the others with $R > 0.9$ are discarded (VSI_{VT}, VSI_K, VSI_{HC}, VSI_{NH}). Only C_a, C_v, C_d and I_D made an exception to this selection rule because they remain almost constant with increasing seismic intensity, thus being not useful for IDA purposes.

Finally, the most uncorrelated, meaningful and representative IMs that have been selected and used for the construction of IDA curves are: PGA, RMSA, I_C, I_A, P_D, CAV, $S_a(T1)$, ASI_{VT}, PGV, RMSV, SED, CAD, $S_v(T1)$, I_H, PGD, RMSD, $S_d(T1)$, DSI_{NH} and E_I ($m{=}19$ with reference to Eq. (4.1)). They are highlighted in Figs. 4.2a-d, whereas correlation coefficients between them are reported in Fig. 4.2e.
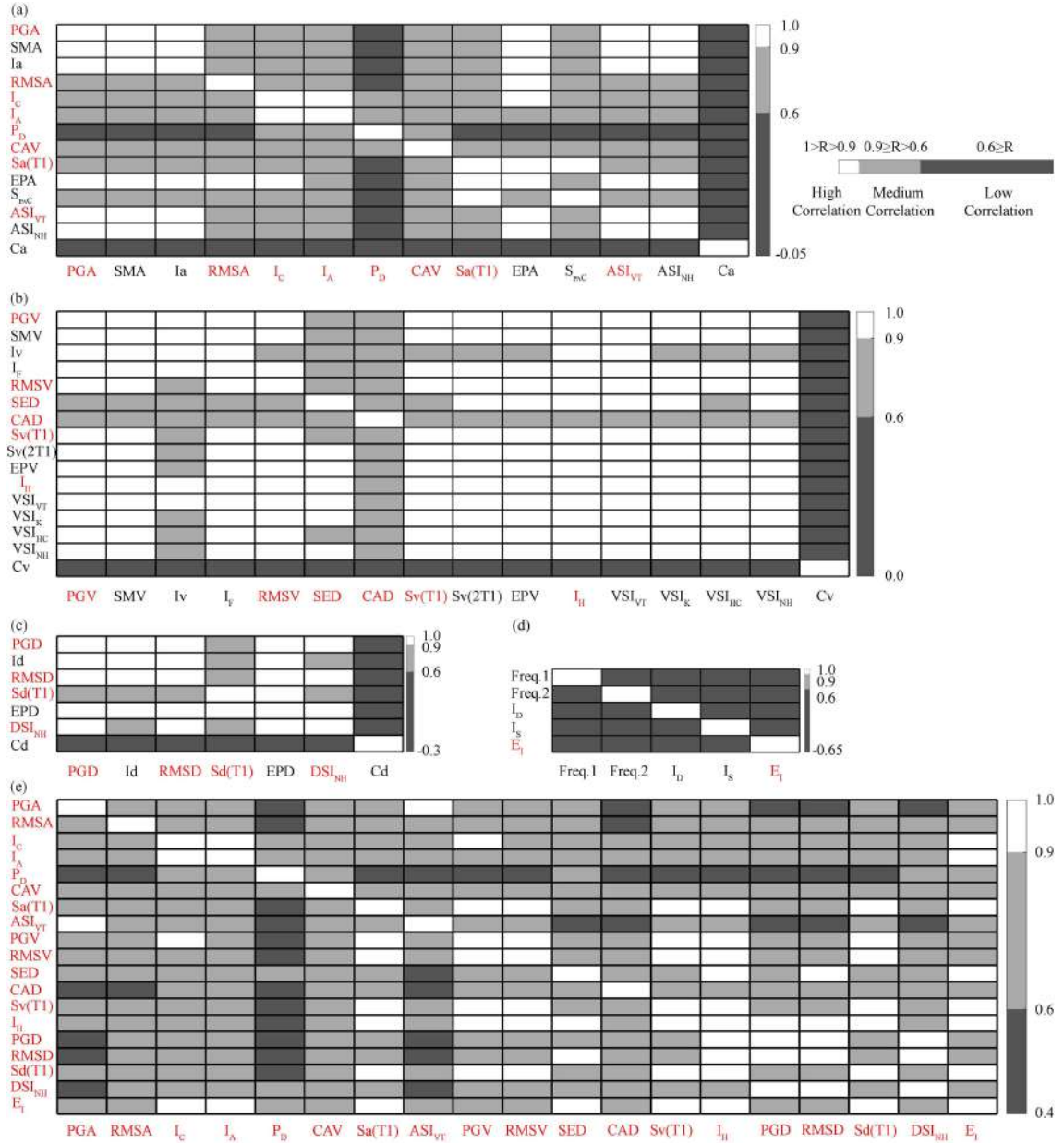
Figure 4.2: Correlation between IMs: correlation coefficients R between acceleration-related (a), velocity-related (b), displacement-related (c) and mixed IMs (d); correlation coefficients between the selected IMs for IDA (e). Note that the latter are highlighted with red color.

4.4   Application example: the Brick House

The proposed method in Section 4.2 is applied and validated through the Finite Element (FE) model of a well-known case study, the Brick House. It is a benchmark tested on the National Laboratory for Civil Engineering (LNEC) shaking table in Lisbon, Portugal, whose experimental results act as a reference for calibration of the numerical counterpart. The tests, carried out in the scope of the workshop "Methods and Challenges on the Out-of-Plane Assessment of Existing Masonry Buildings" (Lourenço et al. 2017), aimed at assessing the out-of-plane performance of the mock-up under seismic loading. A detailed FE model of the structure is developed and non-linear dynamic analyses are carried out to obtain numerical insight into the seismic response of the building specimen, identifying its most vulnerable parts. Section 4.4.1 presents the case study, including the validation of the FE model of the structure. The selection of seismic input used for non-linear dynamic analysis is reported in Section 4.4.2 while non-linear seismic IDA curve sets are illustrated in Section 4.4.3. Finally, Section 4.4.4 is devoted to presenting the results on earthquake-induced damage localization and quantification via non-linear seismic IDA. Main conclusions are summarized in Section 4.5.

4.4.1   Experimental testing and FE modeling

The Brick House was built using regular fired clay bricks with an English bond masonry arrangement, yielding a wall thickness of around 23.5 cm. The house presented three walls arranged according to a U shape layout (see Fig. 4.3): the façade wall with a central opening and a gable on top, and the two orthogonal sidewalls acting as abutments, of which only one was pierced by a window.

Unidirectional seismic loading in the perpendicular direction to the façade was applied with an increasing input intensity testing protocol up to collapse. The pre-processed N64E strong ground motion component of the Christchurch (New Zealand) earthquake of February 21$^{\text{st}}$ 2011 was used. In this way, the façade was loaded in the out-of-plane direction, while the sidewalls were loaded in-plane but, given the presence of a window in one of them, an asymmetric dynamic behavior was observed, leading to significant torsion of the structure. The seismic test sequence included eight (8) steps of increasing intensity, where the last one reached a PGA of about 12.47 m/s^2. The collapse mechanism observed at the end presented partial collapse of the gable top of the façade and the lateral wall with
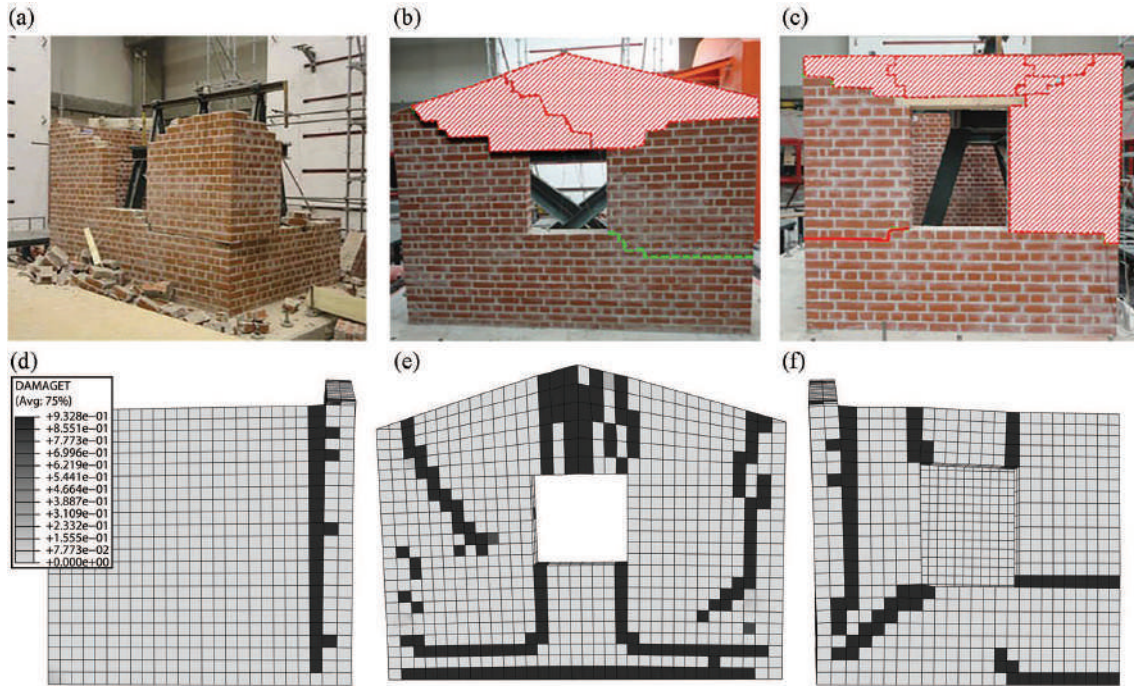
Figure 4.3: Experimental results: brick masonry prototype after shaking table test (a) and collapse mechanism schemes (b, c) (Candeias et al. 2017). Numerical model validation: damage obtained by the corresponding FE model after the Christchurch (N64E component) earthquake simulation (d-f).

window, while the other sidewall remained almost intact (see Figs. 4.3a-c). The instrumentation included twenty (20) unidirectional accelerometers and six (6) linear variable displacement transducers (LVDTs), placed in different locations for measuring the absolute acceleration responses of the structure as well as the input signals on the shake table, and the out-of-plane displacements of the façade, respectively. Further details concerning the mock-up, seismic testing campaign, instrumentation setup, damage pattern and observed collapse mechanisms are presented in (Candeias et al. 2017).

A 3D FE model of the Brick House mock-up has been built using the ABAQUS 6.10 platform (Simulia 2010). A free meshing of solid eight-node linear brick elements C3D8R with the mean dimension of about 10 cm (two elements in thickness) has been adopted, resulting into a total of 5595 nodes, 16785 DOFs and 3460 elements. The choice of such a mesh dimension has been determined based on a preliminary sensitivity analysis, here omitted for the sake of brevity, looking for a compromise between accuracy of the solution

and control of computational costs. The model has been assumed as fixed to the ground. At the constitutive level, the same material has been assigned to the whole structure as homogeneous, assuming an isotropic behavior. Linear mechanical parameters of the masonry can be found in (Candeias et al. 2017), as estimated after in-situ characterization experimental tests on six (6) wallets.

The numerical prediction of the behavior of masonry structures still represents a complex issue due to the difficulties to adequately simulate the non-linear cyclic response of the masonry material. In this regard, the non-linear FE modeling and mechanical behavior of the masonry material have been here reproduced, as suggested in literature works on seismic vulnerability analysis (Valente and Milani 2016), using the CDP constitutive model proposed by Lubliner (Lubliner et al. 1989) and subsequently modified by Lee and Fenves (Lee and Fenves 1989) for cyclic loading and damage implementation. More information on CDP model is detailed in Section 3.3.2 with the principal scheme illustrated in Fig. 3.8 and description of main equations (Eqs. (3.10) and (3.11)).

In the case of the Brick House mock-up, despite the absence of data to accurately describe the non-linear behavior of the material in tension and the failure of experimental diagonal compression tests, the post-elastic material response (with specific reference to the mortar) in tension and compression (assumed to be exponentially decreasing) has been suggested in (Gams et al. 2017).

For the present numerical model, the proposed linear (Candeias et al. 2017) and non-linear (Gams et al. 2017) parameters resulted very useful for the calibration process. It should be emphasized that, for obtaining full consistency between numerically predicted and experimentally recorded response accelerations, an additional manual tuning was needed. The following linear parameters are adopted: Young's modulus E, Poisson's ratio ν, specific weight γ, and tensile and compressive strength (σ_t and σ_c), as reported in Tab. 4.6. The ratio between σ_t and σ_c is equal to about 0.1. Regarding CDP, with reference to the suggested values, slightly different but reasonable damage parameters in tension have been adopted (see Tab. 4.7). The description of the failure condition and of the post-peak behavior depends upon the tensile stresses, σ_t, the cracking strains, $\tilde{\varepsilon}_t^{\text{ck}}$, and the tensile damage variable, d_t. The behavior of the masonry has been reproduced up to the ultimate limit state, considering damage in tension only. CDP complementary parameters for defining flow potential, yield surface and viscosity are reported in Tab. 4.8. In detail, ψ

Table 4.6: Mechanical parameters adopted on the Brick House FE numerical model.

E $[kN/m^2]$	ν [-]	γ $[kN/m^3]$	σ_t $[kN/m^2]$	σ_c $[kN/m^2]$
3.62e+06	0.3	18.9	250	2480

Table 4.7: Uniaxial stress–strain and scalar tensile damage values utilized in the CDP model for the masonry material.

σ_t $[kN/m^2]$	$\tilde{\varepsilon}_t^{ck}$ $[-]$	d_t $[-]$
252	0.0e-00	0.00
198	3.0e-05	0.20
99	8.0e-05	0.40
45	1.1e-04	0.70
22	1.8e-04	0.90

Table 4.8: CDP parameters defining flow potential, yield surface and viscosity.

ψ [deg]	ϵ $[-]$	σ_{b0}/σ_{c0} $[-]$	K_c $[-]$	μ $[-]$
30	0.1	1.16	0.667	0

represents the dilation angle in the p–q plane. The flow potential eccentricity, ϵ, is a small positive number that defines the rate at which the hyperbolic flow potential approaches its asymptote. The parameter σ_{b0}/σ_{c0} represents the ratio of initial equibiaxial compressive yield stress to initial uniaxial compressive yield stress. K_c is the ratio between second stress invariants on the tensile and compressive meridians at initial yield for any given value of the pressure invariant, such that the maximum principal stress is negative. Finally, μ indicates the viscosity parameter, which is set equal to 0 (default value in ABAQUS/Explicit).

The validation of the Brick House FE model has been performed by investigating its damage pattern predicted after the Christchurch earthquake numerical simulation, using the same input motion of the experimental tests (Kita et al. 2019a). Figs. 4.3d-f illustrate the numerically obtained damage pattern, which is consistent with the experimental collapse mechanism observed during the shaking table test and shown in Figs. 4.3a-c. Furthermore, as displayed in the plots of Fig. 4.4, numerically predicted and experimentally measured
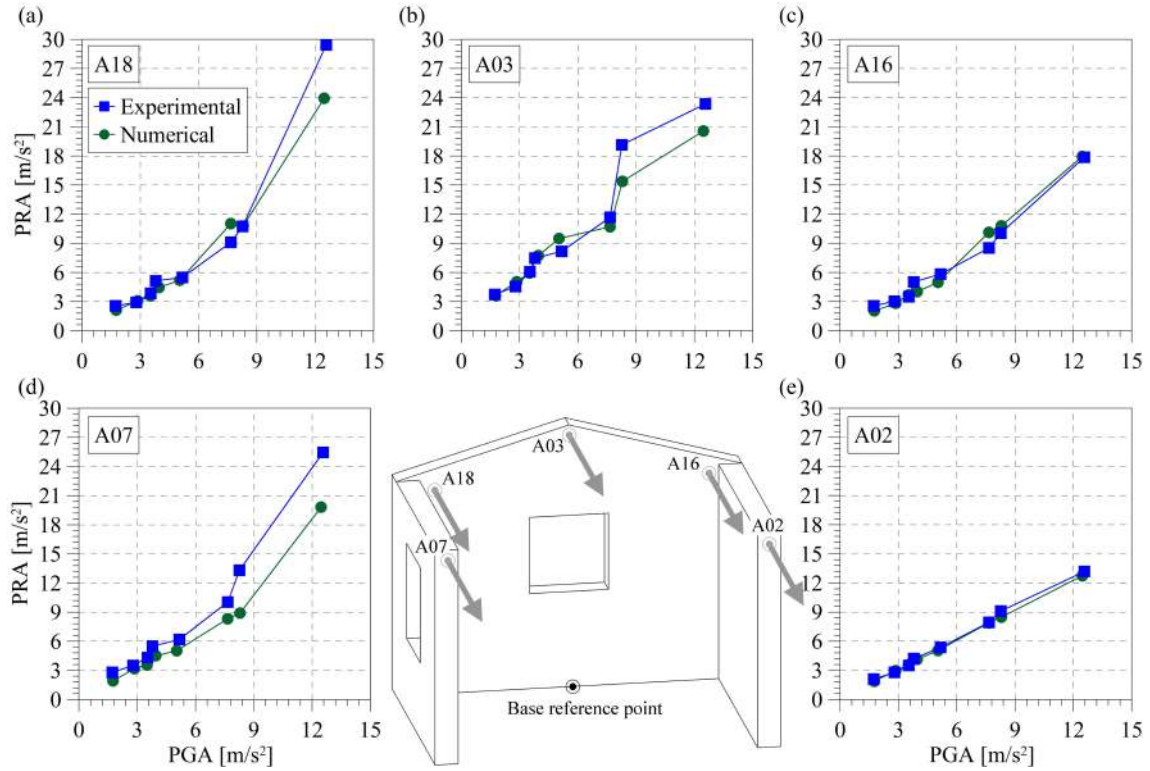
Figure 4.4: Numerical model validation: plots of experimental versus numerical PRAs, with reference to the top accelerometers (A07, A18, A03, A16 and A02). Note that PGA is measured at the base reference point.

response accelerations have been compared in five (5) strategic and meaningful reference points. Given the consistency of damage pattern and plots of PRAs, the model can be considered validated, hence ready for IDA.

The DMs used in the present case study are output variables obtained from ABAQUS numerical model, namely: tensile damage parameter, d_t, plastic strain magnitude, *PEMAG*, and first principal plastic strain, $\varepsilon_1^{\mathrm{pl}}$. For damage localization purposes, the Brick House FE model has been partitioned into ten (10) parts (see Fig. 4.5), thus allowing a local IDA-based estimation of DMs, computed as average values weighted over the volume of the numerical elements of every single part of the FE model (volume-averaged damage parameter). Also, the direction of the application of the seismic loading is indicated with a double-sided arrow.
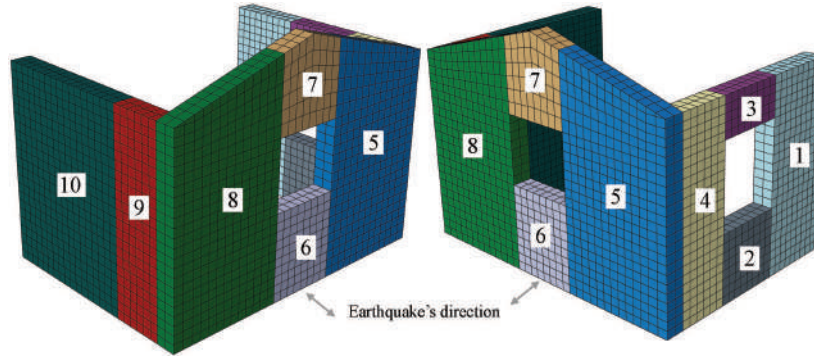
Figure 4.5: The ten (10) parts of the Brick House numerical model defined for damage localization purposes through IDA. The double-sided arrow indicate the direction of application of the seismic loading (applied as base excitation).

4.4.2 Seismic input selection

A *multi-record IDA study*, whose output is an *IDA curve set* (Vamvatsikos and Cornell 2002), has been performed for each part of the structure. When subjected to different ground motions, a model will often produce quite dissimilar responses that are difficult to predict a priori, being unable to fully capture the behavior that a building may display in a future event. Indeed, given the high dependence on the chosen record and taking into account the record-to-record variability of structural responses, a suite of ground motion records has been considered. As suggested by technical standards (EN 1998-1 2005), seven (7) seismic records have been used, aimed at covering a full range of responses and with different seismic characteristics in terms of amplitude, energy or frequency content. This allows for capturing several possible damage and collapse mechanisms.

The seismic input (scaled at increasing levels) used for non-linear dynamic analysis is usually defined in terms of acceleration time series whose response spectra result compatible with a specific target response spectrum. In the present case study, in order to have an average response spectrum (obtained from the combination of the seven used accelerograms) consistent with the prescribed elastic one, the selected ground motion accelerograms, whose main original characteristics are synthesized in Tab. 4.9, have been individually scaled and matched to the elastic response spectrum prescribed by the New Zealand Standards (NZS) 1170.5:2004 (NZS 2004b; NZS 2004a), for the site of Christchurch city, assuming a Hazard Factor Z = 0.3 (updated after Christchurch earthquake (Gerstenberger et al. 2011)), Return Period Factor Rs/Ru = 1, D subsoil category and 2.5 km distance to the nearest major

Table 4.9: Original characteristics of the selected strong ground motions subsequently matched to the Christchurch response spectrum for IDA. PGAs refer to spectrum-matched accelerograms.

EQ. ID [−]	Station ID [−]	Epicenter [−]	Date [dd/mm/yyyy]	Mw [−]	Fault [−]	PGA [m/s^2]
IT0164ya	ALT	Irpinia	23/11/1980	6.9	Normal	4.645
IT0788xa	ANT	L'Aquila	06/04/2009	6.3	Normal	5.057
IT0789xa	AQA	L'Aquila	06/04/2009	6.3	Normal	3.931
IT0789ya	AQA	L'Aquila	06/04/2009	6.3	Normal	4.550
IT0806ya	FMG	L'Aquila	06/04/2009	6.3	Normal	3.532
IT0095xa	NRC	Ussita	26/10/2016	5.9	Normal	5.101
IT0095ya	NRC	Ussita	26/10/2016	5.9	Normal	5.371

fault (Kita et al. 2019a). The spectrum matching/compatibility has been realized by SeismoMatch earthquake engineering software (Seismosoft 2018). It is an application capable of adjusting real earthquake accelerograms to match a site-specific target response spectrum using the spectral matching techniques proposed by (Abrahamson 1992; Hancock et al. 2006; Atik and Abrahamson 2010). SeismoMatch has been widely used in the literature for obtaining spectrum-compatible earthquakes to be used in non-linear dynamic analysis (Tesfamariam et al. 2014; Rossetto et al. 2016; Shahi et al. 2017; Fitzgerald and Basu 2017; Huang et al. 2018). Realistic acceleration time series have been generated by adjusting the real accelerograms summarized in Tab. 4.9, while keeping the strong ground motion non-stationarity, thus resulting in response spectra compatible with the Christchurch response spectrum. The time histories of the unscaled spectrum-matched accelerations are illustrated in Fig. 4.6a. Corresponding response spectra are plotted in Fig. 4.6b, together with the elastic response spectrum prescribed by the NZS. It is worth noting that, from here on, earthquakes reported in Tab. 4.9 will be identified with a suffix "_m", in order to take into account time histories of spectrum-matched accelerations ("_m" is for indicating matched). The unidirectional seismic loadings applied in the perpendicular direction to the façade have been scaled-up at incremental amplitude levels for IDA (Pasticier et al. 2008; Chácara et al. 2019) by means of appropriate SFs (λ, $\mathbf{a}_\lambda = \lambda \cdot \mathbf{a}_1$ in (Vamvatsikos and Cornell 2002)) equal to 1, 1.5, 2, 2.5, ..., 5, resulting to a total of sixty-three (63) non-linear time history analyses.
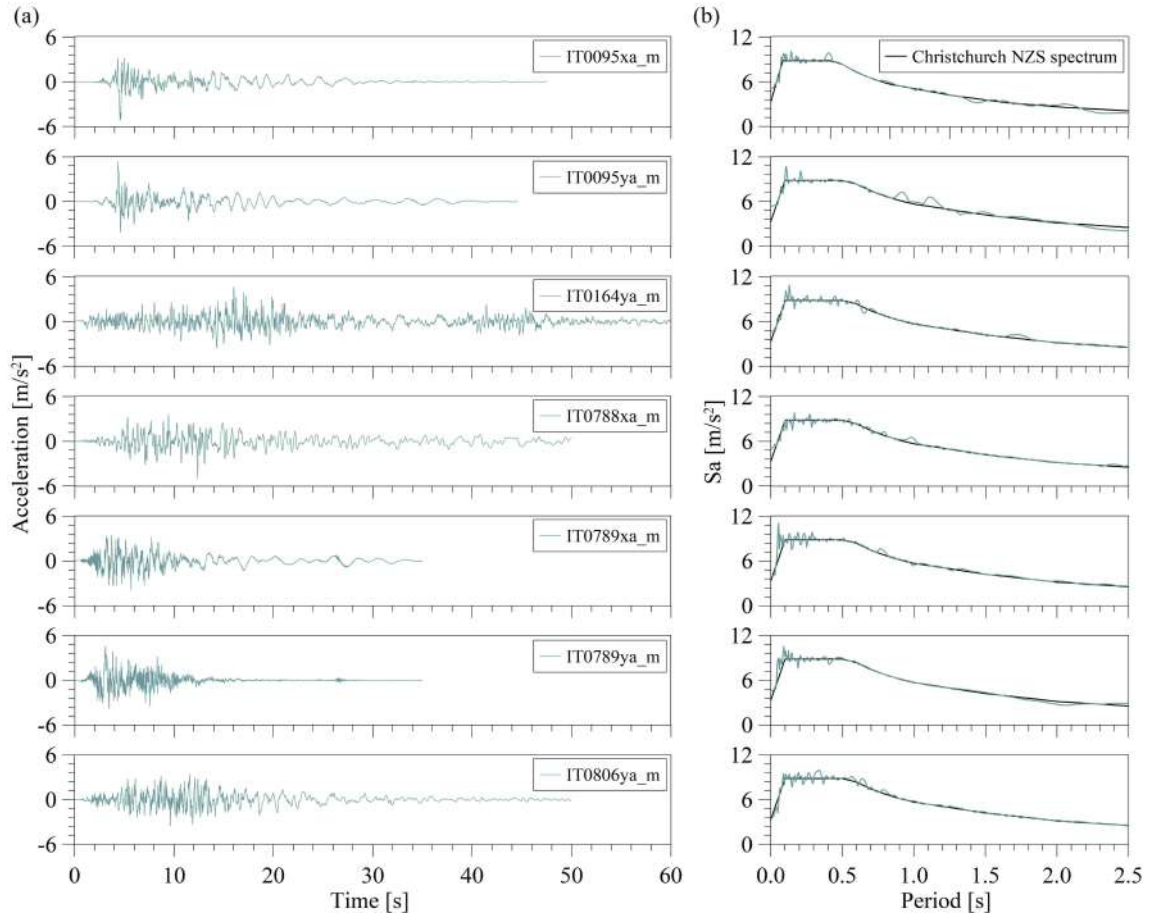
Figure 4.6: Plots of the seven (7) unscaled acceleration time histories used for IDA (a) and corresponding response spectra (together with Christchurch's NZS spectrum) (b).

4.4.3   Non-Linear Seismic IDA Curve Sets

Considering the ten (10) parts, *IDA curve sets* (see Eq. (4.1)) relate the local DMs to the set of preselected IMs described in Section 4.3 (see Fig. 4.2e). Subsequently to the correlation study, a second selection step has been carried out by rapidly investigating the dispersion of IDA curves. As stated in Section 4.1, an IM is considered to be efficient if it provides a relatively small dispersion of the structural response, so a smaller dispersion of the averaged numerically computed DM for a given IM leads to a higher confidence and higher accuracy in the estimation of the mean DM itself for that IM, so to more accurate results. In this context, some of the IMs have been further discarded due to the large dispersion of their corresponding IDA curve sets: RMSA, P_D, CAV,

RMSV, SED, CAD, PGD, RMSD, S_d(T1), DSI_{NH} and E_I. Therefore, the most efficient IMs ultimately considered for IDA are the following eight (8): PGA, I_C, I_A, S_a(T1), ASI, PGV, S_v(T1) and I_H. In particular, considering the dynamic properties of the Brick House, ASI has been computed the same as ASI_{VT}, but limiting the integral (see Tab. 4.2) from 0 to the structure's first-mode period. These IMs (m^*=8) can be collected into the vector $\mathbf{IM}^* = (PGA, I_C, I_A, S_a(T1), ASI, PGV, S_v(T1), I_H)$. Finally, the IDA curve sets (each containing seven (7) curves plus their mean curve) obtained from tensile damage and first principal plastic strain versus the aforementioned eight (8) IMs have been studied. Their dispersion has been investigated through the mean values of the RMSE of single curves computed with respect to the mean curve, as described in Eq. (4.2), where $i = 1, .., 10$ (10 parts), $j = 1, .., m^*$ (8 IMs) and $k = 1, .., l$ (l=7, the number of earthquakes used for IDA) have been considered for the present case study. As an example, $\mathbf{\Delta DM_{7,1}^2} = (\Delta DM_{7,1}^{2,1}, \Delta DM_{7,1}^{2,2}, ..., \Delta DM_{7,1}^{2,q})$ is the vector difference between the 2nd (IDA curve of IT0788xa_m earthquake, see Tab. 4.9) and mean damage, with reference to the 7th part of the model and using the 1st intensity measure (PGA). After applying Eq. (4.2), Fig. 4.7 and Fig. 4.8 show $RMSE_{i,j}$ for the ten (10) parts, in the case of tensile damage and first principal plastic strain, respectively. Note that the first quantity
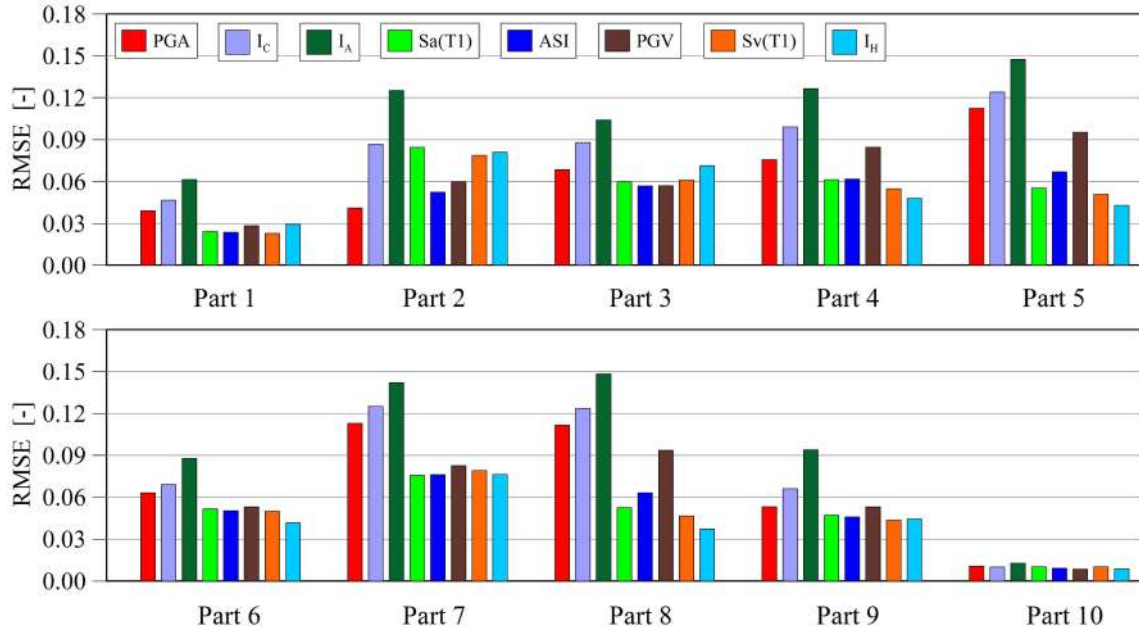
Figure 4.7: Dispersion of the IDA curve sets by means of $RMSE_{i,j}$: tensile damage Vs PGA, I_C, I_A, S_a(T1), ASI, PGV, S_v(T1) and I_H.
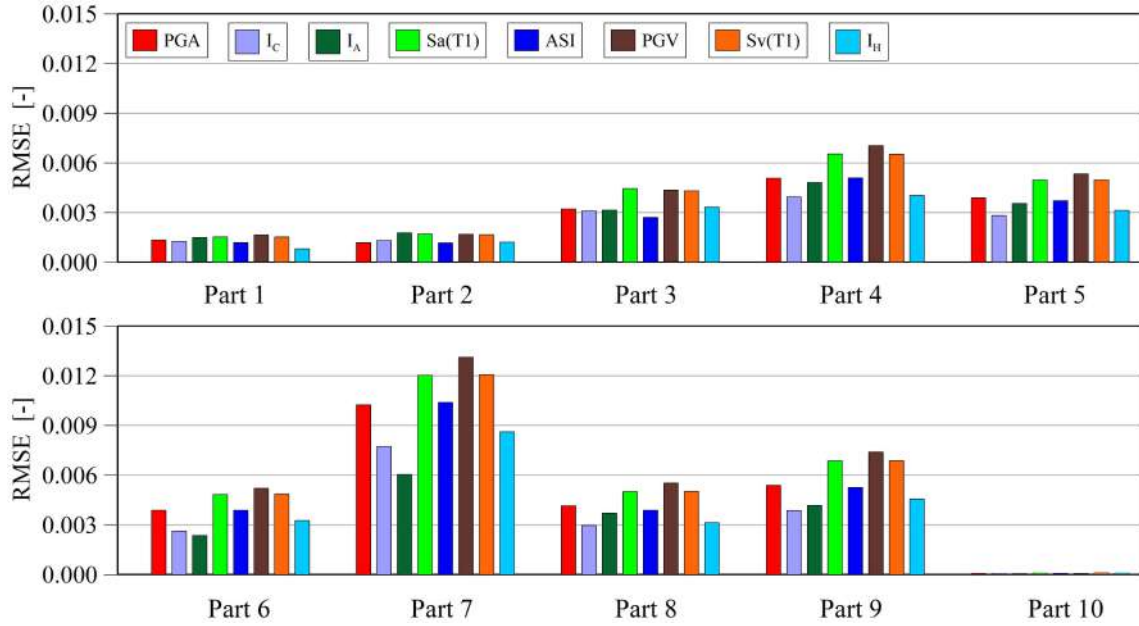
Figure 4.8: Dispersion of the IDA curve sets by means of $RMSE_{i,j}$: first principal plastic strain Vs PGA, I_C, I_A, $S_a(T1)$, ASI, PGV, $S_v(T1)$ and I_H.

is irreversible (meaning that tensile damage can only increase upon loading, it takes into account the cumulative history of damage), while the second quantity will change according to the load direction (increasing or decreasing). In the case of tensile damage d_t, Fig. 4.7 shows that the most efficient IMs in terms of consistently lower dispersion are ASI and I_H, whereas I_C and I_A are the best ones for first principal plastic strain ε_1^{pl} (see Fig. 4.8).

For the sake of brevity, only the IDA curve sets corresponding to two of the aforementioned IMs are presented here. Fig. 4.9 shows the ten (10) plots of d_t versus ASI, whereas the ten (10) plots of ε_1^{pl} versus I_C are shown in Fig. 4.10. In addition to the set of curves, mean curves are depicted with a thick black line. By investigating these plots, it is possible to identify the least and most vulnerable parts of the structure. Figs. 4.9a,j indicate that parts 1 and 10 are the least damaged parts, with maximum values of tensile damage of about 0.4 and 0.15, respectively (40% and 15% reduction of Young's modulus). By examining Figs. 4.9d,e,g,h it is clear that the most damaged parts are 4, 5, 7 and 8, with maximum tensile damage equal to about 0.9, being this the maximum value adopted by the CDP model (meaning 10% residual stiffness in tension). Part 7 seems to be the first part to be damaged over time with increasing seismic intensity, followed by parts 5, 8 and
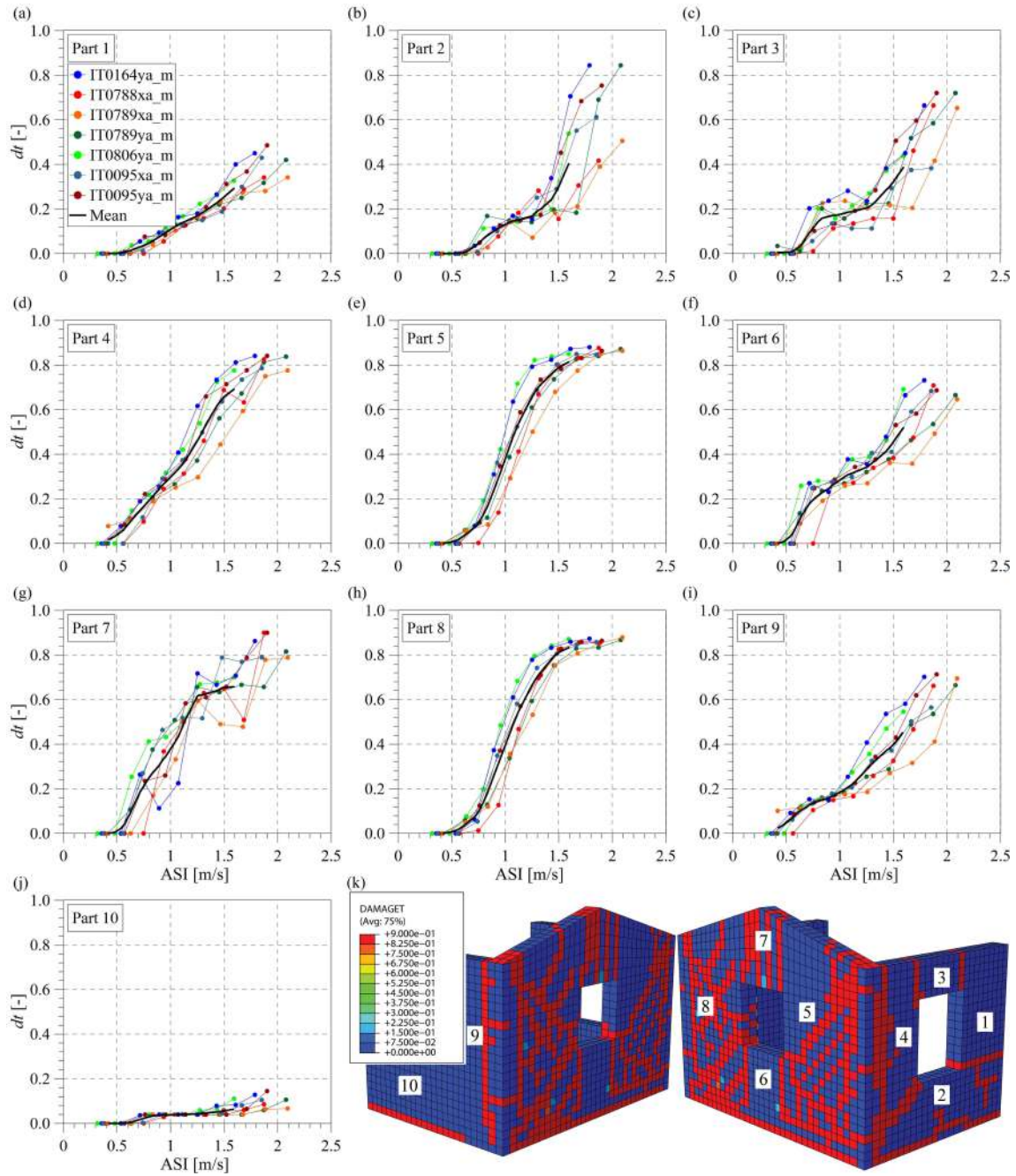
Figure 4.9: The IDA curve sets and corresponding mean curves: plots of tensile damage (d_t) versus ASI (a-j). Tensile damage contour plots at the end of the non-linear dynamic analyses with IT0788xa_m earthquake scaled at SF=3 (axonometric views) (k).
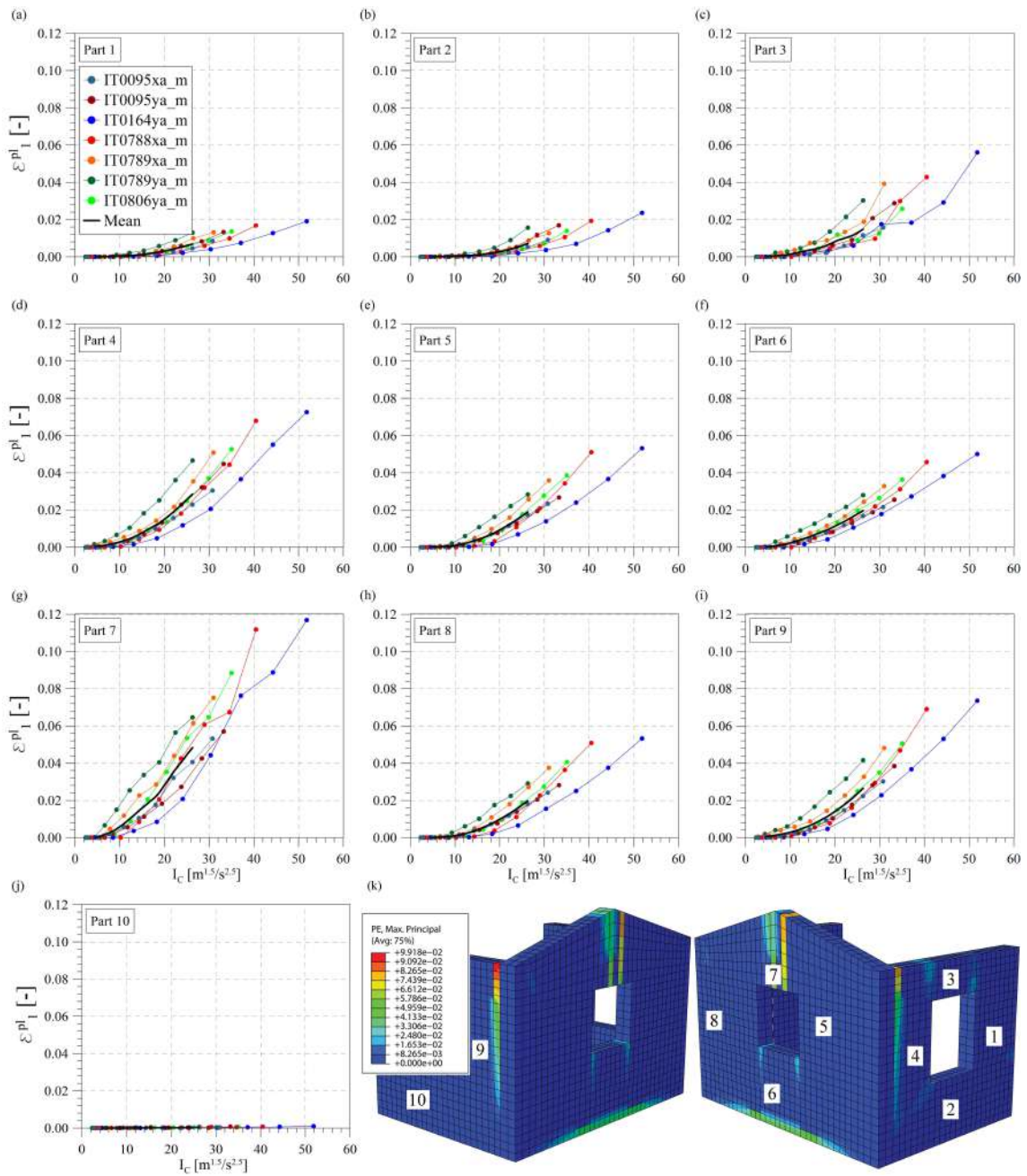
Figure 4.10: The IDA curve sets: plots of first principal plastic strain ($\varepsilon_1^{\mathrm{pl}}$) versus $\mathrm{I_C}$ (a-j). Contour plots obtained in the last step of the non-linear dynamic analysis with IT0788xa_m earthquake scaled at SF=3 (k).

4. Considering the unidirectional seismic loading, parts 5 and 8, as parts of the façade wall with out-of-plane loading, present a high level of damage even because they suffer due to the presence of the two orthogonal sidewalls, acting as abutments. Also, part 4 results to be more damaged than part 9, due to the presence of the opening in the sidewall (these two parts are in a symmetrical position). All these observations are in good agreement with the damaging process and pattern observed in the experimental tests (see Fig. 4.3).

On the other hand, the first principal plastic strain $\varepsilon_1^{\mathrm{pl}}$ represents a measure of the tensile deformation at a given time, which is strongly related to the formation and actual development/opening of cracks. With reference to the last time step, plots in Fig. 4.10 show that $\varepsilon_1^{\mathrm{pl}}$ presents its highest values in parts 7 and 4, which correspond to the top gable and the adjacent part of the sidewall with opening, respectively. Parts 1 and 10 are confirmed to be the least damaged ones.

For a better understanding of the damage pattern obtained via IDA, contour plots of d_t and $\varepsilon_1^{\mathrm{pl}}$ at the last step of the non-linear dynamic analysis carried out with IT0788xa_m earthquake scaled at SF=3 are also reported in the same figures. Tensile damage is clearly predominant in parts 7, 5, 8 and 4, whereas first principal plastic strain is concentrated in parts 7 and 4. Overall, the experimental crack formation and collapse mechanism/damage pattern (Candeias et al. 2017) are confirmed by the IDA curve sets, considering both d_t and $\varepsilon_1^{\mathrm{pl}}$. Still, tensile damage as a cumulative parameter seems conceptually more adequate for damage characterization and localization.

Given the limited possibility to show all the best IDA curve sets, only two are presented in this Section. For the interested reader, they are all reported in Appendix B.1. In particular, the IDA curve sets obtained in the case of d_t (from Fig. B.2 to Fig. B.9) and $\varepsilon_1^{\mathrm{pl}}$ (from Fig. B.10 to Fig. B.17) are presented for the ten (10) parts of the Brick House, each containing seven (7) curves plus their mean curve. In addition, the damage pattern evolution with increasing levels of earthquake input is illustrated in Fig. B.1 in terms of d_t contour plots obtained at the last step of the IDAs with IT0806xa_m earthquake.

4.4.4 IDA-based damage identification

After the construction of the IDA curve sets, higher levels of identification (localization and quantification) of earthquake-induced damage have been achieved for the ten (10) parts of the structural model, by using Eqs. (4.4) and (4.5) and IMs of arbitrary real seismic events. For this purpose, three near-field ground motion records belonging to the 2016 Central Italy seismic sequence (Chiaraluce et al. 2017), appropriately scaled-up in the present case, have been used: (i) the acceleration recorded at Castelluccio station (North-South component) of Norcia Mw6.5 earthquake occurred on October 30th; (ii) the East-West component of the acceleration recorded in Amatrice station, close to the epicenter of Accumoli Mw6.0 earthquake occurred on August 24th; (iii) the acceleration recorded at Campi station (North-South component) of Ussita Mw5.9 shock of October 26th (Ubertini et al. 2018). With regard to the Brick House, the first record, scaled with SF=1.25, has been considered as low seismic intensity; the second record has been scaled with SF=1.75, representing a medium seismic intensity; and the last one with SF=2.75 represents a high seismic intensity. Scaled-up acceleration time histories are shown in Fig. 4.11. Some very preliminary results of damage identification on the Brick House can be found in (Kita et al. 2019a).

Taking advantage of the least dispersed IDA curve sets, obtained with PGA, I_C, I_A, S_a(T1), ASI, PGV, S_v(T1) and I_H, and illustrated more in detail in Appendix B.1 (from Fig. B.2 to Fig. B.9), the set of eight (8) IMs has allowed to firstly localize and subsequently quantify earthquake-induced damages. These IMs have been computed from the three seismic records depicted in Fig. 4.11. With reference to part 6 only, Fig. 4.12 illustrates IDA-based estimated damages using IMs contained inside vectors $\mathbf{IM^{*N}}$, $\mathbf{IM^{*A}}$ and $\mathbf{IM^{*U}}$ for
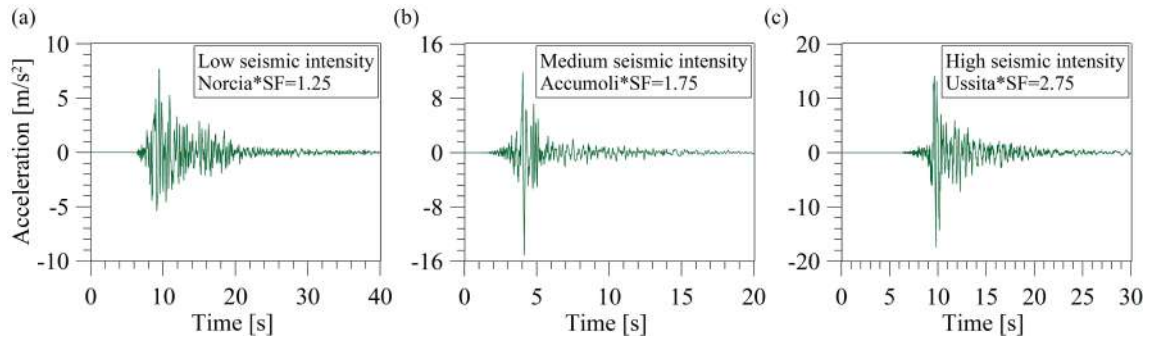
Figure 4.11: Scaled acceleration records of seismic events used for earthquake-induced damage localization and quantification: SF=1.25 scaled-up Norcia earthquake (a), SF=1.75 scaled Accumoli shock (b) and SF=2.75 scaled-up record of Ussita earthquake (c).
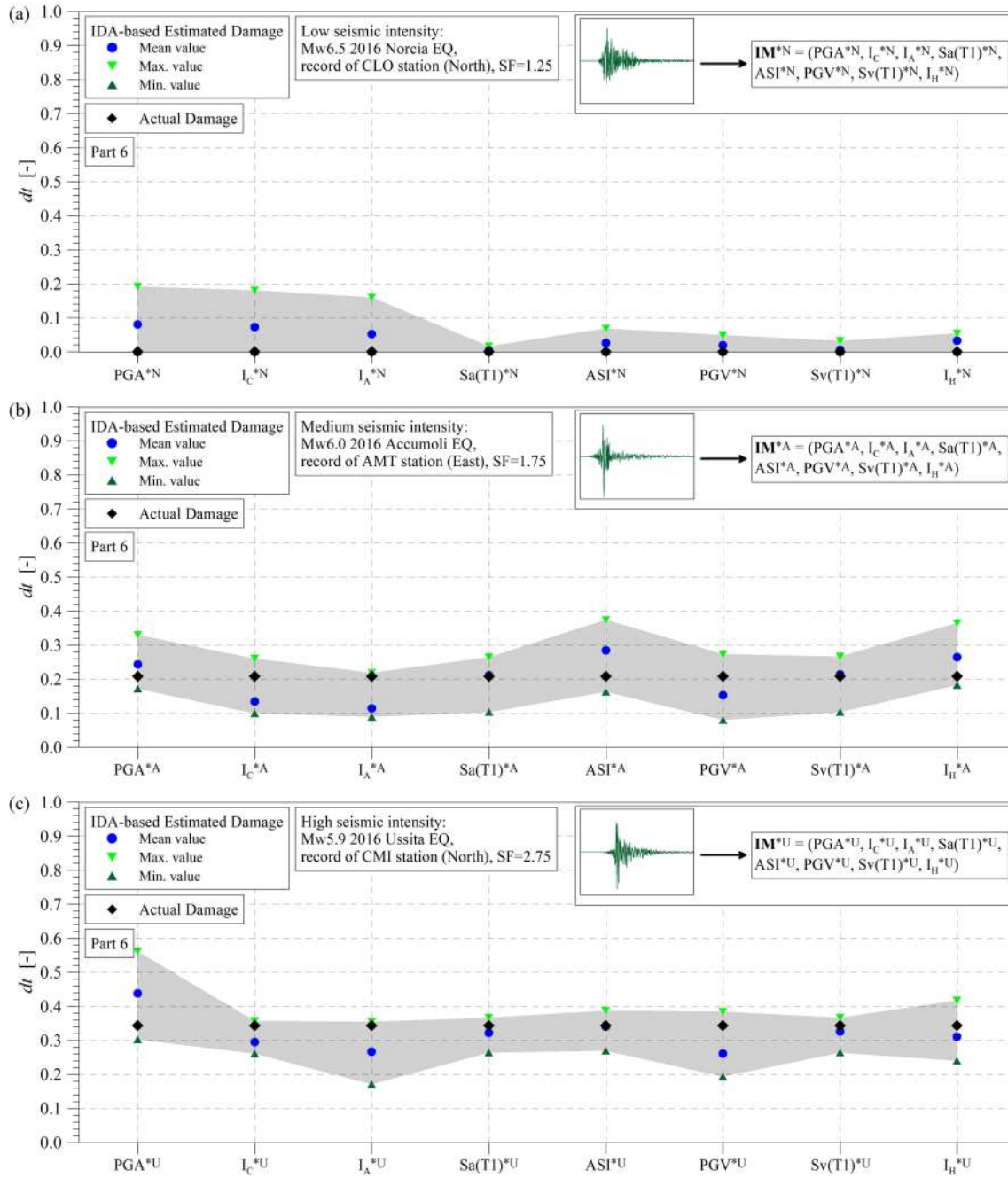
Figure 4.12: Part 6: IDA-based tensile damage (minimum, maximum and mean values) estimated with Norcia, Accumoli and Ussita earthquakes by means of the eight (8) selected IMs into Eq. (4.3). For comparative purposes, actual damage (d_t) is also reported.

Norcia, Accumoli and Ussita, respectively, on the sets of seven (7) curves and the corresponding mean curves (see Eq. (4.3)). IDA-based damages have been estimated in terms of minimum, maximum and mean values, the latter obtained from the mean curve. An IDA-based damage estimation zone, delimited by the minimum and maximum damages obtained with the eight (8) IMs, is highlighted by an infilled area with light grey color. Also, for comparative purposes, actual damages have been reported in the plots. They represent numerically computed mean damage parameters in different portions, in particular, the tensile damages d_t obtained from the non-linear dynamic analyses carried out considering the three seismic records plotted in Fig. 4.11. In general, a relatively good consistency between numerical actual damages and IDA-based ones can be observed. A first important aspect concern the agreement between actual damage and weighted mean IDA-based estimation. Besides consistency between mean values, another important condition regards the estimation of the range of damage, i.e. the difference between the maximum and minimum IDA damage: obviously the smaller the better. As an example, in the case of Ussita earthquake (see Fig. 4.12c), the best consistency between mean damages can be if ASI is used for IDA-based damage estimation. On the other hand, the estimated range of damage is very small using I_C. Both considerations, consistency between mean damages and reduced as much as possible damage ranges, are of particular importance in earthquake-induced damage quantification. In this spirit, the idea of using not all IMs, but carefully selecting only some of them, taking into account a compromise of the aforementioned two considerations, can lead to a better IDA-based damage estimation. For this purpose, IDA-based damages obtained from every single IM have been averaged by using combinations of these IMs, namely Scenarios 1, 2 and 3. Scenario 1 comprises all m^* IMs, while the 2nd and the 3rd combine only some parameters, aiming at reducing the estimated mean ranges and obtaining a better consistency with actual damages.

The abovementioned eight (8) IDA curve sets (obtained with PGA, I_C, I_A, $S_a(T1)$, ASI, PGV, $S_v(T1)$ and I_H) have been considered. The weighting coefficients of the corresponding m^*=8 best IMs, $\alpha_{i,j}$, have been computed as the inverse of $RMSE_{i,j}$ (see Eq. (4.2)), thus depending on the IDA curve sets dispersion. Mean values of IDA-estimated damage obtained from every single IM have been averaged through these weighting coefficients $\alpha_{i,j}$ according to Eqs. (4.4) and (4.5). In this context, by using the set of the m^* IMs in Eq. (4.5), IDA-based tensile damages have been estimated, in terms of weighted average ranges (maximum and minimum) and weighted mean values for all the ten (10) parts of the model. Fig. 4.13 shows IDA-based tensile damages in the case of three earthquakes and three Sce-

narios of combinations of IMs. In general, a good agreement between actual damages and IDA-based estimated damages can be highlighted. The d_t values of the ten (10) regions fall within the corresponding IDA-based estimated average ranges. The proper combinations of only a few IMs (e.g. Scenario 3) have allowed full consistency between actual damages and IDA-based damages for the ten (10) parts of the structure. In addition, for a better understanding of the damage pattern obtained via IDA, contour plots of numerically computed actual damage d_t obtained at the last step of the non-linear dynamic analysis are positioned on the side of each plot, highlighting increasing damage with increasing seismic intensity (contour range from 0 to 1.0). By increasing the seismic intensity from low to high, it is clearly demonstrated that earthquake-induced damages concentrate in specific parts of the structural model, such as parts 7, 5 and 8, whereas parts 1 and 10 present the lowest values of estimated tensile damage (maximum $d_t \leq 0.1$-0.2).

Finally, for a more direct comparison, Fig. 4.14 illustrates weighted mean IDA-based tensile damages plotted versus actual damages, d_t, for the three seismic events for all parts of the model. It can be highlighted that, passing from Scenario 1 to 3, there is a clear trend of improvement in matching, with a closer allocation along the diagonal.
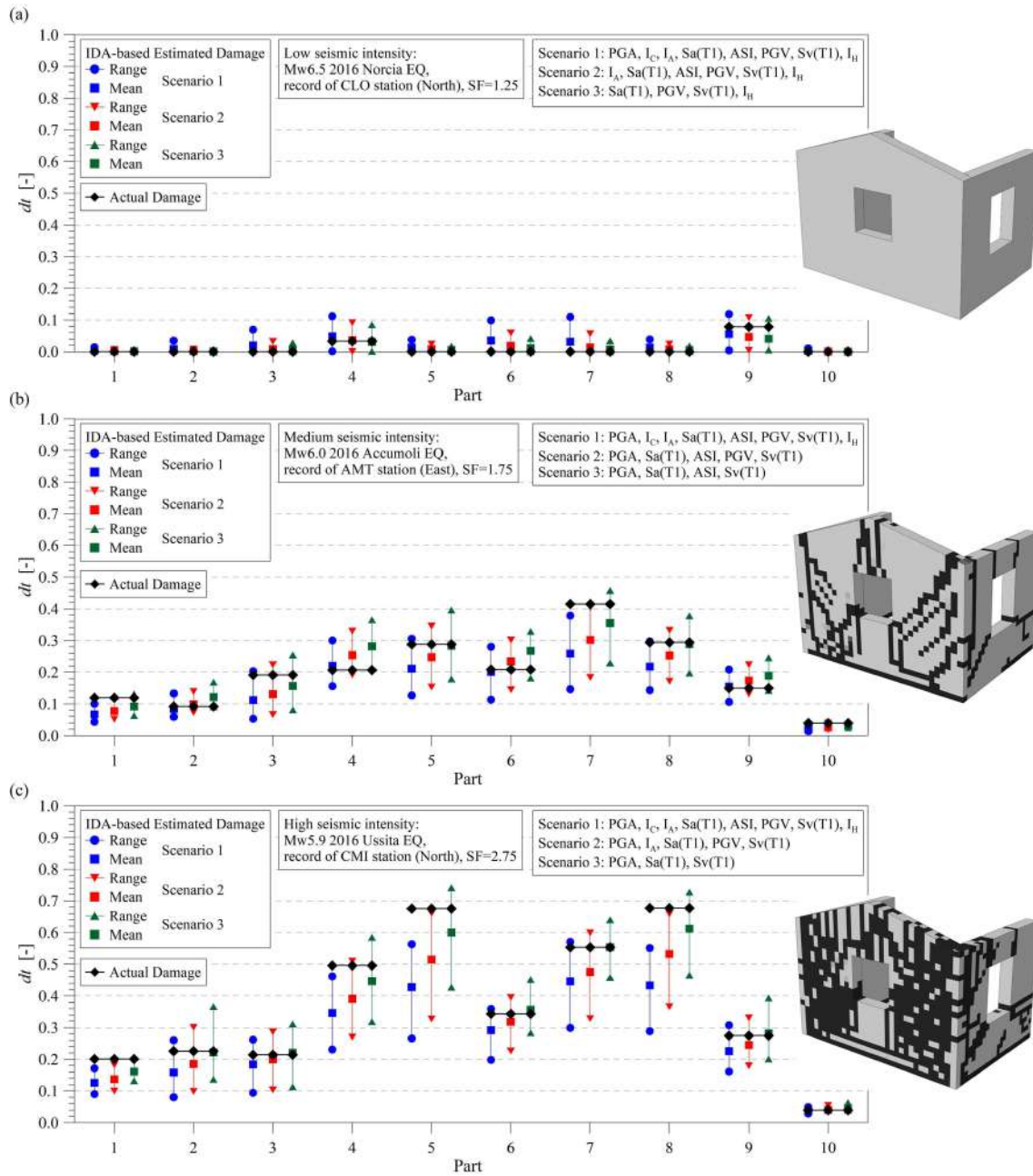
Figure 4.13: Comparison between actual damage (d_t) and IDA-based estimated tensile damage, considering different combinations of IMs for the three selected real ground motion records. Note that IDA-based damage is expressed in terms of weighted average ranges and mean values obtained from the IDA curve sets and corresponding mean curves, respectively.
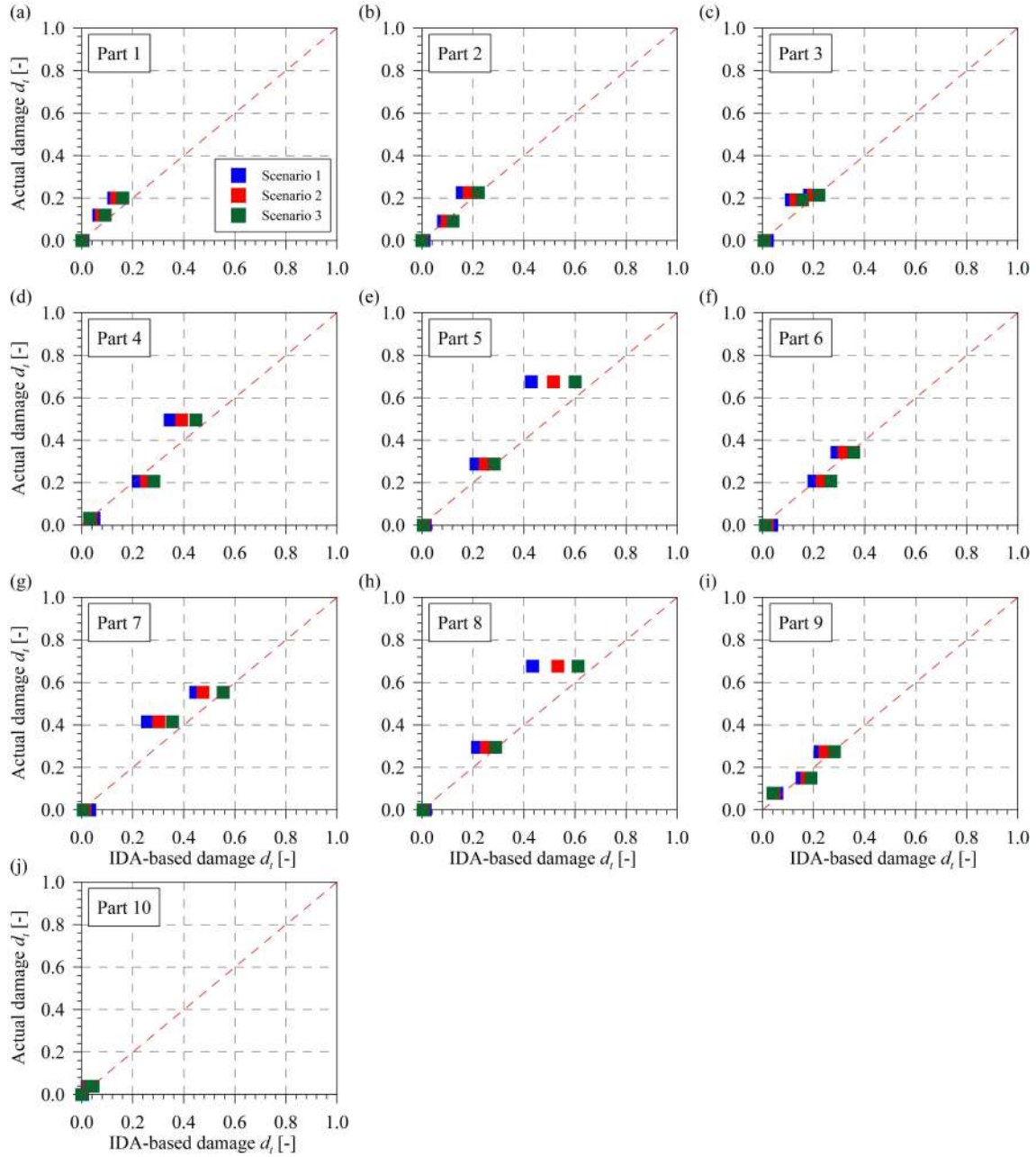
Figure 4.14: Comparison between actual damage (d_t) and weighted mean IDA-based estimated tensile damage, considering different combinations of IMs (Scenarios 1, 2 and 3) for the three selected real ground motion records.

In addition to tensile damage, the same procedure has been applied in the case of first principal plastic strain, $\varepsilon_1^{\mathrm{pl}}$, for IDA-based damage localization and quantification. The least dispersed IDA curve sets, illustrated more in detail in Appendix B.1, have been considered. The set of eight (8) IMs has allowed to firstly localize and subsequently quantify earthquake-induced first principal plastic strain damages. With reference to part 6 only, after applying Eq. (4.3), Fig. 4.15 illustrates IDA-based estimated damages, in terms of minimum, maximum and mean values, the latter obtained from the mean curve. Both aspects, agreement between actual damage and weighted mean IDA-based estimation as well as the minimum possible estimated damage range, have been taken into account also for first principal plastic strain as DM. As an example, in this case, considering the Ussita earthquake (see Fig. 4.15c), the best consistency between mean damages can be if I_C is used for IDA-based damage estimation. On the other hand, the estimated range of damage is very small using PGV. Subsequently, by carefully using only some of IMs (Scenarios 1, 2 and 3) a better IDA-based damage estimation has been achieved. Considering weight coefficients $\alpha_{i,j}$, (see Eq. (4.4)), averaged mean values of IDA-based first principal plastic strain damages have been estimated, in terms of weighted average ranges and weighted mean values for all the ten (10) parts of the model.

After applying Eq. (4.5), Fig. 4.16 shows IDA-based estimated first principal plastic strains against $\varepsilon_1^{\mathrm{pl}}$ actual damages obtained from the non-linear dynamic analyses carried out with the three seismic records of the 2016 Central Italy seismic sequence. Also in the case of $\varepsilon_1^{\mathrm{pl}}$, a good agreement between actual damages and IDA-based estimated damages can be highlighted, as well as proper combinations of only a few IMs have allowed full consistency for the ten (10) parts of the structure. Contour plots of $\varepsilon_1^{\mathrm{pl}}$ actual damage are illustrated in the same figure, highlighting increasing damage with increasing seismic intensity (contour range from 0 to 0.045). Fig. 4.16 further confirms that part 7 (top gable) is the most damaged portion of the model, while parts 1 and 10 are the safest ones. Both in the case of d_t and $\varepsilon_1^{\mathrm{pl}}$, the estimation of weighted average ranges and mean values resulted to be more accurate than the simple average estimation (not weighted), due to narrower damage ranges themselves.

Fig. 4.17 concludes the results illustrating weighted mean IDA-based $\varepsilon_1^{\mathrm{pl}}$ plotted versus actual damages, for the three seismic events for all parts of the model. Switching from Scenario 1 to 3, there is a clear trend of improvement in matching, with a closer allocation along the diagonal.
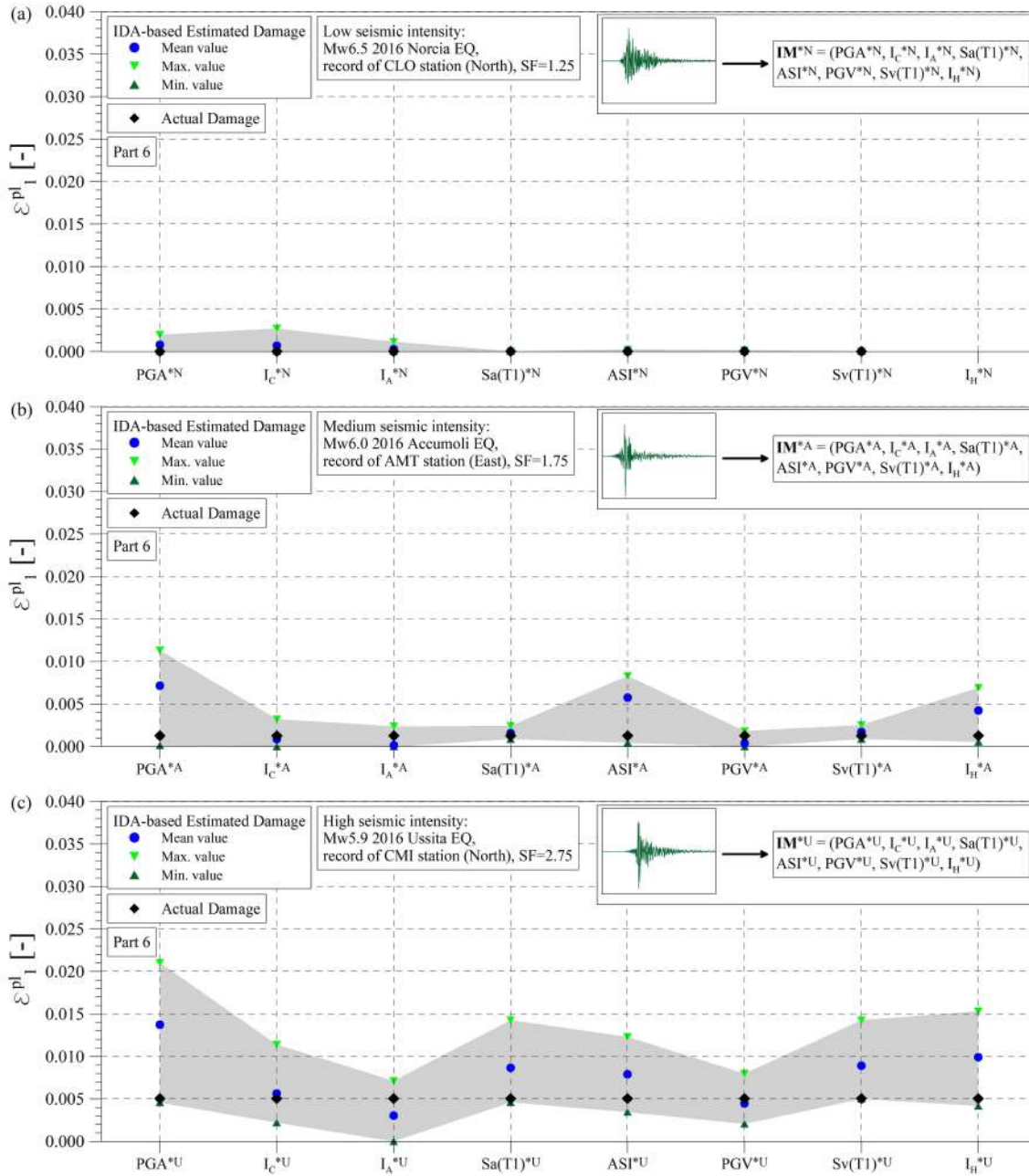
Figure 4.15: Part 6: IDA-based first principal plastic strain ($\varepsilon_1^{\mathrm{pl}}$) (minimum, maximum and mean values) estimated with Norcia, Accumoli and Ussita earthquakes by means of the eight (8) selected IMs into Eq. (4.3). For comparative purposes, actual damage is also reported.
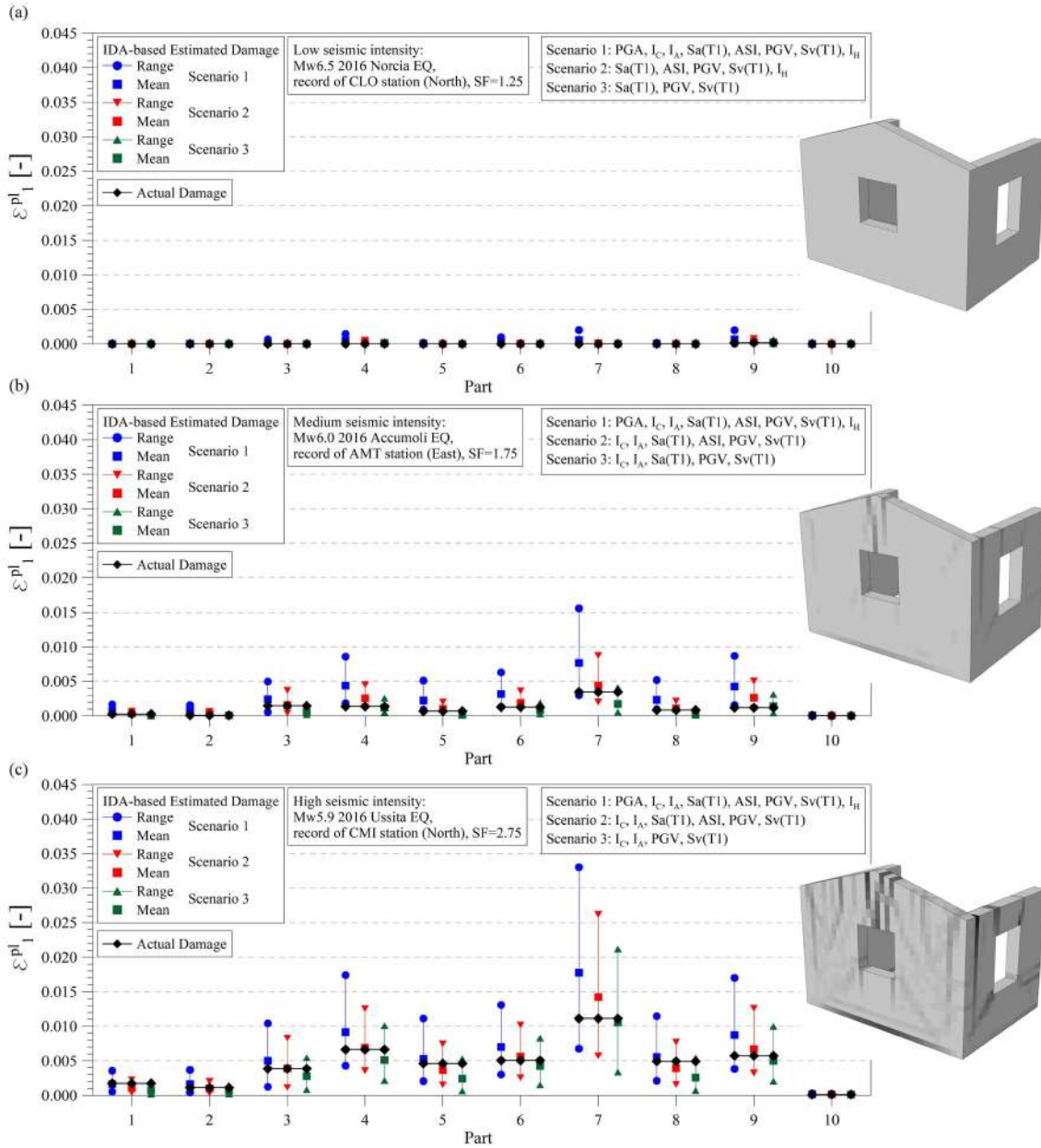
Figure 4.16: Comparison between actual damage and IDA-based estimated first principal plastic strain $(\varepsilon_1^{\mathrm{pl}})$, considering different combinations of IMs for the three selected real ground motion records. Note that IDA-based damage is expressed in terms of weighted average ranges and mean values obtained from the IDA curve sets and corresponding mean curves, respectively.
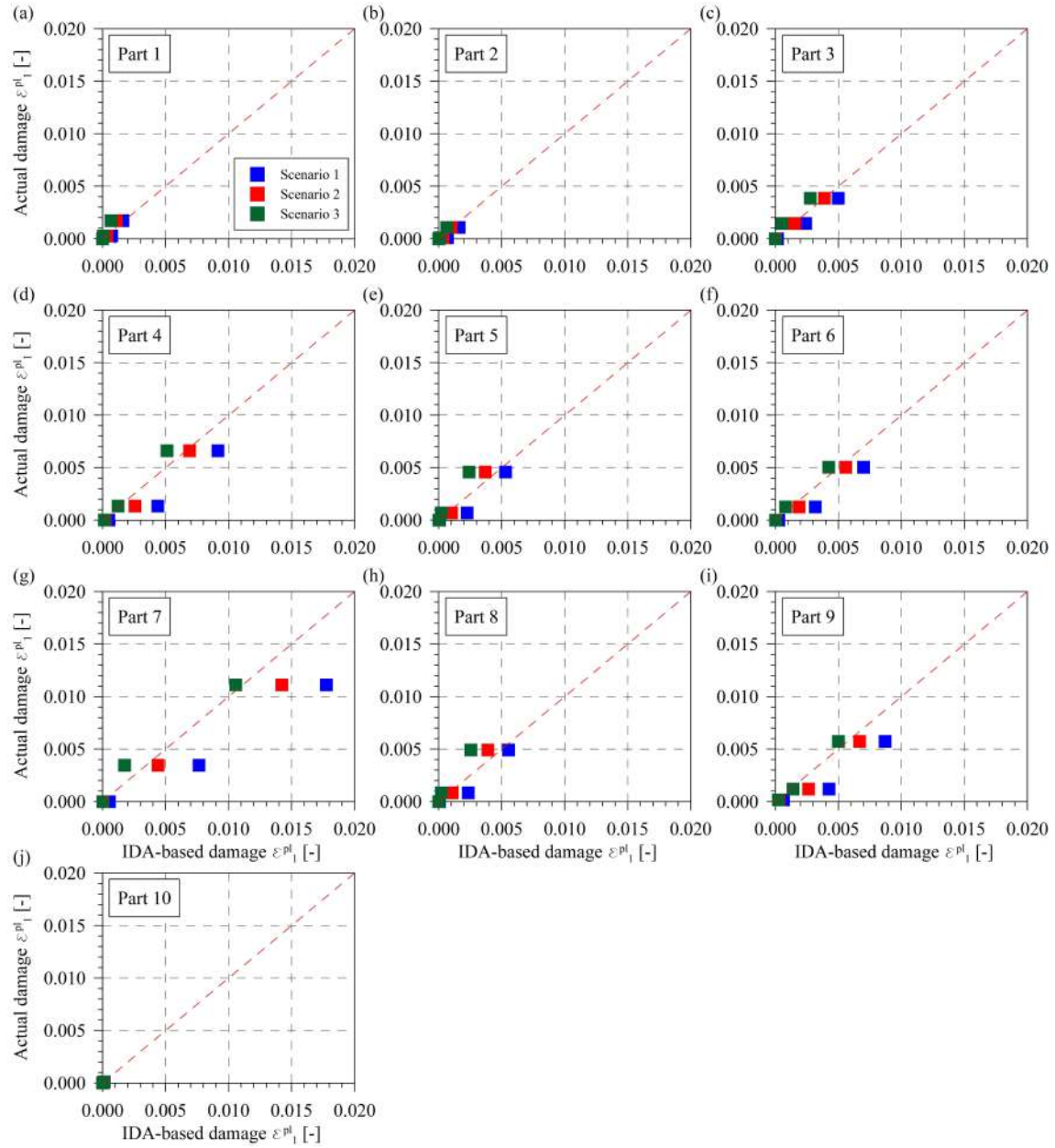
Figure 4.17: Comparison between actual damage $(\varepsilon_1^{\text{pl}})$ and weighted mean IDA-based estimated first principal plastic strain, considering different combinations of IMs (Scenarios 1, 2 and 3) for the three selected real ground motion records.

4.5   Conclusions

An innovative IDA-based method aimed at rapid localization and quantification of earthquake-induced damages in masonry structures has been presented. It is based on Incremental Dynamic Analysis carried out from a numerical model and using data recorded during seismic events. In particular, the method relies on an a priori construction of multidimensional IDA curve sets relating meaningful local damage parameters to selected seismic intensity measures such that, when an earthquake occurs, IMs computed from the seismic data (e.g. the base acceleration and/or seismic response measured by the monitoring system installed on the structure or measurements from a nearby seismic station) are used and local damage conditions are immediately estimated using the mathematical relation obtained through multidimensional IDA analysis. It is numerically validated through application to a reduced-scale masonry structure, the Brick House, which represents a notable benchmark, object of previous studies by several authors.

The main results are summarized below.

- Full consistency between numerical and experimental response accelerations of the benchmark case study has been obtained, together with a good agreement between FE numerical damage pattern and mock-up collapse mechanism.

- Statistical correlation analysis has allowed an investigation on the intensity measures' interdependence, and subsequently a first selection, passing from a large to a limited number of uncorrelated independent parameters.

- Ten (10) IDA curve sets, one for every part of the FE model, have been constructed considering tensile damage, plastic strain magnitude and first principal plastic strain as damage measures.

- The dispersion of IDA curves has been investigated, allowing a second refined selection of the most efficient intensity measures: Peak Ground Acceleration, Characteristic Intensity, Arias Intensity, Spectral Acceleration, Acceleration Spectrum Intensity, Peak Ground Velocity, Spectral Velocity and Housner Intensity.

- A more in-depth investigation of the dispersion, by means of the root mean square errors of the IDA curve sets, has allowed identifying the best intensity parameters for the specific damage measures considered, in the case of tensile damage (Acceler-

ation Spectrum Intensity and Housner Intensity) and for first principal plastic strain (Characteristic Intensity and Arias Intensity).

- Non-linear IDA results have enabled to localize damage mostly in parts 7, 5, 8 (façade wall), as well as in part 4 (sidewall with opening) of the Brick House numerical model, in agreement with the damage observed experimentally. Tensile damage seems conceptually more adequate for damage characterization and localization.

- Considering three acceleration records of the 2016 Central Italy seismic sequence, IDA curves have been found suitable for earthquake-induced damage localization and quantification for the ten (10) parts of the structural model with an acceptable level of approximation. An overall weighted average estimation of damage ranges and mean values have been achieved by means of weighting coefficients depending on the IDA curve sets dispersion. The consistency between actual damages and weighted mean IDA-based values, as well as the desirable as small as possible IDA-based damage ranges, have been considered reasonable for damage quantification. Three scenarios resulting from different combinations of IMs have been taken into account, allowing to obtain a good agreement with damages obtained via the non-linear dynamic analyses.

The results demonstrate that the proposed seismic IDA-based SHM procedure is capable of rapidly and correctly localizing and quantifying earthquake-induced damage, thereby showing great potential for damage assessment of masonry structures in the context of monitoring for preventive conservation of architectural heritage.

Chapter 5

IDA-based damage identification in the San Pietro Bell Tower

In this Chapter, the application and validation of the proposed IDA-based method described in Section 4.2 are presented with reference to a medieval monumental CH masonry building: the bell tower of the Basilica of San Pietro in Perugia, Italy. Section 5.1 presents the case study, including a brief overview of the bell tower, with historical background, as well as the geometrical and material survey. In addition, the main aspects of the assessment of the bell tower after the 2016 Central Italy seismic sequence, with focus on the vibration-based earthquake-induced damage detection, are introduced. Section 5.2 is devoted to presenting the results on earthquake-induced damage localization and quantification via non-linear seismic IDA, highlighting, in particular, the belfry as the most damaged (damageable) structural portion of the bell tower. For this purpose, seismic input, as well as seismic response intensity measures are successfully exploited. Earthquake-induced damages for the three parts of the San Pietro structural model, are localized and quantified in terms of overall weighted average estimation of damage ranges and mean values. Main conclusions are finally summarized in Section 5.3.

5.1 Introduction to the case study

Historic masonry towers are very common CH buildings in Italian cities. They are usually slender structures subjected to significant dead loads, so that they might exhibit high sensitivity to dynamic actions, such as swinging of bells, traffic-induced micro-tremors, wind and most important, earthquakes. The monumental bell tower of the Basilica of San Pietro dates back to the 13th century and due to its historical and architectural value, it is considered to be one of the major symbols of the city of Perugia (see Fig. 5.1). The structure was subjected to several structural and architectural interventions throughout the centuries: (i) between 1387 and 1393 it was completely demolished and rebuilt as a defensive tower, (ii) radical restoration was carried out in the 15th century, leading to its final design in the beautiful Florentine Gothic style attributed to Bernardo Rossellino, (iii) a metallic structure supporting the bells was added in 1932, conceivably to reduce the levels of vibration of the tower under the action of the swinging bells, (iv) the last intervention was carried out in 2002 (Vetturini 2014) after damages caused by the Umbria-Marche earthquake occurred in 1997 (Cattaneo et al. 2000), damages concentrated in the belfry (severe cracks at the base of the columns and diffused cracking on the external walls) and
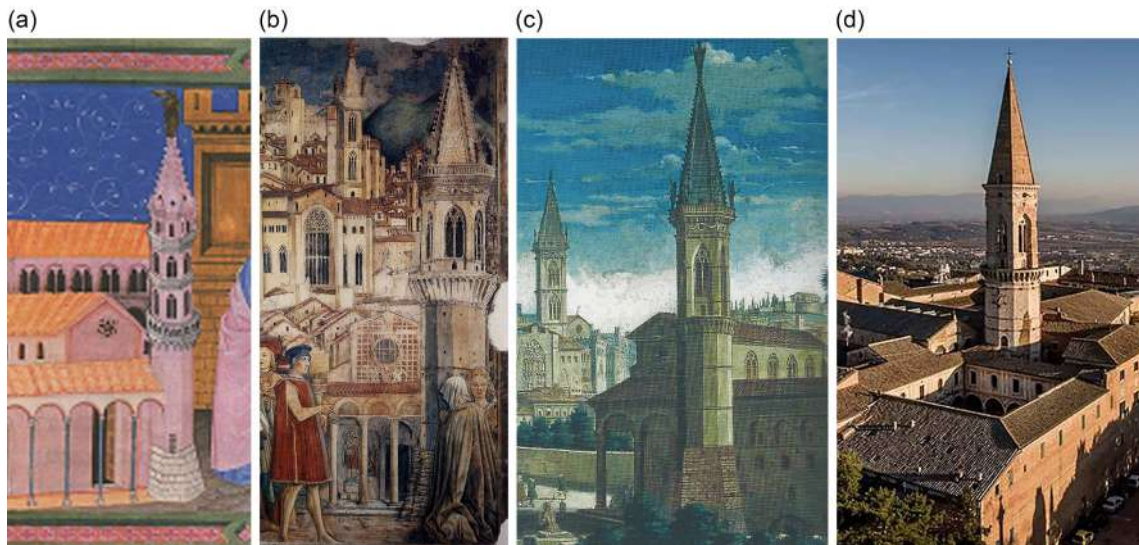
Figure 5.1: The bell tower of the Basilica of San Pietro over the centuries, historic paintings and today: Matricola of the Collegio del Cambio by Matteo di Ser Cambio in 1377 (a), painting inside Palazzo dei Priori in Perugia by Benedetto Bonfigli showing translation of the corpse of St. Ercolano toward the church of San Pietro (1455–1479) (b), painting by Gaspar van Wittel of 18th century (c) and aerial view today (d).

the cusp. Fig. 5.1 shows the historical evolution of the bell tower through three medieval paintings and a current aerial view. Today, it is in a good state of preservation without any significant and visible damage. No damages were observed after the major earthquakes occurred in Italy in recent years: L'Aquila Earthquake, 2009, Emilia Earthquake, 2012, and Central Italy seismic sequence, 2016 (Chiaraluce et al. 2017; Cattari et al. 2019).

The bell tower has a total height of 61.45 m and is restrained up to the first 17 m by the surrounding Basilica, main cloister and convent. The structure can be subdivided in three main structural parts: (i) the shaft, (ii) the belfry and (iii) the cusp (see Fig. 5.2 and Fig.
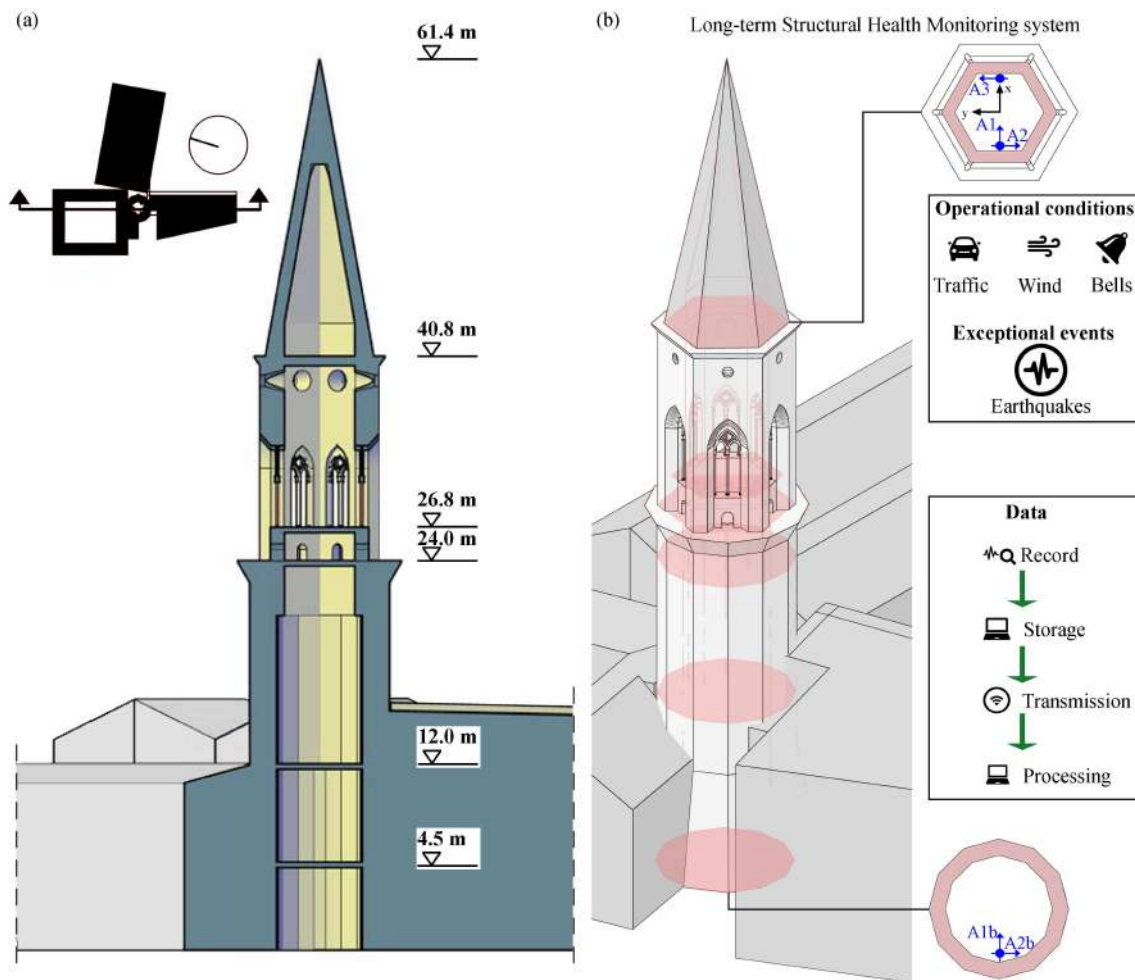
Figure 5.2: Cross-section and heights of significant structural parts of the San Pietro Bell Tower (a) and scheme illustration of the permanent SHM system (b).

119

5.5). The shaft has a dodecagonal cross-section, the belfry an hexagonal cross-section while the cusp completes the tower on the top and has the shape of a pyramid with hexagonal base. The belfry is architecturally characterized by large Gothic openings presenting external frames and columns made of mixed travertine-calcareous stone masonry with some brick replacements. Fig. 5.2a represents a solid representation of the structure consisting of a sectional view, where the three aforementioned structural portions are clearly visible. The shaft is characterized by thick walls made of regular calcareous stone masonry blocks. The external surface of the belfry, including its columns, is made of mixed travertine-calcareous stone masonry with some brick replacements, while the internal surface is made of brick masonry. Finally, the cusp consists of mixed travertine-calcareous stone masonry with an external cover in brick masonry (Ubertini et al. 2016; Cavalagli et al. 2018; Ubertini et al. 2018).

The dynamic behavior of the tower was assessed by means of an AVT carried out on February 15th 2015, which allowed identifying the first seven (7) modes of vibration (natural frequencies, damping ratios and mode shapes) of the structure in the range from 0 to 8 Hz (Ubertini et al. 2016). Afterwards, with the purpose of monitoring the structural integrity of the bell tower and of promptly detecting damages caused by low-return period earthquakes, a simple low-cost vibration-based SHM system was installed in the tower for preventive conservation and CBM, currently active since December 9th 2014. Fig. 5.2b shows the configuration of the permanent vibration-based SHM system: three high-sensitivity uni-axial piezoelectric accelerometers (model PCB 393B12 with 10 V/g sensitivity) are installed at the base of the cusp and two others at the basement (on the ground level). In addition, two temperature sensors (K-type thermocouples, one at the base of the belfry and one at the base of the cusp) and various environmental monitoring sensors were also installed and included in the monitoring system since October 2015. The data acquisition system is located inside the tower and connected via the INTERNET to a dedicated remote server in the Laboratory of Structural Dynamics of the Department of Civil and Environmental Engineering of the University of Perugia, where continuous data are processed through an *ad hoc* developed MatLab code, using each stored 30-minute windows for automated modal identification.

The analysis of continuous dynamic monitoring data highlighted the main characteristics of the response of the tower to wind, swinging bells and low return period earthquakes. Despite the very low levels of vibration in operational conditions, five (5) modes are suc-

cessfully and continuously identified in most of the data sets. Fig. 5.3 shows the time histories of the natural frequencies identified since the beginning of the monitoring, for about five (5) years, every 30 minutes, using a fully automated SSI output-only modal identification technique (Ubertini et al. 2013). Significant seasonal increases from winter to summer conditions, as well as daily fluctuations, are clearly visible in the plots and are conceivably associated with changes in environmental conditions, primarily in ambient temperature (Ubertini et al. 2017).

The adopted SHM procedure for the San Pietro Bell Tower comprises four (4) consecutive steps, as sketched in Fig. 2.1. A fully automated vibration-based SHM procedure was implemented. It is based on output-only fully automated modal parameters tracking and on a multivariate statistical analysis criterion for damage detection. All five (5) modal frequencies, first tracked and then cleansed, are used to build the statistical models for novelty analysis (see Section 2.1), in order to detect anomalous deviations from normal
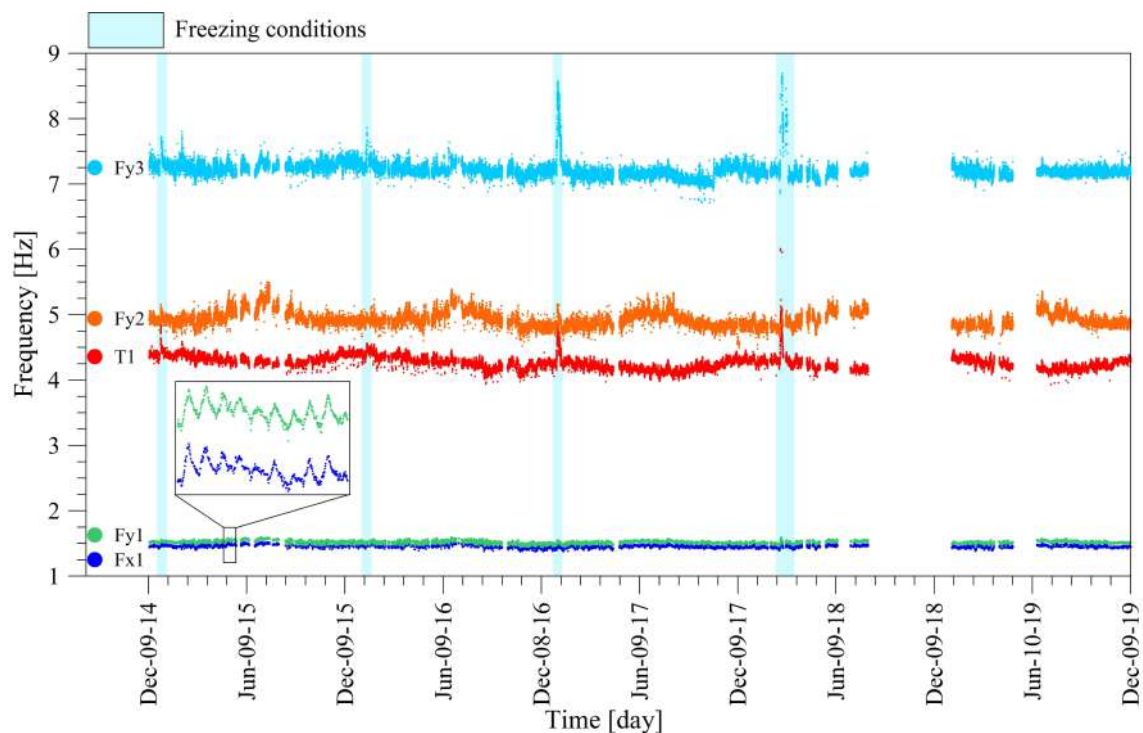
Figure 5.3: Plots of five (5) years continuously identified natural frequencies of the San Pietro Bell Tower since December 2014 (daily fluctuations are also evidenced with a detailed view).

conditions, thus, revealing changes in the structural behavior. The procedure comprises SSI-based automated modal identification, modal tracking, removal of environmental and operational effects from identified modal frequencies and damage detection (see Fig. 2.1). The removal of environmental effects (temperature and humidity) is carried out via a multivariate statistical analysis technique based on MLR. Damage detection is accomplished by application of the tool of control charts based on a well-known statistical distance and with one year of data as a training period. Despite the presence of significant environmental effects on identified natural frequencies of the San Pietro Bell Tower (Ubertini et al. 2017), the proposed SHM method proved effective in detecting very small stationary variations in identified modal frequencies and automatically revealing any anomaly in the structural behavior, typically occurring after an earthquake and possibly related to a developing damage pattern (Ubertini et al. 2016; Ubertini et al. 2017; Cavalagli et al. 2018; Ubertini et al. 2018; Giordano et al. 2019).

The vibration-based SHM system allowed an automated rapid earthquake-induced damage detection of the bell tower after the main shocks of the 2016 Central Italy seismic sequence. Despite the relatively low intensity of the sequence in Perugia (due to the distance from the epicenters equal to about 80 km) and no clear relevant structural damages were observed in any part of the structure, above all in the belfry, the analysis of long-term monitoring data clearly highlighted that small permanent changes in the structural behavior of the bell tower occurred after the earthquakes, with decreases in all identified natural frequencies (Ubertini et al. 2018; Giordano et al. 2019). Such natural frequency decays were fully consistent with what predicted by non-linear finite element simulations and, in particular, with the development of microcracks at the base of the columns of the belfry. Moreover, besides consistent decays in natural frequencies, the long-term vibration-based SHM clearly detected earthquake-induced damage through control charts. The control chart, built according to Eq. (2.2) by using five (5) years of time series of identified natural frequencies after removal of the effects of changing environmental conditions (Eqs. (2.1) and (2.4)), is illustrated in Fig. 5.4. A clear deviation of the structural behavior from normal conditions can be highlighted after Accumoli earthquake, with a notable increase in the relative frequency of outliers, and also later after Ussita and Norcia shocks. In the present case, it can be associated to small damages induced by the three earthquakes, consisting of microcracks at the base of the columns of the belfry, as well as in some key sections of the pointed arches in the same structural portion. Microcracks in these regions are however hardly distinguishable from pre-existing ones and from the physiological
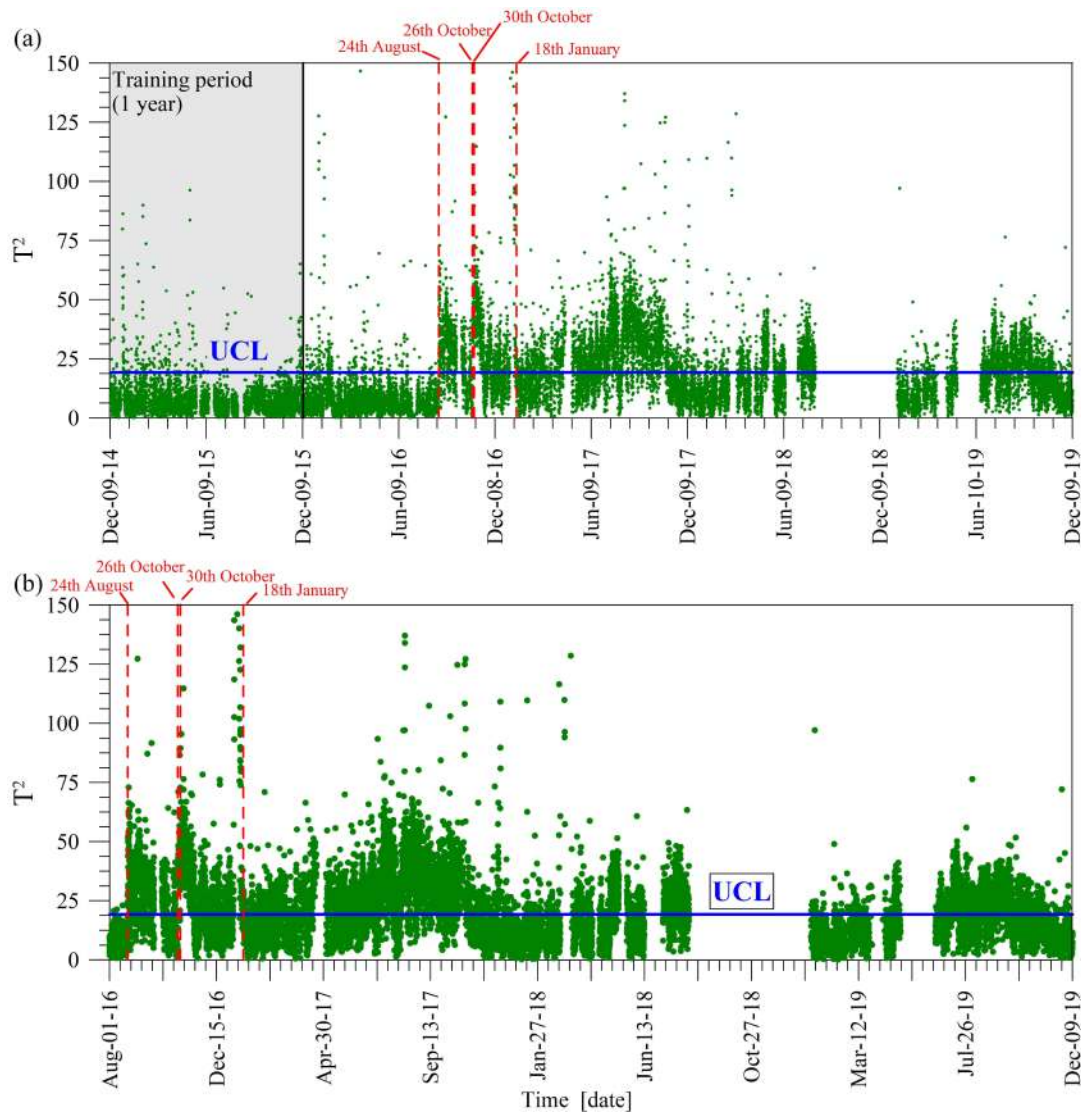
Figure 5.4: Control chart of five (5) years of monitoring period (a) and detailed view showing increased number of outliers after the three main shocks of the 2016 Central Italy seismic sequence (b).

cracking of a masonry structure, which validates the effectiveness of the SHM system in detecting earthquake-induced damage at a stage where this is not yet detectable by visual inspections (Ubertini et al. 2018). The implemented vibration-based continuous monitoring system in the San Pietro Bell Tower resulted in a low-cost tool for automated rapid earthquake-induced damage detection for a full-scale structure, even at an early stage, thus contributing to condition-based maintenance and cost-effective preservation.

123

In order to carry out non-linear incremental dynamic analyses, a detailed 3D numerical model of the structure has been built in the framework of the Finite Element Method (FEM) by using solid hexahedral and tetrahedral elements, in the ABAQUS 6.10 platform (Simulia 2010). In particular, a structured mesh has been adopted in the shaft and the basement regions, while a free mesh has been employed in the belfry and the cusp (see Fig. 5.5). At the constitutive level, the model of the tower has been subdivided into three regions: the shaft, the belfry and the cusp. Stones and brick masonry in different portions of the structure have been modeled as homogeneous and orthotropic, with different mechanical properties depending on the material and texture detected in the various parts of the structure. Such modeling strategy has been exploited in order to obtain a more accurate calibrated model, particularly, in terms of mode shape's consistency (Lourenço 2002). The numerical model has been calibrated by varying the values of uncertain mechanical
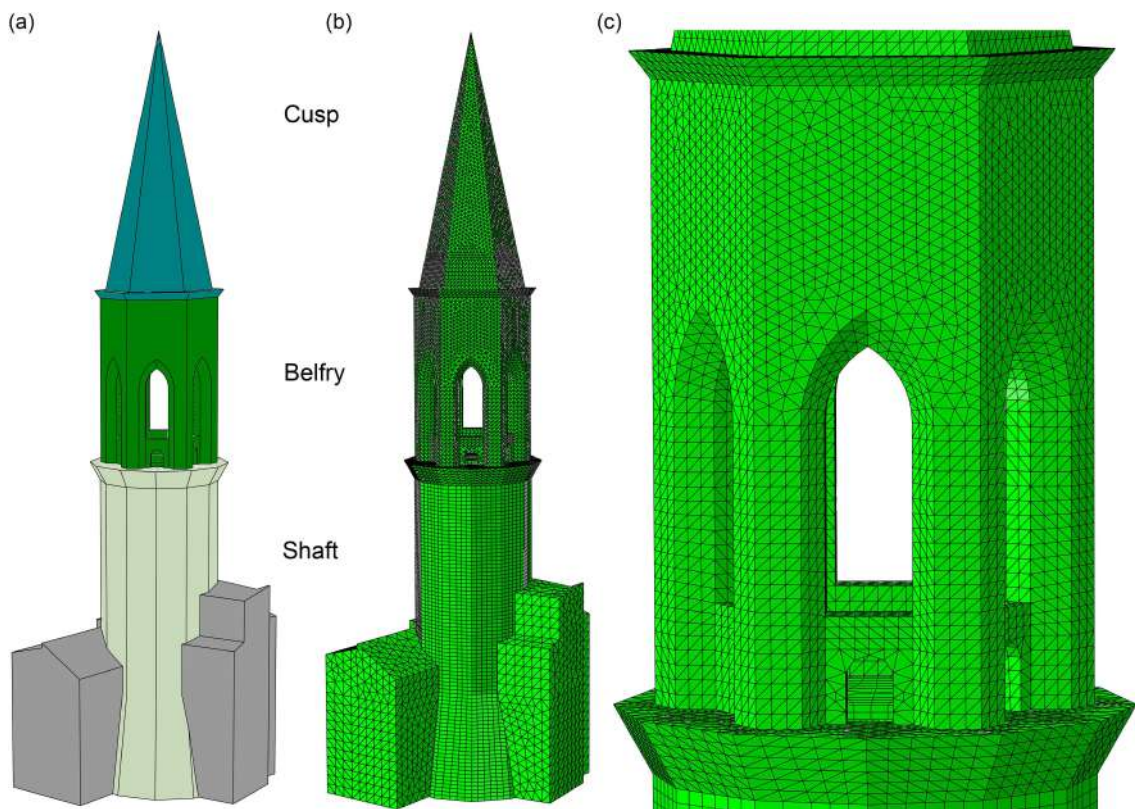
Figure 5.5: Parts of the numerical model defined for damage localization purposes through IDA: Shaft, Belfry and Cusp (a), mesh discretization of the FE numerical model of the San Pietro Bell Tower (b) and detailed view of mesh on the Belfry (c).

parameters through a modal sensitivity analysis and a proper optimization procedure, and on the basis of the experimentally identified natural modes of vibration, in particular, using natural frequencies at the reference temperature of 20°C as the target frequencies (Cavalagli et al. 2018). In order to obtain consistency between numerically and experimentally identified mode shapes, also a proper modeling of the restraints given by the neighboring constructions in the lower part of the bell tower and, primarily, the basilica and the abbey, was found to be crucial. It is worth noting that there is an excellent agreement between experimentally identified natural frequencies at the reference temperature of 20°C ($f_{20°C}$) and numerical ones predicted by FEM analysis (f_{FEM}), with an average relative difference, Δf_{mean}, between the two quantities lower then 3%. For more details on the model and the calibration procedure, the interested reader is referred to (Cavalagli et al. 2018).

The main tuned mechanical parameters of the constituent materials (Young's modulus E, shear modulus G, Poisson's ratio ν and specific weight γ) are summarized in Tab. 5.1. Above all for running numerical non-linear analysis, FEM materials have been modeled with isotropic constitutive behavior. This modeling assumption allows to release the mutual dependence of E, G and ν. In this context, independent values of E, G and ν, have been assigned without any directional criterion (E11=E22=E33=E, G12=G23=G13=G) in order to achieve good results without losing simplicity and accuracy of the FE model (Gentile et al. 2015).

The CDP model (Section 3.3.2, Fig. 3.8) has been also adopted in the case of the San Pietro Bell Tower allowing to perform non-linear seismic incremental dynamic analyses. The use of such a damaging model has required the adoption of an isotropic formulation for the material. It is worth noting that CDP masonry strength parameters have been earlier estimated on the basis of a sensitivity analysis on the input variables required for the constitutive models to define the failure surfaces and the post-peak behavior. For this

Table 5.1: Mechanical parameters assumed in the San Pietro Bell Tower FE model after calibration.

Structural part	E [kN/m^2]	G [kN/m^2]	ν [-]	γ [kN/m^3]
Shaft	4.274E+06	1.238E+06	0.25	26.0
Belfry	4.335E+06	1.787E+06	0.25	17.5
Cusp	1.800E+06	0.563E+06	0.25	18.9

purpose, the good agreement between the damage scenario observed on the structure after the Umbria-Marche seismic event of 1997 and the same damage predicted by the numerical model using the seismic record of the same earthquake have allowed a reliable estimation of strength parameters (Cavalagli et al. 2018). The CDP material properties are summarized in Tab. 5.2, in terms of tension stiffening and tension damage. The description of the failure condition and of the post-peak behavior depends upon the tensile stresses, σ_t, the cracking strains, $\tilde{\varepsilon}_t^{\mathrm{ck}}$, and the tensile damage variable, d_t. The behavior of the masonry has been reproduced up to the ultimate limit state, considering damage in tension only.

Table 5.2: Uniaxial stress–strain (tension stiffening) and scalar tensile damage values utilized in the three parts of the numerical model.

Shaft			Belfry			Cusp		
σ_t [kN/m^2]	$\tilde{\varepsilon}_t^{\mathrm{ck}}$ [$-$]	d_t [$-$]	σ_t [kN/m^2]	$\tilde{\varepsilon}_t^{\mathrm{ck}}$ [$-$]	d_t [$-$]	σ_t [kN/m^2]	$\tilde{\varepsilon}_t^{\mathrm{ck}}$ [$-$]	d_t [$-$]
400	0.00E-00	0.00	220	0.00E-00	0.00	220	0.00E-00	0.00
300	1.75E-04	0.55	140	7.39E-05	0.45	140	1.66E-05	0.55
210	3.77E-04	0.80	70	1.65E-04	0.60	70	3.86E-04	0.70
40	7.59E-04	0.90	20	2.44E-04	0.90	20	5.83E-04	0.90

5.2   IDA-based earthquake-induced damage localization and quantification

5.2.1   Seismic input selection

As already introduced in Section 4.1, seismic input selection represents a key issue in non-linear dynamic analysis of structures. Certainly, among different types of acceleration time-histories, natural accelerograms are the best for seismic action representation. The increasing presence of numerous online databases of strong-motion records has shifted the focus mainly towards the use of natural accelerograms. A suite of ground motion records is used also in the case of the San Pietro Bell Tower, aimed at covering a full range of responses and with different seismic characteristics in terms of amplitude, energy or frequency content.

The seismic input for IDA of structures is usually defined in terms of acceleration time series whose response spectra result compatible with a specific target response spectrum. The implementation of code provisions for record selection can be very useful. To address this issue, the commercial software REXEL was developed to provide computer-aided ground-motion selection, consistent with the design spectrum and seismic hazard at the site of interest (Iervolino et al. 2009). It is a tool for the selection of ground-motion records, in particular, the automatic selection and scaling of spectrum compatible ground-motions for dynamic analysis of structures (available at the website of the Rete dei Laboratori Universitari di Ingegneria Sismica, ReLUIS – www.reluis.it). REXEL allows the search for combinations of compatible natural accelerograms, in other words, record sets matching either user-defined target spectra or design spectra according to the Italian technical standard code, NTC08 and NTC18 (NTC08 2008; NTC18 2018), and the EC8. The REXEL accelerometric recordings rely on several databases: the ITalian ACcelerometric Archive (ITACA), the European Strong Motion Database (ESD) and Selected Input Motions for Displacement-Based Assessment and Design (SIMBAD).

In the case of the San Pietro Bell Tower, seven (7) natural spectrum-compatible seismic groups of accelerograms (two horizontal components) have been obtained by REXEL and used as seismic inputs for non-linear incremental dynamic analysis. As stated in Section 4.1, natural accelerograms (earthquake records) represent the best ones for running IDA. After a search on the ITACA database by REXEL, Fig. 5.6 shows the combination of fourteen (14) spectra compatible with the site of the bell tower, compared to the Perugia
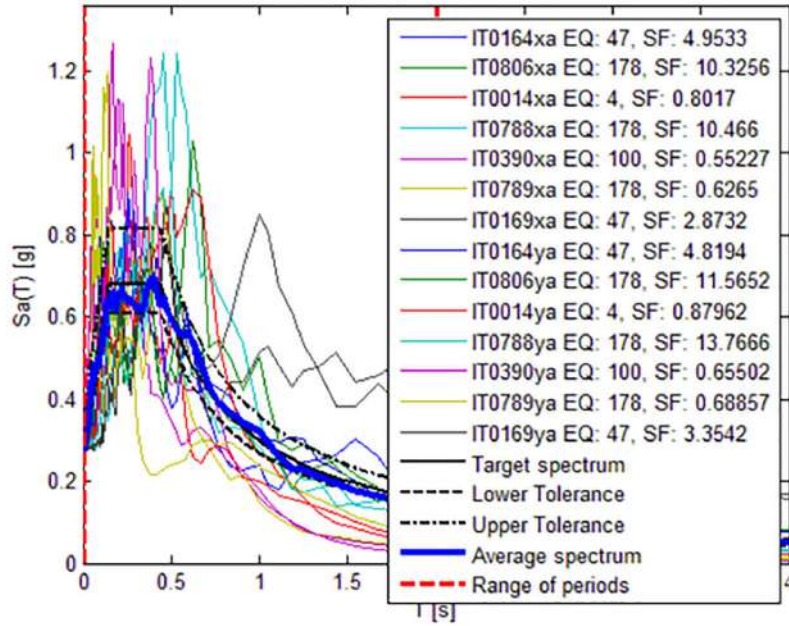
Figure 5.6: Plots of fourteen (14) response spectra compatible with the target response spectrum (site of the San Pietro Bell Tower). Average spectrum is depicted in blue thick line.

target elastic response spectrum, the latter generated according to NTC08. The Perugia site conditions and the other parameters necessary to define the target response spectrum related to the Ultimate Limit State have been taken into account. As displayed in the plot, there is a good consistency between the target and the average spectrum of the seven (7) groups of accelerograms found by REXEL. The corresponding spectrum-matched accelerograms are defined in terms of two-components acceleration time series whose response spectra result compatible with the Perugia (bell tower site) response spectrum.

The main original characteristics of the seven (7) natural selected ground motions used for IDA on the San Pietro Bell Tower are synthesized in Tab. 5.3, while the time histories of the corresponding unscaled spectrum-matched acceleration time histories (both horizontal components) are plotted in Fig. 5.7. It is worth noting that the present seismic loading is bidirectional, whereby components are applied in the two horizontal directions to the FE model of the bell tower: x component in East-West and y in North-South direction. They have been scaled at increasing levels for IDA by means of appropriate SFs synthesized in Tab. 5.4 (λ, $\mathbf{a}_\lambda = \lambda \cdot \mathbf{a}_1$, as suggested in (Vamvatsikos and Cornell 2002)).
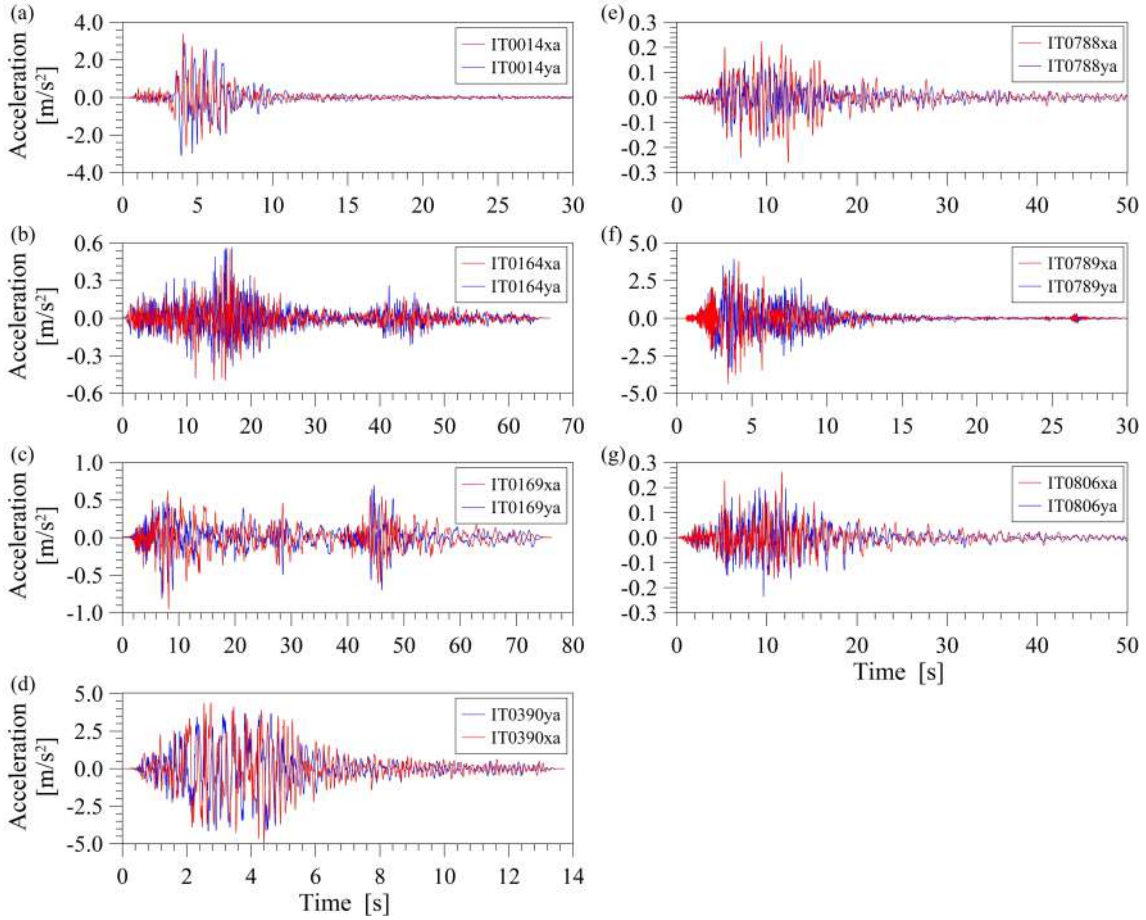
Figure 5.7: Plots of the seven (7) spectrum-compatible unscaled seismic records (acceleration time series) used for IDA of the San Pietro Bell Tower: x component is input in East-West direction while y in North-South direction.

Table 5.3: Main characteristics of strong ground motions used for Incremental Dynamic Analysis of the FE model of the San Pietro Bell Tower.

EQ. ID [−]	Station ID [−]	EQ. name [−]	Date [dd/mm/yyyy]	Mw [−]	Fault [−]	PGA_x [m/s²]	PGA_y [m/s²]
IT0014	TLM1	Friuli	06/05/1976	6.4	Thrust	3.390	3.090
IT0164	ALT	Irpinia	23/11/1980	6.9	Normal	0.549	0.564
IT0169	BSC	Irpinia	23/11/1980	6.9	Normal	0.946	0.810
IT0390	NCR	Umbria-Marche	23/09/1997	6.0	Normal	4.922	4.150
IT0788	ANT	L'Aquila	06/04/2009	6.3	Normal	0.260	0.197
IT0789	AQA	L'Aquila	06/04/2009	6.3	Normal	4.339	3.950
IT0806	FMG	L'Aquila	06/04/2009	6.3	Normal	0.263	0.235

Table 5.4: Scale factors (SFs) applied to the unscaled accelerograms used for Incremental Dynamic Analysis of the San Pietro Bell Tower.

EQ. ID	Scale factor											
IT0014	0.01	0.05	0.10	0.20	0.30	0.40	0.50	0.60	0.70	0.80	0.90	1.00
IT0164	0.01	0.05	0.10	0.20	0.30	0.50	0.70	1.00	2.00	3.00	5.00	6.00
IT0169	0.01	0.05	0.10	0.20	0.30	0.50	1.00	1.50	2.00	2.50	3.00	3.50
IT0390	0.01	0.05	0.10	0.15	0.20	0.25	0.30	0.40	0.50	0.60	0.70	0.80
IT0788	0.10	0.20	0.30	0.50	1.00	3.00	5.00	7.00	9.00	10.00	12.00	14.00
IT0789	0.01	0.05	0.10	0.15	0.20	0.25	0.30	0.40	0.50	0.60	0.70	0.80
IT0806	0.10	0.20	0.30	0.50	0.80	1.00	3.00	5.00	7.00	10.00	12.00	13.00

5.2.2   Non-Linear Seismic IDA Curve Sets with seismic input IMs

The most uncorrelated, meaningful and representative IMs, that have been identified by means of the statistical correlation study and whose results are summarized in Section 4.3 (see Fig. 4.2e), are PGA, RMSA, I_C, I_A, P_D, CAV, $S_a(T1)$, ASI_{VT}, PGV, RMSV, SED, CAD, $S_v(T1)$, I_H, PGD, RMSD, $S_d(T1)$, DSI_{NH} and E_I (m=19 with reference to Eq. (4.1)). These seismic input IMs have been used in the case of the San Pietro Bell Tower for the construction of IDA curves. In this context, the obtained IDA curve sets relate the local DMs (with reference to shaft, belfry and cusp parts) to the preselected IMs. Similarly to the Brick House (a second selection step based on a rapid visual investigation of the dispersion), the curve sets presenting a relatively large dispersion have been discarded and only the less scattered have been subsequently used for damage identification. In the case of the San Pietro Bell Tower, the definitive most efficient seismic input IMs considered for IDA are the following eleven (11): PGA, RMSA, I_C, I_A, $S_a(T1)$, ASI (computed limiting the integral of Tab. 4.2 from 0 to the tower's first-mode period), PGV, RMSV, $S_v(T1)$, I_H and $S_d(T1)$. With reference to Eq. (4.3), m^*=11 IMs can be collected in the vector $\mathbf{IM}^* = (PGA, RMSA, I_C, I_A, S_a(T1), ASI, PGV, RMSV, S_v(T1), I_H, S_d(T1))$.

While the seismic loadings for IDA are bidirectional, with components applied in the two horizontal directions to the FE model of the bell tower, the IDA curve sets are graphically represented as mean IMs computed using their mean direction versus numerically computed mean DMs, the latter represented by average values weighted over the volume of the numerical elements of each single part of the FE model (volume-averaged damage parameter). The IDA curve sets of the San Pietro Bell Tower (each containing seven (7) curves plus their mean curve) obtained from tensile damage d_t (for instance) versus the

aforementioned eleven (11) seismic input intensity measures have been investigated for the shaft, belfry and cusp. The IDA curves in terms of d_t versus acceleration-related intensity measures are depicted in Fig. 5.8 (PGA, RMSA and I_C) and Fig. 5.9 (I_A, S_a(T1) and ASI). Fig. 5.10 shows the three plots of the curves obtained with the best velocity-related IMs, such as PGV, RMSV, S_v(T1) and I_H. Finally, curves for the shaft, belfry and cusp obtained with S_d(T1) are illustrated in Fig. 5.11. In each graph, in addition to the set of curves, mean curves are depicted with a thick black line.
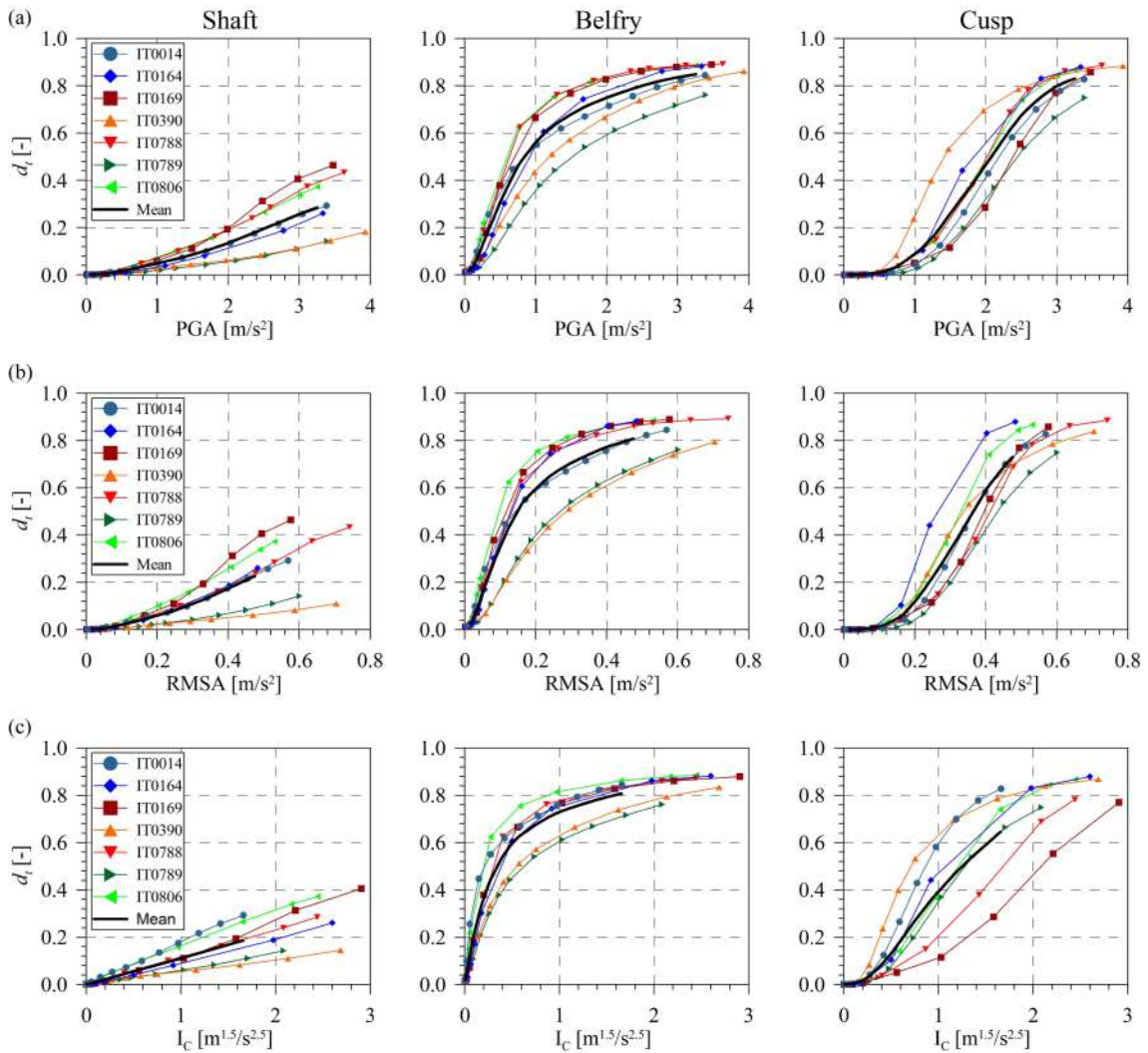
Figure 5.8: The IDA curve sets (shaft, belfry and cusp) and corresponding mean curves: plots of tensile damage, d_t, versus PGA (a), RMSA (b) and I_C (c).

131
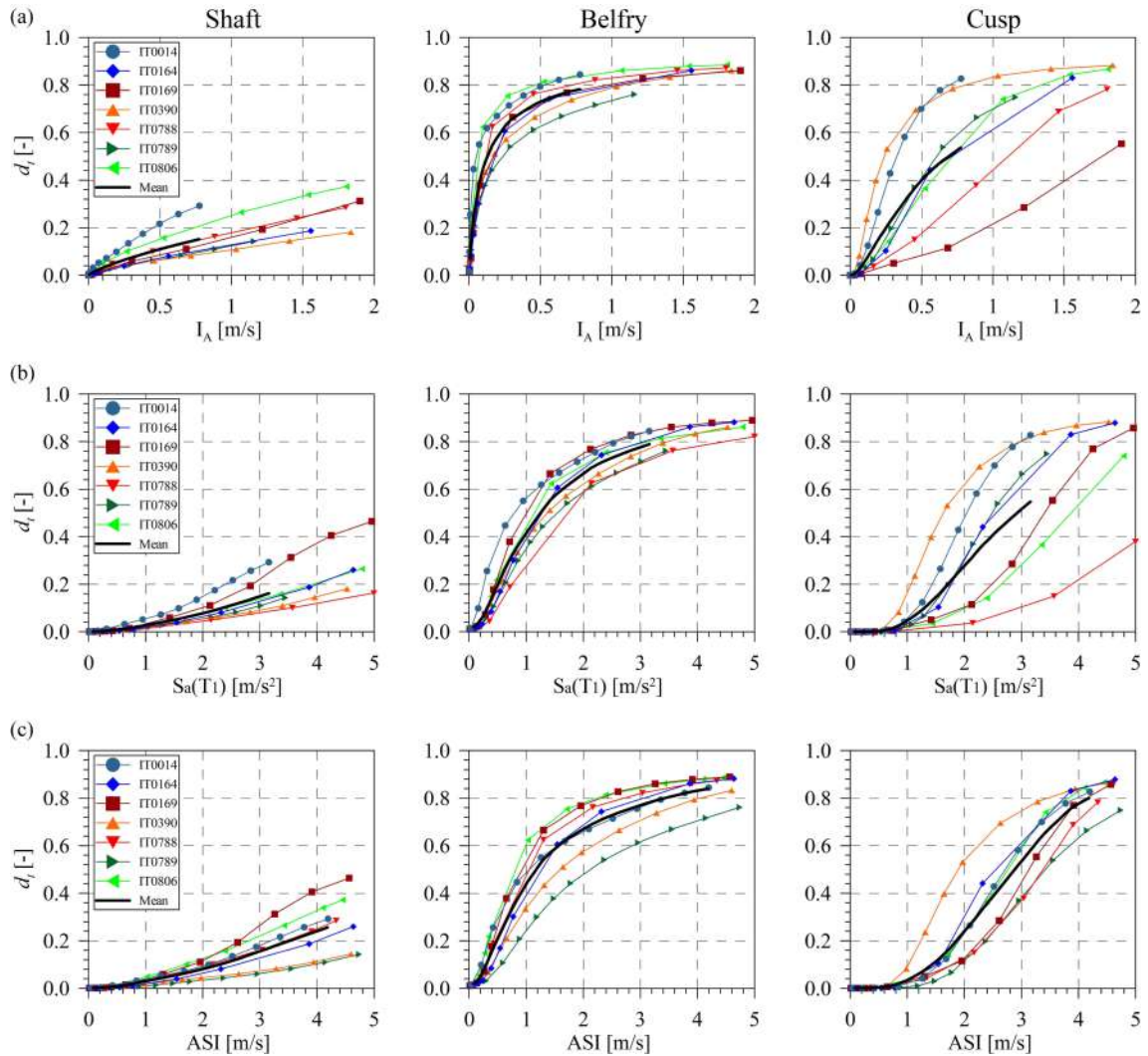
Figure 5.9: The IDA curve sets (shaft, belfry and cusp) and corresponding mean curves: plots of tensile damage, d_t, versus I_A (a), $S_a(T1)$ (b) and ASI (c).

By visually investigating all these plots, it is possible to immediately and directly identify the belfry as the most vulnerable and/or damageable part of the structure, as it was logically expected due to the substantial structural differences in the cross-section and the presence of important openings. Indeed, by considering all seismic input IMs (from Fig. 5.8 to Fig. 5.11), a very fast increase in the slopes of the IDA curves of the belfry can be clearly highlighted, meaning that a slight-to-moderate seismic event can conceivably produce higher damage compared with the other two parts. By examining the plots of the belfry the maximum numerically obtained tensile damage d_t is equal to about 0.85. On
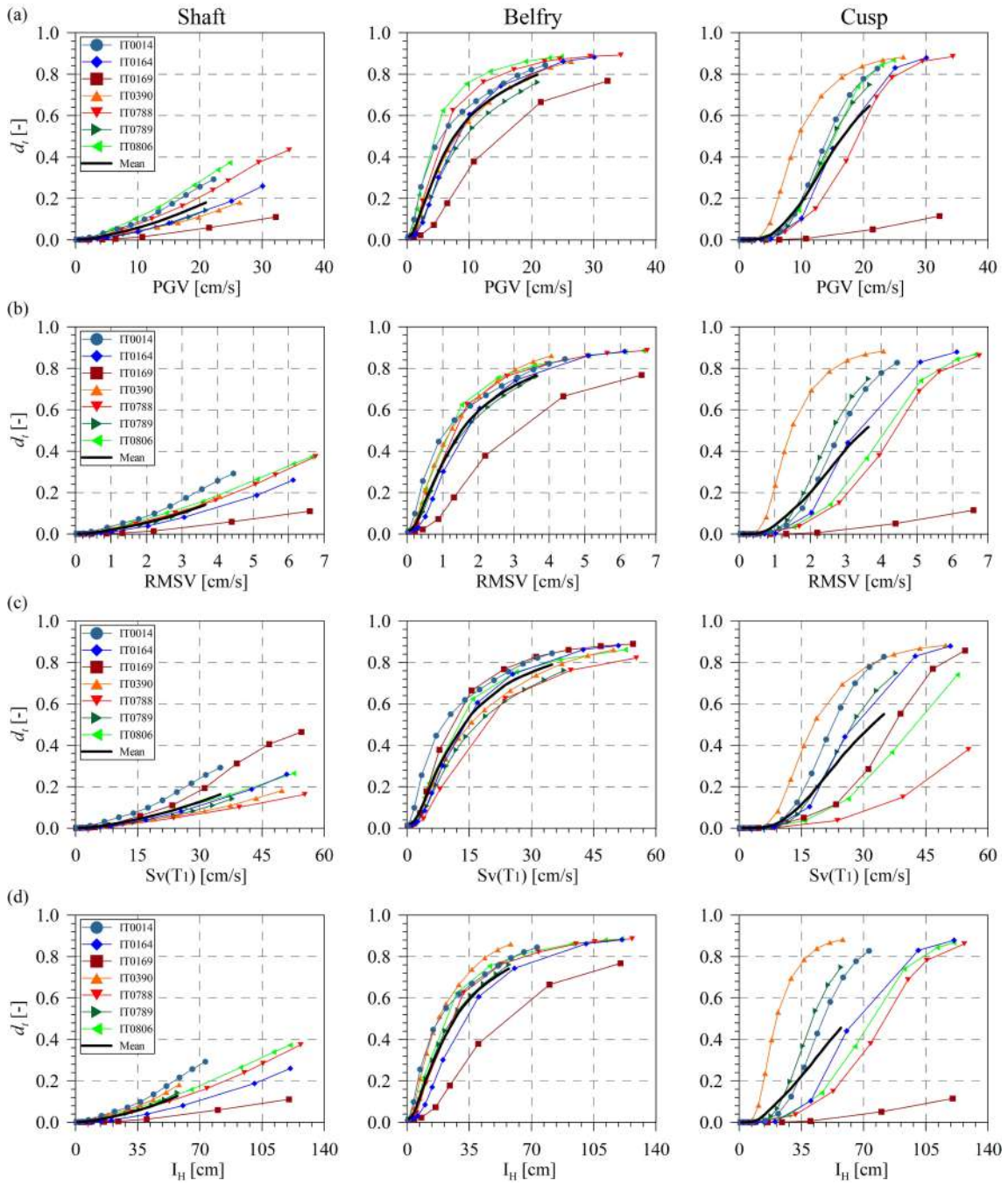
Figure 5.10: The IDA curve sets (shaft, belfry and cusp) and corresponding mean curves: plots of tensile damage, d_t, versus PGV (a), RMSV (b), S_v(T1) (c) and I_H (d).
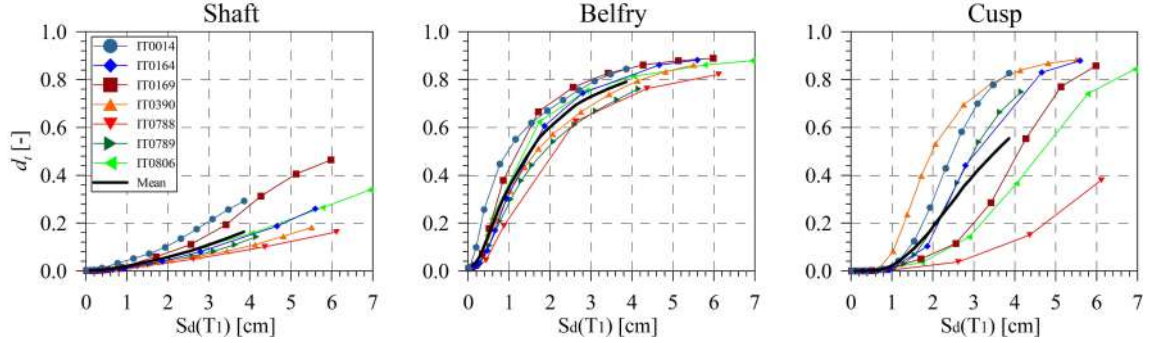
Figure 5.11: The IDA curve sets (shaft, belfry and cusp) and corresponding mean curves: plots of tensile damage, d_t, versus $S_d(T1)$.

the other hand, the shaft seems to be the least damaged part, with the highest reached values of tensile damage equal to about 0.2 (corresponding to a 20% reduction of Young's modulus). Moreover, the cusp presents higher levels of damage compared to the shaft, but greater IMs' levels are needed to observe similar important damage like the condition of the belfry. In general, a greater dispersion of the IDA curve sets can be observed in the case of the cusp if compared with the shaft and belfry, meaning that the adopted DM is not robust enough in relation to IMs of this macroelement. However, the main focus is concentrated on the IDA results of the belfry, whose dispersion is quite limited. It is worth to note that all these observations, based on the first interpretations of the IDA curve sets of the three parts, are in good agreement with the obtained numerical damaging process presented in past works in the literature (Cavalagli et al. 2018; Ubertini et al. 2018).

In order to identify the most efficient IM, the dispersion of the IDA curve sets has been investigated through the mean values of the RMSEs of single curves computed with respect to the mean curve, as described in the Eq. (4.2). In the case of San Pietro, $\Delta DM_{i,j}^{k,p}$ have been computed considering the following conditions: $i = 1, .., n$ (n=3, three parts considered: shaft, belfry and cusp), $j = 1, .., m^*$ (m^*=11, eleven IMs), $k = 1, .., l$ (l=7, seven earthquakes considered for IDA) and $p = 1, .., q$ (q is the number of samples of the mean curves). As an example, $\mathbf{\Delta DM_{2,10}^6} = (\Delta DM_{2,10}^{6,1}, \Delta DM_{2,10}^{6,2}, ..., \Delta DM_{2,10}^{6,q})$ is the vector difference between the 6th (IDA curve of IT0789 earthquake, see Tab. 5.3) and mean damage, with reference to the 2nd part of the model (belfry) and using the 10th intensity measure (I_H). In this context, Fig. 5.12 investigates the dispersion of the curve sets in the case of tensile damage, d_t, versus the set of eleven (11) seismic input IMs for the shaft, belfry and cusp. If the shaft is considered, Fig. 5.12 shows that the most efficient IMs
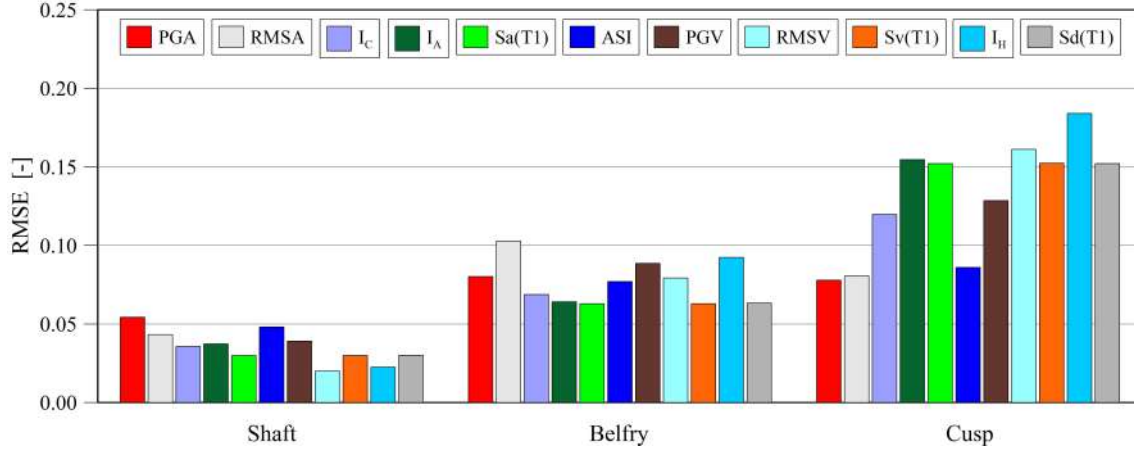
Figure 5.12: Dispersion of the IDA curve sets (shaft, belfry and cusp) by means of $RMSE_{i,j}$ (Eq. (4.2)): tensile damage Vs PGA, RMSA, I_C, I_A, S_a(T1), ASI, PGV, RMSV, S_v(T1), I_H and S_d(T1).

in terms of consistently lower dispersion is RMSV while for the belfry and the cusp are S_a(T1) and PGA, respectively. In addition, it is graphically evident (see also Fig. 5.8, Fig. 5.9, Fig. 5.10 and Fig. 5.11) that curve sets of the cusp are more scattered, while those of the shaft and belfry are significantly better. The dispersion, as computed in terms of RMSEs, is useful for the calculation of weighted mean values of IDA-based estimated damages in the shaft, belfry and cusp, as presented in the following Section.

As already concluded in Section 4.5, tensile damage as a cumulative parameter seems conceptually more adequate for damage characterization and localization. In this context, the main results of damage identification on the San Pietro Bell Tower presented in the next Section are essentially focused on the use of tensile damage, d_t, as DM. However, other DMs have been investigated by the Author such as plastic strain magnitude, $PEMAG$, first principal plastic strain, ε_1^{pl}, and some numerical energy-based damage parameters (e.g. the total energy dissipated in the element by damage). The latter represents an interesting output variable obtained from the CDP model implemented in ABAQUS numerical model, technically called ELDMD. For the interested reader, the IDA curve sets (each containing seven (7) curves plus their mean curve) obtained in the case of total energy dissipated in the element by damage, ELDMD, versus the set of eleven (11) seismic input IMs have been reported in Appendix B.2. In addition, the damage pattern evolution with increasing levels of earthquake input (see SFs in Tab. 5.4) is illustrated in Fig. B.18 in terms of d_t contour plots obtained at the last step of the IDAs with IT0788 earthquake.

5.2.3   IDA-based damage identification with seismic input SHM data

After the construction of the IDA Curve Sets and computation of their coefficients of dispersion, higher levels of identification of earthquake-induced damage have been achieved for the three parts of the structural model (see Fig. 5.5), by using Eqs. (4.4) and (4.5) and seismic input IMs of three real seismic events. Three near-field (with respect to San Pietro) ground motion records belonging to the main earthquakes of the 2016 Central Italy seismic sequence (Chiaraluce et al. 2017), have been used: Accumoli Mw6.0 earthquake of August 24th and the two following major shocks, Ussita Mw5.9 earthquake of October 26th and Norcia Mw6.5 of October 30th 2016. In the case of San Pietro, seismic records at the base of the bell tower during the three main earthquakes of the sequence were not available due to a temporary malfunction of the monitoring system, involving in particular, only the two accelerometers displayed at the base. In this context, acceleration records of Castelnuovo-Assisi (CSA) accelerometric station have been considered. CSA is the closest seismic monitoring station to the bell tower, situated at about 15 km far from the tower and between the latter and the epicenters. After an appropriate downscaling, the ground motion waveforms have been used as seismic inputs for the non-linear dynamic FEM analysis. Such ground motion waveforms have been scaled in order to reproduce the expected values of the PGA at the site of the bell tower, by matching measured and numerically estimated peak acceleration structural responses (Ubertini et al. 2018). Plots of unscaled acceleration time histories are shown in Fig. 5.13, where East-West and North-South components of Accumoli, Ussita and Norcia earthquakes are illustrated. The corresponding scaled waveforms are obtained after the application of SFs reported in Tab. 5.5 and subsequently applied at the base of the numerical model for non-linear dynamic analysis.
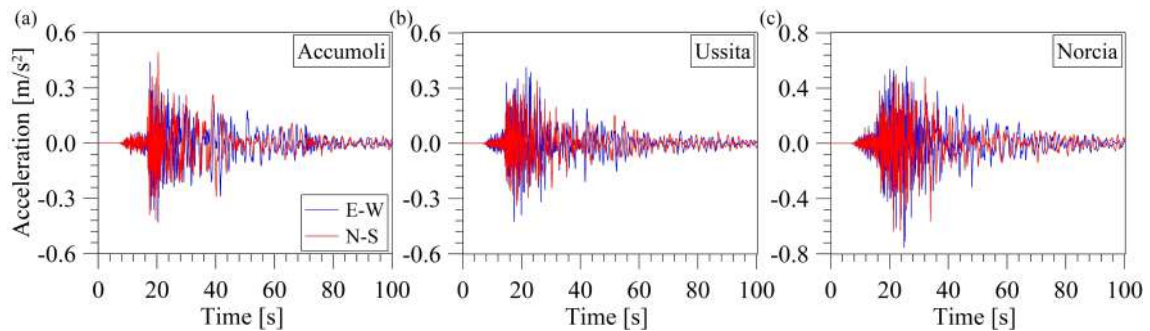
Figure 5.13: Three real seismic events used for earthquake-induced damage localization and quantification in the San Pietro Bell Tower: ground motion records of CSA station during Accumoli earthquake (a), Ussita shock (b) and Norcia earthquake (c).

Table 5.5: Scaling factors applied to the ground motion records of Castelnuovo-Assisi station in the three main earthquakes of the 2016 Central Italy seismic sequence.

	Accumoli	Ussita	Norcia
East-West	0.592	0.496	0.664
North-South	0.696	0.336	0.568

Taking advantage of the IDA curve sets illustrated in Fig. 5.8, Fig. 5.9, Fig. 5.10 and Fig. 5.11, seismic input intensity measures have allowed to firstly localize and subsequently quantify earthquake-induced damages. Eleven (11) IMs have been computed from the three seismic records depicted in Fig. 5.13, previously scaled according to SFs reported in Tab. 5.5. With reference to the belfry part and after applying Eq. (4.3), Fig. 5.14 illustrates IDA-based estimated damages using the seismic measures contained inside vectors $\mathbf{IM^{*A}}$, $\mathbf{IM^{*U}}$ and $\mathbf{IM^{*N}}$ for Accumoli, Ussita and Norcia, respectively. As usual, IDA-based damages have been estimated in terms of minimum, maximum and mean values, the latter obtained from the mean curve (see legend in Fig. 5.14). The IDA-based damage estimation zone, between the minimum and maximum damages, is highlighted with a light grey color. Also, for comparative purposes, actual damages have been reported in the plots. They represent numerically computed mean damage parameters in different portions, in particular, the tensile damages d_t obtained from the non-linear dynamic analyses carried out considering the seismic records plotted in Fig. 5.13. Also in the case of the San Pietro Bell Tower, in general, a relatively good consistency between numerical actual damages and IDA-based ones can be observed. The agreement between actual damage and weighted mean IDA-based estimation, as well as the minimum range of damage (the difference between the maximum and minimum IDA damage: obviously the smaller the better), have been appropriately taken into account. As an example, in the case of Accumoli earthquake (see Fig. 5.14a), the best consistency between mean damages can be if Arias Intensity, I_A, is used for IDA-based damage estimation. On the other hand, for Ussita (see Fig. 5.14b), the estimated range of damage is very small using RMSA, but at the same time, there is a bad matching between mean values. Both considerations, consistency between mean damages and reduced as much as possible ranges, are of particular importance in earthquake-induced damage quantification. Indeed, the idea of using not all IMs, but carefully selecting only some of them, taking into account a compromise of the aforementioned two considerations, can improve IDA-based damage estimation.
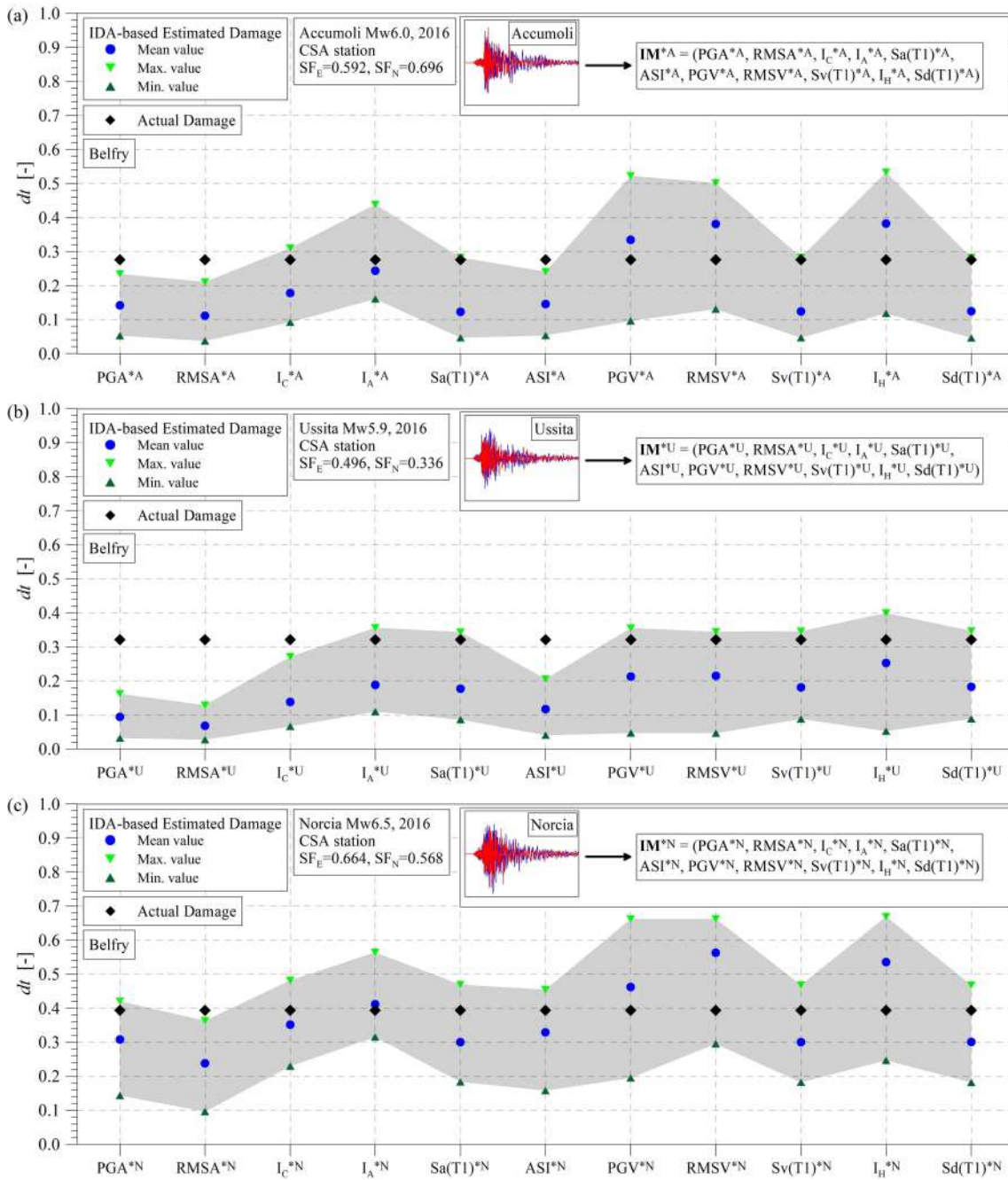
Figure 5.14: Belfry: IDA-based tensile damage (minimum, maximum and mean values) estimated with Accumoli, Ussita and Norcia earthquakes by means of the eleven (11) selected seismic input IMs. For comparative purposes actual damage (d_t) is also reported.
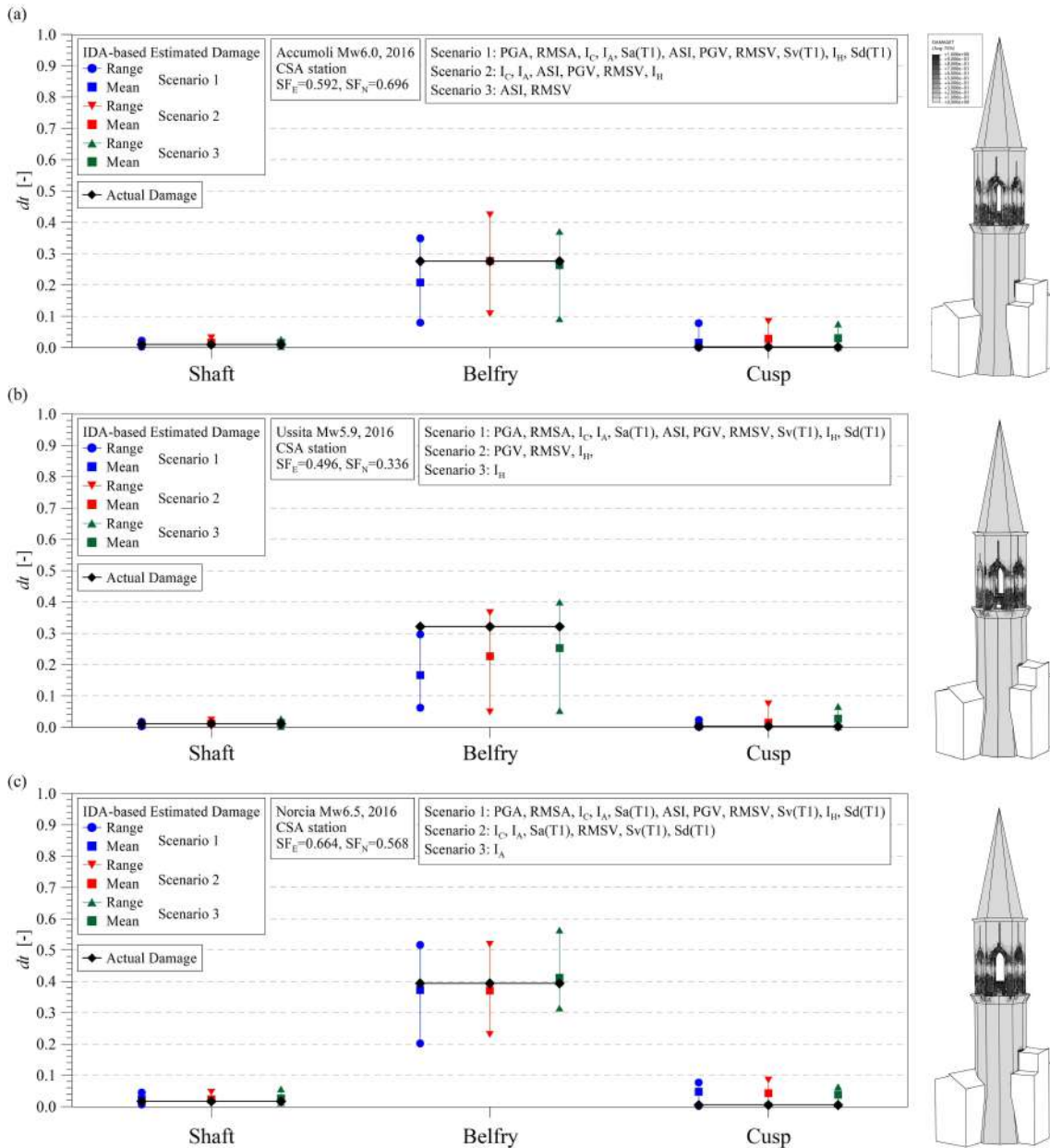
Figure 5.15: Comparison between actual damage (d_t) and IDA-based estimated tensile damage, considering different combinations of IMs for the three selected real ground motion records: Accumoli (a), Ussita (b) and Norcia (c). Note that IDA-based damage is expressed in terms of weighted average ranges and mean values obtained from the IDA curve sets and corresponding mean curves, respectively.

139

Mean values of IDA-estimated damage obtained from each single IM (see Fig. 5.14) have been averaged through weight coefficients $\alpha_{i,j}$ according to Eq. (4.4). Considering also Eq. (4.5), $\alpha_{i,j}$, depending on the corresponding IDA curve sets dispersion, have been computed as the inverse of $RMSE_{i,j}$, which are reported in Section 5.2.2, (see Fig. 5.12). In this context, by using the set of the aforementioned m^* seismic input IMs in Eq. (4.5), IDA-based tensile damages have been estimated, in terms of weighted average ranges (maximum and minimum) and weighted mean values for the shaft, belfry and cusp. Three Scenarios of combinations of IMs have been used: Scenario 1 comprises all m^* IMs, while the 2nd and the 3rd combine only some parameters, with the aim of a better consistency with actual damages and reduced estimated mean ranges. Fig. 5.15 shows IDA-based tensile damages in the shaft, belfry and cusp in the case of three earthquakes and all Scenarios of IMs combined. In general, a good agreement between actual damages and IDA-based estimated damages can be highlighted. The d_t values of the three regions fall within the corresponding IDA-based estimated average ranges. The proper combinations of only a few IMs have allowed a better estimation of weighted average ranges of damage. In addition, for a better understanding of the damage pattern obtained via IDA, contour plots of actual damage numerically obtained at the last step of the non-linear dynamic analysis are positioned on the side of each plot (contour range from 0 to 1.0). The concentration of tensile damage on the belfry region is clearly visible. Finally, in order to have a direct comparison, Fig. 5.16 illustrates weighted mean IDA-based tensile damages plotted versus actual damages, d_t, for Accumoli, Ussita and Norcia seismic events. Passing from Scenario 1 to 3, there is a clear trend of improvement in matching, with a closer allocation along the diagonal. Zoom plots are highlighted in the case of the shaft and cusp ($d_t \leq 0.1$).
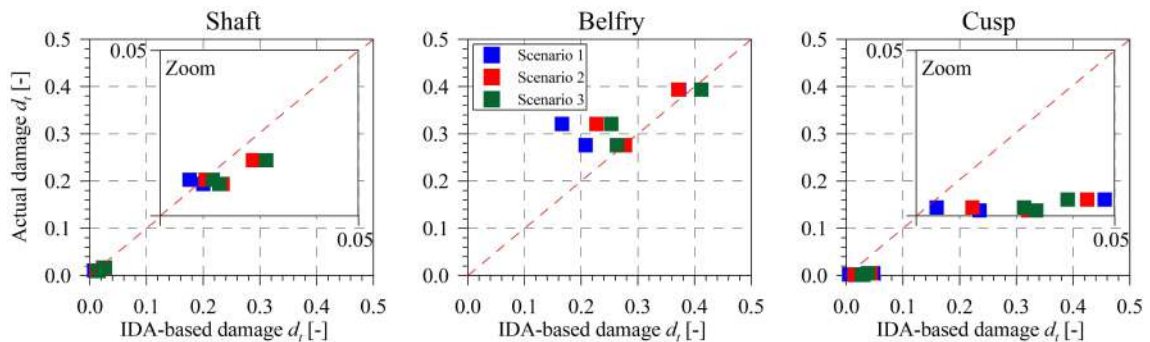
Figure 5.16: Comparison between actual damage (d_t) and weighted mean IDA-based estimated tensile damage, considering different combinations of IMs (Scenarios 1, 2 and 3) for Accumoli, Ussita and Norcia earthquakes. Zoom plots have range of axis from 0 to 0.05.

5.2.4   Non-Linear Seismic IDA Curve Sets with seismic response IMs

In addition to results in Sections 5.2.2 and 5.2.3, the IDA curve sets constructed with seismic response IMs have been also studied in the case of the San Pietro Bell Tower. Seismic response intensity measures have been computed from numerical response acceleration, velocity and displacement time histories of one particular node during all non-linear dynamic analyses. It is the node corresponding to the exact location of the two uni-axial accelerometers A1 and A2 on the top of the tower, as shown in Fig. 5.2b. In this context, once the best IDA curve sets are constructed and available, continuous SHM data from the permanent monitoring system, and in particular seismic events, can be used for damage localization and quantification, as reported in the following paragraphs.

Numerical responses have been successfully used in the case of the San Pietro Bell Tower. Both components, East-West and North-South, have enabled to compute the mean response IMs by using their mean direction, according to definitions reported in Tabs. 4.2, 4.3, 4.4 and 4.5, and considering seismic numerical response time histories. In this context, the IDA curve sets relate seismic response IMs to local numerically computed DMs (averaged over the volume), for the shaft, belfry and cusp. The definitive most efficient seismic response IMs considered for IDA are the following seven (7): Peak Response Acceleration (PRA), Root Mean Square Response Acceleration (RMSRA), Response Characteristic Intensity (RI_C), Response Arias Intensity (RI_A), Peak Response Velocity (PRV), Root Mean Square Response Velocity (RMSRV) and Peak Response Displacement (PRD). In particular, PRA, PRV and PRD are peak parameters, while RMSRA, RI_C, RI_A and RMSRV make up integral measures. In addition, RI_C and RI_A constitute original contribution of the Thesis. Taking into account Eq. (4.4) of the proposed IDA-based method in Section 4.2, $m^*=7$ response intensity measures can be collected in the vector $\mathbf{IM}^* = (PRA, RMSRA, RI_C, RI_A, PRV, RMSRV, PRD)$.

IDA curves in terms of tensile damage d_t versus acceleration-related response intensity measures are depicted in Fig. 5.17 (PRA, RMSRA, RI_C and RI_A). Fig. 5.18 shows the plots of the curves obtained with the best velocity-related IMs, such as PRV and RMRV, while the curves for the shaft, belfry and cusp obtained with PRD are illustrated in Fig. 5.19. In each graph, in addition to the set of curves, mean curves are depicted with a thick black line.
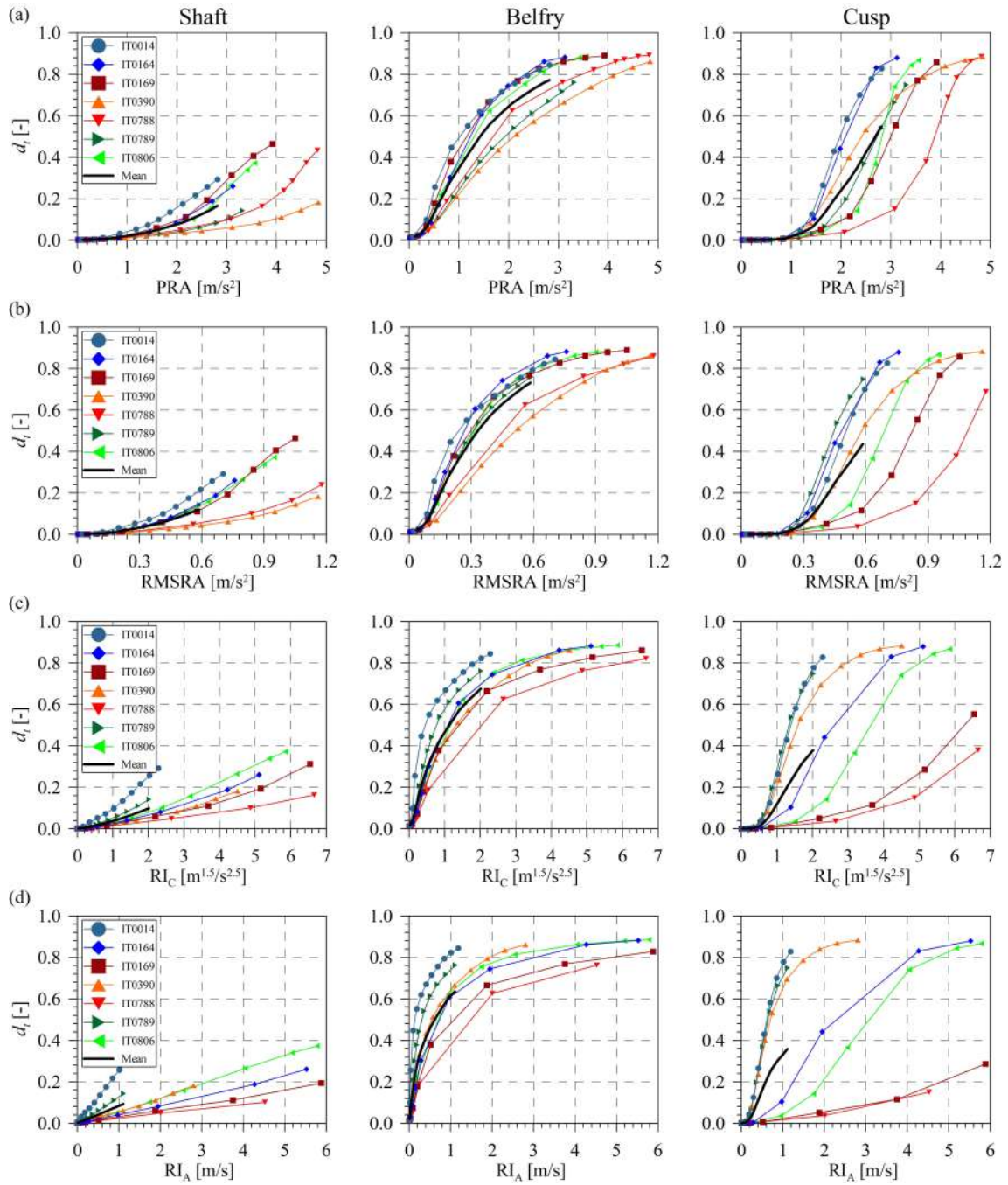
Figure 5.17: The IDA curve sets (shaft, belfry and cusp) and corresponding mean curves: plots of tensile damage, d_t, versus PRA (a), RMSRA (b), RI_C (c) and RI_A (d).
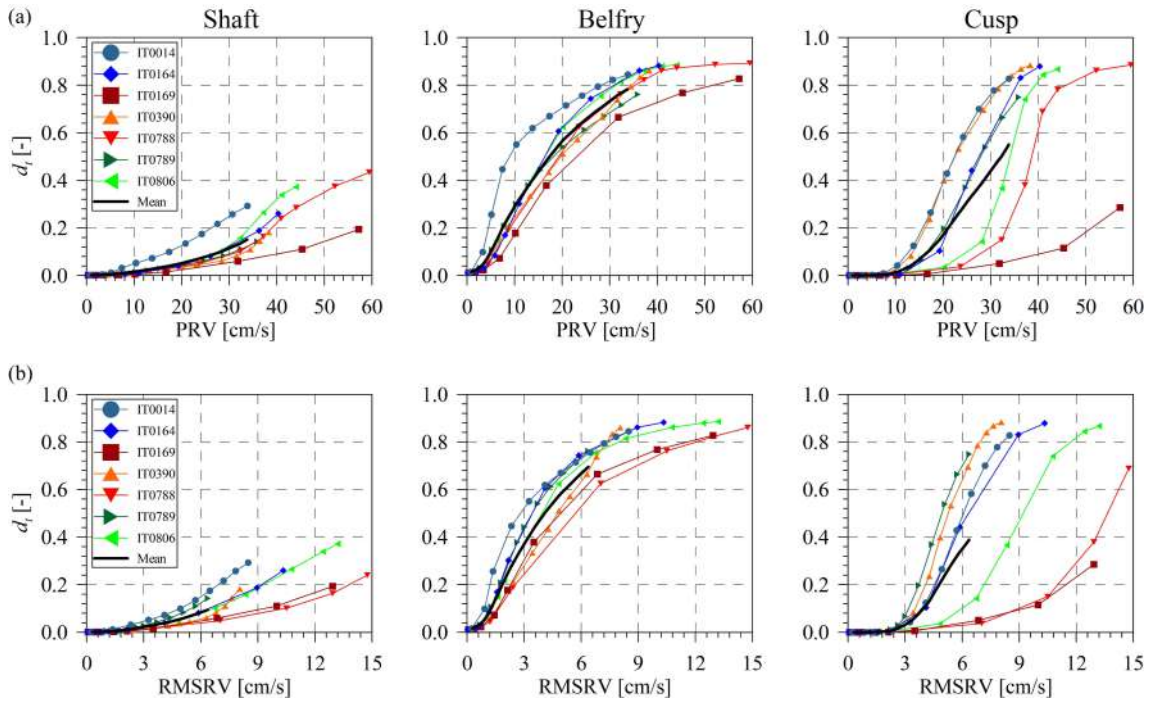
Figure 5.18: The IDA curve sets (shaft, belfry and cusp) and corresponding mean curves: plots of tensile damage, d_t, versus PRV (a) and RMSRV (b).
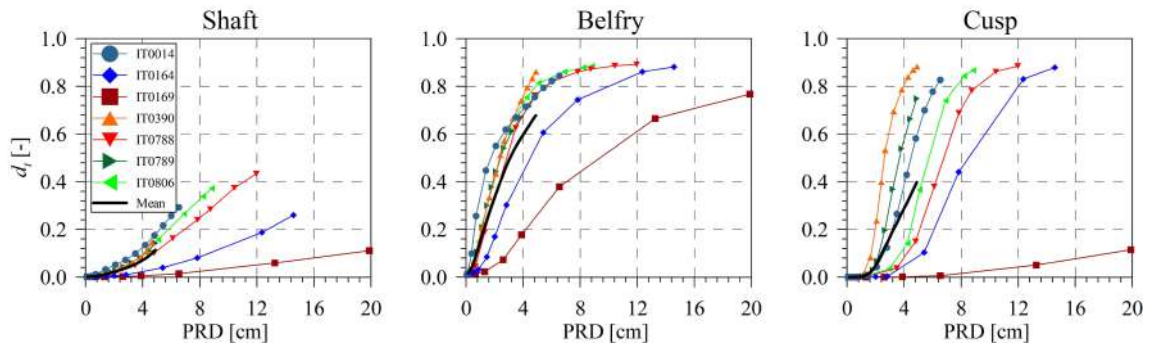
Figure 5.19: The IDA curve sets (shaft, belfry and cusp) and corresponding mean curves: plots of tensile damage, d_t, versus PRD.

Based on a rapid graphical investigation, the very first observations are in clear agreement to the ones presented from the IDA curve sets constructed with seismic input IMs in Section 5.2.2. It is confirmed that the belfry is immediately and directly identified as the most vulnerable and/or damageable part of the structure, while the shaft and the cusp present significantly smaller IDA-based damages. Indeed, considering all seven (7) seismic response

143

IMs (from Fig. 5.17 to Fig. 5.19), a very fast increase in the slopes of the IDA curves of the belfry can be confirmed, with maximum numerically obtained d_t equal to about 0.8. The cusp (maximum d_t equal to about 0.5) presents higher levels of damage with respect to the shaft (maximum d_t equal to about 0.2), but again, larger levels of IMs are needed in order to observe similar important damage compared with the condition of the belfry. Finally, the greatest dispersion observed in the case of the cusp can be confirmed by visually investigating the IDA curve sets of response IMs, meaning that the adopted DM is not robust enough in relation to the structural response of this macroelement.

As presented by the proposed IDA-based method in Section 4.2, the dispersion of the IDA curve sets has been investigated through the mean values of the RMSEs of single curves computed with respect to the mean curve (see Eq. (4.2), considering n=3, m^*=7 and l=7). Coefficients of dispersion, $RMSE_{i,j}$, are illustrated in Fig. 5.20. As shown in the plot, RMSRV can be identified as the most efficient response IM in the case of the shaft. PRV is the one whose IDA curve set presents the less dispersion for the belfry and RMSRA is identified for the cusp. Similarly to the curve sets presented in Section 5.2.2, it is graphically evident that curve sets of the cusp present a higher scatter, compared to the shaft and belfry whose IDA curves are significantly less dispersed. However, again, the main interest in the present case study relies on the damage identification for the belfry. The dispersion coefficients, computed in terms of RMSEs, are useful for the calculation of weighted mean values of IDA-based estimated damages in the shaft, belfry and cusp.
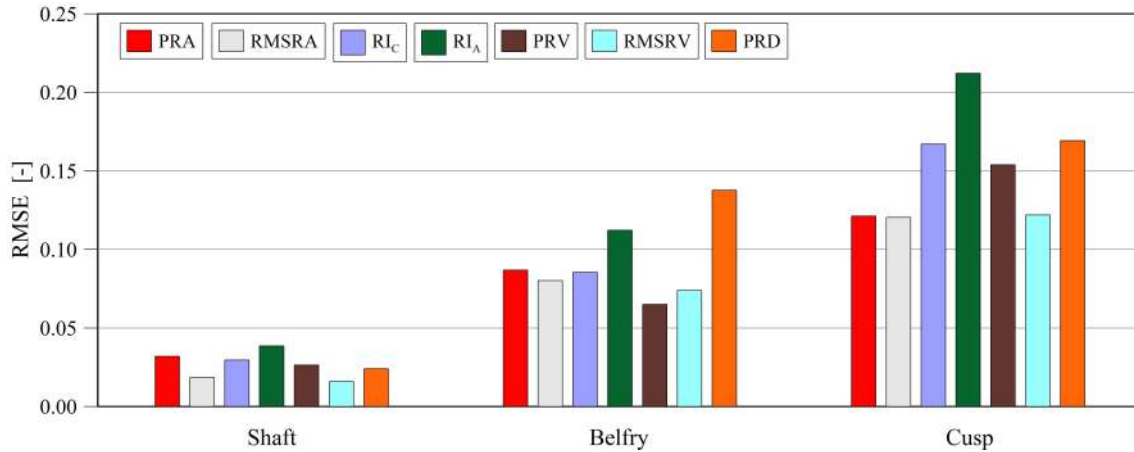
Figure 5.20: Dispersion of the IDA curve sets (shaft, belfry and cusp) by means of $RMSE_{i,j}$ (Eq. (4.2)): tensile damage Vs PRA, RMSRA, RI$_C$, RI$_A$, PRV, RMSRV and PRD.

5.2.5   IDA-based damage identification with seismic response SHM data

The IDA curve sets constructed with seismic response IMs are of great importance in the case of the San Pietro Bell Tower, which has a big amount of SHM data, with a particular focus on recorded seismic events. As already mentioned in Section 5.1, the tower was hit by the three main shocks of the 2016 Central Italy seismic sequence, at a distance of about 80 km from the epicenters. Despite no clear relevant structural damages that were observed in any part of the structure, above all in the belfry, the long-term vibration-based SHM clearly detected earthquake-induced damage, in terms of consistent decays in natural frequencies and control chart. The latter is illustrated in Fig. 5.4, where a clear deviation of the structural behavior from normal conditions can be highlighted after Accumoli earthquake, with a sharp increase in the relative frequency of outliers, and also later after Ussita and Norcia shocks (Ubertini et al. 2018).

The time histories of recorded accelerations on top of the bell tower during the three earthquakes are shown in plots of Fig. 5.21. In particular, East-West and North-South directions are measured by sensors A1 and A2, respectively (see 5.2b). During Accumoli earthquake, acceleration in North-South direction was predominant with a peak value of 76.31 cm/s^2, while, during Ussita and Norcia earthquakes, accelerations in East-West direction were predominant, with peak values of 60.66 cm/s^2 and 94.21 cm/s^2, respectively. It is worth noting that this kind of response can be considered as representative of relatively low-intensity earthquakes at the site of the bell tower, whose return period can be estimated in the order of some years.
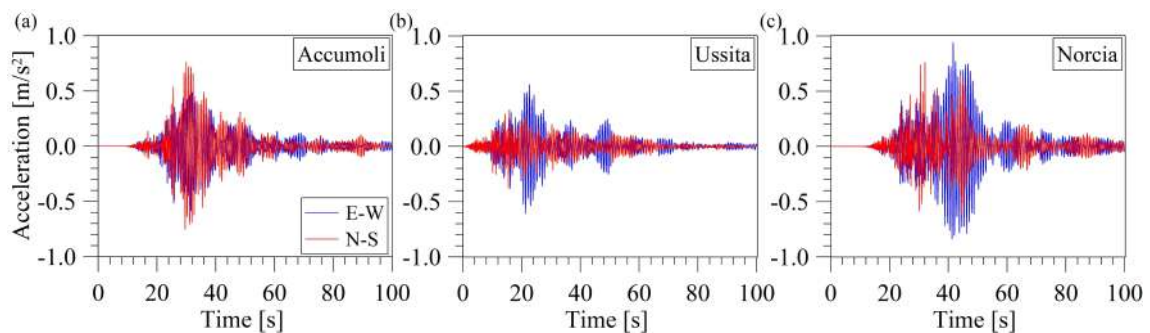
Figure 5.21: Three real seismic events used for earthquake-induced damage localization and quantification in the San Pietro Bell Tower: measured dynamic response on top of the bell tower in terms of acceleration during the three main shocks of the seismic sequence, Accumoli earthquake (a), Ussita earthquake (b) and Norcia earthquake (c).

The IDA curve sets with response IMs have made possible localization and quantification of earthquake-induced damage for the three parts of the structural model (see Fig. 5.5), by using Eq. (4.5) and seven (7) seismic response intensity measures, computed from response seismic records on top of the tower depicted in Fig. 5.21. Taking advantage of the IDA curve sets illustrated in Fig. 5.17, Fig. 5.18 and Fig. 5.19, intensity measures have allowed to firstly localize and subsequently quantify earthquake-induced damages. Only for belfry, Fig. 5.22 illustrates IDA-based estimated damages using seismic response measures collected in vectors $\mathbf{IM^{*A}}$, $\mathbf{IM^{*U}}$ and $\mathbf{IM^{*N}}$ for Accumoli, Ussita and Norcia, respectively (Eq. (4.3)). As usual, damages have been estimated in terms of minimum, maximum and mean values. The IDA-based damage estimation zone is highlighted in light grey color. By visually inspecting plots in Fig. 5.22, a relatively good consistency between numerical actual damages and IDA-based ones is confirmed with respect to previous results. The same matching and/or consistency rule, used in Section 5.2.2, has been applied also to this case. Considerations on the agreement between actual damage and weighted mean IDA-based estimation, together with the desirable as small as possible IDA-based estimated range of damage, have been taken into account. As an example, in the case of Accumoli earthquake (see Fig. 5.22a), the best consistency between mean damages can be if Response Arias Intensity, $\mathrm{RI_A}$, is used for IDA-based damage estimation. On the other hand, the smallest estimated range of damage is obtained RMSRA, but matching between mean values is sacrificed. Again, by carefully selecting only some of the response seismic IMs, and taking into account a compromise of the aforementioned two considerations, IDA-based damage estimation can be significantly improved.

According to Eqs. (4.4) and (4.5) in the proposed method, mean values of IDA-estimated damage obtained from each single IM have been averaged by means of weight coefficients $\alpha_{i,j}$, computed as the inverse of $RMSE_{i,j}$ (see Fig. 5.20). Fig. 5.23 shows IDA-based tensile damages d_t estimated, in terms of weighted average ranges (maximum and minimum) and weighted mean values for the shaft, belfry and cusp, compared to actual d_t. Three Scenarios of combinations of IMs have been considered as previously, aimed at improvement of IDA-based damage estimation. The good results of IDA-based earthquake-induced damage quantification obtained using seismic input IMs are confirmed also in the case of seismic response IMs: a good agreement between actual damages and IDA-based estimated mean damages can be highlighted. The proper combinations of only a few IMs have allowed a better estimation of weighted average ranges of damage.
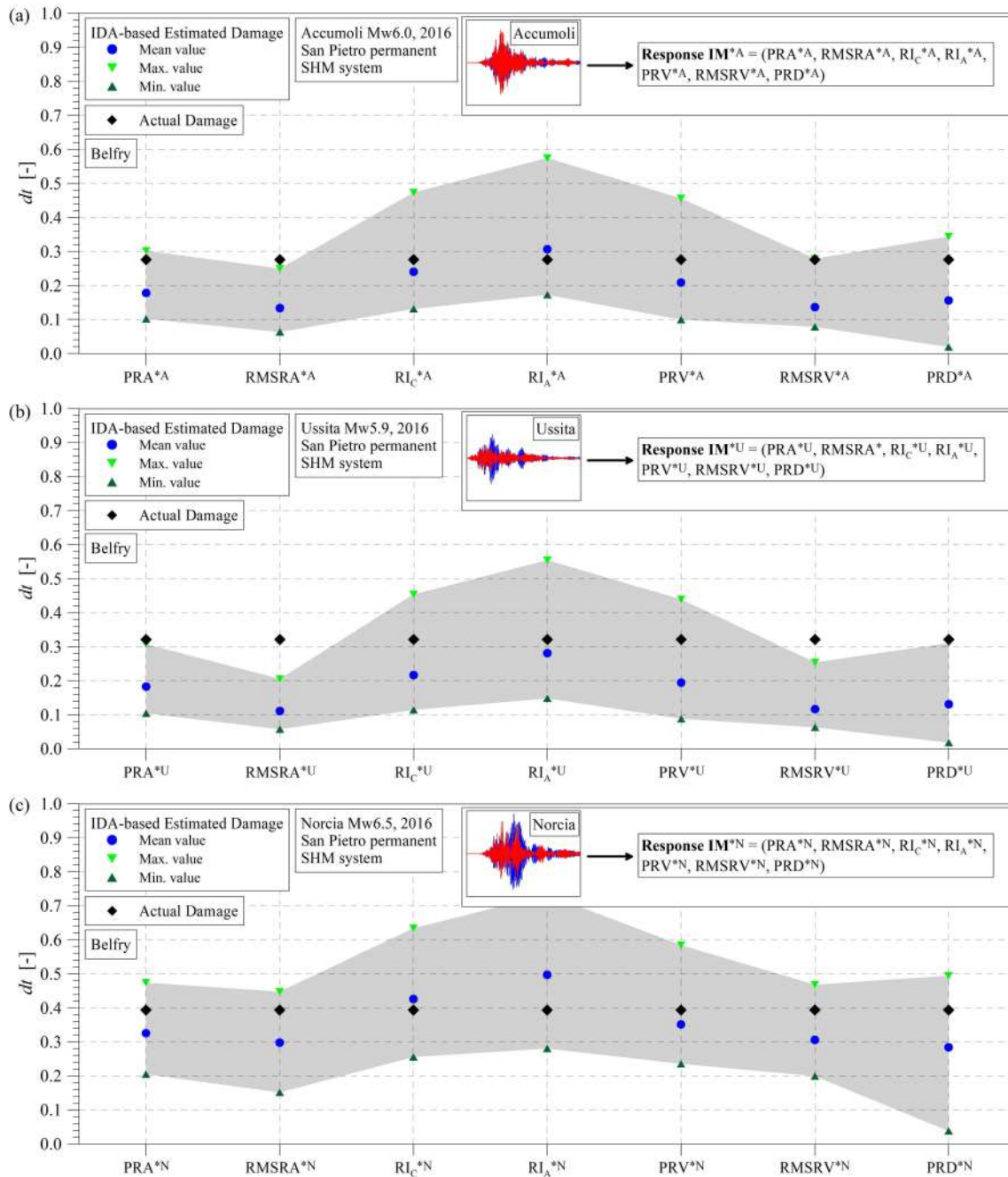
Figure 5.22: Belfry: IDA-based tensile damage (minimum, maximum and mean values) estimated with Accumoli, Ussita and Norcia earthquakes by means of the seven (7) selected seismic response IMs. For comparative purposes actual damage (d_t) is also reported.
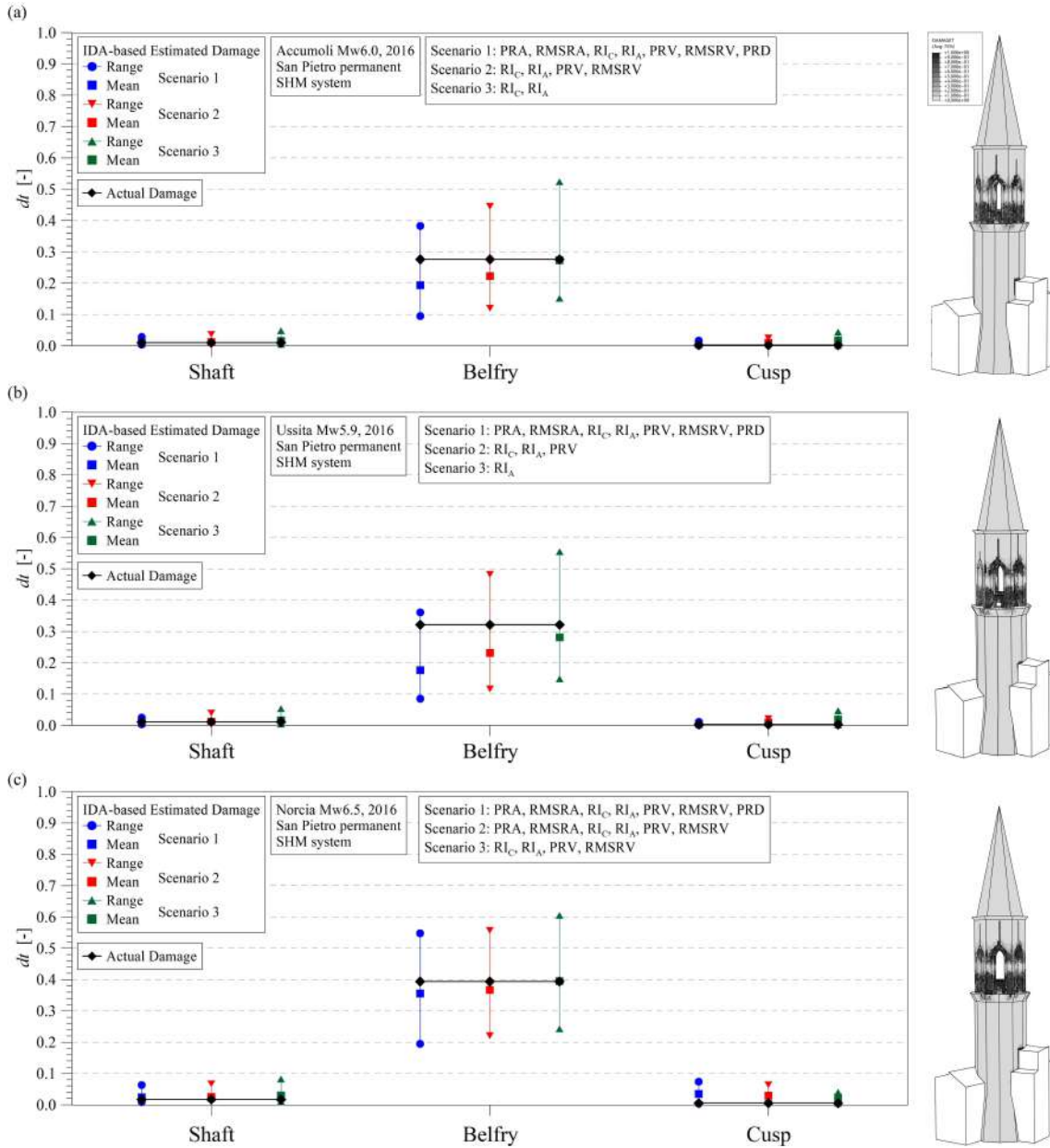
Figure 5.23: Comparison between actual damage (d_t) and IDA-based estimated tensile damage, considering different combinations of seismic response IMs for the three selected real ground motion records: Accumoli (a), Ussita (b) and Norcia (c). Note that IDA-based damage is expressed in terms of weighted average ranges and mean values obtained from the IDA curve sets and corresponding mean curves, respectively.

Finally, Fig. 5.24 depicts a better representation of mean weighted IDA-based damages in terms of tensile parameter d_t. As illustrated, they are plotted against actual damages for the three considered seismic events and with improving scenarios (from Scenario 1 to 3). With the focus on the most vulnerable part of the bell tower, the belfry, a clear trend of improvement in matching, with a closer allocation along the diagonal, can be highlighted. On the other hand, given the low value of the damage for shaft and cusp, the weight of the result is lower.
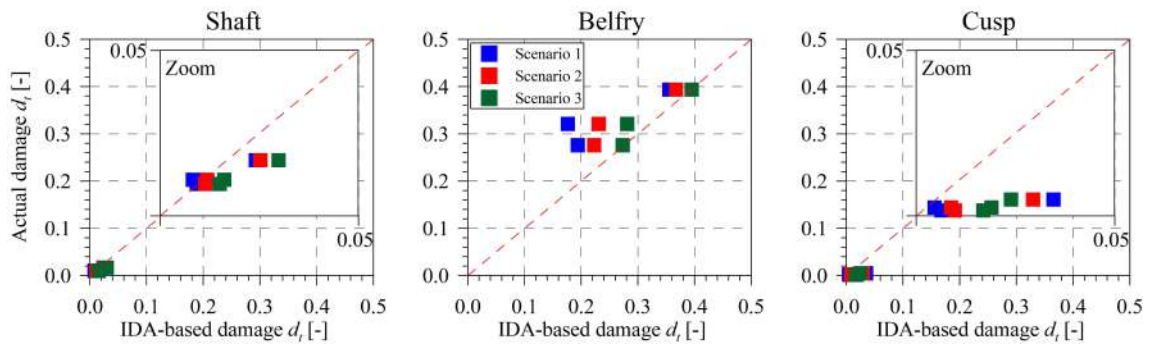
Figure 5.24: Comparison between actual damage (d_t) and weighted mean IDA-based estimated tensile damage, considering different combinations of seismic response IMs (Scenarios 1, 2 and 3) for Accumoli, Ussita and Norcia earthquakes. Note that zoom plots have range of axis from 0 to 0.05.

5.2.6   IDA-based damage identification with seismic input & response SHM data

The availability of experimentally recorded seismic responses on the San Pietro Bell Tower during important earthquakes is very precious. The inclusion of seismic response IMs can certainly improve the results of IDA-based damage localization and quantification. What the results would be if we considered all IDA curve sets? In this context, those obtained with seismic input IMs (Section 5.2.2) and the ones constructed with seismic response IMs (Section 5.2.4) have been exploited for this scope. With reference to the belfry, Fig. 5.25 illustrates IDA-based estimated damages using both seismic input (11) and response (7) IMs for Accumoli, Ussita and Norcia, respectively. As usual, damages have been estimated in terms of minimum, maximum and mean values, the latter obtained from the mean curve. Again, the IDA-based damage estimation zone, between the minimum and maximum damages, is highlighted with a light grey color. It is worth noting that plots in
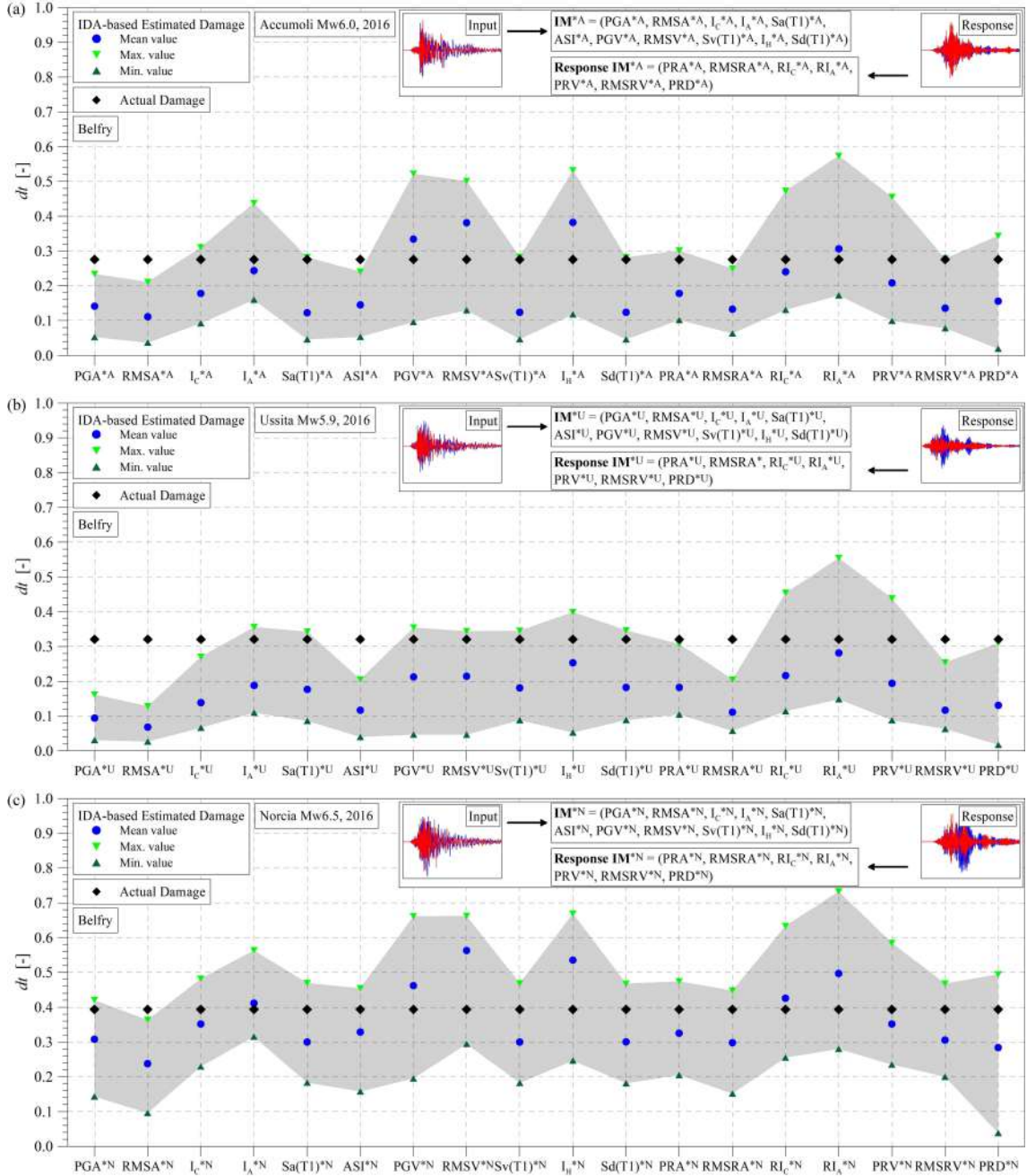
Figure 5.25: Belfry: IDA-based tensile damage (minimum, maximum and mean values) estimated with Accumoli, Ussita and Norcia earthquakes by means of their eighteen (18) (eleven (11) seismic input and seven (7) seismic response) IMs into Eq. (4.3). For comparative purposes actual damage (d_t) is also reported.

Fig. 5.25 highlight the very good consistency between IDA-based results obtained in both cases, with seismic input as well as seismic response IMs. A total of eighteen (18) IMs allows a wider possibility for carefully selecting and combining only some of them, according to Scenarios 2 and 3, in order to have the best consistency between actual damage and weighted mean IDA-based estimation and the most possible reduced range of IDA-based damage.

By applying the procedure proposed in Section 4.2, mean values of IDA-estimated damage obtained from every single IM have been averaged through weight coefficients $\alpha_{i,j}$ according to Eqs. (4.4) and (4.5). Fig. 5.26 shows IDA-based tensile damages estimated in terms of weighted average ranges (maximum and minimum) and weighted mean values for the shaft, belfry and cusp, according to three Scenarios of combined IMs. As demonstrated, by properly combining seismic and response IMs, Scenarios 2 and 3 enable full consistency between actual damages and IDA-based estimated damages for Accumoli and Norcia and clearly better agreement for Ussita earthquake.

Finally, the consistency of IDA-based damage estimation has been investigated in three cases: (i) using only seismic input IMs, (ii) using only seismic response IMs and (iii) using seismic input and response IMs together. Fig. 5.27 illustrates weighted mean IDA-based tensile damages plotted versus actual damages, d_t, for Accumoli, Ussita and Norcia seismic events. If compared with previous applications of separated seismic input (Section 5.2.3) and separated seismic response (Section 5.2.5) IMs, results clearly improve if combined seismic input and seismic response IMs are used. As already mentioned, for San Pietro, the greatest focus of IDA-based damage relates to the results concerning the belfry. By examining the plots in Fig. 5.27, besides better results obtained switching from Scenario 1 to 3 (positioning closer to the diagonal) of each single case, the best consistency has been obtained in the 3$^{\text{rd}}$ case with seismic input and response IMs together: in addition to refined Scenarios 1 and 3, Scenario 2 has significantly improved (two out of three are now positioned exactly over the diagonal).

151
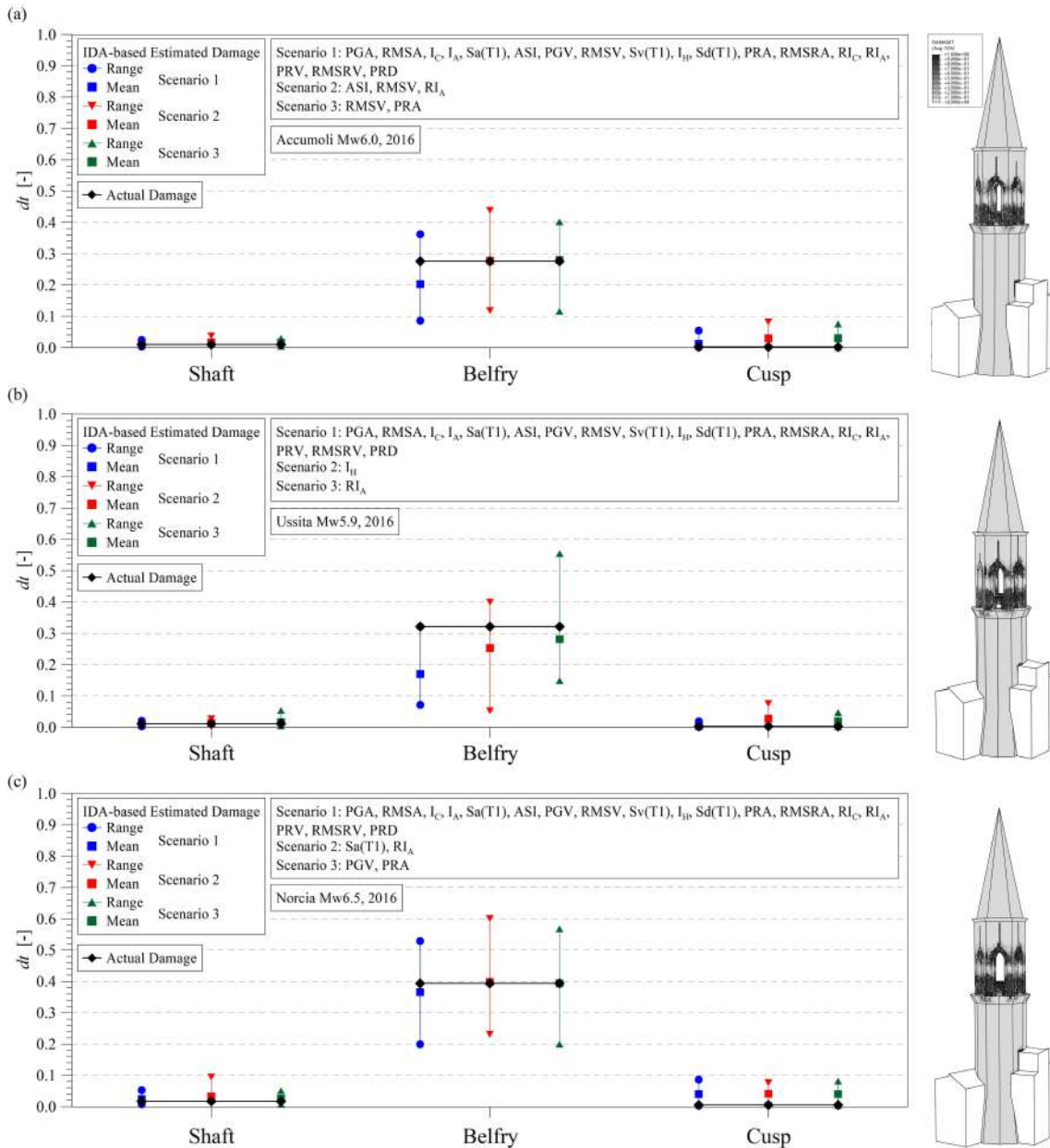
Figure 5.26: Comparison between actual damage (d_t) and IDA-based estimated tensile damage, considering different combinations of seismic input and seismic response IMs for the three selected real ground motion records: Accumoli (a), Ussita (b) and Norcia (c). Note that IDA-based damage is expressed in terms of weighted average ranges and mean values obtained from the IDA curve sets and corresponding mean curves, respectively.
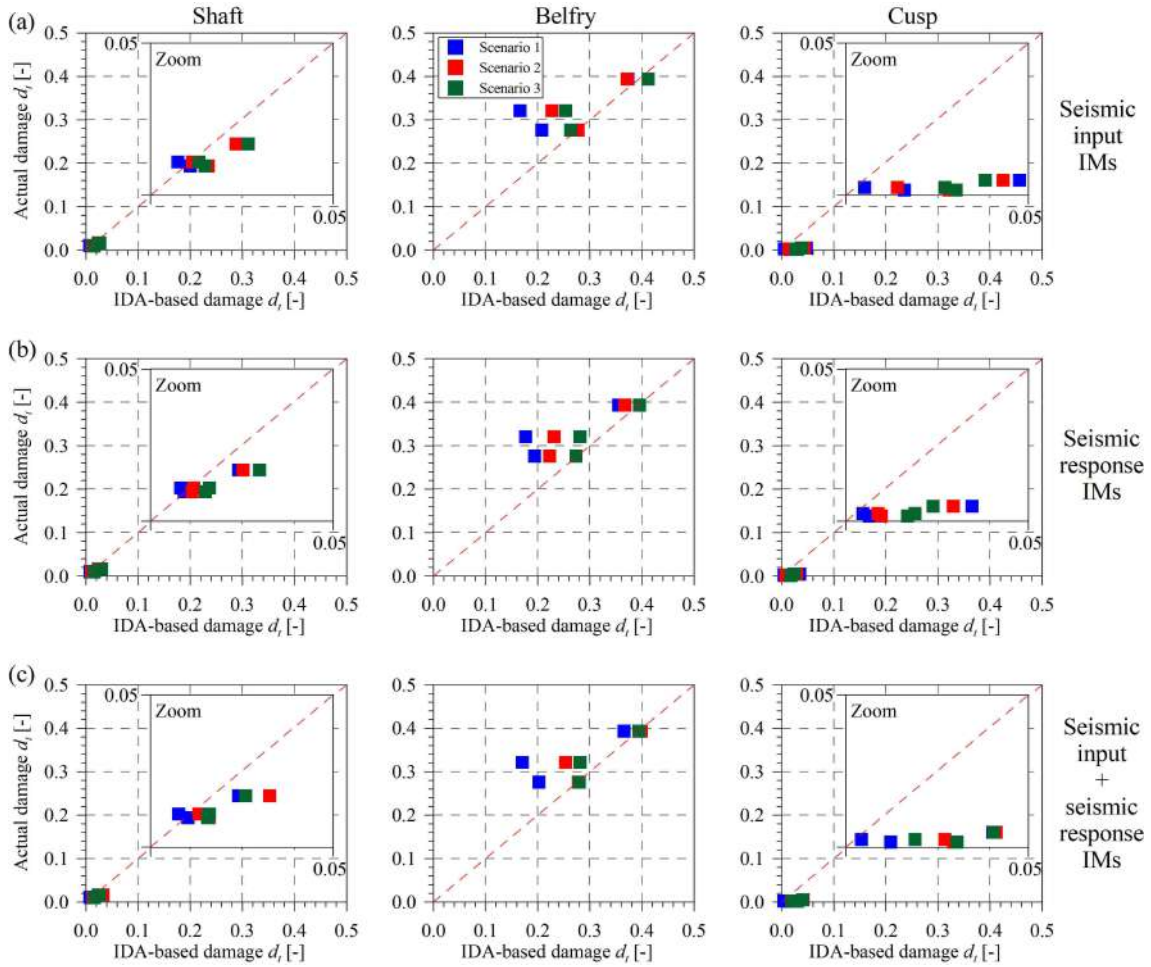
Figure 5.27: Comparison between actual damage (d_t) and weighted mean IDA-based estimated tensile damage, considering different combinations of IMs (Scenarios 1, 2 and 3) for Accumoli, Ussita and Norcia earthquakes: using only seismic input IMs (a), using only seismic response IMs (b) and using seismic input and seismic response IMs combined (c).

5.3   Conclusions

The results of the proposed IDA-based innovative method for earthquake-induced damage identification have been presented in the case of the monumental San Pietro Bell Tower, a CH masonry structure situated in Perugia, Italy, that was hit by important seismic events during the 2016 Central Italy seismic sequence, whereby data-driven damage detection has been already efficiently proved and, to some extent, also damage quantification in the form of permanent variations in natural frequencies. The a priori construction of multi-dimensional IDA curve sets relating meaningful local damage parameters (associated with the shaft, belfry and cusp) to selected seismic intensity measures has been followed by an investigation of their dispersion, allowing to discard some and to keep the most efficient ones. The proposed IDA-based method is numerically validated through application to the FE model of the masonry tower.

The main results are summarized below.

- A more in-depth investigation of dispersion, by means of root mean square errors of the IDA curve sets, has allowed identifying the most efficient intensity parameters.

- Non-linear seismic IDA results have immediately and clearly identified the belfry as the most damaged/damageable part of the structure. It is worth noting that this outcome could be also helpful for strategic positions in which to strengthen the long-term monitoring system of the bell tower, for example adding dynamic as well as static sensors.

- Higher levels of identification of earthquake-induced damage have been achieved for the shaft, belfry and cusp by means of intensity measures of three real seismic events. For this purpose, three near-field (with respect to San Pietro) ground motion records belonging to the main earthquakes of the 2016 Central Italy seismic sequence have been used.

- Given the availability o continuous SHM data of the San Pietro Bell Tower, mostly important experimentally recorded seismic responses during earthquakes, some original response intensity measures (in addition to input measures) have been proposed and found to be equally efficient, even more. Eleven (11) seismic input intensity measures and seven (7) seismic response measures, computed from seismic records at the base and the top of the tower, respectively, have allowed to firstly localize and subsequently quantify earthquake-induced damages.

- An overall weighted average IDA-based estimation of tensile damage ranges (between the minimum and maximum) and weighted mean values have been achieved by means of weighting coefficients depending on the IDA curve sets dispersion. In order to achieve good consistency between mean damages and reduced as much as possible damage ranges, three scenarios have been taken into account, each based on different combinations of the eighteen (18) IMs.

- It is worth noting that the introduction of the additional seismic response intensity measures, with respect to only seismic input ones, has enabled a wider possibility for carefully selecting and combining only some of them, resulting in a refinement of the IDA results in terms of consistency between numerical actual damages and IDA-based ones. Therefore, the results have allowed obtaining a better IDA-based earthquake-induced quantification.

The presented results validated the proposed seismic IDA-based SHM procedure, for rapidly and correctly localizing and quantifying earthquake-induced damage in the case of the San Pietro Bell Tower. The latter represents a very interesting case study, whose SHM data obtained from the permanent vibration-based monitoring system have enabled an important step forward in the validation of the methodology, thereby showing great potential for damage assessment of long-term monitored masonry structures for condition-based maintenance and preventive conservation.

Chapter 6

Concluding remarks

The major objectives and the original contributions of this Thesis have concerned the development and the validation of the proposed DORI methodology aimed at the earthquake-induced damage detection, localization and quantification in historic masonry structures under continuous monitoring. It is based on the combination of data-driven, as well as innovative model-based methods. Specifically, **DORI** addresses the **D**amage identification based on **O**perational modal analysis & **R**apid surrogate modeling & **I**ncremental dynamic analysis for CH masonry buildings subjected to earthquakes.

The first innovative aspect of DORI concerns the proposal of data fusion in the data-driven damage detection method. In particular, the use of static measures as predictors in the dynamic MLR model, in addition to temperature data, have been proposed for data cleansing, achieving consequently an enhanced vibration-based damage detection. It should be recalled that the detection method is OMA-based and relies on the use of long-term vibration-based monitoring data, providing earthquake-induced damage detection by considering pre and post-event structural conditions, highlighting anomalies in the structural behavior.

The second innovative aspect proposed by the DORI methodology regards the extension of the abovementioned enhanced OMA-based data-driven damage detection method through the introduction and implementation of two independent innovative model-based methods, for localization and quantification of earthquake-induced damage in CH buildings permanently monitored for a relatively long period of time. The former is a surrogate model-based method, which combines long-term vibration monitoring data (i.e. OMA) and numerical modeling, while the latter is an IDA-based method. The surrogate modeling constitutes a rapid tool due to its simplicity and limited computational burden, related to the fact that it is based on a linear elastic model. In the present case, the innovative quadratic surrogate model exploits an objective function which is based also on variations in mode shapes, in addition to natural frequencies changes (damage-induced decays), leading to higher accuracy of the results. On the other hand, concerning the other method of DORI, first and foremost, proposing IDA for damage localization and quantification constitutes a new and original contribution of the Thesis, never explored so far in the literature. Unlike surrogate modeling, the IDA method requires a non-linear model. In addition, it employs recorded data during an earthquake for damage identification.

Combining OMA, surrogate modeling and IDA-based methods is clearly convenient. First of all, the OMA-based damage detection results, e.g. in terms of frequency shifts and control chart (novelty detection), are used for comparative and/or complementary purposes with damage identified with SM and IDA, allowing to avoid false positive results. Second, the combination of linear (SM), as well as non-linear (IDA) models can certainly enrich the accuracy of the DORI methodology. Third, IDA relies on the use of the recorded seismic response to an earthquake, whereas OMA and SM are based on long-term vibration monitoring data in operational conditions. In this way, two independent information are fused together for damage identification purposes. In addition, the combination of the SM with the IDA-based method allows reducing the uncertainties related to the latter. In particular, the benefits are related to the mitigation of the uncertainties in the localization task, seeking for the complementary consistency between these two model-based independent methods. The effective combination of the abovementioned three methods leads to the successful application of DORI for earthquake-induced damage detection, localization and quantification in historic masonry structures.

The Thesis deals extensively with the validation of different aspects of the DORI methodology, through application to four case study structures: an internationally well-known laboratory masonry structure and three CH masonry buildings, each presenting different structural and dynamic characteristics, and each presenting specific challenges. They are summarized below.

- The Brick House represents a reduced-scale masonry structure experimentally tested in the context of scientific studies aimed at assessing the seismic and out-of-plane performance of existing masonry buildings subjected to earthquakes. It was tested on the LNEC-3D shaking table, whereby the experimental results have been used as a reference for calibration of the FE model and first validation of the IDA-based earthquake-induced damage identification.

- The Consoli Palace represents an iconic stiff masonry palace where a long-term mixed static-dynamic SHM system has been implemented for more than two years. The availability of static measures (i.e. crack amplitude data) is a precious opportunity for improved data cleansing and consequently achieves an effective data fusion and enhanced data-driven damage detection.

- The Sciri Tower, a medieval civic tower incorporated into a building aggregate, has been under continuous monitoring by means of a simple vibration-based SHM system for about two years. The particular condition of the structural boundaries within the aggregate makes the damage localization task especially challenging.

- The San Pietro Bell Tower is a monumental masonry tower continuously monitored for about five years by a permanent vibration-based SHM system. It is worth noting that the tower experienced the three main shocks of the 2016 Central Italy seismic sequence.

Chapter 2 has presented the validation of the enhanced data-driven method in the case of the Consoli Palace, Chapter 3 has discussed the validation of the surrogate model-based procedure for earthquake-induced damage detection and localization in the case of the Sciri Tower, while results of validation of the proposed seismic IDA-based method have been presented considering two very different masonry structures (one low-rise and one slender), first in the case of the Brick House and subsequently for the San Pietro Bell Tower, in Chapter 4 and Chapter 5, respectively. The specific conclusions, chapter by chapter, are summarized below.

The presented results in Chapter 2 have demonstrated that the adopted enhanced vibration-based SHM tool in the case of the Consoli Palace enables rapid and automated earthquake-induced damage detection, even for small structural damages at an early stage, conceivably caused by a moderate/light seismic event. First of all, an automated SSI-data modal identification tool has allowed to effectively track the evolution in time of the natural frequencies of the six identified modes of the Palace for more than two years, which represents a novelty in the literature given the majority of SHM OMA-applications limited to masonry towers. The inclusion of crack amplitudes as predictors in the dynamic MLR model has successfully improved the statistical reconstruction of natural frequencies, therefore considered as more reliable damage-sensitive features. Subsequently, the advantage of using crack amplitude data as predictors has been demonstrated in novelty detection, by presenting the results of the control chart in the case of the undamaged structure, as well in the damaged one. In particular, the presented results of novelty analysis in the case of the damaged structure have demonstrated that very small artificially imposed variations in eigenfrequencies (frequency shifts of the order of 1%) have been effectively detected. Overall, in the present case of the Consoli Palace under permanent static and dynamic monitoring, it can be stated that all anomalies in the structural behavior have been clearly detected by means of the adopted enhanced vibration-based SHM method combining automated mode tracking, refined multiple data regression and novelty detection.

Chapter 3 has presented the application and validation of an improved version of a quadratic surrogate model-based procedure for earthquake-induced damage detection and localization in the case of the Sciri Tower, using long-term vibration monitoring data and numerical modeling. Damage localization task has been performed by solving an inverse FE model calibration problem, where equivalent elastic properties of selected macrostructural elements have been assessed by continuous minimization of an objective function based not only on experimentally identified and numerically predicted damage-induced decays in natural frequencies but also on changes in mode shapes. The proposed procedure has been validated by considering both simulated damage scenarios, in terms of artificially imposed damage-induced frequency decays, as well as a slight change in structural behavior experimentally observed after a seismic event, demonstrating that the proposed procedure is effective for both damage detection and localization. In addition, the results have been also validated through non-linear dynamic analysis carried out using the FE model, which has correctly localized some slight earthquake-induced damage at the connection between the tower and the aggregate, also confirmed by visual inspections. The proposed method can,

therefore, be considered as an effective and quick tool for rapid post-earthquake damage identification on historic masonry towers based on long-term dynamic monitoring.

The presented results in Chapter 4 have demonstrated that the adopted IDA-based procedure constitutes an innovative method for localization and quantification of earthquake-induced damages in masonry structures, with application to the Brick House. The method relies on a priori IDA carried out from a numerical model and construction of multidimensional IDA curve sets relating meaningful local damage parameters to selected seismic intensity measures such that, when an earthquake occurs, local damage conditions are immediately estimated using intensity measures computed from seismic data. A preliminary statistical correlation analysis of intensity measures has allowed an investigation on their interdependence, and consequently a first selection. Afterwards, the less dispersed IDA curve sets have been constructed by means of the most efficient intensity parameters versus meaningful local damage measures (e.g. tensile damage). The IDA-based tool has demonstrated to correctly localize damage in specific parts of the structure and to quantify earthquake-induced damage with a good level of approximation, in particular, in terms of overall weighted average estimation of damage ranges and weighted mean values. For this purpose, intensity measures computed from three real seismic events have been exploited. Overall, the results have demonstrated that the proposed seismic IDA-based procedure is capable of rapidly and correctly localizing and quantifying earthquake-induced damage, thereby showing great potential for damage assessment of masonry structures in the context of monitoring for preventive conservation of architectural heritage.

Finally, Chapter 5 has presented the results concerning the validation of the proposed seismic IDA-based method in the case of a very important case study, the San Pietro Bell Tower. The results have been particularly interesting due to the integration of the IDA-based damage identification with seismic SHM data, allowing the proposal and exploitation of some original response intensity measures. The tower experienced important seismic events during the 2016 Central Italy seismic sequence, whereby data-driven damage detection has been already efficiently proved and, to some extent, also damage quantification in the form of permanent variations in natural frequencies. The proposed IDA-based method has been applied and validated through the FE model of the structure. In the case of the San Pietro Bell Tower, the multidimensional IDA curve sets have been constructed relating meaningful local damage parameters (associated with the shaft, belfry and cusp) to selected seismic intensity measures, as well as seismic response intensity mea-

sures. They all have immediately identified absolutely the most damaged/damageable part: the belfry. Seismic input and experimentally seismic response records, belonging to the 2016 Central Italy seismic sequence, have been used aiming at earthquake-induced damage localization and quantification. It should be emphasized that the introduction of the additional seismic response intensity measures, with respect to the seismic input ones alone, has allowed a clear refinement of the IDA-based results on earthquake-induced quantification, in particular, a higher consistency between numerical mean actual damages and weighted average IDA-based mean values. The presented results have validated the proposed seismic IDA-based SHM procedure, for rapidly and correctly localizing and quantifying earthquake-induced damage in the case of the San Pietro Bell Tower.

Overall, the DORI methodology proposed in this Thesis has been successfully applied and validated in historic masonry structures, most of which under permanent SHM monitoring for a relatively long period of time. It has demonstrated to be an innovative and valuable tool for earthquake-induced damage detection, localization and quantification in CH buildings, particularly, in the context of rapid post-earthquake damage assessment of long-term monitored CH structures for priority post-event decision making, condition-based maintenance and preventive conservation. Further developments of this research work could concern the application of the DORI methodology to other masonry buildings, with more complex structural configurations and less predictable damage modalities. The methodology could also be particularized to other non-linear dynamic analysis tools, in addition to IDA.

Appendix A

Appendix: Ground motions

Contents:

In this Appendix, the interested reader can consult the list of the selected ground motions used for the statistical correlation study of IMs, reported in Section 4.3. Detailed information is reported. The selection was such as to cover many of the well-known accelerograms from earthquakes of the last fifty (50) years.

A.1   Ground motions

A total of one hundred (100) ground motions have been used in this dissertation for the statistical correlation study of IMs, reported in Section 4.3. This Appendix presents information about the selected ground motions, provided by ITACA (ITalian ACcelerometric Archive) strong motion database (Pacor et al. 2011).

A representation of the distribution of the strong motion data as a function of magnitude (moment magnitude M_w and local magnitude M_L), epicentral distance, subsoil category, hypocentral depth and faulting mechanism is illustrated in Fig. A.1. The informations are also reported in Tab. A.1. In particular, the following descriptions are provided: ITACA seismic event ID, earthquake epicenter and date, moment magnitude M_w and local magnitude M_L, faulting mechanism, focal hypocentral depth, seismic station ID from where the ground motion waveforms have been recorded, and subsoil category (denoted as C.) and epicentral distance (denoted as Ep. d.) of the latter. Ordinary ground motions and pulse-like near-fault ones have been considered. The magnitude of all earthquakes ranges from 4.5 to 7. The vast majority of the time histories are recorded on soil classified as type A (and A*), B (and B*) and C (and C*), according to the EC8 (EN 1998-1 2005) soil-site classification. It is noteworthy to stress that seismic input data are provided in terms of acceleration, velocity and displacement time histories, in East and North directions.
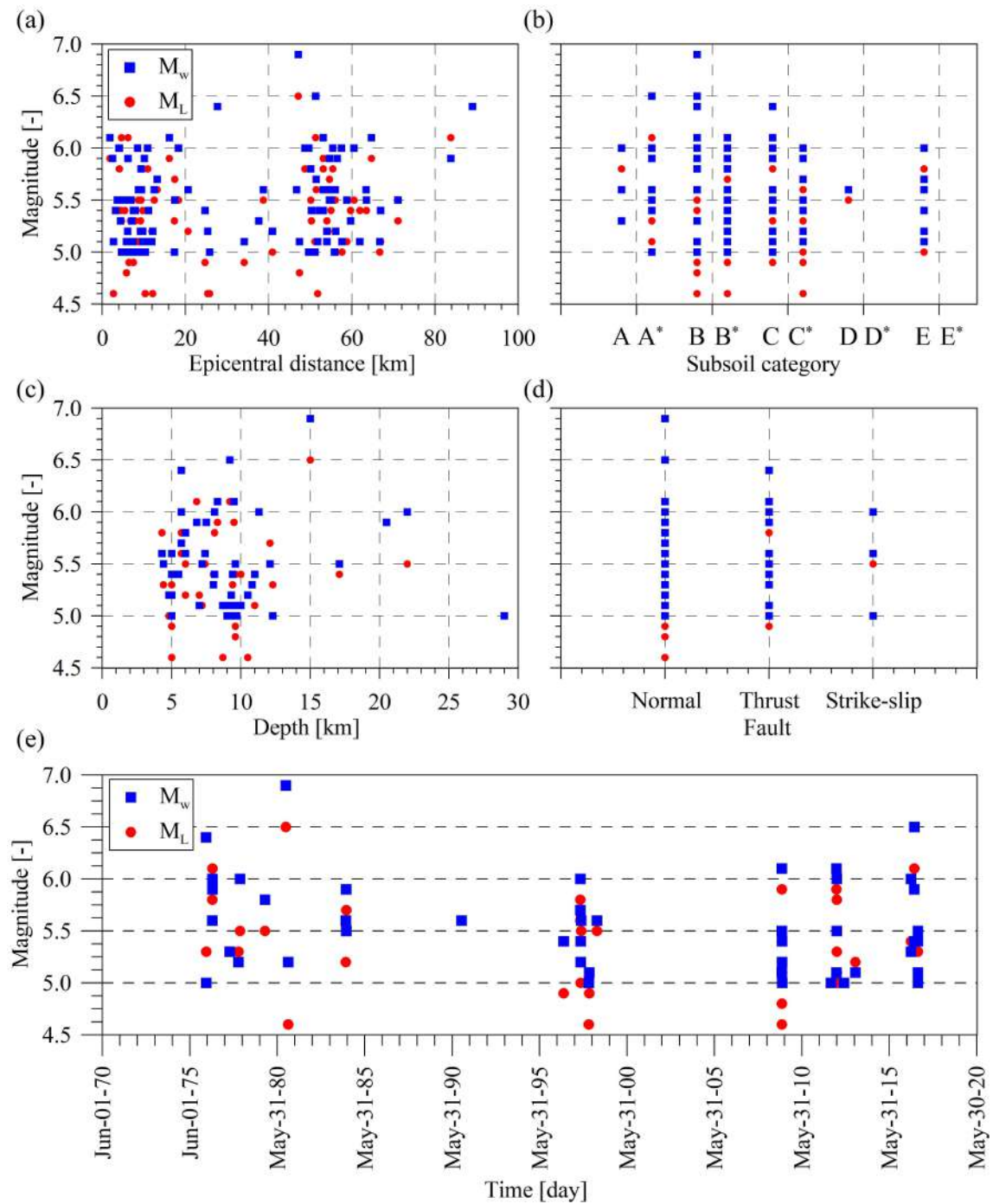
Figure A.1: Plots of earthquake magnitude versus epicentral distance (a), subsoil category (b), hypocentral depth (c), faulting mechanism (d) and time (e) for all strong ground motions used in the statistical correlation analysis of IMs.

164

Table A.1: The main information of selected ground motions.

Event ID [−]	Epicenter [−]	Date [yyyy/mm/dd]	M_w/M_L [−]	Fault [−]	Depth [km]	Station [−]	C. [−]	Ep. d. [km]
EMSC − 20161030_0000029	Norcia	2016/10/30	6.5/6.1	Normal	9.2	IT.NRC	B	4.6
EMSC − 20161030_0000029	Norcia	2016/10/30	6.5/6.1	Normal	9.2	IT.TER	A*	51.3
EMSC − 20160824_0000006	Accumoli	2016/08/24	6.0/6.0	Normal	8.1	IT.AMT	B	8.5
EMSC − 20160824_0000006	Accumoli	2016/08/24	6.0/6.0	Normal	8.1	IT.TLN	B*	57.5
EMSC − 20161026_0000077	C.S.A. Sul Nera	2016/10/26	5.4/5.4	Normal	8.1	IT.CNE	C*	3.2
EMSC − 20161026_0000077	C.S.A. Sul Nera	2016/10/26	5.4/5.4	Normal	8.1	IT.VAL	B*	53.1
EMSC − 20161026_0000095	Visso	2016/10/26	5.9/5.9	Normal	7.5	IT.CNE	C*	2.5
EMSC − 20161026_0000095	Visso	2016/10/26	5.9/5.9	Normal	7.5	IT.SIG	C*	56.5
EMSC − 20170118_0000034	Capitignano	2017/01/18	5.5/5.4	Normal	9.6	IT.PCB	B*	5.4
EMSC − 20170118_0000034	Capitignano	2017/01/18	5.5/5.4	Normal	9.6	IT.FOC	C*	63.5
EMSC − 20170118_0000037	Capitignano	2017/01/18	5.4/5.3	Normal	9.4	IT.PCB	B*	7.9
EMSC − 20170118_0000037	Capitignano	2017/01/18	5.4/5.3	Normal	9.4	IT.UST	A*	50.3
EMSC − 20170118_0000027	Montereale	2017/01/18	5.1/5.4	Normal	10.0	IT.AMT	B	9.7
EMSC − 20170118_0000027	Montereale	2017/01/18	5.1/5.4	Normal	10.0	IT.FOC	C*	61.9
EMSC − 20170118_0000019	C. Amiterno	2017/01/18	5.0/5.1	Normal	9.5	IT.MSCT	B*	8.6
EMSC − 20170118_0000019	C. Amiterno	2017/01/18	5.0/5.1	Normal	9.5	IT.SPM	A*	51.1
EMSC − 20160824_0000013	Norcia	2016/08/24	5.3/5.4	Normal	8.0	IT.NRC	B	4.4
EMSC − 20160824_0000013	Norcia	2016/08/24	5.3/5.4	Normal	8.0	IT.MCT	B*	59.7

| Event ID | Epicenter | Date | M_w/M_L | Fault | Depth | Station | C. | Ep. d. |
[−]	[−]	[yyyy/mm/dd]	[−]	[−]	[km]	[−]	[−]	[km]
IT − 2009 − 0102	Fossa	2009/04/07	5.5/5.4	Normal	17.1	4A.MI05	A*	3.6
IT − 2009 − 0102	Fossa	2009/04/07	5.5/5.4	Normal	17.1	IT.CHT	B*	55.0
IT − 1998 − 0054	Gualdo Tadino	1998/04/03	5.1/4.9	Normal	9.6	IT.NOCE	B*	6.4
IT − 1998 − 0054	Gualdo Tadino	1998/04/03	5.1/4.9	Normal	9.6	IT.SELW	B	34.1
IT − 1997 − 0091	Foligno	1997/10/06	5.4/5.4	Normal	5.5	IT.NCR2	E	11.1
IT − 1997 − 0091	Foligno	1997/10/06	5.4/5.4	Normal	5.5	IT.LNS	C*	52.1
IT − 2012 − 0010	Cavezzo	2012/05/29	5.5/5.3	Thrust	4.4	IV.T0819	C	6.8
IT − 2012 − 0010	Cavezzo	2012/05/29	5.5/5.3	Thrust	4.4	IT.CPC	C*	71.1
IT − 2009 − 0140	L'Aquila	2009/04/09	5.2/5.0	Normal	9.3	IT.PCB	B*	6.1
IT − 2009 − 0140	L'Aquila	2009/04/09	5.2/5.0	Normal	9.3	IT.SPO	B*	56.1
IT − 2009 − 0032	L'Aquila	2009/04/06	5.1/4.6	Normal	8.7	IT.AQM	B*	2.7
IT − 2009 − 0032	L'Aquila	2009/04/06	5.1/4.6	Normal	8.7	IT.NOR	B	51.8
IT − 1976 − 0007	Osoppo	1976/05/11	5.0/5.3	Thrust	12.3	E.FRC	B	4.6
IT − 1976 − 0007	Osoppo	1976/05/11	5.0/5.3	Thrust	12.3	IT.TLM1	B	17.3
IT − 2009 − 0121	L'Aquila	2009/04/09	5.4/5.1	Normal	11.0	IT.PCB	B*	7.7
IT − 2009 − 0121	L'Aquila	2009/04/09	5.4/5.1	Normal	11.0	IT.CHT	B*	66.9
IT − 1997 − 0062	Foligno	1997/10/03	5.2/5.0	Normal	4.8	IT.NCR2	E	9.7
IT − 1997 − 0062	Foligno	1997/10/03	5.2/5.0	Normal	4.8	IT.GBB	B*	40.9
IT − 2009 − 0174	L'Aquila	2009/04/13	5.0/5.0	Normal	9.0	IT.PCB	B*	7.4
IT − 2009 − 0174	L'Aquila	2009/04/13	5.0/5.0	Normal	9.0	IV.TRTR	B*	55.9
IT − 2009 − 0095	L'Aquila	2009/04/07	5.1/4.8	Normal	9.6	IT.AQV	B	5.8
IT − 2009 − 0095	L'Aquila	2009/04/07	5.1/4.8	Normal	9.6	IT.ORC	B	47.4
IT − 2009 − 0084	Pizzoli	2009/04/06	5.1/5.0	Normal	9.7	IT.AQV	B	10.1
IT − 2009 − 0084	Pizzoli	2009/04/06	5.1/5.0	Normal	9.7	IV.GUMA	B*	66.7
IT − 1978 − 0002	South Italy	1978/03/11	5.2/5.3	Normal	5.0	IT.FRR	B*	9.2
IT − 1978 − 0002	South Italy	1978/03/11	5.2/5.3	Normal	5.0	IT.VLS2	C	54.0
IT − 2012 − 0002	Poviglio	2012/01/25	5.0/5.0	Strike-slip	29.0	IT.SRP	C	5.6
IT − 2012 − 0002	Poviglio	2012/01/25	5.0/5.0	Strike-slip	29.0	IT.PTV	C	55.8

Event ID [−]	Epicenter [−]	Date [yyyy/mm/dd]	M_w/M_L [−]	Fault [−]	Depth [km]	Station [−]	C. [−]	Ep. d. [km]
IT − 1996 − 0003	Bagnolo in Piano	1996/10/15	5.4/4.9	Thrust	5.0	IT.NVL	C	7.5
IT − 1996 − 0003	Bagnolo in Piano	1996/10/15	5.4/4.9	Thrust	5.0	IT.SMC1	C*	24.7
IT − 2012 − 0009	San felice sul Panaro	2012/05/20	5.1/5.0	Thrust	9.1	IT.MRN	C	7.4
IT − 2012 − 0009	San felice sul Panaro	2012/05/20	5.1/5.0	Thrust	9.1	IT.CPC	C*	57.6
IT − 2013 − 0005	Fivizzano	2013/06/21	5.1/5.2	Normal	7.0	IT.FVZ	E	11.9
IT − 2013 − 0005	Fivizzano	2013/06/21	5.1/5.2	Normal	7.0	IT.SMP	B*	54.0
IT − 1977 − 0008	Trasaghis	1977/09/16	5.3/5.3	Thrust	10.8	E.FRC	B	7.1
IT − 1977 − 0008	Trasaghis	1977/09/16	5.3/5.3	Thrust	10.8	IT.BRC	A	37.6
IT − 1998 − 0103	Laino Borgo	1998/09/09	5.6/5.5	Normal	7.4	IT.LRG	B	12.5
IT − 1998 − 0103	Laino Borgo	1998/09/09	5.6/5.5	Normal	7.4	IT.GRM	C	38.7
IT − 2012 − 0032	San Possidonio	2012/05/29	5.5/5.1	Thrust	7.2	IT.MRN	C	6.9
IT − 2012 − 0032	San Possidonio	2012/05/29	5.5/5.1	Thrust	7.2	IV.T0815	C*	58.8
IT − 2012 − 0011	Medolla	2012/05/29	6.0/5.8	Thrust	8.1	IT.MRN	C	4.1
IT − 2012 − 0011	Medolla	2012/05/29	6.0/5.8	Thrust	8.1	IT.ISD	C	48.7
IT − 2009 − 0009	L'Aquila	2009/04/06	6.1/5.9	Normal	8.3	IT.AQK	B	1.8
IT − 2009 − 0009	L'Aquila	2009/04/06	6.1/5.9	Normal	8.3	IT.MMP	B*	53.1
IT − 1997 − 0006	Foligno	1997/09/26	6.0/5.8	Normal	5.7	IT.NCR	E	10.9
IT − 1997 − 0006	Foligno	1997/09/26	6.0/5.8	Normal	5.7	IT.PTL	B*	55.4
IT − 1997 − 0004	Foligno	1997/09/26	5.7/5.6	Normal	5.7	IT.NCR	E	13.2
IT − 1997 − 0004	Foligno	1997/09/26	5.7/5.6	Normal	5.7	IT.LNS	C*	51.4
IT − 1976 − 0002	Lusevera	1976/05/06	6.4/6.4	Thrust	5.7	IT.TLM1	B	27.7
IT − 1976 − 0002	Lusevera	1976/05/06	6.4/6.4	Thrust	5.7	IT.CNG	C	89.0
IT − 1976 − 0030	Gemona del Friuli	1976/09/15	6.0/6.0	Thrust	11.3	IV.GMN	B	4.0
IT − 1976 − 0030	Gemona del Friuli	1976/09/15	6.0/6.0	Thrust	11.3	IT.BRC	A	49.6
IT − 1976 − 0025	Udine	1976/09/11	5.6/5.8	Thrust	4.3	IV.GMN	B	9.4
IT − 1976 − 0025	Udine	1976/09/11	5.6/5.8	Thrust	4.3	IT.BRC	A	53.1
IT − 1976 − 0027	Lusevera	1976/09/15	5.9/6.1	Thrust	6.8	IV.GMN	B	6.2
IT − 1976 − 0027	Lusevera	1976/09/15	5.9/6.1	Thrust	6.8	IT.CNG	C	83.8

Event ID	Epicenter	Date	M_w/M_L	Fault	Depth	Station	C.	Ep. d.
[−]	[−]	[yyyy/mm/dd]	[−]	[−]	[km]	[−]	[−]	[km]
IT − 1981 − 0001	Pescopagano	1981/01/16	5.2/4.6	Normal	10.5	IT.CR2	C*	12.1
IT − 1981 − 0001	Pescopagano	1981/01/16	5.2/4.6	Normal	10.5	IT.SLB	B*	25.3
IT − 1980 − 0012	Laviano	1980/11/23	6.9/6.5	Normal	15.0	IT.CLT	B	18.9
IT − 1980 − 0012	Laviano	1980/11/23	6.9/6.5	Normal	15.0	IT.MRT	B	47.1
IT − 2012 − 0008	Finale Emilia	2012/05/20	6.1/5.9	Thrust	9.5	IT.MRN	C	16.1
IT − 2012 − 0008	Finale Emilia	2012/05/20	6.1/5.9	Thrust	9.5	IT.SRP	C	64.7
IT − 1976 − 0027	Lusevera	1976/09/15	5.9/6.1	Thrust	6.8	IV.GMN	B	6.2
IT − 1976 − 0027	Lusevera	1976/09/15	5.9/6.1	Thrust	6.8	IT.CNG	C	83.8
IT − 1990 − 0003	Sicily	1990/12/13	5.6/5.6	Strike-slip	5.0	IT.CAT	D	46.7
IT − 1990 − 0003	Sicily	1990/12/13	5.6/5.6	Strike-slip	5.0	IT.VZZ	B*	63.4
IT − 2012 − 0061	Mormanno	2012/10/25	5.0/5.0	Normal	9.7	IT.0PAP	B*	8.9
IT − 2012 − 0061	Mormanno	2012/10/25	5.0/5.0	Normal	9.7	IT.GRM	C	49.6
IT − 1979 − 0009	Norcia	1979/09/19	5.8/5.5	Normal	6.0	IT.CSC	B	9.3
IT − 1979 − 0009	Norcia	1979/09/19	5.8/5.5	Normal	6.0	IT.SVT	B*	50.1
IT − 1984 − 0002	Perugia	1984/04/29	5.6/5.2	Normal	6.0	IT.NCR	E	20.6
IT − 1984 − 0002	Perugia	1984/04/29	5.6/5.2	Normal	6.0	IT.PGL	C	54.3
IT − 1997 − 0137	Foligno	1997/10/14	5.6/5.5	Normal	6.0	IT.CESM	A*	8.7
IT − 1997 − 0137	Foligno	1997/10/14	5.6/5.5	Normal	6.0	IT.RTI	D	56.0
IT − 1978 − 0004	Patti	1978/04/15	6.0/5.5	Strike-slip	22.0	IT.PTT1	C*	18.3
IT − 1978 − 0004	Patti	1978/04/15	6.0/5.5	Strike-slip	22.0	IT.GRR	A*	60.5
IT − 1984 − 0005	Villetta Barrea	1984/05/11	5.5/5.7	Normal	12.1	E.ATQ	B*	17.4
IT − 1984 − 0005	Villetta Barrea	1984/05/11	5.5/5.7	Normal	12.1	IT.SCF	B*	54.6
IT − 1984 − 0004	Settefrati	1984/05/07	5.9/5.9	Normal	20.5	IT.ATN	A*	10.1
IT − 1984 − 0004	Settefrati	1984/05/07	5.9/5.9	Normal	20.5	IT.BSS	B*	54.6
IT − 1998 − 0028	Foligno	1998/03/21	5.0/4.6	Normal	5.0	IT.SELW	B	10.3
IT − 1998 − 0028	Foligno	1998/03/21	5.0/4.6	Normal	5.0	IT.NRC	B	25.8

Appendix B

Appendix: The IDA Curve Sets

Contents:

In this Appendix, the damage pattern evolution in the case of the Brick House as well as the San Pietro Bell Tower with increasing levels of earthquake input is reported in terms of tensile damage d_t contour plots obtained at the last step of the non-linear dynamic analyses with IT0806xa_m and IT0788 earthquakes, respectively.

In addition, the interested reader can consult all the IDA curve sets, relating the local DMs to the most efficient IMs, of both masonry structures. Only a few of these graphs are illustrared in the corresponding Chapters: for the Brick House in Chapter 4 and the San Pietro Bell Tower in Chapter 5.

B.1   The Brick House

For a better understanding of the damage pattern evolution in the case of the Brick House with increasing levels of earthquake input (see SFs in Section 4.4.2), tensile damage d_t contour plots obtained at the last step of the non-linear dynamic analyses with IT0806xa_m earthquake are illustrated in Fig. B.1.

Considering the ten (10) parts, *IDA curve sets* relate the local DMs to the preselected IMs. According to the correlation study, described in Section 4.3, the most uncorrelated, meaningful and representative IMs that have been selected and used for the construction of IDA curves are: PGA, RMSA, I_C, I_A, P_D, CAV, $S_a(T1)$, ASI_{VT}, PGV, RMSV, SED, CAD, $S_v(T1)$, I_H, PGD, RMSD, $S_d(T1)$, DSI_{NH} and E_I. The most efficient IMs ultimately considered for IDA are the following eight (8): PGA, I_C, I_A, $S_a(T1)$, ASI, PGV, $S_v(T1)$ and I_H ($m^*=8$ with reference to Eq. (4.4)). In this Appendix, the IDA curve sets (each containing seven (7) curves plus their mean curve) obtained in the case of tensile damage, d_t, and first principal plastic strain, ε_1^{pl}, versus the most efficient eight (8) IMs have been reported, from Fig. B.2 to Fig. B.17.
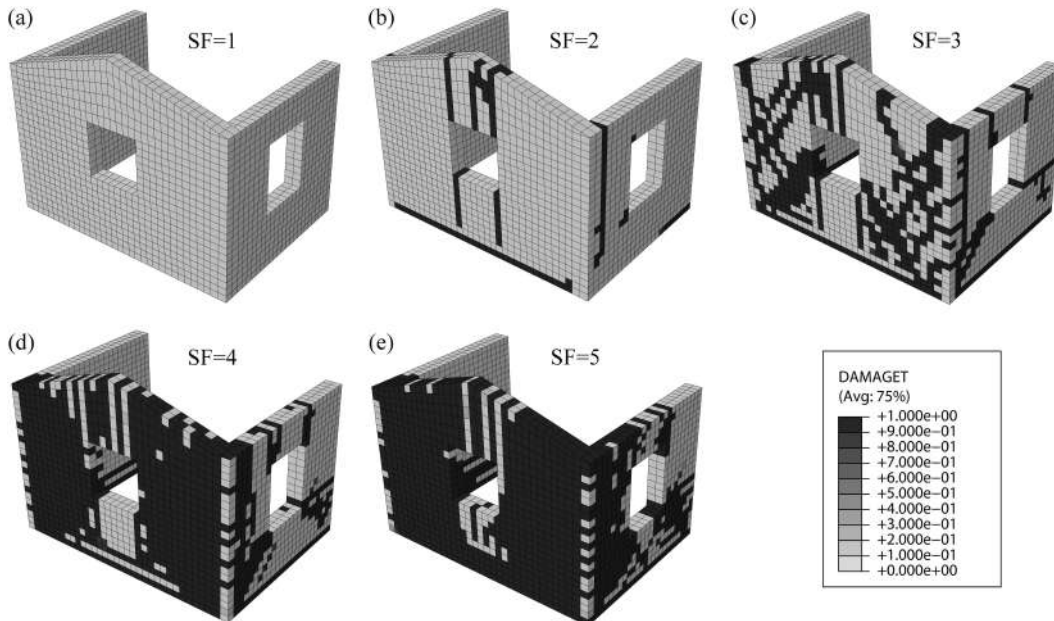
Figure B.1: Tensile damage d_t contour plots on the Brick House obtained at the last step of the IDAs with IT0806xa_m earthquake with increasing levels of the seismic input.

Figure B.2: The IDA curve sets and corresponding mean curves for the ten (10) parts of the Brick House: plots of tensile damage (d_t) versus PGA (a-j).

Figure B.3: The IDA curve sets and corresponding mean curves for the ten (10) parts of the Brick House: plots of tensile damage (d_t) versus I_C (a-j).

Figure B.4: The IDA curve sets and corresponding mean curves for the ten (10) parts of the Brick House: plots of tensile damage (d_t) versus I_A (a-j).

Figure B.5: The IDA curve sets and corresponding mean curves for the ten (10) parts of the Brick House: plots of tensile damage (d_t) versus $S_a(T1)$ (a-j).

Figure B.6: The IDA curve sets and corresponding mean curves for the ten (10) parts of the Brick House: plots of tensile damage (d_t) versus ASI (a-j).

Figure B.7: The IDA curve sets and corresponding mean curves for the ten (10) parts of the Brick House: plots of tensile damage (d_t) versus PGV (a-j).

Figure B.8: The IDA curve sets and corresponding mean curves for the ten (10) parts of the Brick House: plots of tensile damage (d_t) versus $S_v(T1)$ (a-j).
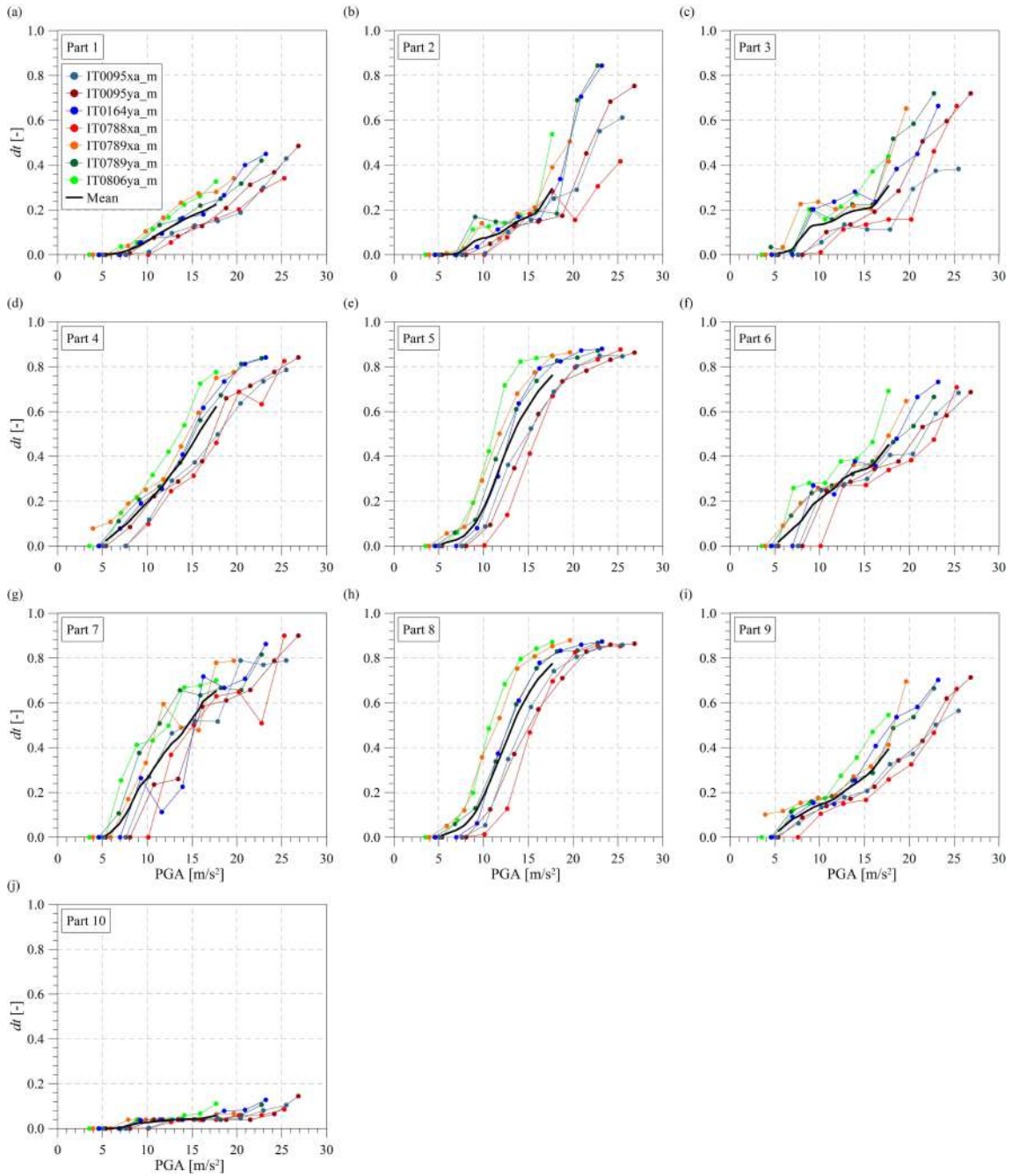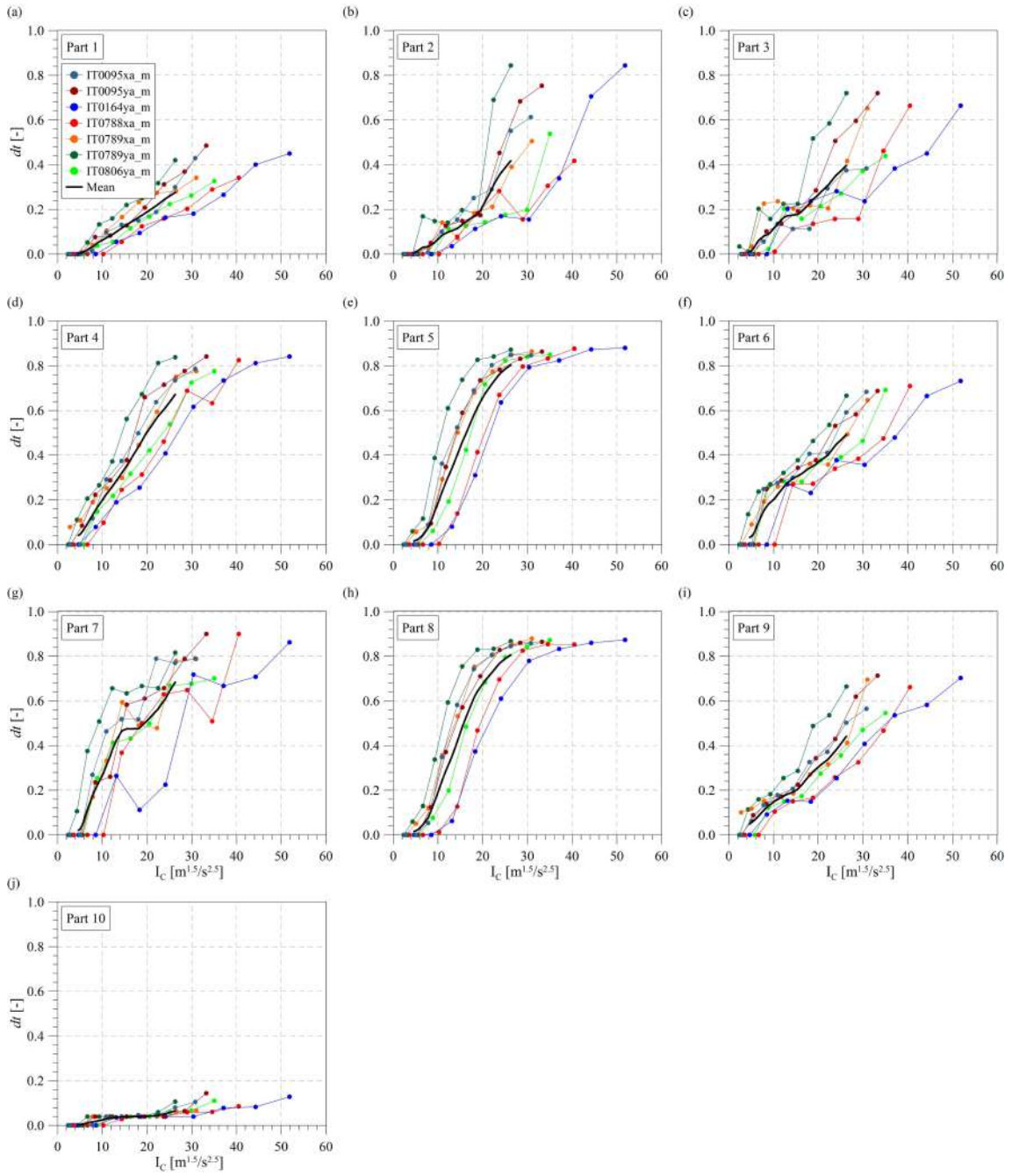
Figure B.9: The IDA curve sets and corresponding mean curves for the ten (10) parts of the Brick House: plots of tensile damage (d_t) versus I_H (a-j).

Figure B.10: The IDA curve sets and corresponding mean curves for the ten (10) parts of the Brick House: plots of first principal plastic strain ($\varepsilon_1^{\mathrm{pl}}$) versus PGA (a-j).

Figure B.11: The IDA curve sets and corresponding mean curves for the ten (10) parts of the Brick House: plots of first principal plastic strain ($\varepsilon_1^{\mathrm{pl}}$) versus $\mathrm{I_C}$ (a-j).
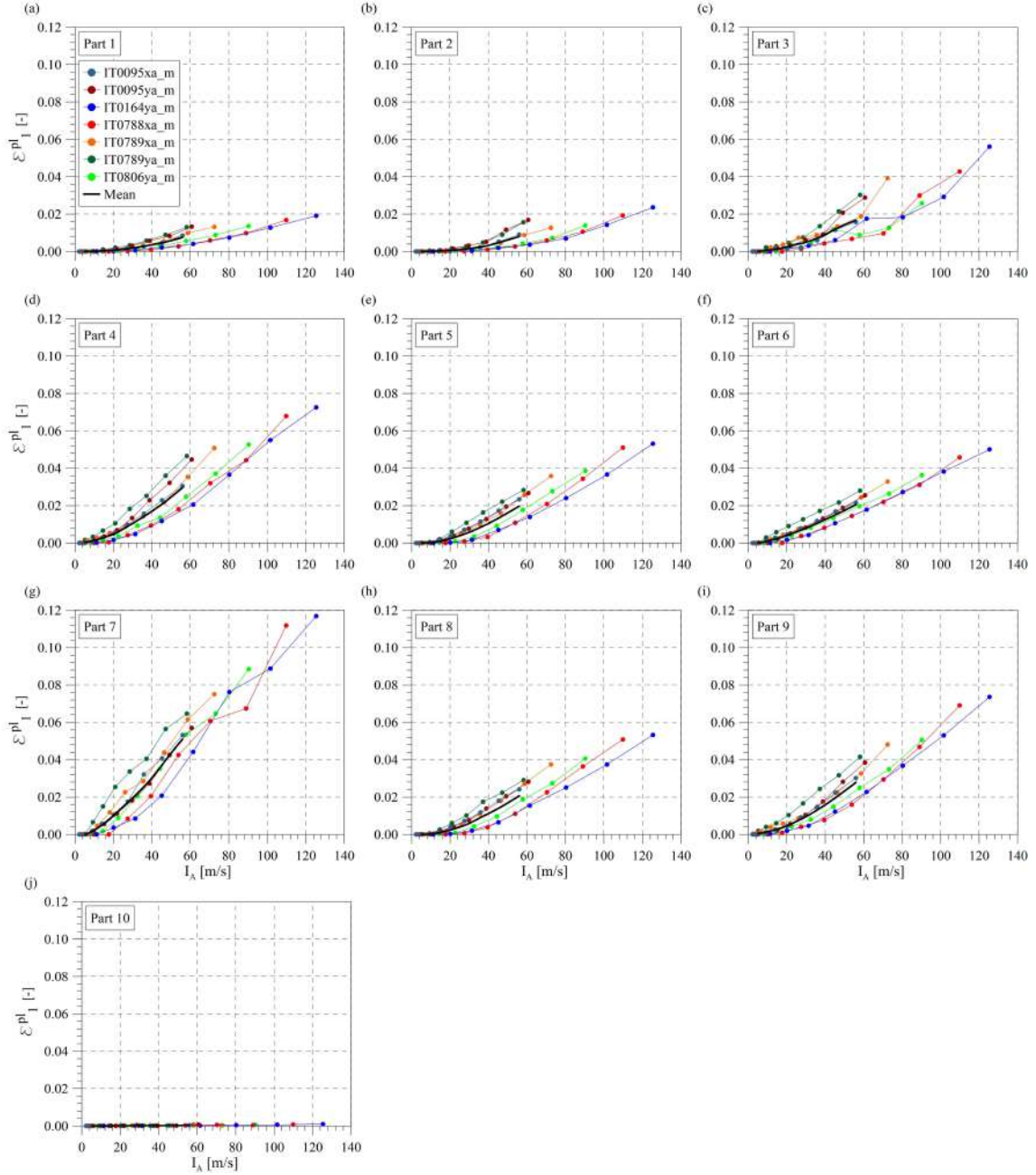
Figure B.12: The IDA curve sets and corresponding mean curves for the ten (10) parts of the Brick House: plots of first principal plastic strain $(\varepsilon_1^{\mathrm{pl}})$ versus $\mathrm{I_A}$ (a-j).
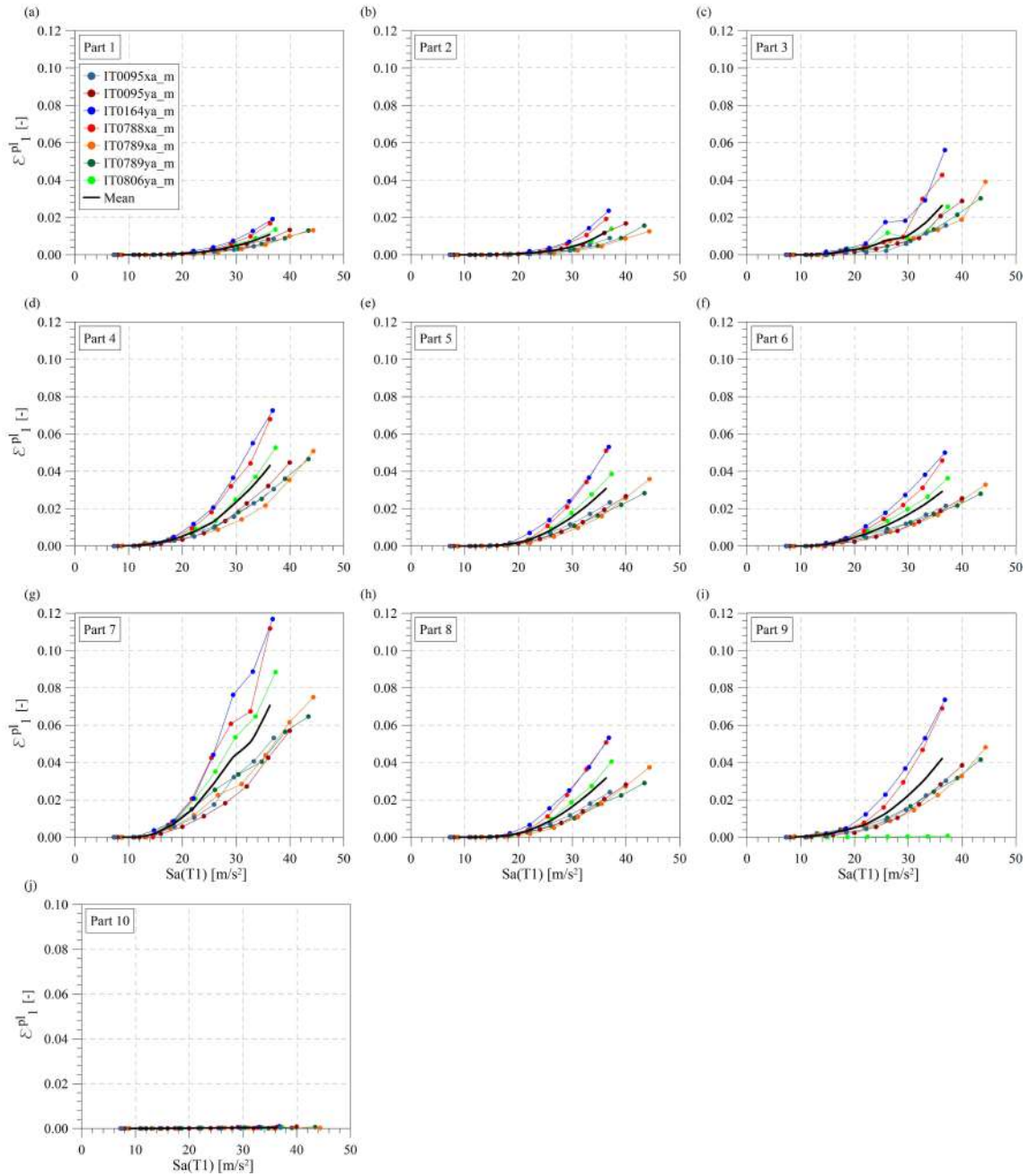
Figure B.13: The IDA curve sets and corresponding mean curves for the ten (10) parts of the Brick House: plots of first principal plastic strain (ε_1^{pl}) versus $S_a(T1)$ (a-j).
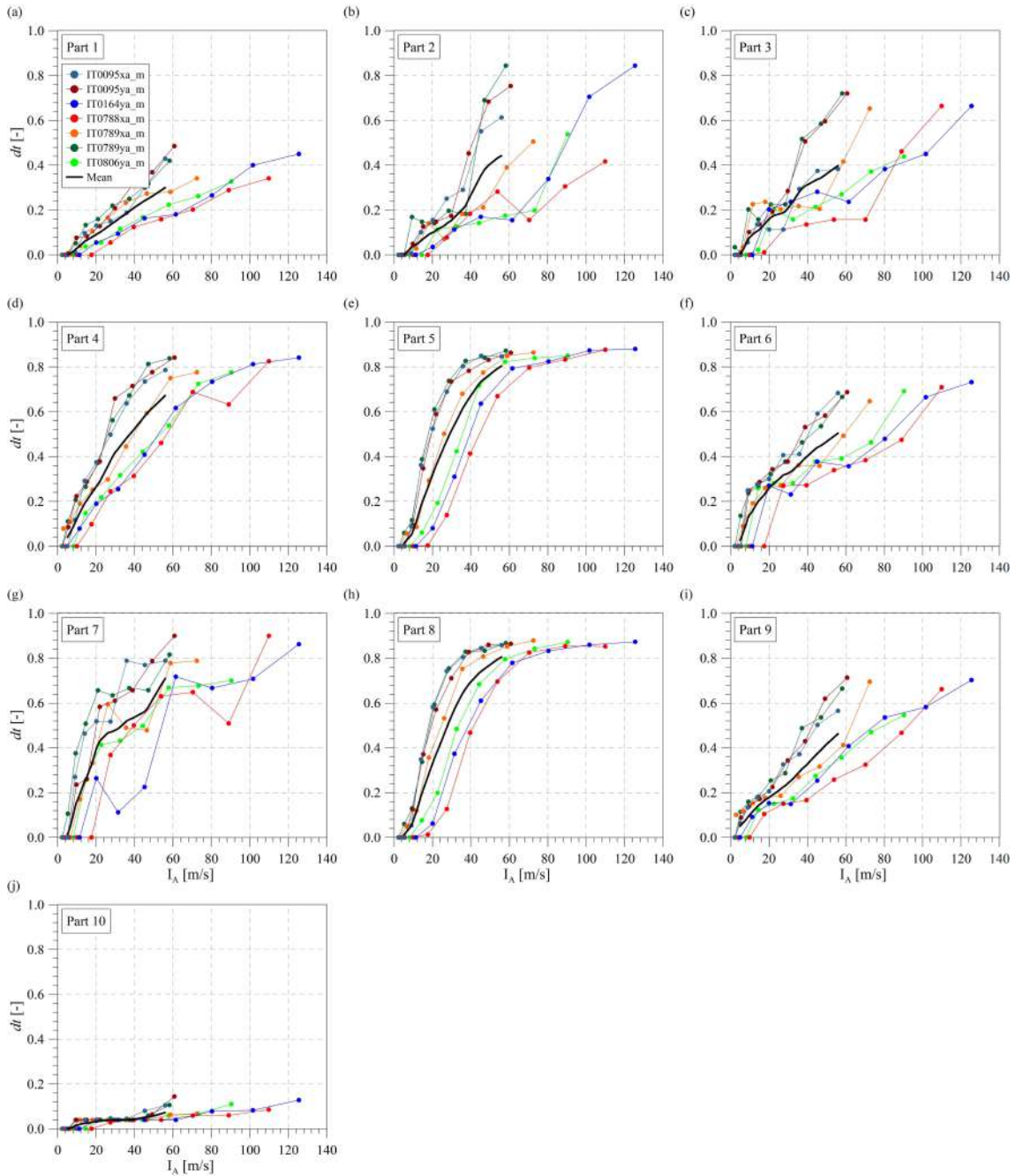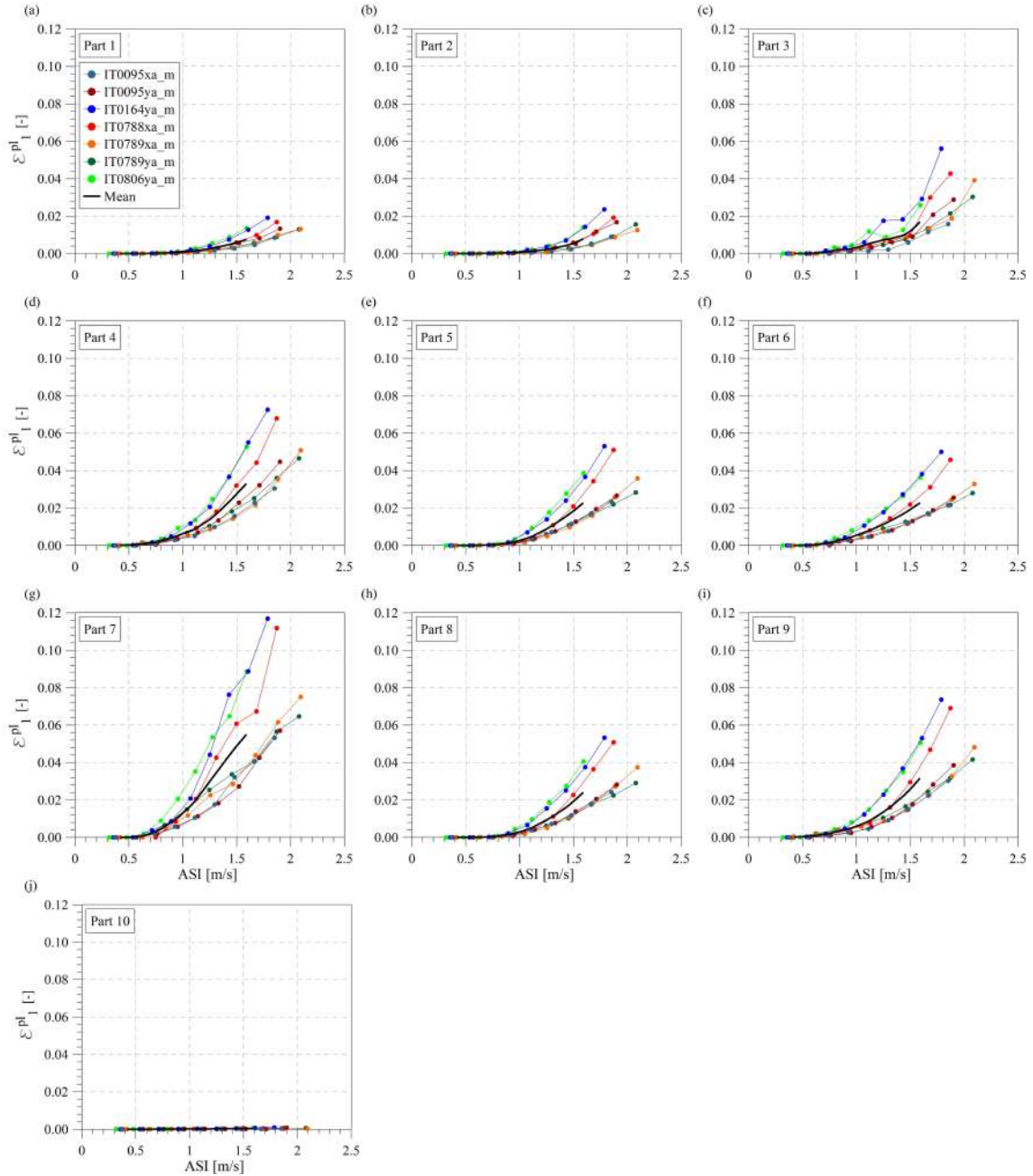
Figure B.14: The IDA curve sets and corresponding mean curves for the ten (10) parts of the Brick House: plots of first principal plastic strain ($\varepsilon_1^{\mathrm{pl}}$) versus ASI (a-j).
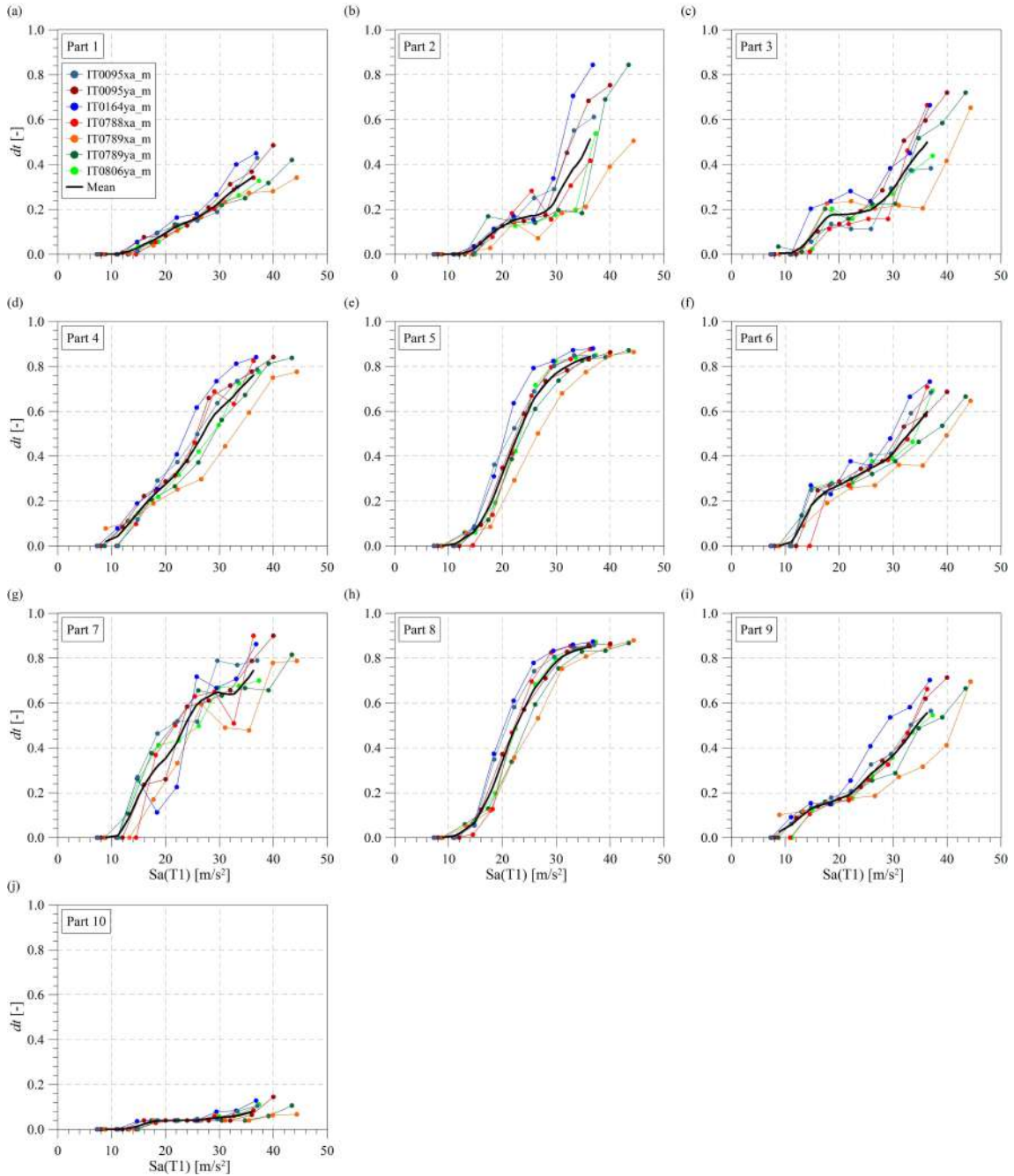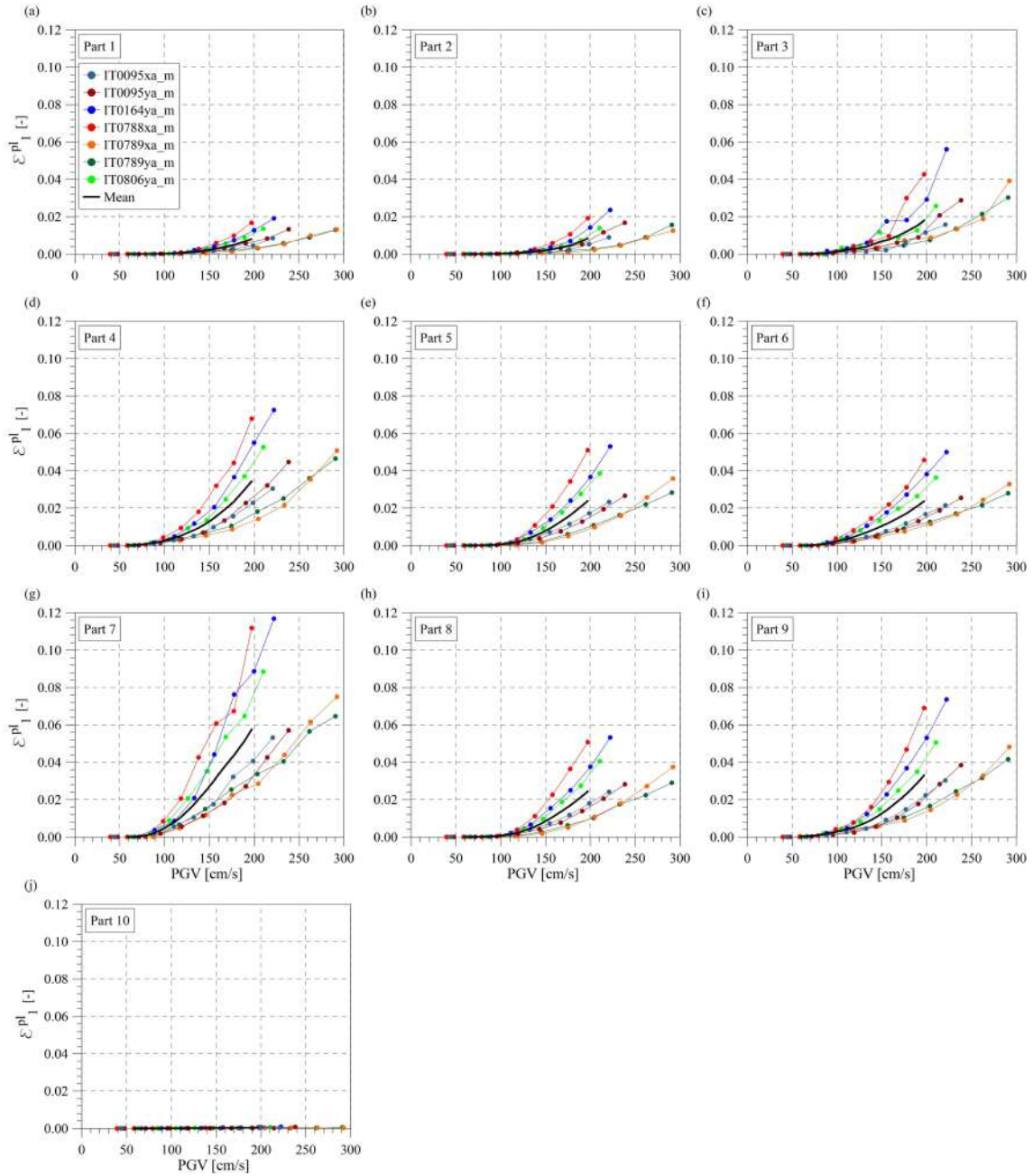
Figure B.15: The IDA curve sets and corresponding mean curves for the ten (10) parts of the Brick House: plots of first principal plastic strain ($\varepsilon_1^{\mathrm{pl}}$) versus PGV (a-j).
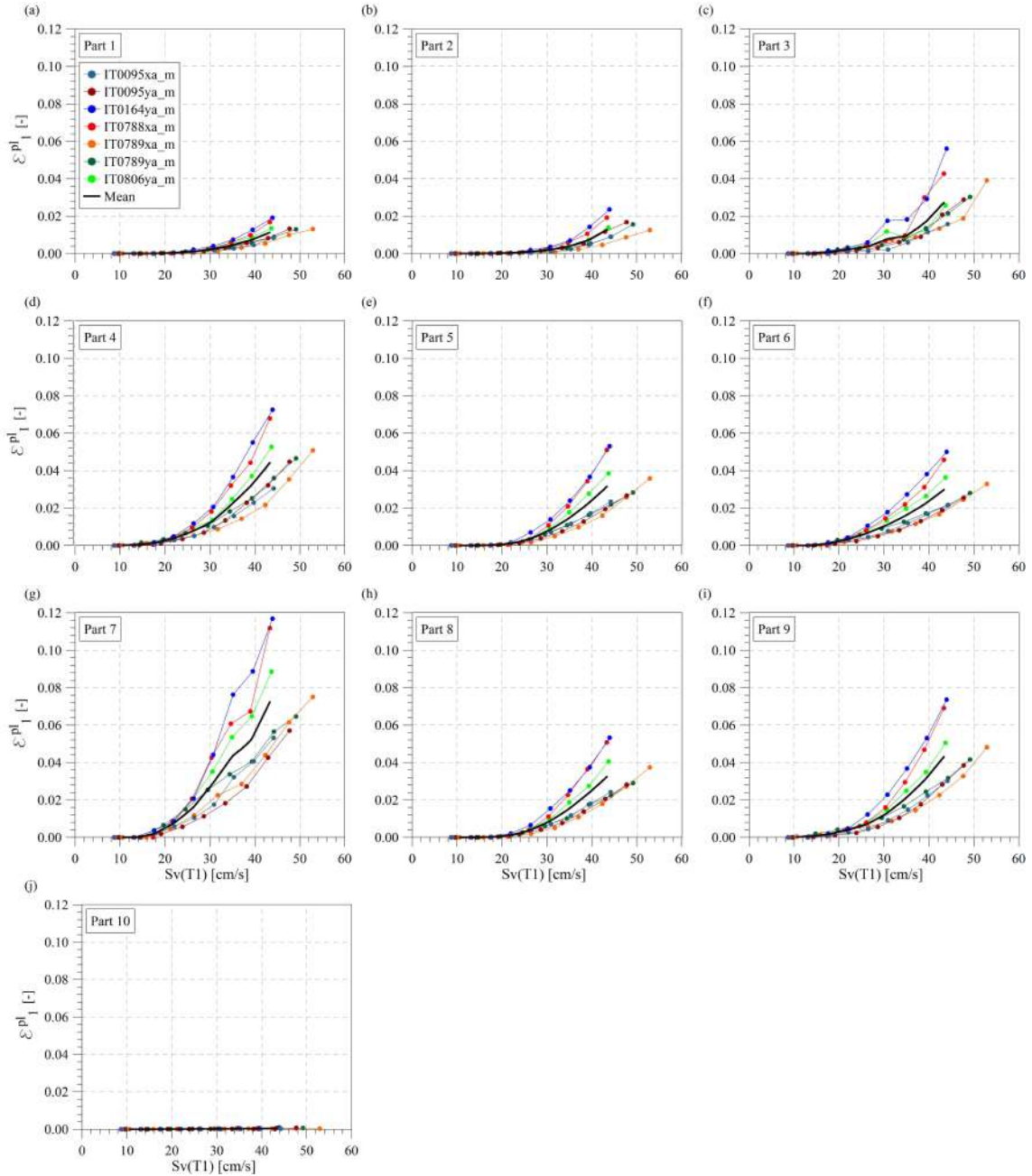
Figure B.16: The IDA curve sets and corresponding mean curves for the ten (10) parts of the Brick House: plots of first principal plastic strain ($\varepsilon_1^{\mathrm{pl}}$) versus $S_v(T1)$ (a-j).
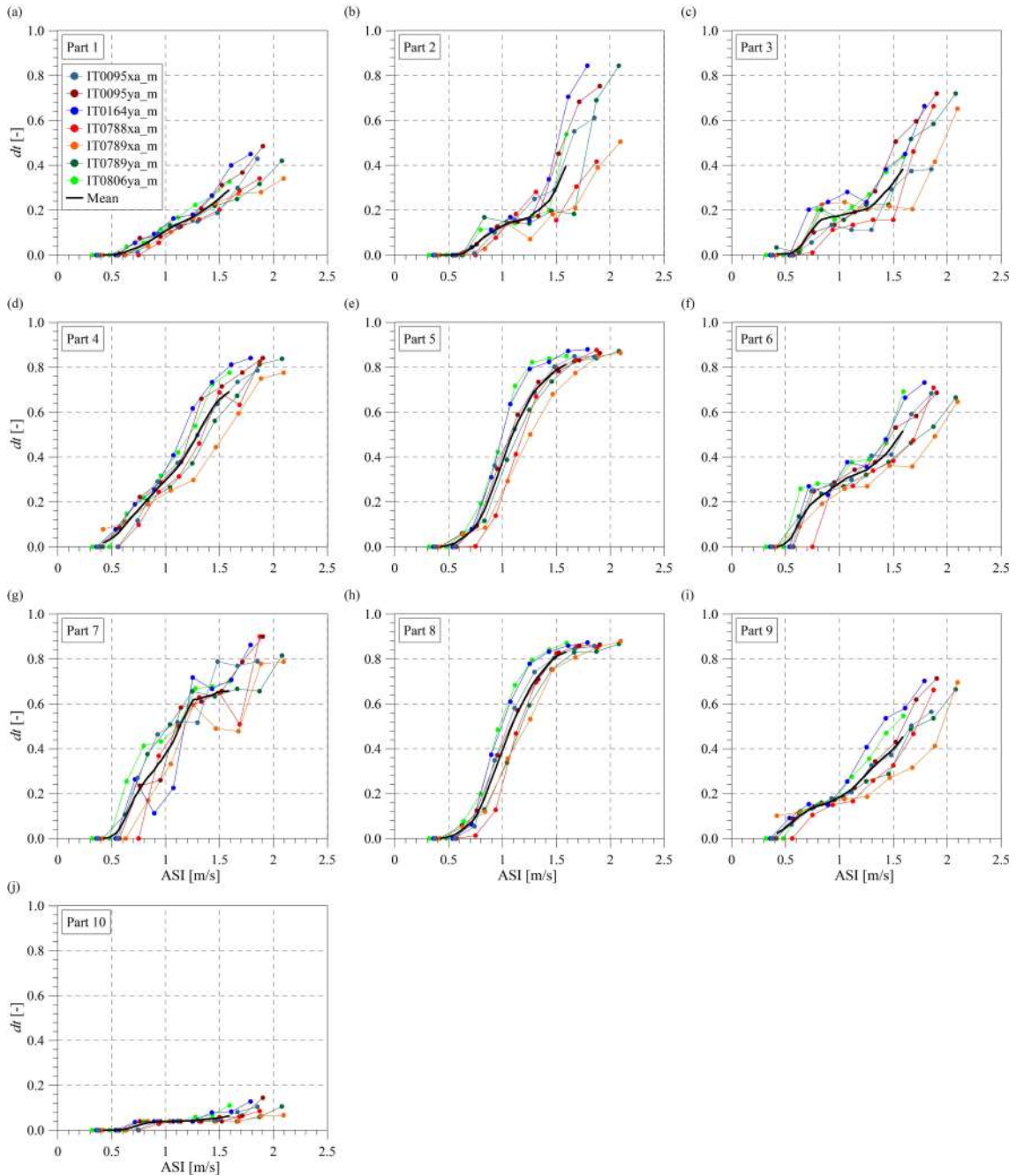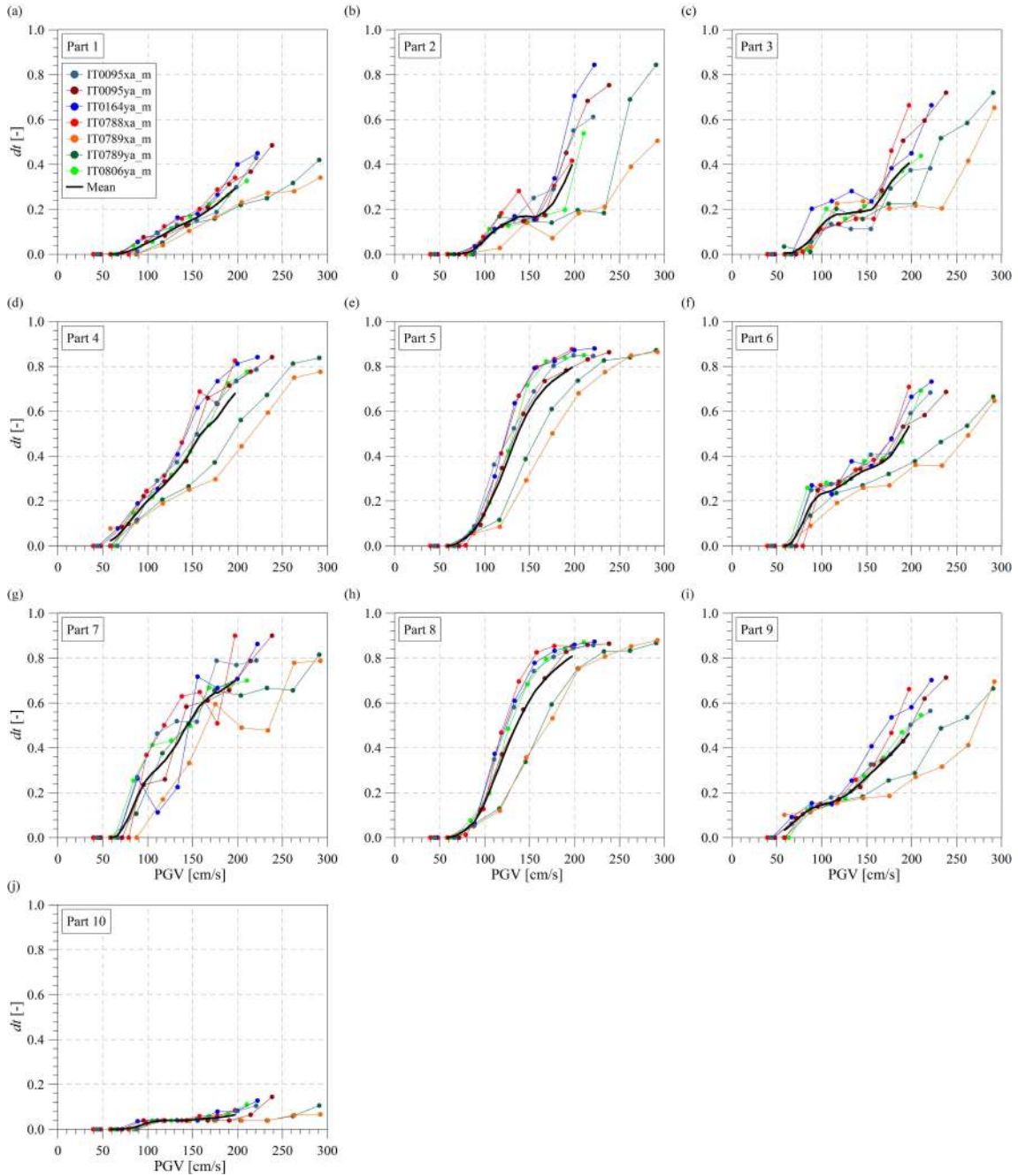
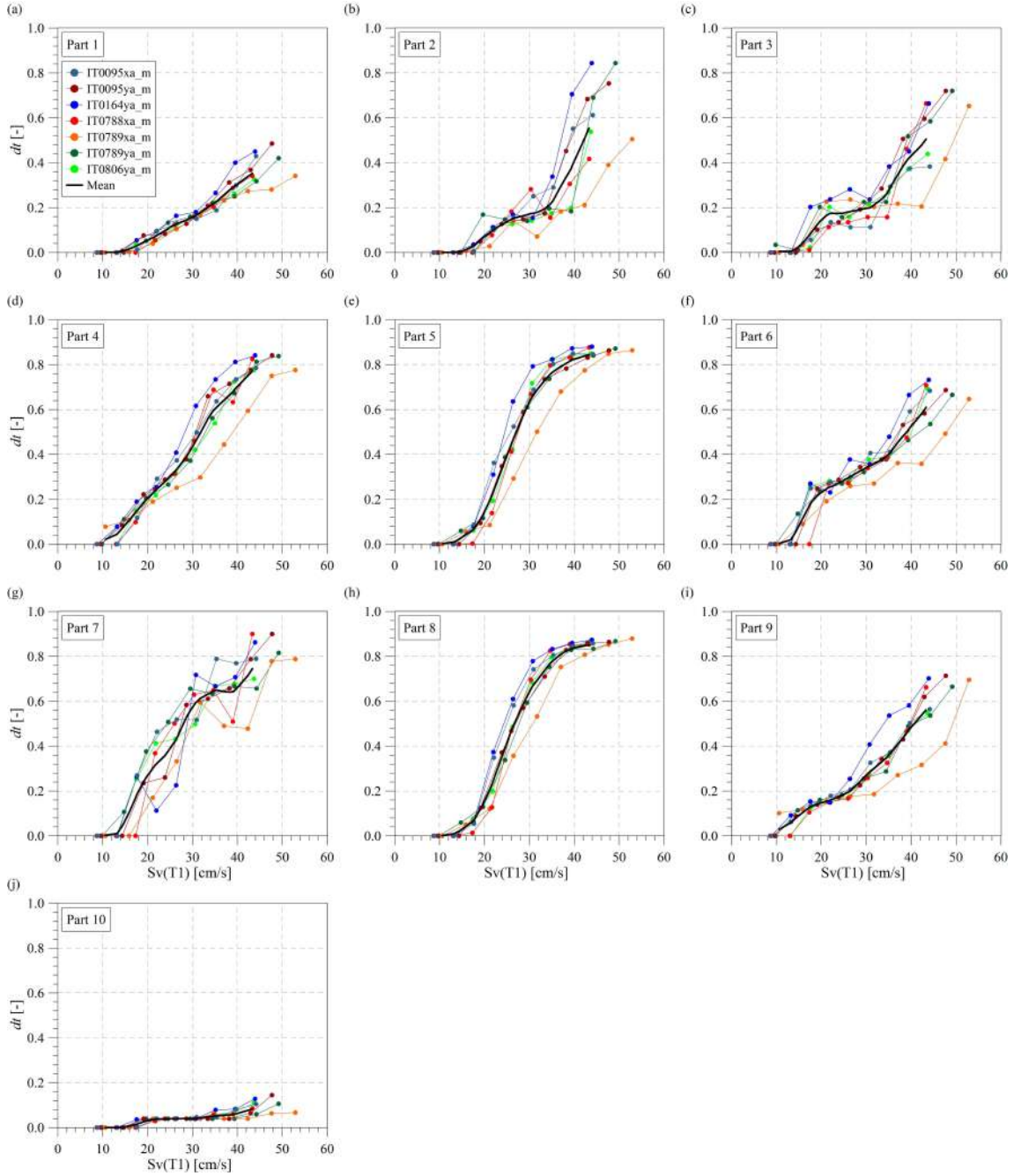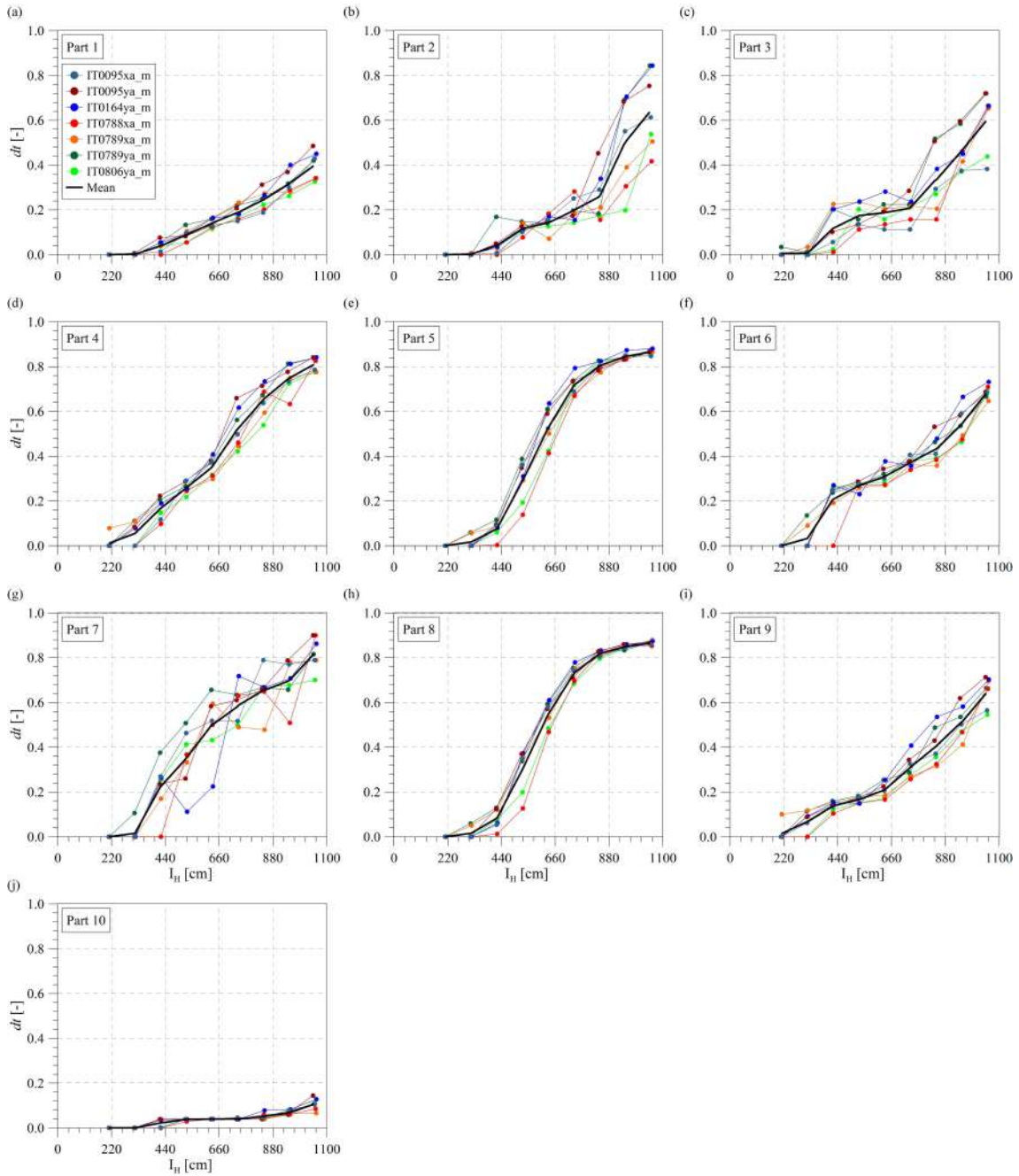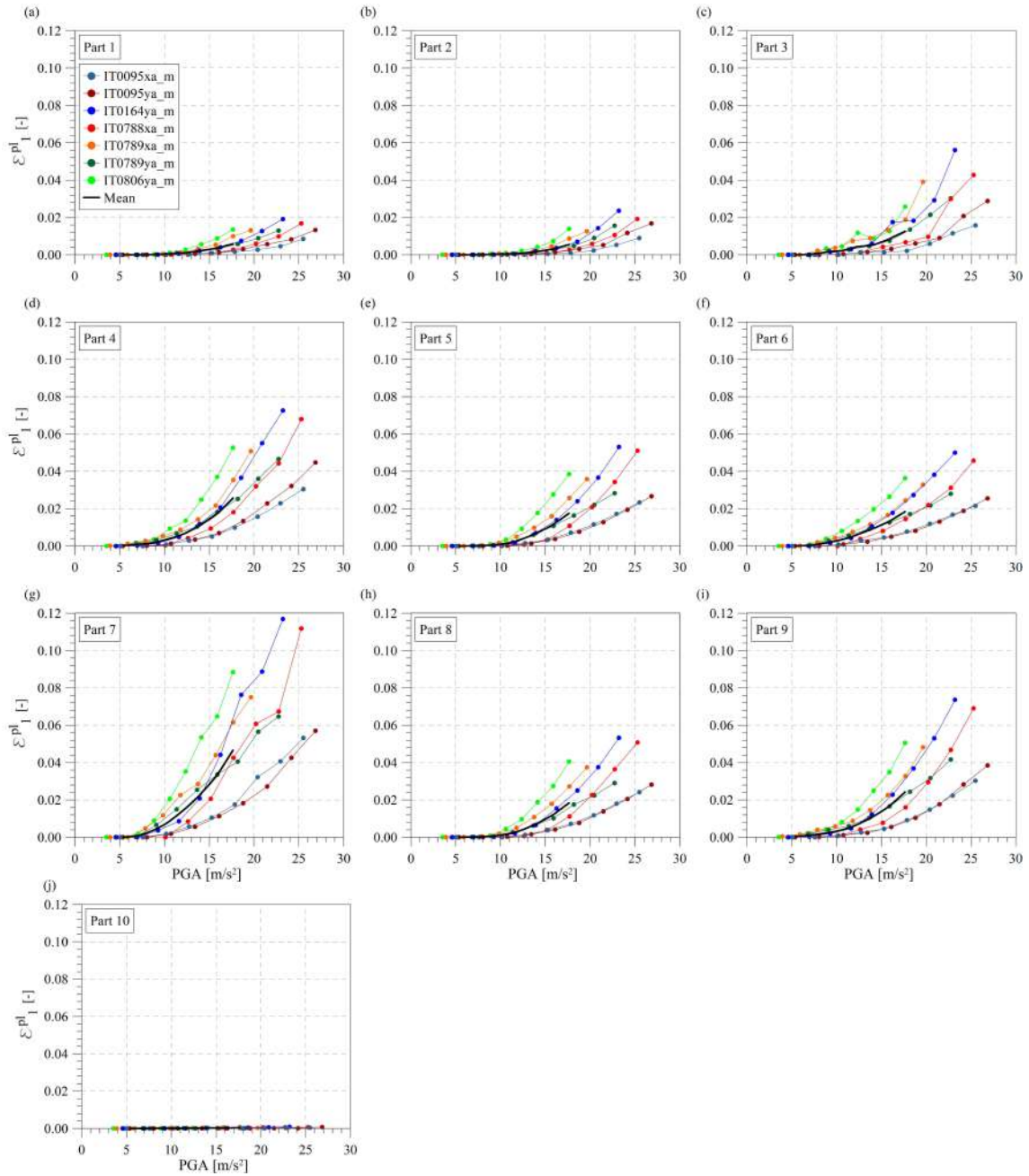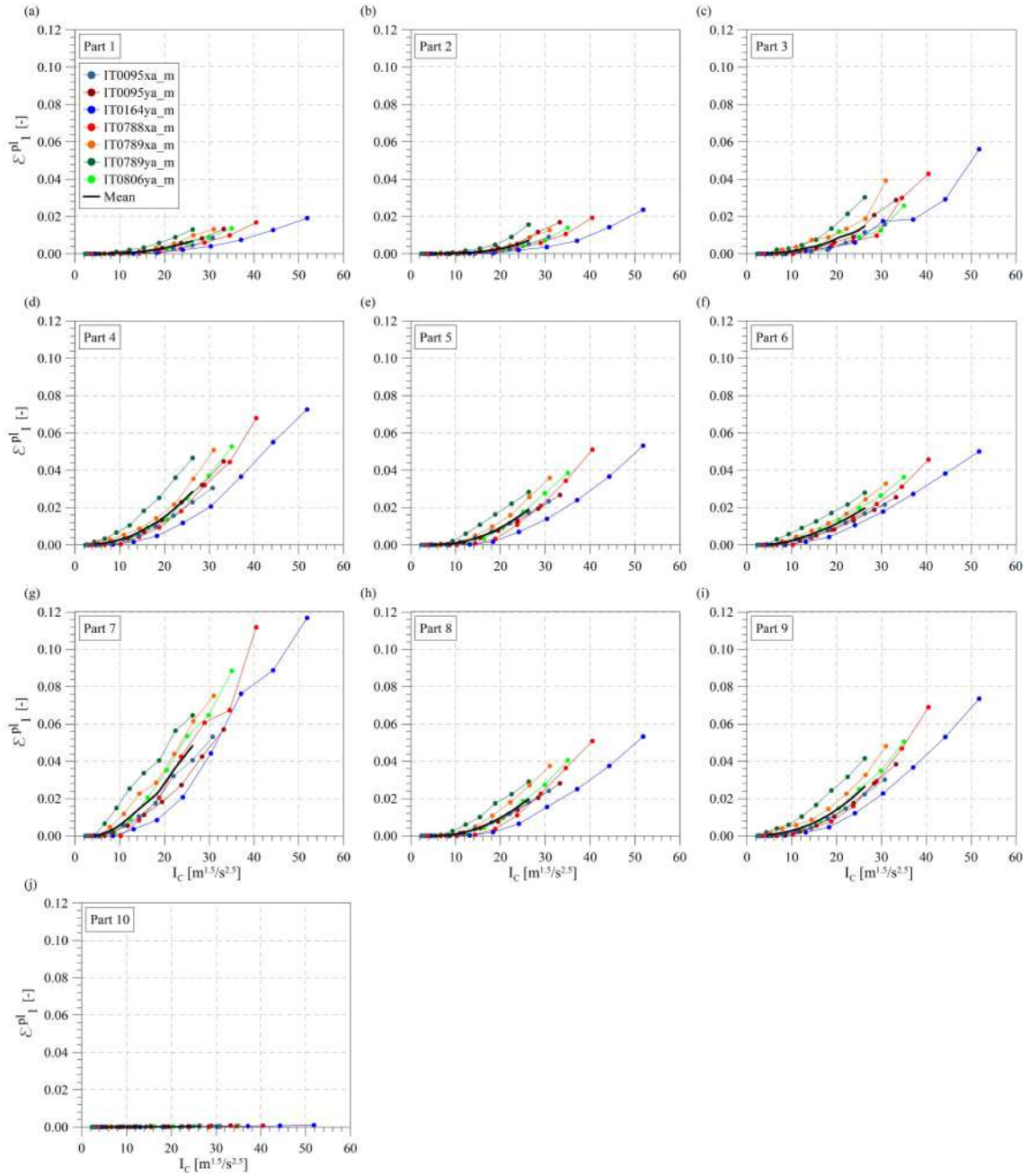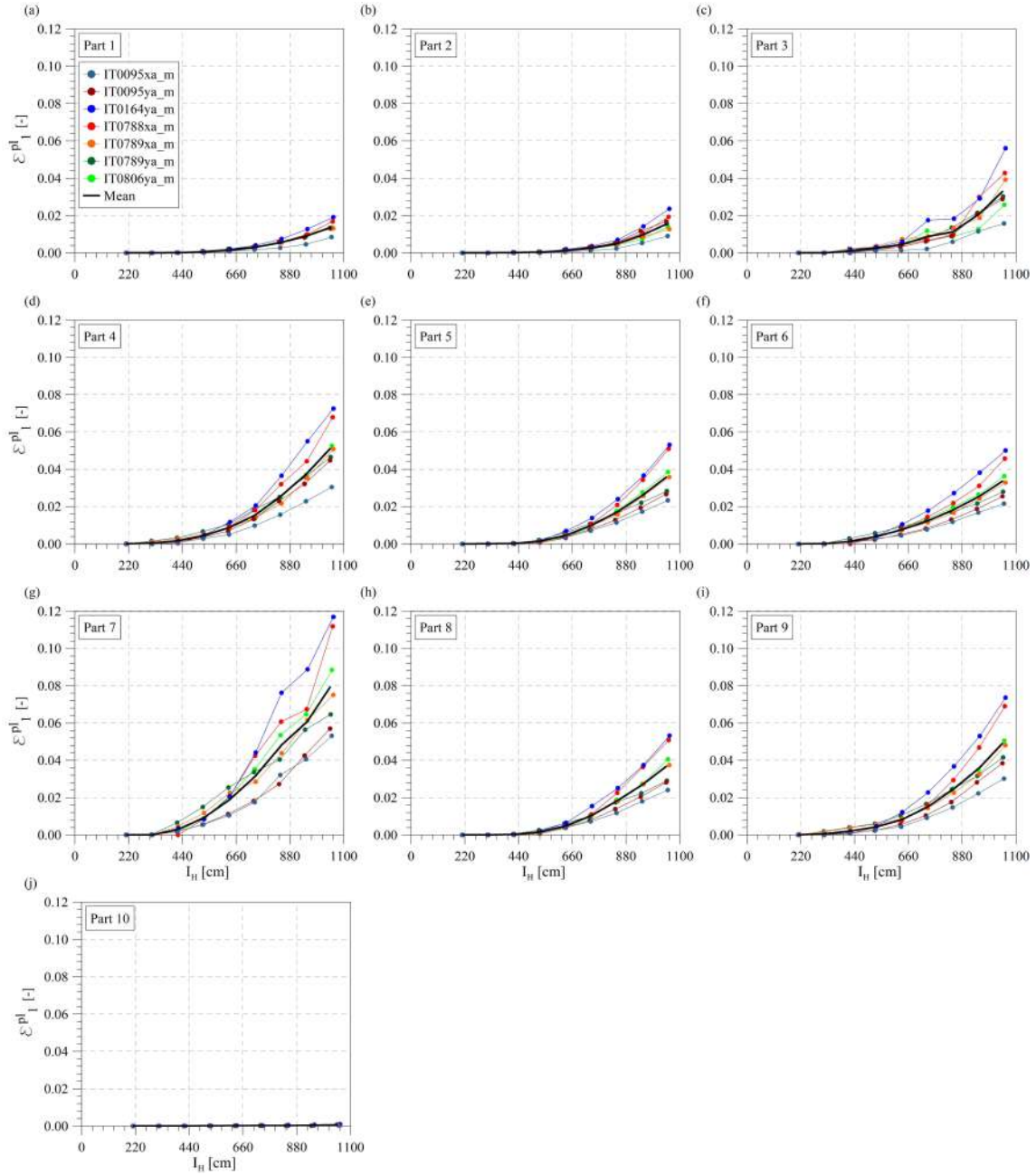Figure B.17: The IDA curve sets and corresponding mean curves for the ten (10) parts of the Brick House: plots of first principal plastic strain (ε_1^{pl}) versus I_H (a-j).

B.2   The San Pietro Bell Tower

Similarly to the Brick House, the damage pattern evolution in the case of the San Pietro Bell Tower with increasing levels of earthquake input (see SFs in Tab. 5.4) is illustreted in Fig. B.18 in terms of tensile damage d_t contour plots obtained at the last step of the non-linear dynamic analyses with IT0788 earthquake.

Considering the shaft, belfry and cusp, *IDA curve sets* relate the local DMs to the pre-elected IMs. In the case of the San Pietro Bell Tower, the most efficient IMs ultimately considered for IDA are the following eleven (11): PGA, RMSA, I_C, I_A, S_a(T1), ASI, PGV, RMSV, S_v(T1), I_H and S_d(T1) (m^*=11 with reference to Eq. (4.4)). In this Appendix, the IDA curve sets (each containing seven (7) curves plus their mean curve) obtained in the case of total energy dissipated in the element by damage, ELDMD (an output variable obtained from CDP model implemented in ABAQUS numerical model, also called damage dissipation energy), versus the aforementioned eleven (11) IMs have been reported, from Fig. B.19 to Fig. B.22.
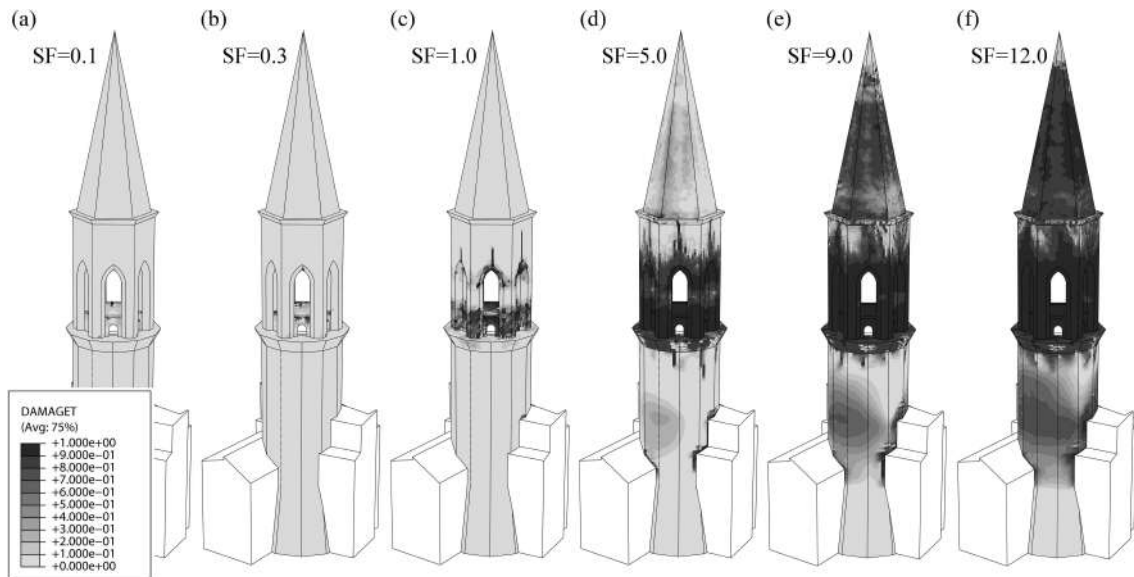
Figure B.18: Tensile damage d_t contour plots on the San Pietro Bell Tower obtained at the last step of the IDAs with IT0788 earthquake with increasing levels of the seismic input.
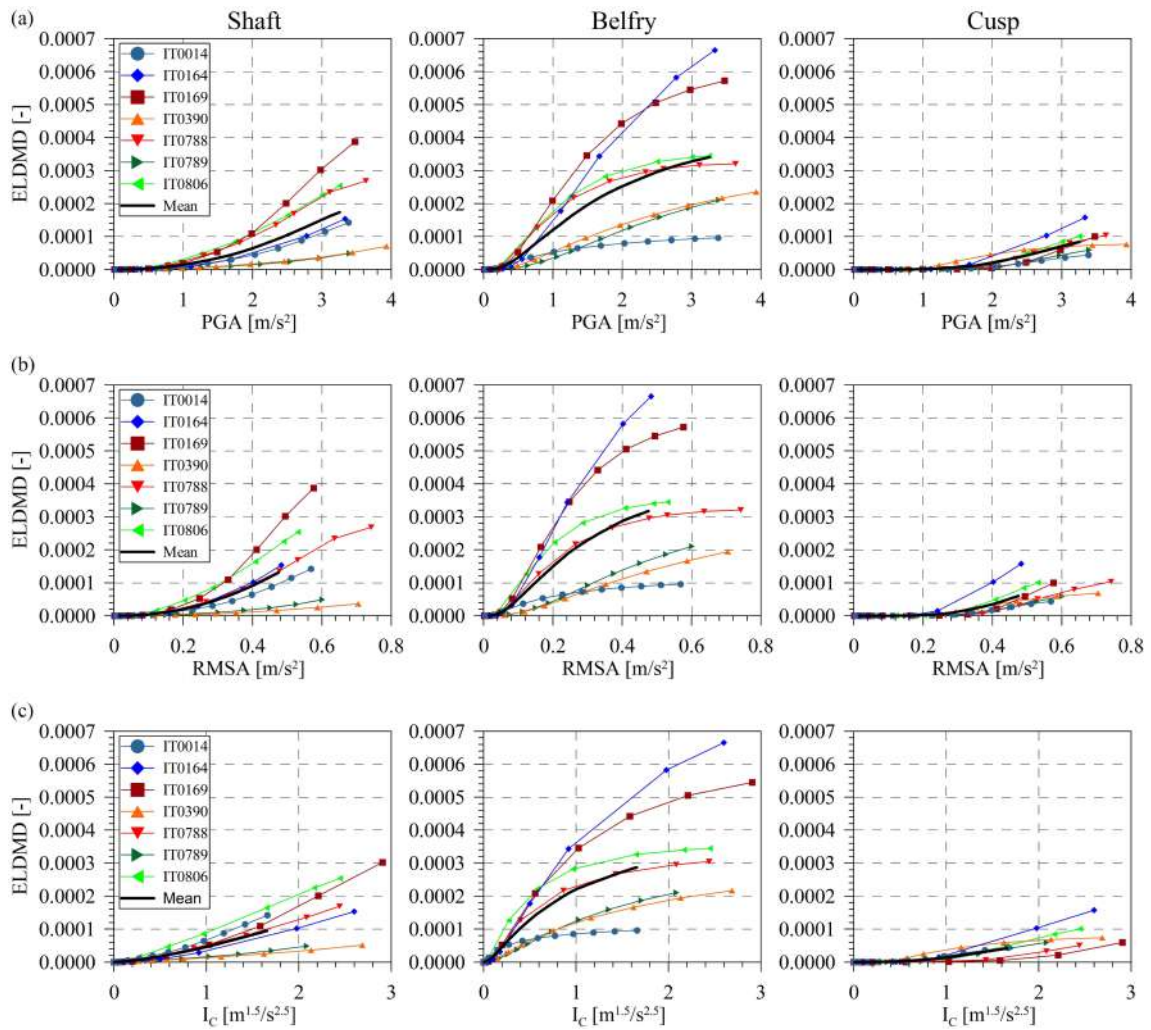
Figure B.19: The IDA curve sets (shaft, belfry and cusp) and corresponding mean curves: plots of ELDMD versus PGA (a), RMSA (b) and I$_C$ (c).
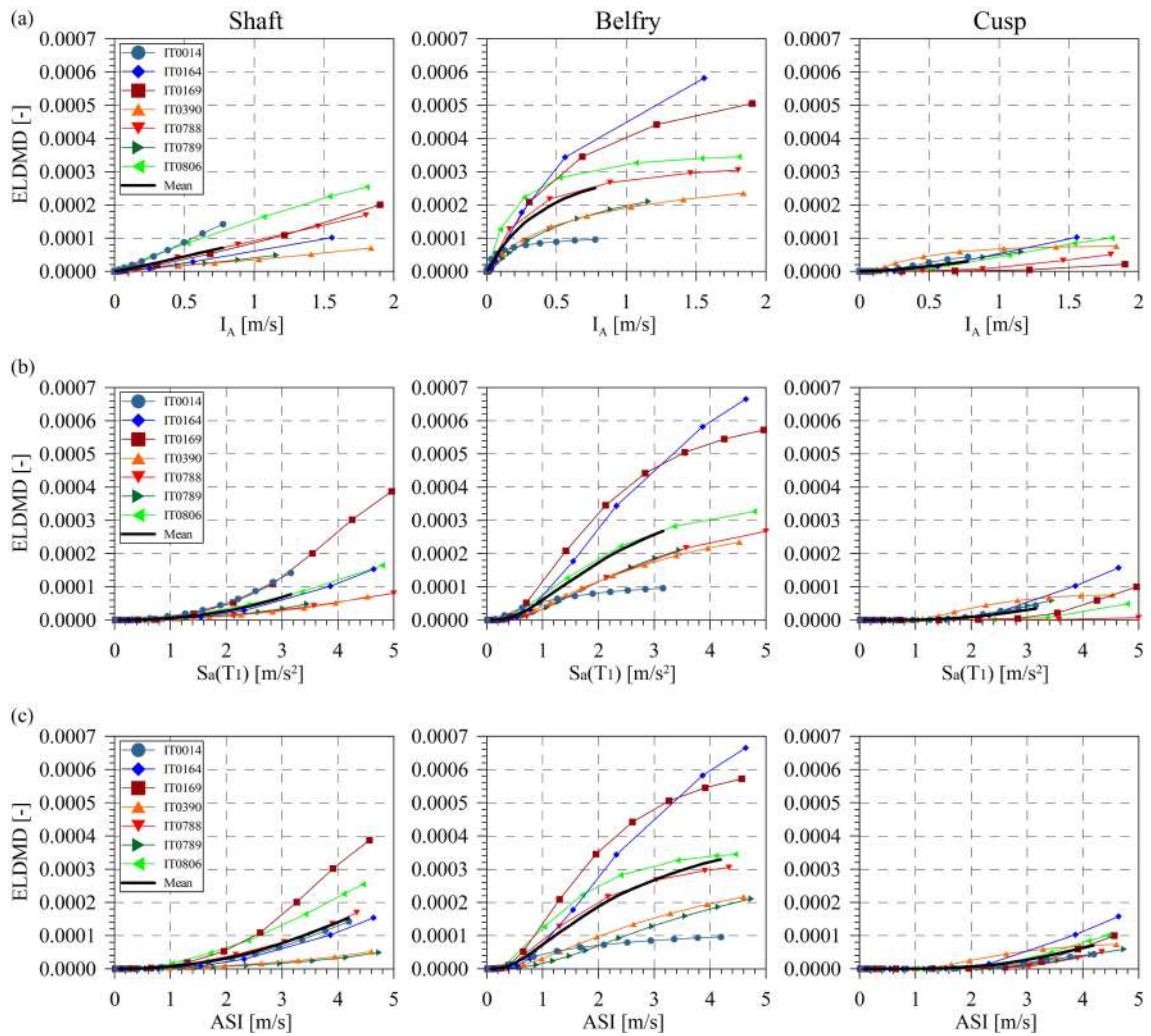
Figure B.20: The IDA curve sets (shaft, belfry and cusp) and corresponding mean curves: plots of ELDMD versus I_A (a), $S_a(T1)$ (b) and ASI (c).
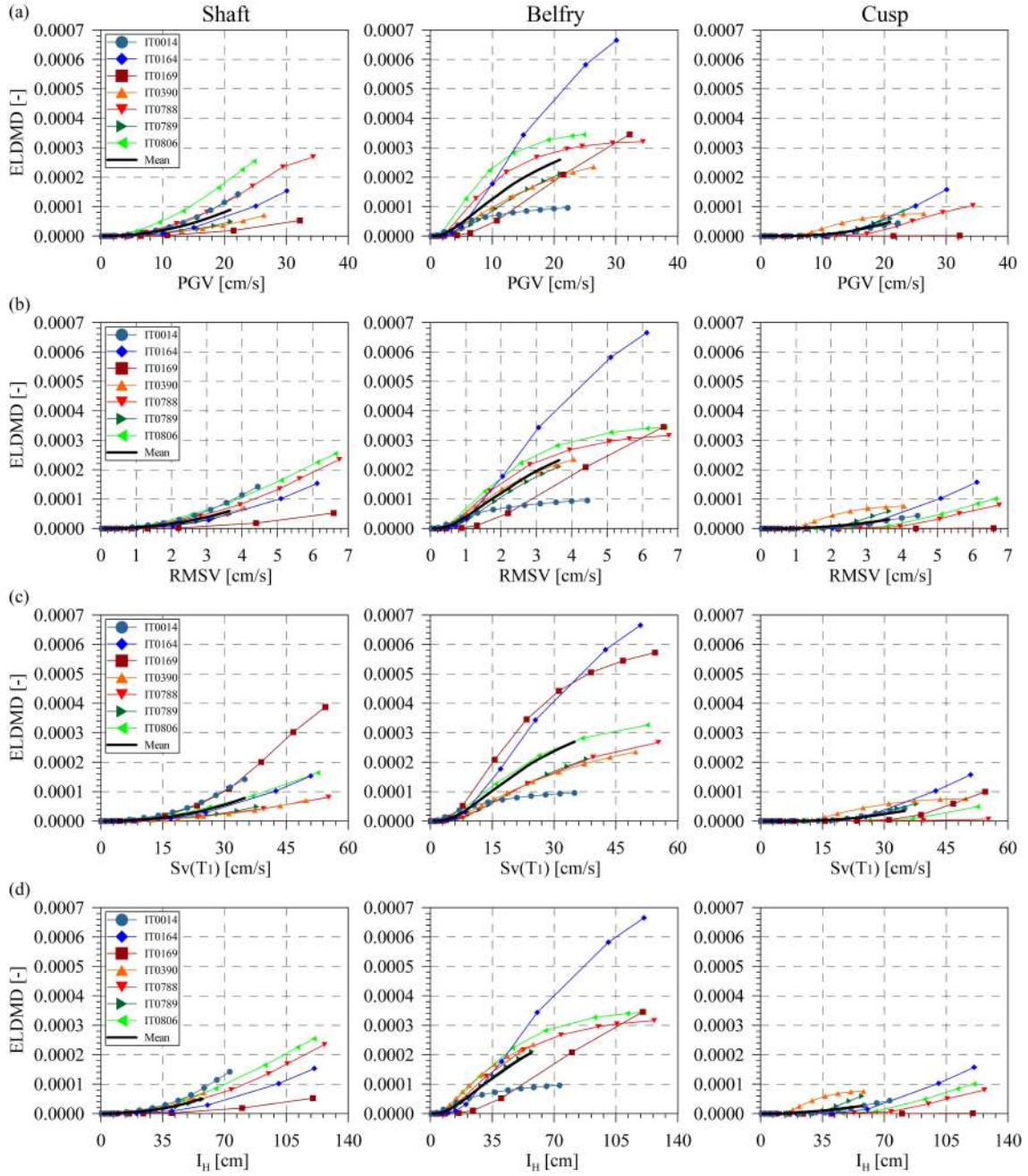
Figure B.21: The IDA curve sets (shaft, belfry and cusp) and corresponding mean curves: plots of ELDMD versus PGV (a), RMSV (b), $S_v(T1)$ (c) and I_H (d).
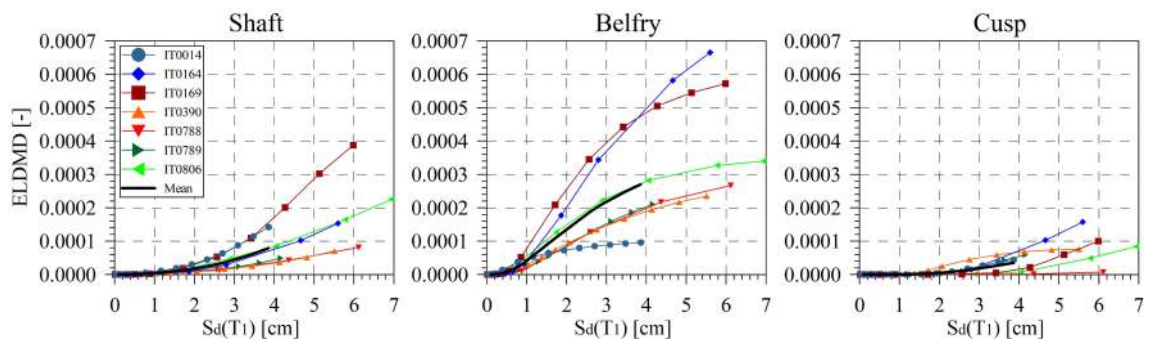
Figure B.22: The IDA curve sets (shaft, belfry and cusp) and corresponding mean curves: plots of ELDMD versus S_d(T1).

Bibliography

Abbati, S. Degli, A.M. D'Altri, D. Ottonelli, G. Castellazzi, S. Cattari, S. De Miranda, and S. Lagomarsino (2019). "Seismic assessment of interacting structural units in complex historic masonry constructions by nonlinear static analyses." In: *Computers and Structures* 213, pp. 51–71.

Abrahamson, N.A. (1992). "Non-stationary spectral matching." In: *Seismological Research Letters* 63 (1), pp. 30–30.

Alvandi, A. and C. Cremona (2006). "Assessment of vibration-based damage identification techniques." In: *Journal of Sound and Vibration* 292 (1-2), pp. 179–202.

An, Y., E. Chatzi, S.H. Sim, S. Laflamme, B. Blachowski, and J. Ou (2019). "Recent progress and future trends on damage identification methods for bridge structures." In: *Structural Control and Health Monitoring* 26.10, pp. 362–381.

Anderson, J.C. and V.V. Bertero (1987). "Uncertainties in Establishing Design Earthquakes." In: *Journal of Structural Engineering* 113 (8), pp. 1709–1724.

Aras, F., L. Krstevska, G. Altay, and L. Tashkov (2011). "Experimental and numerical modal analyses of a historical masonry palace." In: *Construction and Building Materials* 25 (1), pp. 81–91.

Araya, R. and G.R. Saragoni (1980). "Capacity of seismic motion to produce structural damage." In: *Publication SES I 7/80 (156), Division of Structural Engineering, Department of Engineering, University of Chile (in Spanish)*. Santiago, Chile.

— (1984). "Earthquake accelerogram destructiveness potential factor." In: *Proceedings of the 8th World Conference in Earthquake Engineering, EERI*. San Francisco, California, USA, pp. 835–842.

Arias, A. (1970). "A measure of earthquake intensity." In: *Seismic design for nuclear power plants (ed. R.J. Hansen), MIT Press*. Cambridge, Massachusetts, pp. 438–483.

Atamturktur, S. and J.A. Laman (2012). "Finite element model correlation and calibration of historic masonry monuments: review." In: *The Structural Design of Tall and Special Buildings* 21 (2), pp. 96–113.

Atik, L. Al and N.A. Abrahamson (2010). "An improved method for nonstationary spectral matching." In: *Earthquake Spectra* 26 (3), pp. 601–617.

Bartoli, G., A. Chiarugi, and V. Gusella (1996). "Monitoring Systems on Historic Buildings: The Brunelleschi Dome." In: *Journal of Structural Engineering* 122 (6), pp. 663–673.

Bartoli, G., M. Betti, L. Galano, and G. Zini (2019). "Numerical insights on the seismic risk of confined masonry towers." In: *Engineering Structures* 180, pp. 713–727.

Basone, F., L. Cavaleri, F. Di Trapani, and G. Muscolino (2017). "Incremental dynamic based fragility assessment of reinforced concrete structures: Stationary vs. non-stationary artificial ground motions." In: *Soil Dynamics and Earthquake Engineering* 103, pp. 105–117.

Bazzurro, P. and C.A. Cornell (1994a). "Seismic hazard analysis for non-linear structures. I: Methodology." In: *Journal of Structural Engineering* 120 (11), pp. 3320–3344.

— (1994b). "Seismic hazard analysis for non-linear structures. II: Applications." In: *Journal of Structural Engineering* 120 (11), pp. 3345–3365.

Bellino, A., A. Fasana, L. Garibaldi, and S. Marchesiello (2010). "PCA-based detection of damage in time-varying systems." In: *Mechanical Systems and Signal Processing* 24 (7), pp. 2250–226.

Bennati, S., L. Nardini, and W. Salvatore (2005). "Dynamic behaviour of a medieval masonry bell tower. II. Measurement and modelling of the tower motion." In: *Journal of Structural Engineering* 131 (11), pp. 1656–1664.

Bertero, V.V. (1977). "Strength and deformation capacities of buildings under extreme environments." In: *Structural Engineering and Structural Mechanics*, pp. 211–215.

Bianchini, M., P.P. Diotallevi, and J.W. Baker (2009). "Prediction of inelastic structural response using an average of spectral accelerations." In: *Proceedings of the 10th International Conference on Structural Safety and Reliability (ICOSSAR09)*. Vol. 3. Osaka, Japan, pp. 5359–5372.

Bindi, D., L. Luzi, F. Pacor, F. Sabetta, and M. Massa (2009). "Towards a new reference ground motion prediction equation for Italy: update of the Sabetta–Pugliese (1996)." In: *Bulletin of Earthquake Engineering* 7 (3), pp. 591–608.

Bommer, J.J. and A.B. Acevedo (2004). "The use of real earthquake accelerograms as input to dynamic analysis." In: *Journal of Earthquake Engineering* 8, pp. 43–91.

Bommer, J.J. and A. Martinez-Pereira (1999). "The effective duration of earthquake strong motion." In: *Journal of Earthquake Engineering* 3 (2), pp. 127–172.

Boore, D.M. (1983). "Stochastic simulation of high-frequency ground motions based on seismological models of the radiated spectra." In: *Bulletin of the Seismological Society of America* 73, pp. 1865–1884.

Brederode, P., P. De Winter, P. Van Staalduinen, and W. Segers (1986). "Dynamic offshore structure test (DOST) project—a new approach to quality assessment of offshore structures." In: *Proceedings of the conference on Inspection, repair and maintenance IRM/AODC86.*

Brencich, A. and D. Sabia (2008). "Experimental identification of a multi-span masonry bridge: the Tanaro Bridge." In: *Construction and Building Materials* 22 (10), pp. 2087–2099.

Brincker, R. and C.E. Ventura (2015). *Introduction to Operational Modal Analysis.* John Wiley & Sons, 1st edition.

Brownjohn, J.M.W. (2007). "Structural health monitoring of civil infrastructure." In: *Philosophical Transactions of the Royal Society of London A: Mathematical, Physical and Engineering Sciences* 365 (1851), pp. 589–622.

Bru, D., S. Ivorra, M. Betti, J.M. Adam, and G. Bartoli (2019). "Parametric dynamic interaction assessment between bells and supporting slender masonry tower." In: *Mechanical Systems and Signal Processing* 129, pp. 235–249.

Cabanas, L., B. Benito, and M. Herraiz (1991). "Approach to the measurement of the potential structural damage of earthquake ground motions." In: *Earthquake Engineering and Structural Dynamics* 26 (1), pp. 79–92.

Cabboi, A., C. Gentile, and A. Saisi (2017). "From continuous vibration monitoring to FEM-based damage assessment: Application on a stone-masonry tower." In: *Construction and Building Materials* 156, pp. 252–265.

Calcada, M., A. Cunha, and R. Delgado (2002). "Dynamic analysis of metallic arch railway bridge." In: *Journal of Bridge Engineering* 7 (4), pp. 214–222.

Candeias, P.X., A. Campos Costa, N. Mendes, A.A. Costa, and P.B. Lourenço (2017). "Experimental Assessment of the Out-of-Plane Performance of Masonry Buildings Through Shaking Table Tests." In: *International Journal of Architectural Heritage* 11, pp. 31–58.

Casarin, F. and C. Modena (2008). "Seismic Assessment of Complex Historical Buildings: Application to Reggio Emilia Cathedral, Italy." In: *International Journal of Architectural Heritage* 2 (3), pp. 304–327.

Castellazzi, G., A.M. D'Altri, S. de Miranda, A. Chiozzi, and A. Tralli (2018). "Numerical insights on the seismic behavior of a nonisolated historical masonry tower." In: *Bulletin of Earthquake Engineering* 16.2, pp. 933–961.

Cattaneo, M. et al. (2000). "The 1997 Umbria-Marche (Italy) earthquake sequence: analysis of the data recorded by the local and temporary networks." In: *Journal of Seismology* 4 (4), pp. 401–414.

Cattari, S. and S. Lagomarsino (2013). "Seismic assessment of mixed masonry-reinforced concrete buildings by non-linear static analyses." In: *Earthquake and Structures* 4.3, pp. 241–264.

Cattari, S., S. Lagomarsino, A. Karatzetzou, and D. Pitilakis (2015). "Vulnerability assessment of Hassan Bey's Mansion in Rhodes." In: *Bulletin of Earthquake Engineering* 13.1, pp. 347–368.

Cattari, S. et al. (2019). "Discussion on data recorded by the Italian structural seismic monitoring network on three masonry structures hit by the 2016-2017 Central Italy earthquake." In: *Proceedings of the 7th International Conference on Computational Methods in Structural Dynamics and Earthquake Engineering.* Crete, Greece, June 24th-26th 2019.

Cavalagli, N., G. Comanducci, and F. Ubertini (2018). "Earthquake-Induced Damage Detection in a Monumental Masonry Bell-Tower Using Long-Term Dynamic Monitoring Data." In: *Journal of Earthquake Engineering* 22, pp. 96–119.

Cavalagli, N., A. Kita, V.L. Castaldo, A.L. Pisello, and F. Ubertini (2019a). "Hierarchical environmental risk mapping of material degradation in historic masonry buildings: An integrated approach considering climate change and structural damage." In: *Construction and Building Materials* 215, pp. 998–1014.

Cavalagli, N., A. Kita, S. Falco, F. Trillo, M. Costantini, and F. Ubertini (2019b). "Satellite radar interferometry and in-situ measurements for static monitoring of historical monuments: the case of Gubbio, Italy." In: *Remote Sensing of Environment* 235, p. 111453.

Chácara, C., F. Cannizzaro, B. Pantò, I. Caliò, and P.B. Lourenço (2019). "Seismic vulnerability of URM structures based on a Discrete Macro-Element Modeling (DMEM) approach." In: *Engineering Structures* 201, p. 109715.

Chiaraluce, L. et al. (2017). "The 2016 Central Italy Seismic Sequence: A First Look at the Mainshocks, Aftershocks, and Source Models." In: *Seismological Research Letters* 88 (3), pp. 757–771.

Clementi, F., A. Pierdicca, A. Formisano, F. Catinari, and S. Lenci (2017). "Numerical model upgrading of a historical masonry building damaged during the 2016 Italian

195

earthquakes: the case study of the Podesta palace in Montelupone (Italy)." In: *Journal of Civil Structural Health Monitoring* 7 (5), pp. 703–717.

Comanducci, G., F. Ubertini, and A.L. Materazzi (2015). "Structural health monitoring of suspension bridges with features affected by changing wind speed." In: *Journal of Wind Engineering and Industrial Aerodynamics* 141, pp. 12–26.

Comanducci, G., F. Magalhães, F. Ubertini, and A. Cunha (2016). "On vibration-based damage detection by multivariate statistical techniques: Application to a long-span arch bridge." In: *Structural Health Monitoring* 15 (5), 505–524.

Comerford, J.B., P. Salvaneschi, M. Lazzari, P. Bonaldi, G. Ruggeri, M. Fanelli, G. Giusepetti, and G. Mazza (1992). "The role of AI technology in the management of dam safety: the DAMSAFE system." In: *Dam Engineering* 3 (4), pp. 215–226.

Cosenza, E. and G. Manfredi (1997). "The improvement of the seismic-resistant design for existing and new structures using damage criteria." In: *Proceedings of the Seismic design methodologies for the next generation of codes.* Netherland, pp. 119–130.

— (2000). "Damage indices and damage measures." In: *Progress in Structural Engineering and Materials* 2 (1), pp. 50–59.

Dackermann, U., W.A. Smith, and R.B. Randall (2014). "Damage identification based on response-only measurements using cepstrum analysis and artificial neural networks." In: *Structural Health Monitoring* 13 (4), pp. 430–444.

Deraemaeker, A., E. Reynders, G. De Roeck, and J. Kullaa (2008). "Vibration-based structural health monitoring using output-only measurements under changing environment." In: *Mechanical Systems and Signal Processing* 22 (1), pp. 34–56.

Dervilis, N., K. Worden, and E.J. Cross (2015). "On robust regression analysis as a means of exploring environmental and operational conditions for SHM data." In: *Journal of Sound and Vibration* 347, pp. 279–296.

Doebling, S.W., C.R. Farrar, M.B. Prime, and D.W Shevitz (1996). "Damage Identification and Health Monitoring of Structural and Mechanical Systems From Changes in Their Vibration Characteristics: A Literature Review." In: *Technical Report: LA-13070-MS, ON: DE96012168, TRN: 96:003834; Los Alamos National Laboratory, NM (USA).*

Dolce, M., M. Nicoletti, A. De Sortis, S. Marchesini, D. Spina, and F. Talanas (2017). "Osservatorio sismico delle strutture: the Italian structural seismic monitoring network." In: *Bulletin of Earthquake Engineering* 15 (2), 621—641.

Douglas, B.M. and W.H. Reid (1982). "Dynamic Tests and System Identification of Bridges." In: *Journal of the Structural Division* 108.10, pp. 2295–2312.

Douglas, J. et al. (2015). "Evaluation of seismic hazard for the assessment of historical elements at risk: description of input and selection of intensity measures." In: *Bulletin of Earthquake Engineering* 13 (1), pp. 49–65.

EN 1998-1, Eurocode 8 (2005). *Design of structures for earthquake resistance. Part 1: General rules, seismic action and rules for buildings.* European Committee for Standardization, Brussels, Belgium.

EPRI (1988). "A criterion for determining exceedance of the operating basis earthquake." In: *Electrical Power Research Institute (EPRI), Palo Alto, California, USA* NP-5930.

Fagundes, C., R. Bento, and S. Cattari (2017). "On the seismic response of buildings in aggregate: Analysis of a typical masonry building from Azores." In: *Structures* 10, pp. 184–196.

Fajfar, P., T. Vidic, and M. Fischinger (1990). "A measure of earthquake motion capacity to damage medium-period structures." In: *Soil Dynamics and Earthquake Engineering* 9 (5), pp. 236–242.

Farrar, C.R. and K. Worden (2007). "An introduction to structural health monitoring." In: *Philosophical Transactions of the Royal Society A* 365 (1851), pp. 303–315.

— (2012). *Structural Health Monitoring: A Machine Learning Perspective.* John Wiley & Sons, 1st edition.

FEMA (2000a). *Recommended seismic design criteria for new steel moment-frame buildings. Report No. FEMA-350.* Washington, DC: SAC Joint Venture, Federal Emergency Management Agency.

— (2000b). *Recommended seismic evaluation and upgrade criteria for existing welded steel moment-frame buildings. Report No. FEMA-351.* Washington, DC: SAC Joint Venture, Federal Emergency Management Agency.

Fitzgerald, B. and B. Basu (2017). "A monitoring system for wind turbines subjected to combined seismic and turbulent aerodynamic loads." In: *Structural Monitoring and Maintenance* 4.2, pp. 175–194.

Formisano, A. (2017). "Theoretical and numerical seismic analysis of masonry building aggregates: case studies in San Pio Delle Camere (L'Aquila, Italy)." In: *Journal of Earthquake Engineering* 21 (2), pp. 227–245.

Formisano, A., G. Florio, R. Landolfo, L. Krstevska, and L. Tashkov (2012). "Experimental and numerical investigation on a monumental masonry building damaged by the Abruzzo earthquake." In: *Proceedings of the 8th International Conference on Structural Analysis of Historical Constructions - SAHC 2012.* WrocLaw, Poland, October 15th–17th 2012, pp. 1520–2528.

Formisano, A., L. Krstevska, G. Di Lorenzo, R. Landolfo, and L. Tashkov (2018a). "Experimental ambient vibration tests and numerical investigation on the Sidoni Palace in Castelnuovo of San Pio (L'Aquila, Italy)." In: *International Journal of Masonry Research and Innovation* 3 (3), pp. 269–294.

Formisano, A., G. Vaiano, F. Fabbrocino, and G. Milani (2018b). "Seismic vulnerability of Italian masonry churches: The case of the Nativity of Blessed Virgin Mary in Stellata of Bondeno." In: *Journal of Building Engineering* 20, pp. 179–200.

Foti, D., M. Diaferio, N.I. Giannoccaro, and M. Mongelli (2012). "Ambient vibration testing, dynamic identification and model updating of a historic tower." In: *NDT & E International* 47, pp. 88–95.

Fugate, M.L, H. Sohn, and C.R. Farrar (2001). "Vibration-based damage detection using statistical process control." In: *Mechanical Systems and Signal Processing* 15 (4), pp. 707–721.

Fuller, W.A. (2009). *Introduction to statistical time series, vol 428*. Hoboken: John Wiley & Sons, 2nd edition.

Gams, M., A. Anžlin, and M. Kramar (2017). "Simulation of Shake Table Tests on Out-of-Plane Masonry Buildings. Part (III): Two-Step FEM Approach." In: *International Journal of Architectural Heritage* 11, pp. 94–102.

Garcia-Macias, E., A. Kita, and F. Ubertini (2019). "Synergistic application of operational modal analysis and ambient noise deconvolution interferometry for structural and damage identification in historic masonry structures: three case studies of Italian architectural heritage." In: *Structural Health Monitoring* in press.

Gentile, C. and A. Saisi (2007). "Ambient vibration testing of historic masonry towers for structural identification and damage assessment." In: *Construction and Building Materials* 21 (6), pp. 1311–1321.

Gentile, C., A. Saisi, and A. Cabboi (2015). "Structural Identification of a Masonry Tower Based on Operational Modal Analysis." In: *International Journal of Architectural Heritage* 9 (2), pp. 98–110.

Gentile, C., M. Guidobaldi, and A. Saisi (2016). "One-year dynamic monitoring of a historic tower: damage detection under changing environment." In: *Meccanica* 51 (11), pp. 2873–2889.

Gentile, C., A. Ruccolo, and A. Saisi (2019). "Continuous Dynamic Monitoring to Enhance the Knowledge of a Historic Bell-Tower." In: *International Journal of Architectural Heritage*, pp. 1–13.

Gerstenberger, M.C., G.H. McVerry, D.A. Rhoades, M.W. Stirling, K.R. Berryman, and T.H. Webb (2011). *Update of the Z-Factor for Christchurch Considering Earthquake Clustering Following the Darfield Earthquake.* New Zealand: GNS Science (N.Z.) report 2011/29, 20p. URL: https://books.google.it/books?id=kbD6pwAACAAJ.

Giordano, P.F., F. Ubertini, N. Cavalagli, A. Kita, and M.G. Masciotta (2019). "Four years of Structural Health Monitoring of the San Pietro Bell Tower in Perugia, Italy: two years before the earthquake versus two years after." In: *International Journal of Masonry Research and Innovation* in press-forthcoming article.

Gkoktsi, K., A. Giaralis, R.P. Klis, V. Dertimanis, and E. Chatzi (2019). "Output-Only Vibration-Based Monitoring of Civil Infrastructure via Sub-Nyquist/Compressive Measurements Supporting Reduced Wireless Data Transmission." In: *Frontiers in Built Environment* 5, p. 111.

Grant, D.N. and R. Diaferia (2012). "Assessing adequacy of spectrum-matched ground motions for response history analysis." In: *Earthquake Engineering and Structural Dynamics* 42 (9), pp. 1265–1280.

Hancock, J., J. Watson-Lamprey, N.A. Abrahamson, J.J. Bommer, A. Markatis, E. McCoy, and R. Mendis (2006). "An improved method of matching response spectra of recorded earthquake ground motion using wavelets." In: *Journal of Earthquake Engineering* 10, pp. 67–89.

Hidalgo, P. and R.W. Clough (1974). "Earthquake Simulator Study of a Reinforced Concrete Frame." In: *Report No. EERC 74-13, Earthquake Engineering Research Center, University of California.* Berkeley, California, USA.

Hough, S.E and R.G. Bilham (2006). *After the earthquakes – Elastic rebound on an urban planet.* Oxford University Press, Inc.

Housner, G.W. (1952). "Spectrum intensities of strong motion earthquakes." In: *Proceedings in Symposium on Earthquake and Blast Effects on Structures.* Los Angeles, California, pp. 20–36.

Housner, G.W. and P.C Jennings (1982). "Earthquake design criteria." In: *Proceedings of Earthquake Engineering Research Institute, EERI Monograph Series.* Berkeley, California, USA.

Huang, X., O.S. Kwon, E. Bentz, and J. Tcherner (2018). "Method for evaluation of concrete containment structure subjected to earthquake excitation and internal pressure increase." In: *Earthquake Engineering and Structural Dynamics* 47.6, pp. 1544–1565.

Husid, L.R. (1969). "Caracteristicas de terremotos, Analisis general." In: *Revista del IDIEM* 8, pp. 21–42.

Iervolino, I. and C.A. Cornell (2005). "Record Selection for Nonlinear Seismic Analysis of Structures." In: *Earthquake Spectra* 21, pp. 685–713.

Iervolino, I., C. Galasso, and E. Cosenza (2009). "REXEL: computer aided record selection for code-based seismic structural analysis". In: *Bulletin of Earthquake Engineering* 8, pp. 339–362.

Ivorra, S. and F.J. Pallares (2006). "Dynamic investigations on a masonry bell tower." In: *Engineering Structures* 28 (5), pp. 660–667.

Ivorra, S., D. Foti, V. Gallo, V. Vacca, and D. Bru (2019). "Bell's dynamic interaction on a reinforced concrete bell tower." In: *Engineering Structures* 183, pp. 965–975.

Jaishi, B., W.X. Ren, Z.H. Zong, and P.N. Maskey (2003). "Dynamic and seismic performance of old multi-tiered temples in Nepal." In: *Engineering Structures* 25 (14), pp. 1827–1839.

Kambhatla, N. and T.K. Leen (1997). "Dimension reduction by local principal component analysis." In: *Neural Computation* 9 (7), pp. 1493–1516.

Kappos, A.J. (1991). "Analytical prediction of the collapse earthquake for R/C buildings: Suggested methodology." In: *Earthquake Engineering and Structural Dynamics* 20 (2), pp. 167–176.

Karanikoloudis, G. and P.B. Lourenço (2018). "Structural assessment and seismic vulnerability of earthen historic structures. Application of sophisticated numerical and simple analytical models." In: *Engineering Structures* 160, pp. 488–509.

Kawashima, K. and K. Aizawa (1989). "Bracketed and normalized durations of earthquake ground acceleration." In: *Earthquake Engineering and Structural Dynamics* 18, pp. 1041–1051.

Kita, A., N. Cavalagli, and F. Ubertini (2018). "First results of mixed static-dynamic structural health monitoring of Consoli Palace in Gubbio." In: *Proceedings of the 10th International Masonry Conference*. Milan, Italy, July 9th-11th 2018, pp. 2380–2395.

Kita, A., N. Cavalagli, M.G. Masciotta, P.B. Lourenço, and F. Ubertini (2019a). "Earthquake-induced damage localization through non-linear dynamic analysis." In: *Proceedings of the 7th International Conference on Computational Methods in Structural Dynamics and Earthquake Engineering*. Crete, Greece, June 24th-26th 2019.

Kita, A., N. Cavalagli, and F. Ubertini (2019b). "Temperature effects on static and dynamic behavior of Consoli Palace in Gubbio, Italy." In: *Mechanical Systems and Signal Processing* 120, pp. 180–202.

Ko, J.M. and Y.Q. Ni (2005). "Technology developments in structural health monitoring of large-scale bridges." In: *Engineering Structures* 27 (12), pp. 1715–1725.

Kramer, S.L. (1996). *Geotechnical Earthquake Engineering.* Upper Saddle River, New Jersey: Prentice Hall International Series in Civil Engineering and Engineering Mechanics, 1st Edition.

Krstevska, L., L. Tashkov, N. Naumovski, G. Florio, A. Formisano, A. Fornaro, and R. Landolfo (2010). "In-situ experimental testing of four historical buildings damaged during the 2009 L'Aquila earthquake." In: *Proceedings of the Cost Action C26 Final Conference: Urban Habitat Constructions under Catastrophic Events.* Naples, Italy, September 16th-18th 2010, pp. 427–432.

Lagomarsino, S. and S. Cattari (2015a). "PERPETUATE guidelines for seismic performance-based assessment of cultural heritage masonry structures." In: *Bulletin of Earthquake Engineering* 13 (1), pp. 13–47.

— (2015b). "Seismic performance of historical masonry structures through pushover and nonlinear dynamic analyses." In: *Geotechnical, Geological and Earthquake Engineering* 39, pp. 265–292.

Lee, J. and G.L. Fenves (1989). "Plastic-Damage Model for Cyclic Loading of Concrete Structures." In: *Journal of Engineering Mechanics* 124 (8), pp. 892–900.

Limongelli, M.P., E. Chatzi, and A. Anžlin (2018). "Condition assessment of roadway bridges: From performance parameters to performance goals." In: *Baltic Journal of Road and Bridge Engineering* 13, pp. 345–356.

Lorenzo, G. Di, A. Formisano, L. Krstevska, and R. Landolfo (2019). "Ambient vibration test and numerical investigation on the St. Giuliano church in Poggio Picenze (L'aquila, Italy)." In: *Journal of Civil Structural Health Monitoring* 9 (4), pp. 477–490.

Lourenço, P.B. (2002). "Computations on historic masonry structures." In: *Progress in Structural Engineering and Materials* 4 (3), pp. 301–319.

— (2006). "Recommendations for restoration of ancient buildings and the survival of a masonry chimney." In: *Construction and Building Materials* 20 (4), pp. 239–251.

Lourenço, P.B., N. Mendes, A.A. Costa, and A. Campos Costa (2017). "Methods and Challenges on the Out-of-Plane Assessment of Existing Masonry Buildings." In: *International Journal of Architectural Heritage* 11, pp. 1–1.

Lubliner, J., J. Olive, S. Oller, and E. Onate (1989). "A Plastic-Damage Model for Concrete." In: *International Journal of Solids and Structures* 25.3, pp. 229–326.

Luco, N. and C.A. Cornell (2000). "Effects of connection fractures on SMRF seismic drift demands." In: *Journal of Structural Engineering* 126 (1), pp. 127–136.

Mackie, K.R. and B. Stojadinovic (2003). "Seismic Demands for Performance-Based Design of Bridges." In: *PEER Report 312.*

Magalhães, F., A. Cunha, and E. Caetano (2009). "Online automatic identification of the modal parameters of a long span arch bridge." In: *Mechanical Systems and Signal Processing* 23 (22), pp. 316–329.

— (2012). "Vibration based structural health monitoring of an arch bridge: From automated OMA to damage detection." In: *Mechanical Systems and Signal Processing* 28, pp. 212–228.

Masaeli, H., F. Khoshnoudian, and S. Musician (2018). "Incremental dynamic analysis of nonlinear rocking soil-structure systems." In: *Soil Dynamics and Earthquake Engineering* 104, pp. 236–249.

Masciotta, M.G., J.C.A. Roque, L.F. Ramos, and P.B. Lourenço (2016). "A multidisciplinary approach to assess the health state of heritage structures: The case study of the Church of Monastery of Jerónimos in Lisbon." In: *Construction and Building Materials* 116, pp. 169–187.

Masciotta, M.G., L.F. Ramos, and P.B. Lourenço (2017). "The importance of structural monitoring as a diagnosis and control tool in the restoration process of heritage structures: A case study in Portugal." In: *Journal of Cultural Heritage* 27, pp. 36–47.

Masciotta, M.G., A. Barontini, L.F. Ramos, P. Amado-Mendes, and P.B. Lourenço (2019). "An overview on structural health monitoring: From the current state-of-the-art to new bio-inspired sensing paradigms." In: *International Journal of Bio-Inspired Computation* 14 (1), pp. 1–26.

Materazzi, A. L. and F. Ubertini (2011). "Eigenproperties of suspension bridges with damage." In: *Journal of Sound and Vibration* 330 (26), pp. 6420–6434.

McCann, M.W. and H.C. Shah (1979). "Determining strong motion duration of earthquakes." In: *Bulletin of the Seismological Society of America* 69 (4), pp. 1253–1265.

Mehanny, S.S. and P.P Cordova (2004). "Development of a two-parameter seismic intensity measure and probabilistic design procedure." In: *Journal of Engineering and Applied Science* 51 (2), pp. 233–252.

Mosavi, A.A., D.Dickey, R.Seracino, and S.Rizkalla (2012). "Identifying damage locations under ambient vibrations utilizing vector autoregressive models and Mahalanobis distances." In: *Mechanical Systems and Signal Processing* 26, pp. 254–267.

Mujica, L.E., J. Rodellar, A. Fernandez, and A. Guemes (2011). "Q-statistic and T2-statistic PCA-based measures for damage assessment in structures." In: *Structural Health Monitoring* 10 (5), pp. 539–553.

Myers, R.H., D.C. Montgomery, and C.M. Anderson-Cook (2016). *Response Surface Methodology: Process and Product Optimization Using Designed Experiments.* John Wiley & Sons, 4th edition.

Nau, J.M. and W.J. Hall (1984). "Scaling methods for earthquake response spectra." In: *Journal of Structural Engineering* 110 (7), pp. 1533–1548.

Newmark, N.M. and W.J. Hall (1982). "Earthquake spectra and design." In: *EERI Monograph Series.*

NTC08, Ministero delle Infrastrutture (2008). *Approvazione delle nuove Norme tecniche per le costruzioni. Decreto Ministeriale 14 Gennaio 2008. Supplemento ordinario alla Gazzetta Ufficiale, n.29 del 4 Febbraio 2008 - Serie generale(in Italian).* Rome, Italy: Istituto Poligrafico e Zecca dello Stato.

NTC18, Ministero delle Infrastrutture (2018). *Aggiornamento delle Norme tecniche per le costruzioni. Decreto Ministeriale 17 Gennaio 2018. Supplemento ordinario alla Gazzetta Ufficiale, n.42 del 20 Febbraio 2018 - Serie generale(in Italian).* Rome, Italy: Istituto Poligrafico e Zecca dello Stato.

Ntotsios, E., C. Papadimitriou, P. Panetsos, G. Karaiskos, K. Perros, and P.C. Perdikaris (2008). "Bridge health monitoring system based on vibration measurements." In: *Bulletin of Earthquake Engineering* 7 (2), p. 469.

Nuttli, O.W. (1979). "The relation of sustained maximum ground acceleration and velocity to earthquake intensity and magnitude." In: *Miscellaneous Paper S-71-1, Report 16, U.S. Army Corps of Engineers, Waterways Experiment Station.* Vicksburg, Mississippi.

NZS, 1170.5 Supp 1 (2004a). *Structural Design Actions - Part 5: Earthquake actions-New Zealand - Commentary.* Standards New Zealand.

NZS, 1170.5:2004 (2004b). *Structural Design Actions - Part 5: Earthquake actions-New Zealand.* Standards New Zealand.

Oh, C.K. and H. Sohn (2009). "Damage diagnosis under environmental and operational variations using unsupervised support vector machine." In: *Journal of Sound and Vibration* 325 (1–2), 224–239.

Oliveira, C.S., E. Cakti, D. Stengel, and M. Branco (2012). "Minaret behavior under earthquake loading: The case of historical Istanbul." In: *Earthquake Engineering and Structural Dynamics* 41 (1), pp. 19–39.

Overschee, P. Van and B.L. De Moor (1996). *Subspace identification for linear systems: theory-implementation-applications.* the Netherlands: Kluwer Academic Publishers.

Pacor, F. et al. (2011). "Overview of the Italian strong motion database ITACA 1.0." In: *Bulletin of Earthquake Engineering* 9 (6), pp. 1723–1739.

Park, Y-J. and A.H.-S. Ang (1985). "Mechanistic seismic damage model for reinforced concrete." In: *Journal of Structural Engineering* 111 (4), pp. 722–739.

Park, Y-J., A.H.-S. Ang, and Y.K. Wen (1985). "Seismic damage analysis of reinforced concrete buildings." In: *Journal of Structural Engineering* 111 (4), pp. 740–757.

Pasticier, L., C. Amadio, and M. Fragiacomo (2008). "Non-linear seismic analysis and vulnerability evaluation of a masonry building by means of the SAP2000 V.10 code." In: *Earthquake Engineering and Structural Dynamics* 37.3, pp. 467–485.

Pau, A. and F. Vestroni (2008). "Vibration analysis and dynamic characterization of the Colosseum." In: *Structural Control Health Monitoring* 15 (8), pp. 1105–1121.

Pellegrini, D., M. Girardi, P.B. Lourenço, M.G. Masciotta, N. Mendes, C. Padovani, and L.F. Ramos (2018). "Modal analysis of historical masonry structures: Linear perturbation and software benchmarking." In: *Construction and Building Materials* 189, pp. 1232–1250.

Pena, F., P.B. Lourenço, N. Mendes, and D.V. Oliveira (2010). "Numerical models for the seismic assessment of an old masonry tower." In: *Engineering Structures* 32 (5), pp. 1466–1478.

Perez, V. (1974). "Time dependent spectral analysis of thirty-one strong motion earthquake records." In: *Open File Report 74-48, U.S. Geological Survey*. Reston, Virginia.

Pieraccini, M., D. Dei, M. Betti, G. Bartoli, G. Tucci, and N. Guardini (2014). "Dynamic identification of historic masonry towers through an expeditious and no–contact approach: application to the Torre del Mangia in Siena (Italy)." In: *Journal of Cultural Heritage* 15 (3), pp. 275–282.

Plevris, V., G. Solorzano, and N. Bakas (2019). "Literature review of historical masonry structures with machine learning." In: *Proceedings of the 7th International Conference on Computational Methods in Structural Dynamics and Earthquake Engineering*. Crete, Greece, June 24th-26th 2019.

Psycharis, I.N., D.Y.Papastamatiou, and A.P. Alexandris (2000). "Parametric investigation of the stability of classical columns under harmonic and earthquake excitations." In: *Earthquake Engineering and Structural Dynamics* 29 (8), pp. 1093–1109.

Rainieri, C. and G. Fabbrocino (2010). "Automated output-only dynamic identification of civil engineering structures." In: *Mechanical Systems and Signal Processing* 24 (3), pp. 678–695.

Ramos, L.F., L. Marques, P.B. Lourenço, G. DeRoeck, A. Campos-Costa, and J. Roque (2010). "Monitoring historical masonry structures with operational modal analysis: two case studies." In: *Mechanical Systems and Signal Processing* 24 (5), pp. 1291–1305.

Ramos, L.F., R. Aguilar, and P.B. Lourenço (2011). "Operational modal analysis of historical constructions using commercial wireless platforms." In: *Structural Health Monitoring* 10 (5), pp. 511–521.

Ramos, L.F., R. Aguilar, P.B. Lourenço, and S. Moreira (2013). "Dynamic structural health monitoring of Saint Torcato church." In: *Mechanical Systems and Signal Processing* 35 (1-2), pp. 1–15.

Reed, J.W., N. Anderson, N.C. Chokshi, R.P. Kennedy, W.J. Metevia, D.K. Ostrom, and J.D. Stevenson (1988). "A criterion for determining exceedance of the operating basis earthquake: Final report." In: *Report NP-5930, Electric Power Research Institute - EPRI.* Palo Alto, California, USA.

Reynders, E., J. Houbrechts, and G. De Roeck (2012). "Fully automated (operational) modal analysis." In: *Mechanical Systems and Signal Processing* 29, pp. 228–250.

Riddell, R. (2007). "On Ground Motion Intensity Indices." In: *Earthquake Spectra* 23 (1), pp. 147–173.

Riddell, R. and J.E. Garcia (2001). "Hysteretic energy spectrum and damage control." In: *Earthquake Engineering and Structural Dynamics* 30 (12), pp. 1791–1816.

Rossetto, T., P. Gehl, S. Minas, C. Galasso, P. Duffour, J. Douglas, and O. Cook (2016). "FRACAS: A capacity spectrum approach for seismic fragility assessment including record-to-record variability." In: *Engineering Structures* 125, pp. 337–348.

Rytter, A. (1993). *Ph.D. Thesis: Vibrational Based Inspection of Civil Engineering Structures.* University of Aalborg, Aalborg, Denmark.

Saisi, A., C. Gentile, and M. Guidobaldi (2015). "Post-earthquake continuous dynamic monitoring of the Gabbia Tower in Mantua, Italy." In: *Construction and Building Materials* 81, pp. 101–112.

Saisi, A., C. Gentile, and A. Ruccolo (2018). "Continuous monitoring of a challenging heritage tower in Monza, Italy." In: *Journal of Civil Structural Health Monitoring* 8 (1), pp. 77–90.

Sandi, H. (1985). "Engineering Aspects and Possible Refinements of the Concept of Seismic Intensity." In: *Proceedings of the 12th Regional Seminar on Earthquake Engineering.* Vol. 3. Halkidiki, Greece, pp. 5359–5372.

Sarhosis, V., G. Milani, A. Formisano, and F. Fabbrocino (2018). "Evaluation of different approaches for the estimation of the seismic vulnerability of masonry towers." In: *Bulletin of Earthquake Engineering* 16 (3), pp. 1511–1545.

Sarma, S.K. and K.S. Yang (1987). "An evaluation of strong motion records and a new parameter A95." In: *Earthquake Engineering and Structural Dynamics* 15, pp. 119–132.

Sehgal, S. and H. Kumar (2016). "Structural dynamic model updating techniques: A state of the art review." In: *Archives of Computational Methods in Engineering* 23 (3), pp. 515–533.

Seismosoft, corp. (2018). *SeismoMatch - A computer program for spectrum matching of earthquake records*. Available from URL: www.seismosoft.com.

Shahi, R., N. Lam, E. Gad, J. Wilson, and K. Watson (2017). "Seismic Performance Behavior of Cold-Formed Steel Wall Panels by Quasi-static Tests and Incremental Dynamic Analyses." In: *Journal of Earthquake Engineering* 21 (3), pp. 411–438.

Simulia, corp. (2010). *Abaqus Analysis User's Manual. Volume III: Materials*. Dessault Systèmes, USA.

Sohn, H., C.R. Farrar, F.M. Hemez, and J.J. Czarnecki (2002a). "A Review of Structural Health Monitoring Literature 1996-2001." In: *Technical Report: LA-UR-02-2095; Los Alamos National Laboratory, United States*.

Sohn, H., K. Worden, and C.R. Farrar (2002b). "Statistical damage classification under changing environmental and operational conditions." In: *Journal of Intelligent Material Systems and Structures* 13 (9), 561–574.

Spyrakos, C.C., I.G. Raftoyiannis, and J.C. Ermopoulos (2004). "Condition assessment and retrofit of a historic steel-truss railway bridge." In: *Journal of Constructional Steel Research* 60 (8), pp. 1213–1225.

Tashkov, L., L. Krstevska, N. Naumovski, G. De Matteis, and G. Brando (2010). "Ambient Vibration Tests on Three Religious Buildings in Goriano Sicoli Damaged During the 2009 L'Aquila Earthquake." In: *COST ACTION C26: Urban Habitat Constructions under Catastrophic Events - Proceedings of the Final Conference*, pp. 433–438.

Tesfamariam, S., S.F. Stiemer, C. Dickof, and M.A. Bezabeh (2014). "Seismic Vulnerability Assessment of Hybrid Steel-Timber Structure: Steel Moment-Resisting Frames with CLT Infill." In: *Journal of Earthquake Engineering* 18 (6), pp. 929–944.

Thun, J.L. Von, L.H. Roehm, G.A. Scott, and J.A. Wilson (1988). "Earthquake ground motions for design and analysis of dams." In: *Proceedings of Earthquake Engineering and Soil Dynamics II - Recent Advances in Ground-Motion Evaluation, Geotechnical Special Publication, ASCE*. Vol. 20. United States, pp. 463–481.

Torelli, G., D. D'Ayala, M. Betti, and G. Bartoli (2019). "Analytical and numerical seismic assessment of heritage masonry towers." In: *Bulletin of Earthquake Engineering* 180, pp. 1–40.

Torres, W., J.L. Almazan, C. Sandoval, and R. Boroschek (2017). "Operational modal analysis and FE model updating of the Metropolitan Cathedral of Santiago, Chile." In: *Engineering Structures* 143, pp. 169–188.

Trifunac, M.D. and A.G. Brady (1975). "A study on the duration of strong earthquake ground motion." In: *Bulletin of the Seismological Society of America* 65, pp. 581–626.

Trifunac, M.D. and B. Westermo (1977). "A note on the correlation of frequency-dependent duration of strong earthquake ground motion with the MMI and geologic condition at the recording stations." In: *Bulletin of the Seismological Society of America* 67 (3), pp. 917–927.

Ubertini, F., C. Gentile, and A.L. Materazzi (2013). "Automated modal identification in operational conditions and its application to bridges." In: *Engineering Structures* 46, pp. 264–278.

Ubertini, F., G. Comanducci, and N. Cavalagli (2016). "Vibration-based structural health monitoring of a historic bell-tower using output-only measurements and multivariate statistical analysis." In: *Structural Health Monitoring* 15.4, pp. 438–457.

Ubertini, F., G. Comanducci, N. Cavalagli, A.L. Pisello, A.L. Materazzi, and F. Cotana (2017). "Environmental effects on natural frequencies of the San Pietro bell tower in Perugia, Italy, and their removal for structural performance assessment." In: *Mechanical Systems and Signal Processing* 82, pp. 307–322.

Ubertini, F., N. Cavalagli, A. Kita, and G. Comanducci (2018). "Assessment of a monumental masonry bell-tower after 2016 Central Italy seismic sequence by long-term SHM." In: *Bulletin of Earthquake Engineering* 16 (2), pp. 775–801.

Valente, M. and G. Milani (2016). "Seismic assessment of historical masonry towers by means of simplified approaches and standard (FEM)." In: *Construction and Building Materials* 108, pp. 74–104.

— (2018). "Effects of Geometrical Features on the Seismic Response of Historical Masonry Towers." In: *Journal of Earthquake Engineering* 22 (1), pp. 2–34.

— (2019a). "Damage assessment and collapse investigation of three historical masonry palaces under seismic actions." In: *Engineering Failure Analysis* 98, pp. 10–37.

— (2019b). "Earthquake-induced damage assessment and partial failure mechanisms of an Italian Medieval castle." In: *Engineering Failure Analysis* 99, pp. 292–309.

Valente, M., G. Milani, E. Grande, and A. Formisano (2019). "Historical masonry building aggregates: advanced numerical insight for an effective seismic assessment on two row housing compounds." In: *Engineering Structures* 190, pp. 360–379.

Vamvatsikos, D. (2002). *Ph.D. Thesis: Seismic Performance, Capacity and Reliability of Structures as Seen Through Incremental Dynamic Analysis*. Stanford, California, USA.

Vamvatsikos, D. and N.A. Cornell (2002). "Incremantal dynamic Analysis." In: *Earthquake Engineering and Structural Dynamics* 31 (3), pp. 491–514.

Vanmarcke, E.H. and S.P. Lai (1977). "Strong motion duration of earthquakes." In: *Report R77-16, Massachusetts Institute of Technology*. Cambridge, Massachusetts.

Venanzi, I., A. Kita, N. Cavalagli, L. Ierimonti, and F. Ubertini (2019). "Continuous OMA for Damage Detection and Localization in the Sciri tower in Perugia, Italy." In: *Proceedings of the 8th International Operational Modal Analysis Conference (IOMAC)*. Copenhagen, Denmark, May 13th-15th 2019.

— (2020). "Earthquake-induced damage localization in an historic masonry tower through long-term dynamic monitoring and FE model calibration." In: *Bulletin of Earthquake Engineering*, pp. 1–28.

Vetturini, R. (2014). "Campanile del Complesso Monumentale di San Pietro in Perugia (in Italian)." In: *document available online at http://divisare.com/projects/247982-riccardo-vetturini-campanile-del-complesso-monumentale-di-s-pietro-in-perugia*.

Worden, K., G. Manson, and N.R.J. Fieller (2000). "Damage detection using outlier analysis." In: *Journal of Sound and Vibration* 229 (3), pp. 647–667.

Worden, K., H. Sohn, and C.R. Farrar (2002). "Novelty detection in a changing environment: regression and interpolation approaches." In: *Journal of Sound and Vibration* 258 (4), pp. 741–761.

Yakut, A. and H. Yilmaz (2008). "Correlation of Deformation Demands with Ground Motion Intensity." In: *Journal of Structural Engineering* 134 (12), pp. 1818–1828.

Yan, A.M., G. Kerschen, P. De Boe, and J.C. Golinval (2005a). "Structural damage diagnosis under varying environmental conditions part I: a linear analysis." In: *Mechanical Systems and Signal Processing* 19 (4), pp. 847–864.

— (2005b). "Structural damage diagnosis under varying environmental conditions part II: local PCA for non-linear cases." In: *Mechanical Systems and Signal Processing* 19 (4), pp. 865–880.

Ye, L., Q. Ma, Z. Miao, H. Guan, and Y. Zhuge (2013). "Numerical and comparative study of earthquake intensity indices in seismic analysis." In: *The Structural Design of Tall and Special Buildings* 22 (4), pp. 362–381.

Zhu, T.J., W.K. Tso, and A.C. Heidebrecht (1988). "Effect of peak ground a/v ratio on structural damage." In: *Journal of Structural Engineering* 114 (5), pp. 1019–1037.